NASA-CR-199,231

NASA-CR-199231
19960009472

The Telecommunications and Data Acquisition Progress Report 42-122

April–June 1995

Joseph H. Yuen
Editor

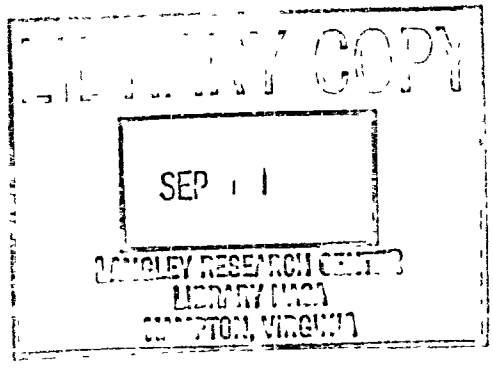

August 15, 1995

National Aeronautics and
Space Administration

Jet Propulsion Laboratory
California Institute of Technology
Pasadena, California

The Telecommunications and Data Acquisition Progress Report 42-122

April–June 1995

Joseph H. Yuen
Editor

August 15, 1995

National Aeronautics and
Space Administration

Jet Propulsion Laboratory
California Institute of Technology
Pasadena, California

N96-16638

The research described in this publication was carried out by the Jet Propulsion Laboratory, California Institute of Technology, under a contract with the National Aeronautics and Space Administration

Reference herein to any specific commercial product, process, or service by trade name, trademark, manufacturer, or otherwise, does not constitute or imply its endorsement by the United States Government or the Jet Propulsion Laboratory, California Institute of Technology

Preface

This quarterly publication provides archival reports on developments in programs managed by JPL's Telecommunications and Mission Operations Directorate (TMOD), which now includes the former Telecommunications and Data Acquisition (TDA) Office In space communications, radio navigation, radio science, and ground-based radio and radar astronomy, it reports on activities of the Deep Space Network (DSN) in planning, supporting research and technology, implementation, and operations Also included are standards activity at JPL for space data and information systems and reimbursable DSN work performed for other space agencies through NASA The preceding work is all performed for NASA's Office of Space Communications (OSC)

TMOD also performs work funded by other NASA program offices through and with the cooperation of OSC The first of these is the Orbital Debris Radar Program funded by the Office of Space Systems Development It exists at Goldstone only and makes use of the planetary radar capability when the antennas are configured as science instruments making direct observations of the planets, their satellites, and asteroids of our solar system The Office of Space Sciences funds the data reduction and science analyses of data obtained by the Goldstone Solar System Radar The antennas at all three complexes are also configured for radio astronomy research and, as such, conduct experiments funded by the National Science Foundation in the U S and other agencies at the overseas complexes These experiments are either in microwave spectroscopy or very long baseline interferometry

Finally, tasks funded under the JPL Director's Discretionary Fund and the Caltech President's Fund that involve TMOD are included

This and each succeeding issue of *The Telecommunications and Data Acquisition Progress Report* will present material in some, but not necessarily all, of the aforementioned programs

This Page Intentionally Left Blank

Contents

OSC TASKS
DSN Advanced Systems
TRACKING AND GROUND-BASED NAVIGATION

COMMUNICATIONS, SPACECRAFT–GROUND

DSN Systems Implementation
NETWORK UPGRADE AND SUSTAINING

Water Vapor Radiometer Measurements of the Tropospheric Delay Fluctuations at Goldstone Over a Full Year

S J Keihm
Microwave, Lidar, and Interferometer Technology Section

One year of near-continuous water vapor radiometer (WVR) measurements at DSS 13 has provided a database for characterizing the Goldstone tropospheric delay properties in a statistical sense. The results have been expressed in terms of the Allan standard deviation of delay and compared to a previous model for Goldstone fluctuations and the specifications of the Cassini Gravitational Wave Experiment (GWE). The new WVR data indicate that average fluctuation levels at hour time scales or less are ≈30-percent lower than the earlier Goldstone model predictions. At >1-h time scales, the WVR indicated fluctuation levels are in closer agreement with the model, although noise floor limitations may be artificially raising the average WVR-derived atmospheric fluctuation levels at the longer time scales. When scaled to two-way Doppler tracking at 20-deg elevation, as will occur for the GWE, these results indicate that Goldstone winter tropospheric delay fluctuations will typically be a factor of 10 larger than the GWE requirements at 1000 s and a factor of 4 larger at 10,000 s.

I. Introduction

Variations in the atmospheric path delay due to fluctuations in water vapor density are a major, if not the dominant, error source in dual-frequency or high single-frequency [e.g., Ka-band (32 GHz)] radio metric measurements such as very long baseline interferometry (VLBI) and Doppler spacecraft tracking. The current model for the spatial and temporal fluctuations of vapor density at Goldstone [1] indicates that the error budget requirements for the Cassini Gravitational Wave Experiment (GWE) cannot be met for any time scales from 100 to 10,000 s without an independent calibration of the vapor-induced delay fluctuations along the signal link line of sight. The fluctuation model is based on relatively small water vapor radiometer (WVR), VLBI, and radiosonde data sets from the three DSN sites and does not include sufficient sampling to characterize diurnal and seasonal variations. For the purpose of Cassini GWE planning, it is clearly desirable to assess the accuracy and variability of the current Goldstone fluctuation model. An improved, more detailed model will facilitate evaluation of the GWE tropospheric calibration error budget, since demands on a number of components of the calibration system scale linearly with the level of fluctuations.

Since October 5, 1993, the JPL R6 WVR has been operating almost continuously at Deep Space Station (DSS) 13, obtaining sky brightness temperature measurements at frequencies of 20.7 and 31.4 GHz. Data

processing through September 1994 has been completed, providing a rich data set for characterizing vapor-induced path delay fluctuations on all time scales >200 s and determining variations with time of day and season The WVR does not measure dry air delay variations However, because the vapor-induced fluctuations are much larger than the dry fluctuations at all time scales, the WVR measurements essentially characterize the total effect of atmospheric refractivity fluctuations This article describes the WVR results primarily in terms of zenith path delay variability, using the Allan standard deviation (ASD) parameter [2] In Section II, brief instrument and operation descriptions for the R6 WVR will be presented Pertinent details of the WVR processing are presented in the Appendix Results are presented in Section III After displaying the daily and monthly averaged path delay time series for the year's data, emphasis is placed on the ASD of the measured delays over time intervals relevant to the Cassini GWE, 200 to 12,800 s Seasonal and day/night contrasts are illustrated Section IV discusses implications for the Cassini GWE tropospheric calibration effort, and Section V summarizes the results

II. R6 WVR Instrument Description and Operation

The R6 water vapor radiometer (Fig 1) is a two-channel instrument that measures sky brightness temperatures at 20 7 and 31 4 GHz Design specifications are described in detail in [3] For each channel, the IF bandwidth is 100 MHz (double side band) and the antenna beamwidth is 7 deg with beam efficiency equal to 99 9 percent for ± 15 deg around beam center The mechanical mount allows elevation scanning from horizon to horizon and azimuth scanning over ≈ 85 percent of the full circle Both the elevation and azimuth slewing rates are ≈ 3 deg/s Estimated elevation position accuracy is 0 5 deg Estimated absolute antenna temperature accuracy is 0 5 K, based on tip curve calibration and correlations of gain variations with measured instrument temperatures (see Appendix) The measured 1-s antenna temperature noise is ≈ 0 06 K, and this value is characteristic of the precision of 1-s measurements over time scales of minutes or less At longer time scales, instrument temperature variations cause gain changes that cannot be perfectly monitored in the processing, leading to a reduction in precision Based on previous experiments with side-by-side WVRs,[1] antenna temperature precision of 0 1 K has been estimated over time scales of hours A more detailed discussion of the WVR calibration processing is given in the Appendix

At the DSS-13 site, the R6 WVR is deployed on the northeast corner of the control building, approximately 400 m from the 34-m DSN antenna It has operated since October 5, 1993, in a continuous tipping-curve mode that provides calibration monitoring in clear weather and sky brightness temperature measurements for all nonraining conditions at elevation positions of 30, 42, 90 (zenith), 138, and 150 deg If alternating azimuths are specified in the operating program, then four azimuth positions are sampled for each of the nonzenith elevation positions (since the 138- and 150-deg positions are equivalent to the 30- and 42-deg elevations but at opposite azimuth) The complete tip curve elevation sequence is 30, 42, 90, 138, 150, 138, 90, 42, and 30 deg, requiring ≈ 4 min to complete Most of the time is spent in the changing of elevation positions, during which time no sky measurements are obtained At each fixed elevation position, 1 s of sky integrations are obtained for each channel with the receiver switched to the feedhorn, followed by 1 s of base count measurements (each channel) obtained with the receiver switched to an internal ambient reference load This sequence of measurements provides absolute gain calibration by effectively using the known cosmic background brightness temperature as a cold target and the internal reference load as an ambient target Details of the tip curve calibration formulation are included in the Appendix

Using derived gain functions, updated every 3 days, zenith brightness temperature time series were computed by averaging the two 90-deg elevation sky and base counts of each tip curve and applying the radiometer calibration equation (Appendix) Thus, each brightness temperature comprised 2 s of sky integration over a ≈ 4-min interval with effective ΔT noise of ≈ 0 04 K

---

[1] S J Keihm, *Water Vapor Radiometer Intercomparison Experiment Platteville, Colorado, March 1–14, 1991*, JPL D-8898 (internal document), Jet Propulsion Laboratory, Pasadena, California, 1991

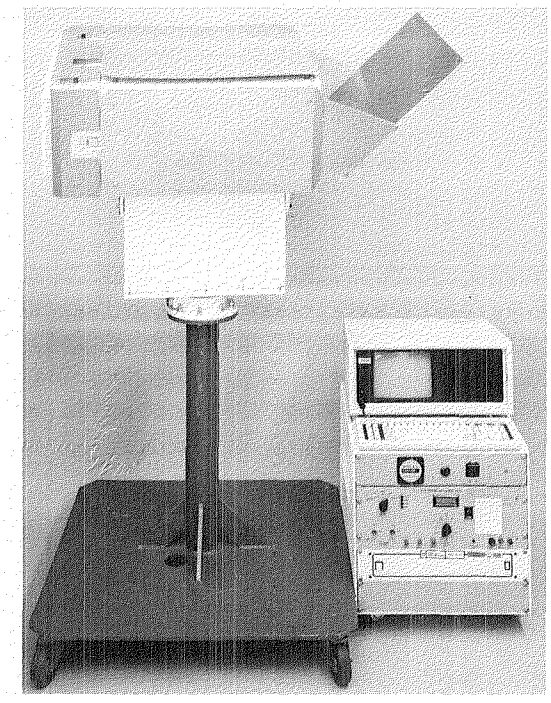

Fig. 1. R6 water vapor radiometer deployed at Goldstone DSS 13.

III. Results

A. Path Delay Time Series

The WVR-measured 20.7- and 31.4-GHz zenith brightness temperatures from October 1993 through September 1994 were converted to a Goldstone zenith path delay (PD) time series using the retrieval algorithm described in the Appendix. A 1-month segment of the 4-min sampled PD time series is shown in Fig. 2. The September 1994 interval was chosen because it exhibits the full range of Goldstone conditions and some of the most rapid large-scale variations seen in the data. (The missing data through September 6 are due to an operational failure that commenced on August 26.) Path delay variations of 5 to 10 cm are seen to occur over time scales of hours on the 8th, 10th, 17th, 24th, and 27th of the month. There is also a week-long interval of extremely dry conditions (PD $\approx$5 cm) followed by a week of much more humid conditions (PD $\approx$11 cm). The September data illustrate the potential variability of Goldstone summer conditions. Winter conditions are generally drier and more stable, as illustrated in the January results (Fig. 3). Typical winter path delays are in the 3- to 5-cm range, with occasional fluctuations to the $\approx$10-cm level.

Daily-averaged path delays for the entire 1-year data set are shown in Fig. 4. Both clear and cloudy conditions are included in the averaging over 24-h intervals. Seasonal variations are apparent. Large fluctuations occur throughout the year, although their durations appear much shorter during the winter months. The measured path delay annual mean for Goldstone is 6.4 cm. The average 24-h standard variation is 0.9 cm.

B. Path Delay Fluctuation Statistics

The Allan standard deviation is useful for distinguishing the relative contributions of true path delay fluctuations from WVR instrument effects. It is also the parameter used to define the requirements and

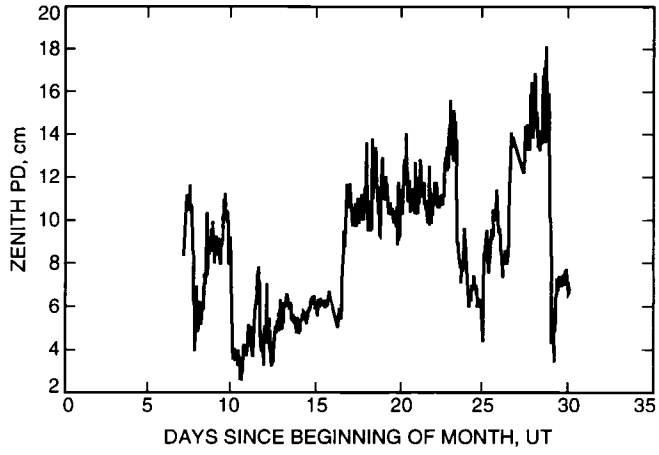

Fig 2 WVR-derived zenith wet path delay at DSS 13, September 1994

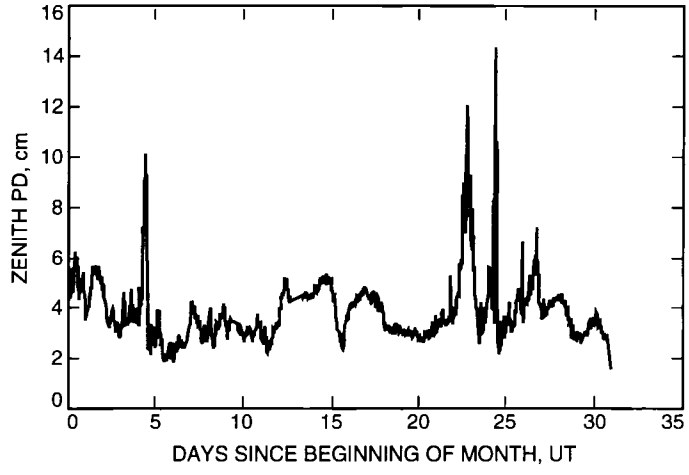

Fig 3 WVR-derived zenith wet path delay at DSS 13, January 1994

goals for tropospheric delay calibration for the Cassini GWE For a time interval Δt, the ASD for vapor-induced delay, δ, is defined as

$$ASD(\Delta t) = \left\{ \frac{\left\langle [\delta(t + 2\Delta t) - 2\delta(t + \Delta t) + \delta(t)]^2 \right\rangle}{2(\Delta t)^2} \right\}^{1/2} \quad (1)$$

in s/s where <> denotes ensemble averaging, $\delta = PD/c$ is the delay in s, and c equals the speed of light Equation (1) essentially characterizes the nonlinear variability of the delay or, equivalently, the variability after any linear trend is removed

The ASD of delay may be calculated from the WVR measurements by the application of Eq (1) after the brightness temperature measurements have been converted to the delay variable The results to be presented are based on ≈24-h intervals of continuous clear weather data only Clouds do not add a significant component to the delay or delay fluctuations However, they do contribute significantly to

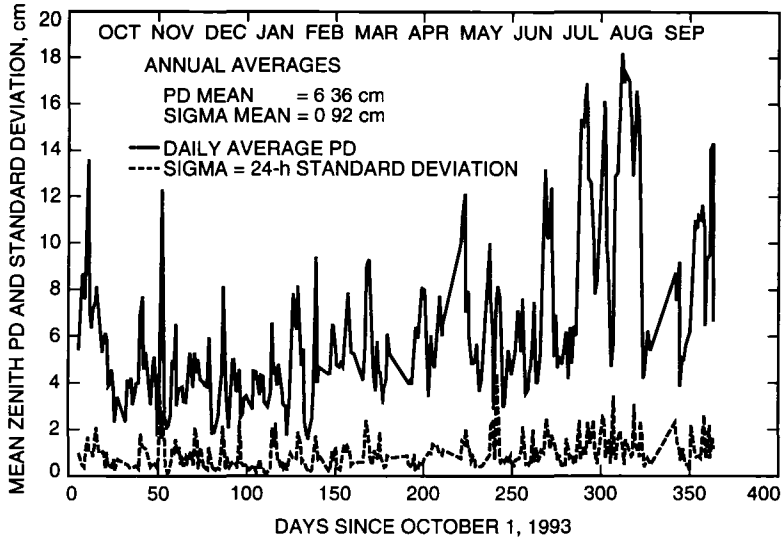

Fig 4 WVR-derived daily and standard deviation of zenith path delay at DSS 13, October 1993 through September 1994

the brightness temperature measurements of both WVR channels Because clouds have spatial structure comparable to and smaller than the WVR beams, path delay retrievals under cloudy conditions are inherently "noisy," and it is difficult to differentiate between the true variability that would be seen by a DSN antenna and the WVR-measured variability that is contaminated by the beam-smearing effects

When only clear weather data are included, the path delay variability can be calculated using only the 20 7-GHz brightness temperature measurements ASD values have been computed for Δt values of 200, 400, 800, 1600, 3200 6400, and 12,800 s using ≈24-h WVR data intervals from October 1993 through September 1994 The continuous clear weather TB20 7 data sets were first interpolated at 200-s intervals to facilitate the computations of Eq (1) The results are shown in Figs 5(a) through 5(d) for four of the time scales that nearly span the intervals of interest (100 to 10,000 s) for the Cassini GWE The Δt = 200-s data include a +22-percent correction that accounts for the suppression of the ASD due to each sample being the average of two zenith measurements ≈100 s apart [2] At longer time scales, the effect is negligible Also shown in the plots are the previous model for the Goldstone mean fluctuations and the WVR ASD measurement noise floor that would be produced by the estimated precision (varying with Δt due to gain fluctuations) of the individual TB20 7 measurements

The "Goldstone model" refers to the Kolmogorov turbulence model for atmospheric refractivity variations [1] and the derived annual mean structure constant parameter for Goldstone [4] The basic assumptions are that the magnitude of vapor-induced spatial variations in refractivity vary with the 1/3 power of distance, and that temporal variations are caused by spatial variations that are translated over a site by the wind The constant of proportionality between the fluctuations' magnitude and the 1/3 power of distance is called the structure constant, C_N, and its value, for a given level of delay variability, depends on the assumptions of effective troposphere height and wind speed Based primarily on VLBI measurements, and assuming effective tropospheric height and wind speed of 2 km and 8 m/s, the Goldstone model is characterized by a structure constant of $C_N = 7\ \ 10^{-8}\ \mathrm{m}^{-1/3}$ and has been used to calculate the "Goldstone Model" fluctuation levels referred to in Figs 5 through 7

The first clear impression from the Fig 5 results is that the WVR-measured average Goldstone fluctuations are significantly lower than previously modeled, especially at the shorter time scales The WVR

[2] R Linfield, Jet Propulsion Laboratory, Pasadena, California, provided the calculations for assessing the effect of two-sample averaging on the 200-s time scale ASD measurements

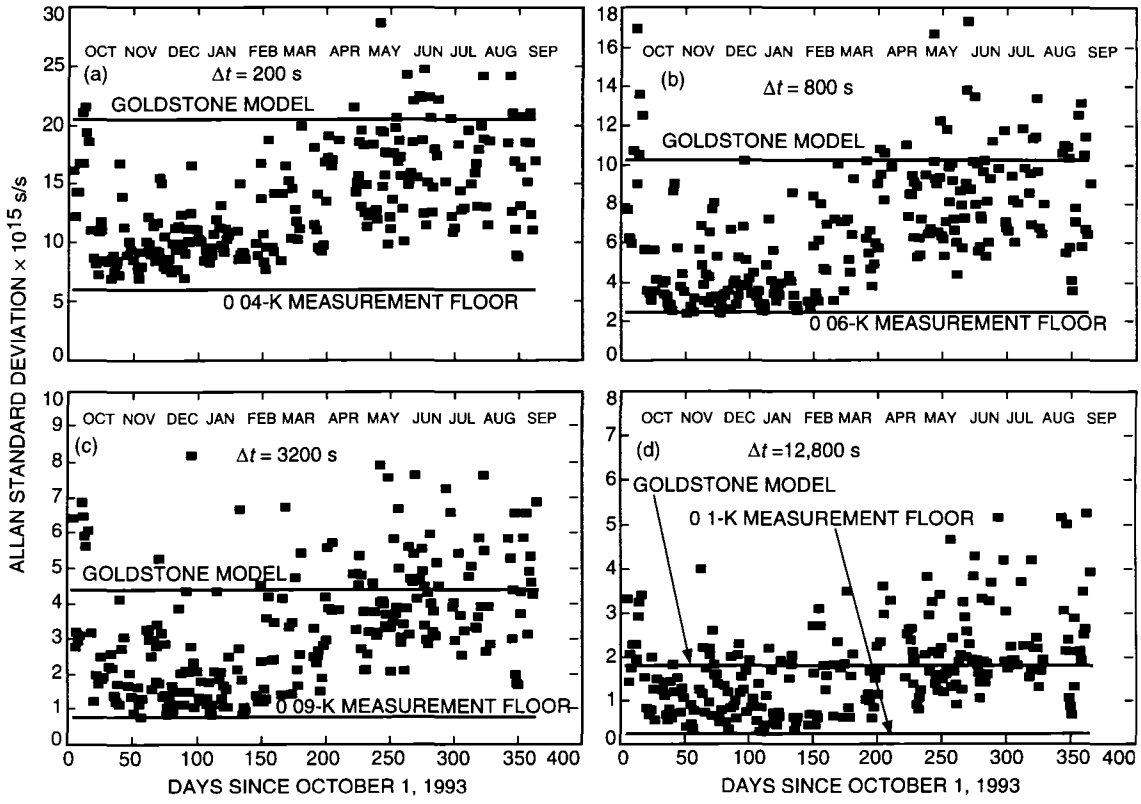

Fig 5 WVR-derived Allan standard deviation of one-way zenith path delay at DSS 13, October 1993 through September 1994 Each data point represents the ASD calculated from ≈24 hours of continuous cloud-free measurements (a) Δt = 200 s, (b) Δt = 800 s, (c) Δt = 3200 s, and (d) Δt = 12,800 s

data indicate that the October 1993 through September 1994 mean fluctuation levels were ≈30- to 35-percent lower than the previous Goldstone model at time scales <1 h At the longer time scales, the current WVR results approach the Goldstone model in terms of all-season average

In examining the results shown in Figs 5(a) through 5(d), it is important to keep in mind that the WVR measurement "noise" floor determines a lower bound of measurable tropospheric fluctuations For the ASD measurements, contributions from the instrument and troposphere add in quadrature, so that data close to the true measurement noise floor only place an upper bound on the true tropospheric component The measurement noise floors shown in Figs 5(a) through 5(d) are estimates based on the inherent instrument noise temperature, integration time, and gain stability At all time scales, a significant fraction of the data is dominated by instrument variations, and the true atmospheric fluctuation levels lie below the indicated noise floors Thus, "average" conditions as determined by the WVR measurements will always be biased high, dependent on the true instrument noise floor

The second conclusion inferred from the WVR ASD results is that there are large seasonal variations in the average fluctuation levels and large scatter throughout the year To derive an updated Goldstone model with seasonal dependence, the data of Fig 5 have been averaged by month, as shown in Fig 6 Also shown in Fig 6 are monthly averaged ASD results for subsets of the original 24-h intervals, including only the 9 p m through 5 a m local nighttime measurements As expected, the night-only fluctuations show a general reduction in fluctuation levels relative to the 24-h data, with the effect most pronounced at the shortest time scales However, the day/night contrast is strongly seasonally dependent, with the largest differences during the summer months and almost no difference during the November through February time frame, when overall fluctuation levels are lowest

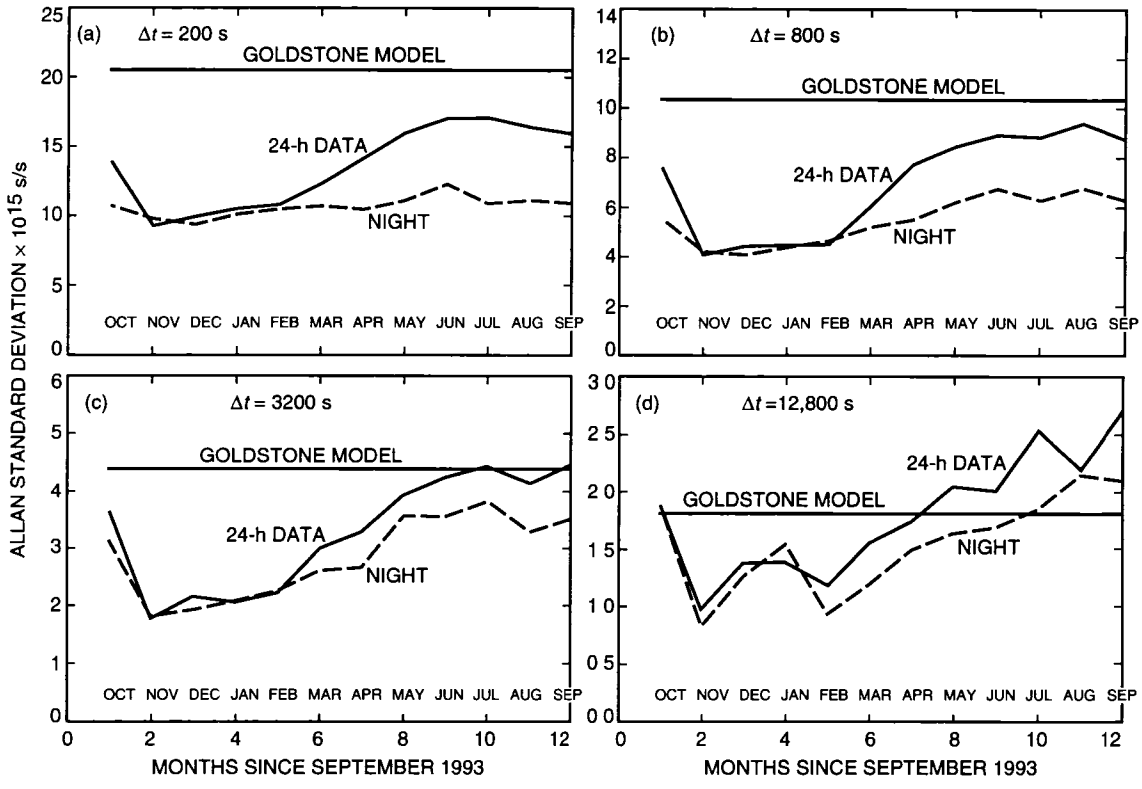

Fig 6 Monthly averaged Allan standard deviation of one-way zenith path delay at DSS 13 The "night" data refer to calculations that used only 9 p m through 5 a m local time WVR measurements (a) Δt = 200 s, (b) Δt = 800 s, (c) Δt = 3200 s, and (d) Δt = 12,800 s

IV. Implications for Cassini GWE

The WVR-derived results for Goldstone path delay fluctuations, with seasonal and day/night dependencies, provide a means for assessing the troposphere's expected impact on radio metric measurements For the Cassini Gravitational Wave Experiment, planned for Goldstone during winter months, the detection threshold will be limited by uncalibrated troposphere delay fluctuations The importance of the effect is illustrated by comparing the measured average fluctuations for Goldstone with the Cassini specifications[3] of tolerable uncalibrated fluctuation levels, as shown in Fig 7 The WVR-derived fluctuation levels have been recomputed to account for the two-way Doppler tracking mode of the GWE at 20-deg elevation, the lowest elevation angle to be used in the experiment For time scales $\geq$200 s, the tropospheric fluctuations scale approximately linearly with air mass, resulting in a factor of 3 increase for 20-deg elevation relative to zenith For Δt intervals $\leq \approx t_{RT}/2$, where t_{RT} is the GWE round-trip travel time, the two-way ASD is $\approx \sqrt{2}$ times the one-way ASD For $\Delta t \approx t_{RD}$, the one-way and two-way ASD values are equal For $\Delta t >> t_{RT}$, the two-way/one-way ASD ratio approaches a value of 2 The net effect of converting the modeled and measured one-way zenith ASD values shown in Fig 6 to two-way 20-deg elevation fluctuation levels, shown in Fig 7, is an increase by a factor of $\approx$4, with the results not significantly sensitive to the signal round-trip travel time The selected value of t_{RT} = 6400 s is near the average for the planned GWE measurements

For time scales from 200 to 1000 s, average winter conditions at Goldstone will require a calibration correction of a factor of $\approx$10 to meet the GWE requirements at 20-deg elevation At 10,000 s, the average

[3] *Cassini Radio Science Ground System D-Level and Cost Review* (internal document), Jet Propulsion Laboratory, Pasadena, California, February 27, 1995

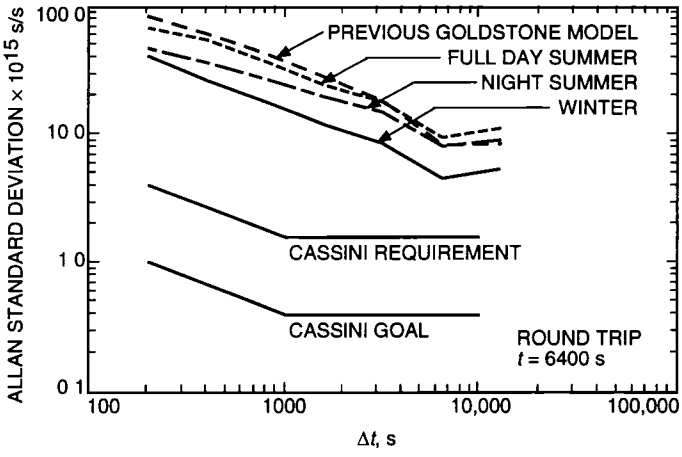

Fig 7 Comparison of modeled and WVR-measured two-way Allan standard deviation for Goldstone at 20-deg elevation with Cassini Gravitational Wave Experiment requirements and goals

winter fluctuation levels exceed the GWE requirements by a factor of 4 To meet the GWE goals, the tropospheric calibration requirements will be 4 times more stringent at all time scales Expressed equivalently, at the 200- to 1000-s time scales, the GWE requirement/goal at 20-deg elevation will necessitate an independent tropospheric calibration system that removes 90/98 percent of the expected level of fluctuations At the longest GWE time scales, the demands on the calibration system will be less severe but still require measurements with significantly greater stability than now obtainable from the current generation of water vapor radiometers

V. Summary

One year of near-continuous WVR measurements at DSS 13 has provided a database for characterizing the Goldstone tropospheric delay properties in a statistical sense For the period from October 5, 1993, through September 30, 1994, the mean zenith wet path delay was 6 4 cm with an average standard deviation of 0 9 cm over 24-h intervals The path-delay time series data revealed expected seasonal dependencies with frequent large day-to-day variations, especially in the summer months

Calculations based on ≈24-h intervals of clear data produced wet delay fluctuation levels over 1 full year, expressed as the Allan standard deviation of zenith delay Compared to the previous Goldstone model, the annually averaged WVR results are 30- to 35-percent lower for all time scales from 200 s to 30 min For time scales of ≈1 to 4 h, the WVR–Goldstone model differences decrease from ≈25 to 0 percent The apparent convergence between the WVR results and the previous Goldstone model at the longest time scales may be partially attributed to the noise floor of the WVR measurements

Seasonal variations of ±30 to 40 percent from the annual mean ASD occur at all time scales, with the November through March period lowest and the June through September period highest Day/night contrasts are apparent during the summer months, for which 9 p m through 5 a m fluctuation levels are 20- to 30-percent lower than the 24-h averages No significant day/night contrasts were revealed in the November through March time frame For clear conditions, it is not expected that the annual or seasonally averaged Goldstone fluctuation levels will vary significantly from year to year Based on the annual repeatability of clear weather 31-GHz atmospheric noise measurements from the Madrid DSN station,[4]

[4] S J Keihm, B L Gary, and S J Walter, *Spain 31 GHz Observations of Sky Brightness Temperatures June 1990–June 1992*, JPL D-10710 (internal document), Jet Propulsion Laboratory, Pasadena, California, October 1, 1992

an upper limit of ≈15 percent is estimated for year-to-year variations in the average Goldstone fluctuation levels Since almost a second full year of Goldstone WVR data is now available, the representativeness of the new Goldstone model can be tested

Comparisons of measured fluctuation levels with the Cassini GWE error budget reveal that an advanced calibration system must be implemented to meet the GWE requirements and approach the GWE goals at all time scales For expected winter conditions, the calibration system must remove up to 98 percent of the tropospheric signal, dependent on time scale and elevation angle, to approach the GWE goals This will require a nearly order-of-magnitude improvement relative to current WVR instrument stability

Acknowledgments

R Denning and R Swindlehurst of the Microwave, Lidar, and Interferometer Technology Section refurbished the R6 WVR and operating software prior to Goldstone deployment In almost 2 years of near-continuous operation, no major failures have occurred C Goodson, G Bury, and the entire operations personnel at DSS 13 provided the daily monitoring of the R6 WVR operations that has produced 90-percent efficient data acquisition since the instrument deployment in October of 1993 R Linfield, S Walter, L Teitelbaum, and M Mahoney provided incisive comments and very useful recommendations in their reviews of preliminary drafts of this article

References

[1] R N Treuhaft and G E Lanyi, "The Effect of Dynamic Wet Troposphere on Radio Interferometric Measurements," *Radio Sci* , vol 22, no 22, pp 251–265, 1987

[2] D W Allan, "Statistics of Atomic Frequency Standards," *Proc IEEE*, vol 54, no 2, pp 221–230, 1966

[3] G M Resch, M C Chavez, and N I Yamane, "Description and Overview of an Instrument Designed to Measure Line-Of-Sight Delay Due to Water Vapor," *The Telecommunications and Data Acquisition Progress Report 42-72, October–December 1982*, Jet Propulsion Laboratory, Pasadena, California, pp 1–19, February 15, 1983

[4] R P Linfield and J Z Wilcox, "Radio Metric Errors Due to Mismatch and Offset Between a DSN Antenna Beam and the Beam of a Troposphere Calibration Instrument," *The Telecommunications and Data Acquisition Progress Report 42-114, April–June 1993*, Jet Propulsion Laboratory, Pasadena, California, pp 1–13, August 15, 1993

Appendix
WVR Data Processing

Conversion of radiometer detector counts to sky brightness temperatures requires the determination of a system gain and offset and the monitoring of any variation of these parameters with time Offset is provided by the detector response to an internal reference load of known temperature Gain is provided by extrapolating the tip curve data to determine the detector response to the known cosmic background flux

$$G = \frac{CT_{base} - CT_{cos}}{T_{base} - T_{cos}} \tag{A-1}$$

where CT_{base} are the base load (reference) counts for base temperature T_{base}, and CT_{cos} are the extrapolated antenna counts for a target temperature of T_{cos} In the actual calibration processing, both gain and atmospheric opacity are determined together by requiring the brightness temperature (TB) values obtained from the antenna counts versus elevation data to fit the air mass dependence predicted by the simplified form of the radiative transfer equation, assuming a horizontally stratified atmosphere

$$TB(M) = T_{base} - \frac{CT_{base} - CT_{sky}(M)}{G} = T_{eff} \left(1 - e^{-M\tau}\right) + T_{cos} \; e^{-M\tau} \tag{A-2}$$

where $M = 1/\sin(el)$ is air mass, τ is the zenith opacity, T_{eff} is the effective radiating temperature of the atmosphere, and $CT_{sky}(M)$ are the elevation-dependent detector counts when the switch is set to the antenna position Given the sky counts for $M = 1\,0$, $1\,5$, and $2\,0$, Eq (A-2) can be solved iteratively for both τ and G Gain results are insensitive to uncertainties in T_{eff} For all of the Goldstone R6 processing, a value of T_{eff} =285 K was used

Departures from horizontal stratification, primarily in the atmospheric distribution of water vapor, contribute scatter to the clear weather tip-curve gain determinations Variations of instrument component losses with ambient temperature cause significant gain variations on longer time scales These effects are smoothed and monitored by correlating tip-derived gains with each channel's mixer temperature The estimated resultant gain precision is ≈0 03 percent (≈0 1 K in TB) over time scales of hours Absolute accuracies for both channels are estimated at the 0 5-K level, with the major uncertainties due to uncorrected detector nonlinearities and beam-smearing effects on the tip gain determinations For the Goldstone R6 data, gain function fits were performed for three-day tip data sets The three-day intervals were chosen as a compromise between the considerations of processing labor and the time variability of gain fit parameters

Brightness temperatures computed from the first equality of Eq (A-2) are converted to path delay using a statistical algorithm based on radiosonde data from Desert Rock, Nevada, a site with comparable climatology and nearly the same surface elevation as Goldstone Using the zenith brightness temperature results from both the 20 7- and 31 4-GHz channels, both integrated cloud liquid (L_z) and vapor-induced path delay (PD) are computed

$$L_z(\mu\text{m}) = -146 - 8\,81 \;\; TB_{20\,7} + 22\,99 \;\; TB_{31\,4} \tag{A-3}$$

$$PD \text{ (cm)} = -4\,95 + 0\,374 \;\; TB_{20\,7} + 0\,358 \;\; TB_{31\,4} \quad \text{for } L_z < 100 \tag{A-4}$$

$$PD\ (\text{cm}) = -1\ 24 + 0\ 695\ \ TB_{20\ 7} - 0\ 333\ \ TB_{31\ 4} \quad \text{for } L_z > 100 \tag{A-5}$$

For clear conditions, path delays can also be computed from the single-channel (20 7-GHz) brightness temperatures

$$PD\ (\text{cm}) = -2\ 83 + 0\ 524\ \ TB_{20\ 7} \tag{A-6}$$

Estimated errors in derived path delay values are $\pm 0\ 5$ cm (absolute) for clear conditions and $\pm 0\ 8$ cm for cloudy ($L_z > 100$) conditions The precision of path delay variations is estimated to be $\approx 0\ 05$ cm over hour time scales and is not sensitive to the retrieval algorithm uncertainties

A Test of Water Vapor Radiometer-Based Troposphere Calibration Using VLBI Observations on a 21-Kilometer Baseline

R P Linfield, L P Teitelbaum, and L J Skjerve
Tracking Systems and Applications Section

S J Keihm, S J Walter, and M J Mahoney
Microwave, Lidar, and Interferometer Technology Section

R N Treuhaft
Radar Science and Engineering Section

Simultaneous very long baseline interferometry (VLBI) and water vapor radiometer (WVR) measurements on a 21-km baseline showed that calibration by WVRs removed a significant fraction of the effect of tropospheric delay fluctuations for these experiments. From comparison of the residual delay variations within scans and between scans, the total tropospheric contribution to the delay residuals for each of the three 5- to 20-hour sessions was estimated as 1, 17, and 10 percent, with the first value being uncertain. The observed improvement in rms residual delay from WVR calibration during these three sessions was 4, 16, and 2 percent, respectively. The improvement is consistent with the estimated 2- to 3-mm path delay precision of current WVRs. The VLBI measurements, of natural radio sources, were conducted in April and May 1993 at Goldstone, California. Dual-frequency (2.3- and 8.4-GHz) observations were employed to remove the effects of charged particles from the data. Measurements with co-pointed WVRs, located within 50 m of the axis of each antenna, were performed to test the ability of the WVRs to calibrate line-of-sight path delays. Factors that made WVR performance assessment difficult included (1) the fact that the level of tropospheric fluctuations was smaller than is typical for Goldstone during these experiments and (2) VLBI delay variations on longer time scales (i.e., over multiple scans) contained uncalibrated instrumental effects (probably a result of slow temperature variations in the VLBI hardware) that were larger than the tropospheric effects.

I. Introduction

Ground-based observations at radio frequencies of compact natural radio sources or spacecraft can yield highly accurate position or velocity measurements. Very long baseline interferometry (VLBI) measures the relative delay in arrival time of wave fronts from a source at two or more sites. Spacecraft range

and Doppler tracking measure the delay, or its time derivative, of a round-trip radio signal transmitted between the ground and the spacecraft In order to extract an angular position from a VLBI delay, a distance from a range measurement, or a radial velocity from a Doppler measurement, nongeometric components of the delay/delay rate must be removed Many of these delay error sources can be estimated from VLBI data, provided that the functional form of the delay signatures of the error sources is known, and that these functional forms are significantly different from those induced by source angular position shifts As an example, a clock offset and a linear (in time) clock rate can be estimated (and subtracted) from VLBI observations if multiple sources are observed or if one source is observed for an extended period of time

The troposphere contributes approximately 7 ns of delay at the zenith, equivalent to a path length increase of $\Delta l_{zen} \approx 2\ 1$ m (Hereafter, whenever a length is given for a delay, the delay in time units is that length divided by the speed of light) At an elevation angle θ, the effective path length increase is $\approx \Delta l_{zen}/\sin\theta$ One can solve for the mean tropospheric zenith delay over some period of time by using a mapping function to relate the delay $\tau(\theta)$ at elevation angle θ to the zenith delay τ_{zen} ($\tau(\theta) = \tau_{zen}/\sin\theta$ is an approximate mapping function) Because of inhomogeneities in tropospheric refractivity, due primarily to inhomogeneities in water vapor density, estimating and subtracting such a mean troposphere will still leave a residual tropospheric delay that will corrupt the data

The residual tropospheric delay was the largest error source in the astrometric VLBI observations of [1], where the authors were able to reduce the effects of the troposphere to ~1 cm on a 10,000-km baseline This corresponds to an angular error of ~1 nanoradian (nrad), or 200 microarcseconds over angular scales of 30 deg on the sky In order to achieve angular accuracies better than 1 nrad with VLBI, direct calibration of tropospheric delay is required A sufficiently accurate line-of-sight delay calibration would enable substantial improvements in the accuracy of VLBI and spacecraft Doppler tracking measurements

Because water vapor accounts for nearly all the small-scale structure in refractivity at microwave frequencies, efforts to calibrate line-of-sight delay have focused on measurements of water vapor Water vapor radiometers (WVRs) measure thermal emission from water vapor at microwave frequencies In order to test WVR wet delay calibration techniques, we designed and conducted a short-baseline VLBI experiment By using a short baseline (21 km instead of the 3000- to 10,000-km baselines typically used for astrometric VLBI), many nontropospheric error sources were greatly reduced Any geophysical modeling errors at each antenna cancel nearly perfectly over such a short baseline Source position and Earth rotation/orientation errors result in very small delay errors The short baseline allowed the use of the VLBI phase delay data type (described in Section IV), greatly reducing the thermal noise level We expected tropospheric and instrumental (VLBI hardware) effects to be the two largest contributions to the measured residual delays

II. Wet Troposphere Calibration

A. Wet Delay Formulation

The effect of the atmosphere on the propagation of a microwave signal, expressed as a range correction, or path delay τ, is the difference between the electrical and geometric path lengths

$$\tau = \int_0^\infty (n-1)ds = 10^{-6}\int_0^\infty N(s)ds \tag{1}$$

Here n is the refractive index, N is the refractivity, defined as the difference between the refractive index and unity, in parts per million, and the integrals are evaluated along the line-of-sight path through the atmosphere

The refractivity is typically expressed as the sum of dry and wet (water vapor-induced) components [2], in which the dry component depends only on the density of dry air and the wet component depends on water vapor density ρ_v and physical temperature T Using the formulation of [3], the wet refractivity component N_{wet} can be expressed as

$$N_{wet} = \left(K_1 \rho_v + K_2 \frac{\rho_v}{T}\right) Z_w^{-1} \tag{2}$$

The Z_w, which accounts for nonideal gas behavior, has a value of 1 0 within 2×10^{-3} for atmospheric conditions [4] Using the laboratory measurements of [5] for the constants K_1 and K_2, the wet delay τ_{wet} can be expressed as

$$\tau_{wet} = 10^{-6} \int_0^\infty \left(0\ 1095 \rho_v + 1733 \frac{\rho_v}{T}\right) ds \tag{3}$$

Here ρ_v is in units of g/m^3, T is in kelvins, and τ_{wet} is in seconds

Extensive evaluation [6] of the theoretical and experimental determinations of the vapor-induced refractivity component indicates that the relationship expressed in Eq (3) is accurate at the 0 5-percent level At microwave frequencies below 30 GHz, the wet refractivity component is practically nondispersive and the wet delay can be considered to be frequency independent

B. WVR Measurements of the Wet Delay

Measurement of thermal emission from the optically thin 22-GHz water vapor spectral line is one potential method for calibrating the line-of-sight wet delay A WVR measures sky brightness temperatures T_b at one or more frequencies near the 22-GHz peak, with an additional channel above 30 GHz to correct for emission from liquid water when clouds are present (e g , [2]) Portable WVRs are steerable in both azimuth and elevation and typically have half-power beam widths (HPBW) of 6 to 9 deg

WVR calibration is achieved by the use of an ambient reference target and tipping curves for system gain determination During tip curve operations, WVRs obtain sky measurements over a range of elevation angles and utilize an extrapolation to zero air mass M ($M \equiv 1/\sin\theta$, where θ is the elevation angle) to establish the cosmic background temperature as the cold reference The tip curve calibration method produces absolute brightness temperatures with accuracies <1 K and precisions <0 1 K for hour time scales For periods during which tip curves are not available (e g , during VLBI tracking), gain variations are estimated through their correlations with instrument temperatures These correlations are established by one day or more of prior tip data

The link between measured WVR brightness temperature T_b and atmospheric properties is provided by the standard microwave equation of radiative transfer for a nonscattering medium in local thermodynamic equilibrium [7]

$$T_b = \int_0^\infty T(s) \alpha(\rho_v, T, P) e^{-\tau(s)} ds + T_{MB} e^{-\tau(\infty)} \tag{4}$$

The optical depth, $\tau(s)$, is

$$\tau(s) = \int_0^s \alpha(\rho_v, T, P) ds \tag{5}$$

In Eqs (4) and (5), $\alpha(\rho_v, T, P)$ is the volume absorption coefficient, including contributions from molecular oxygen, water vapor, and suspended cloud liquid (when present) The absorption depends upon the water vapor density ρ_v (and liquid density when clouds are present), the temperature T, and the pressure P, each of which in turn is a function of position along the line-of-sight path The T_{MB} is the blackbody temperature of the cosmic microwave background radiation

For clear-sky conditions, WVR brightness temperature T_b and the wet path delay τ_{wet} are highly correlated, because both are approximately proportional to the integrated water vapor content along the line of sight This correlation has been demonstrated in a number of experiments that compared WVR-derived path delays to direct measurements with weather balloons [8,9] and inferred values from Global Positioning System (GPS) measurements [10,11]

Given a set of WVR brightness temperature measurements, the vapor-induced path delays are usually computed from a statistical retrieval (e g , [12]) Atmospheric profiles measured by radiosonde flights at selected sites are used to generate a computational database of path delays and corresponding WVR brightness temperatures for a wide range of atmospheric conditions Two or more years of twice-daily radiosonde profiles are typically used to characterize site conditions A linear fit to the database produces an equation relating path delay to WVR brightness temperatures For typical WVR measurement errors of 0 5 K, formal errors for retrieved zenith path delay of 2 to 3 mm are commonly obtained This corresponds approximately to a 2- to 3-percent error for calibration of average ($\approx$10-cm) zenith wet path delays at sites used for spacecraft tracking Other WVR wet path delay errors are described in Section II C

Independent wet delay calibration must be highly accurate in order to improve the accuracy of VLBI astrometric or spacecraft Doppler measurements (Spacecraft range measurements are currently limited by calibration uncertainty in the delays through electronics, rather than by the troposphere) VLBI astrometric measurements can be used to determine line-of-sight tropospheric delay to within $\approx$1 cm [1] The line-of-sight wet delay for an elevation angle of 15 deg is typically 30 to 70 cm, so a calibration precision (if not accuracy) of $\sim$1 percent is needed in order to improve the accuracy of astrometric VLBI or Doppler data A precision several times better than 1 percent is desired Although WVRs have been tested against radio interferometric measurements previously [13],[1] wet delay calibration at the 1-percent level has never been demonstrated The purpose of our observations was to find the limiting errors for such a demonstration

C. Error Sources in WVR Measurements of Wet Path Delay

The 2- to 3-mm formal error in WVR-derived zenith wet delay stated in Section II B includes only the effects of 0 5-K WVR "noise" and the variability of temperature and vapor height distribution The formal error represents the rms accuracy that one would expect for WVR measurements with zero bias, a perfect absorption model, and a pencil beam In applying WVR measurements as wet delay corrections for other instruments, a number of other error sources must be considered Because our observations measured the difference in delay at the two sites, our sensitivity to some classes of WVR errors was reduced

1. Unmonitored Gain Variations. WVR measurement errors are not properly characterized as pure noise with zero bias The most serious instrumental uncertainty is due to unmonitored gain variations over time scales of minutes–hours, due primarily to temperature variations of the WVR electronic

[1] C D Edwards, "Water Vapor Radiometer Line-of-Sight Calibration Capabilities," JPL Interoffice Memorandum 335 1-90-015 (internal document), Jet Propulsion Laboratory, Pasadena, California, March 30, 1990

components For the WVRs used in this experiment, gain variations were monitored to the 0 05- to 0 1-percent level, either by estimating the gain from its strong correlation with mixer temperature measured during tip curve calibration or by time interpolation between tip curve data obtained before and after the VLBI observations A 0 1-percent gain uncertainty corresponds to a 0 3-K WVR measurement error and a 1- to 2-mm uncertainty in the retrieved wet delay

2. WVR Elevation Pointing Errors. WVR pointing errors can be significant at low elevation angles where brightness temperature varies most strongly with air mass For the extremely dry conditions encountered at Goldstone during our observations, at 30 deg, the lowest WVR elevation angle employed, WVR brightness temperatures decreased by approximately 1 K for an elevation increase of 1 deg For elevation uncertainties $\sim$0 3 deg, typical of the Goldstone WVRs, the net effect on the wet delay retrieval error is $\leq$1 to 2 mm at a $\geq$30-deg elevation angle

3. Vapor Absorption Model Error. The absolute uncertainty in any single measurement of WVR-derived wet delay is normally dominated by the 5-percent uncertainty [14] in the adopted vapor absorption model that links measured brightness temperatures to integrated vapor and path delay For the dry Goldstone conditions, with average zenith wet delays of $\sim$5 cm, this absolute error component is 2 to 3 mm However, its effect was <1 mm, because the role of the WVRs in this VLBI experiment was to monitor the difference in delay between two sites, and the line-of-sight wet path delays at the two sites were similar

4 Beam Offset and Mismatch Errors The expected differences between wet delays sensed by WVR and DSN antennas depend on integration time, elevation angle, and the beam mismatch and beam axis offset between the instruments For the Goldstone experiment, WVRs with conical 6- to 9-deg HPBW beams were deployed $\approx$50 m from the DSS-13 (26-m-diameter) and DSS-15 (34-m-diameter) antennas Both of the DSN antennas have essentially cylindrical beams in the troposphere Based on a turbulence model for the troposphere [15], the expected delay difference between the WVR and DSN beams for integration times >2 min and elevation angles >20 deg is <0 15 mm [16]

D. Additional Instrumentation

The formal or "inherent" WVR path delay retrieval error of 2 to 3 mm, described in Section II B, is due primarily to variations of air temperature and water vapor density along the line of sight To calibrate this error, additional instrumentation was deployed at Goldstone for the VLBI/WVR experiment At DSS 15, a microwave temperature profiler (MTP) [17] was deployed Using elevation-scanning measurements near the 60-GHz O_2 absorption band, the MTP provides atmospheric temperature profile data with accuracies of 1 to 2 K for altitudes below 3 km [18], where most of the water vapor resides

In order to characterize the state of the atmosphere during the observations and to obtain independent site measurements of the vertical temperature and vapor density profiles, radiosondes were launched approximately every 6 hours Our launch sites were 200 to 400 m from each antenna Comparisons of the radiosonde measurements near the ground with measurements made by co-located surface sensors indicated that the radiosonde temperature and pressure measurements were accurate to 1 deg C and 3 mbar, respectively However, similar comparisons revealed large and variable discrepancies in relative humidity measurements We were thus unable to improve WVR path delay retrievals by constraining the relative height distribution of the vapor The humidity sensors were a brand of carbon hygristors known to have problems at low humidity levels Because of problems with the humidity sensors, we used the radiosonde data for only two purposes First, the temperature profiles were used as validation for the MTP measurements of lower troposphere temperature profiles Second, optical tracking of radiosonde flights at DSS 13 provided measurements of wind velocity and direction as a function of altitude These measurements were used in modeling the magnitude of tropospheric turbulence effects on our VLBI data

III. Observations and Data Reduction

A. VLBI

We conducted six VLBI observing sessions, their dates and durations are given in Table 1 We used two antennas of NASA's Deep Space Network in Goldstone, California DSS 13 (26-m diameter) and DSS 15 (34-m diameter) The two antennas are separated by 21 3 km along azimuth 313 deg (DSS 15 is north and west of DSS 13)

Table 1 VLBI observing dates, 1993

Session	Start day	Start UT	Duration, h
1	112	05 10	5 7
2	116	04 10	6 7
3	122	05 30	28 8
4	128	16 50	24 0
5	130	04 50	5 2
6	131	04 20	5 7

In addition, we observed with a 34-m-diameter antenna (DSS 65) in Madrid, Spain, during the first 24 h of session 3 and with a 34-m-diameter antenna (DSS 45) in Canberra, Australia, during all of session 4 Time on the DSS 15–DSS 65 baseline in session 3 and the DSS 15–DSS 45 baseline in session 4 had been previously allocated for astrometric VLBI observations For these two sessions, we used the observing schedules created for those observations These schedules were designed to provide geometric strength (i e , allow the separation of baseline, source position, and tropospheric effects) on long baselines The schedules emphasized two to four observations of each source, with each observation typically near rise, set, or transit at one of the two stations Only results on the DSS 13–DSS 15 baseline are reported in this article

For the other four 5- to 7-h sessions, our observing schedule was modified from an astrometric VLBI schedule to use stronger sources and have elevation angles >30 deg (thus allowing the co-pointing of WVRs, which cannot point below 30 deg without significant ground contamination of the measured brightness temperatures) In addition, we scheduled some long scans (300 to 700 s) on strong sources (typical scans were ≈150 s in length)

All VLBI observations used the Mk III recording system [19] in mode C, with five 2-MHz channels spanning 2200 to 2300 MHz (S-band) and nine 2-MHz channels spanning 8215 to 8583 MHz (X-band) Using two observing bands allows a calibration of the dispersive delay due to charged particles in the Earth's ionosphere and the interplanetary medium (For an observing frequency ν well above the plasma frequency, the charged particle delay is proportional to ν^{-2})

After each 2-MHz channel was mixed to baseband, it was sampled at the Nyquist rate, digitized to 1 bit, and recorded on tape In addition, the digitized data from DSS 15 were sent over optical fiber to DSS 13, where the DSS 13–DSS 15 baseline was correlated with the real-time Block II correlator [20] The correlated data were written to disk for later processing The results presented in this article are based upon data correlated in real time at DSS 13

As a test of the accuracy of the real-time correlator, the data recorded on tape during session 5 were correlated with the JPL–CIT Block II correlator The quality of tape playback was poor, and only 53 scans could be decoded The difference between the S-/X-band group delays from the two correlators had a mean of 155 ps and a standard deviation of 3 5 ps The mean delay offset is thought to be due to

details in the application of manual phase calibration in the observable extraction process (routine FIT) [21] Because this offset looks exactly like a clock offset, it will not affect later results The 3 5-ps rms is due at least in part to the poor quality of tape playback However, even if it were due entirely to errors in the real-time correlator, it would be too small to significantly affect the results presented in Section V

In order to calibrate the variation of instrumental delays with frequency and time, phase calibration was used at each antenna Phase calibration tones were injected between the feed horn and the first stage RF amplifier, and later extracted by the correlator for use in correcting interferometric delays At DSS 15, a phase calibration unit with a cable stabilizer [22] was used This stabilizer greatly reduces the effect of path length changes between the hydrogen maser frequency standard on the ground and the tone generator at the feed horn The entire system has an estimated error of $\leq$10 ps over 24 h due to diurnal temperature changes Over time scales $\leq$6 h, the nonlinear delay errors were several times smaller than 10 ps At DSS 13, the phase calibration unit did not have cable stabilization, and the instrumental delay calibration errors were, therefore, larger (this is discussed further in Section VI)

The postprocessing routine FIT was used to extract the residual phase from the correlated data for each scan, along with the derivatives of this phase with respect to frequency (group delay) and time (phase rate) The values of these quantities from the correlator model were added to the residual values to obtain total observables The total phase produced in this way contained integer cycle ambiguities These were resolved by a technique described in Section IV When the integer cycle ambiguities were removed, the phase delay τ_{ph} could be calculated as $\tau_{ph} = \phi/\nu_{avg}$, where ϕ is the total phase at a mean observing frequency ν_{avg}

B WVRs

During each of the six VLBI sessions, WVRs were deployed near each of the two Goldstone antennas A J-series WVR (J3) [23] was located 50-m north of the DSS-13 azimuth axis, and a D-series WVR (D2)[2] was located 40-m south of the DSS-15 azimuth axis Both WVRs observed simultaneously in two channels, 20 7 and 31 4 GHz, with effective bandwidths of 320 MHz The J3 instrument also has a 22 2-GHz channel (at the peak of the water vapor line), but this channel was not used during our observations The estimated thermal noise level for 5- to 6-s integrations was approximately 0 06 K for D2 and 0 10 K for J3, corresponding to path delay errors of $\approx$0 4 mm (D2) and $\approx$0 6 mm (J3) Thermal WVR noise was not a limiting error source in this experiment

During VLBI source measurements, the WVRs were co-pointed with the DSS-13 and DSS-15 antennas whenever viewing conditions allowed However, unlike the two large radio antennas, the WVRs observed in a constant direction during a scan Neither WVR was capable of taking data while slewing The WVR 6- to 9-deg beams are subject to significant side lobe pickup whenever a substantial obstruction lies within $\sim$20 deg of the beam axis Prior to the experiment, the WVRs were operated in a horizon scanning mode to establish the azimuth-dependent minimum elevation angles free of ground pickup For most observations and azimuths, 30 deg was chosen as a safe elevation angle lower limit At DSS 15, where the D2 WVR sat on the ground to the south and substantially below the VLBI antenna, elevation angles $<$75 deg were precluded for source azimuths in the range ($-$45 deg, +45 deg)

While performing line-of-sight measurements during VLBI scans, both WVRs observed the sky nearly continuously, with 6-s interruptions once per minute to measure a reference load The J3 WVR observed this load by internal switching, while the D2 unit slewed its antenna away from the radio source line of sight to an external ambient target During gaps of 2 or more minutes between VLBI source measurements, the WVRs performed tip curves to monitor gain variations For the J3 unit, the tip curves obtained during the VLBI observing gaps provided interpolation points for gain calibration during the 6-h sessions For

[2] S J Keihm, *Water Vapor Radiometer Intercomparison Experiment Platteville, Colorado, March 1–14, 1991*, JPL D-8898 (internal document), Jet Propulsion Laboratory, Pasadena, California, 1991

the D2 unit, calibration variations were tracked using an empirical correlation between gain and mixer temperature established from tip curve data obtained prior to and following the VLBI observing sessions The D2 tip curves obtained during gaps within the VLBI observing sessions provided a check on the precision of the mixer temperature gain tracking technique

IV. Analysis

Data from the first three sessions were not usable for subsequent analysis During session 1, instrumental phase calibration was not available at DSS 13 During session 2, hardware problems caused the loss of a large fraction of the VLBI data and most of the WVR data During session 3, technical problems caused the instrumental phase calibration at DSS 13 to be too noisy to use The number of usable scans, defined as having working phase calibration, adequate signal-to-noise ratio (SNR) for phase connection (discussed below), and valid WVR data from both DSS 13 and DSS 15, are given for all six sessions in Table 2

Table 2 Quantity of usable data from each session

Session	No of usable scans
1	0
2	0
3	0
4	87
5	46
6	33

A. Calculating VLBI Phase Delays

The extraction of total VLBI delays for each scan at both S- and X-band was described in Section III A The one standard deviation (1σ) thermal noise $\Delta\tau_{SNR}$ in delay measurements, due to limited SNR in the data, is approximately

$$\Delta\tau_{SNR_g} \approx \frac{k}{2\pi\Delta\nu_{span}\ SNR} \qquad \text{for group delay} \tag{6}$$

$$\Delta\tau_{SNR_{ph}} \approx \frac{1}{2\pi\nu_{avg}\ SNR} \qquad \text{for phase delay} \tag{7}$$

The $\Delta\nu_{span}$ is the spanned bandwidth at X-band (368 MHz), and ν_{avg} is the mean X-band observing frequency (8405 MHz) The SNR is the signal-to-noise ratio for the entire scan, when all nine X-band frequency channels are combined The k is a dimensionless factor that depends upon the spacing of channels over the spanned bandwidth For channels stacked at the two band edges, $k = 2$ For uniform channel spacing, $k = 3\sqrt{2}$ For the spacings used during these observations, $k \approx 3$ The derivation of Eqs (6) and (7) follows from the fact that, for thermal noise, the phase error (in radians) of a complex value is equal to the fractional amplitude error Although the measured "charged-particle-free" delays are linear combinations of S- and X-band delays, the errors are dominated by the X-band delay errors because the X-band delay weights in the linear combination are a factor of $(\nu_X/\nu_S)^2 \approx 14$ times larger than the S-band weights

The values of $\Delta\tau_{SNR_g}$ ranged from <1 ps to >30 ps, with $\Delta\tau_{SNR_g} \geq 10$ ps for many scans Because the goal of this experiment was to look for mm-level effects (1 mm corresponds to ≈ 3 ps), we used the phase delay observable τ_{ph}

$$\tau_{ph} \equiv \frac{\phi}{\nu_{avg}}$$

Here ϕ is the total phase in cycles, including integer cycles, at the mean X-band frequency ν_{avg} Use of the phase delay reduced $\Delta\tau_{SNR}$ a factor of $\approx$20 below that for the group delay

The group delays were used to resolve integer cycle ambiguities (i e , to "connect phase" from one scan to the next) in the phase delays In order for this to be accomplished, the thermal noise in the group delays had to be sufficiently small that the probability of making a cycle error was negligible If we set a 5-σ threshold for a cycle error (defined as an error in the group delay of >0 5 cycle), then

$$\Delta\tau_{SNR_g} < \frac{0\,1}{\nu_{avg}}$$

This leads to

$$SNR > \frac{10k\nu_{avg}}{2\pi\Delta\nu_{span}} \approx \frac{30\nu_{avg}}{2\pi\Delta\nu_{span}}$$

For S- and X-band, the constraints on SNR are

$$SNR_{\mathrm{S}} > 110$$

$$SNR_{\mathrm{X}} > 110$$

Because charged particles affect group and phase delays with opposite signs, it was not possible to perform phase connection using raw delays The following procedure was used First, the S- and X-band group delays were used to derive a charged-particle-free group delay, $\tau_g(S/X)$, and an electron column density, N_g The accuracy of both quantities was limited by thermal noise in the group delays Second, N_g was used to remove most of the charged-particle contribution to the S- and X-band phase delays Using $\tau_g(S/X)$, the integer cycle ambiguities in these phase delays were determined The corrected phase delays were then used to estimate very high SNR charged-particle-free phase delays, $\tau_{ph}(S/X)$, which were used for subsequent analysis This procedure could also have used the phase delays to determine the electron column density with high precision, but this quantity was not needed for the analysis in this experiment

B. VLBI Parameter Estimation

The charged-particle-free phase delays for each observing session were analyzed using JPL's program MODEST (for model and estimation) [24] First, an a priori model delay was subtracted from each scan This model included atmospheric, source, baseline, relativistic, and geophysical parameters For the short baseline in this experiment, many components of this model gave a negligible contribution The dominant components of the model consisted of (1) a geometric term, based on UT1 (i e , universal time corrected for Earth rotation irregularities UT1−UTC), station locations for the two antennas, and source positions converted from J2000 to date via precession, nutation, and aberration, and (2) a media term,

consisting of tropospheric delay differences The a priori differential dry zenith delays were derived from surface pressures at the two antennas and the elevation angles of the sources For our a priori model of wet delay differences, we used either zero (i e , no calibration) or the station-differenced line-of-sight WVR wet path delay estimates Both options were used for all sessions so that the effectiveness of WVR calibration could be quantified

The model subtraction produced a set of residual delays The estimation process did an unweighted least-squares fit to these residuals, solving for one or more parameters Equal weighting was used because the thermal noise was much less than other error sources (tropospheric fluctuations and instrumental effects) In all cases, a constant clock offset was estimated Other parameters estimated during some runs were a residual mean zenith troposphere difference and a correction to the baseline vector between the two antennas

The clocks at the two antennas were derived from the same frequency standard However, the cable lengths distributing this standard to the two antennas were different, so that the mean differenced clock value at the two antennas was nonzero This parameter reduced the rms scatter among the residuals (i e , the interscan residuals) to <30 ps for sessions 5 and 6 and ≈80 ps for session 4

The residual mean zenith-troposphere difference parameter primarily represented the session-averaged difference in the wet delays (DSS 15 consistently had a larger wet delay than DSS 13) However, it also accounted for any calibration error in the dry delay difference between the two sites

For session 4, when there were a large number of scans with broad sky coverage, an attempt was made to solve for a correction to the vector baseline between the two antennas However, solving for these additional three parameters resulted in minimal reduction to the interscan residuals For all results reported below, the baseline was left unchanged from its a priori value, derived from multiple previous VLBI observations

Because most or all VLBI astrometric and geodetic results have been based on group delays, we checked for possible systematic errors in the calculation and treatment of phase delays Group delays were used in comparison runs of MODEST for sessions 5 and 6, both with and without WVR calibration The resulting VLBI interscan group delay rms values were equal, in all cases, to the residual phase delay rms values with ≈10 ps of noise added in quadrature We conclude that any systematic errors in the phase delays were substantially less than 10 ps

C. WVR-Based Delay Residuals

Site-differenced line-of-sight wet delays were determined from the WVR data at ≈6-s intervals for each VLBI source observation The two-channel line-of-sight WVR brightness temperatures were first converted to zenith-equivalent brightness temperatures using the effective radiating temperature approximation to Eq (4) in [2]

$$T_b(M) = T_{eff} - (T_{eff} - T_{MB})\, e^{-\tau(M)} \tag{8}$$

The value of T_{eff} used was 285 K The T_{MB} is the cosmic background microwave temperature, and M is the air mass ($M \equiv 1/\sin\theta$, where θ is the elevation angle) Given a value for $T_b(1)$ (i e , T_b at the zenith), $\tau(1)$ can be computed and the path delay can be accurately mapped to any other elevation angle >15 deg using the relation $\tau(M) = \tau(1)/\sin\theta$

Once converted to zenith, the WVR brightness temperatures were used to determine zenith path delay A linear retrieval algorithm was based on correlations between Desert Rock, Nevada, radiosonde measurements of zenith path delay and computed WVR brightness temperatures The brightness temperatures were generated from the radiosonde data using the modified Liebe vapor absorption model [14]

Desert Rock is considered the site equivalent of Goldstone, both in altitude and average moisture content The path delay retrieval algorithm generates three path delay values for each input set of WVR zenith brightness temperatures one using both channels and one each using the channels independently For most operating conditions, the two-channel algorithm provides the most accurate path delay results For time intervals under cloudless conditions for which the behavior of one channel is anomalous or subject to larger than normal gain uncertainties, the single-channel algorithms can be applied using data from the more reliable channel Other algorithms, which augmented the WVR data with MTP measurements of the lower troposphere temperature profile, were also tried, but produced no additional reduction in the final VLBI site-differenced residuals

When the WVR data were included in the VLBI processing, the derived zenith WVR delays were mapped to the DSN antenna elevation for each pass If no obstructions precluded co-pointing, the mapping coincided with the original WVR pointing These data are considered the highest-quality WVR measurements of path delay correction and were assigned a quality flag of 3 If co-pointing did not occur but the WVR and VLBI antennas were aligned within one WVR HPBW (7 deg), then a quality flag of 2 was assigned If there was some indication of WVR ground pickup of magnitude <1 K, then a quality flag of 1 was assigned With evidence of ground pickup exceeding 1 K or any indication of anomalous WVR calibration behavior, the quality flag was set to 0 For all results reported in the following section, only quality flag ≥ 2 data were utilized These data comprised ≈ 70 percent of the passes of VLBI observation sessions 4, 5, and 6

V. Results

A. Interscan Delay Residuals

The results of the MODEST runs for sessions 4 through 6 are summarized in Tables 3 and 4 Results without VLBI troposphere estimation are listed in Table 3, results with VLBI troposphere estimation are listed in Table 4 All entries in these tables correspond to VLBI scan-averaged phase delay residuals Column 3 in each table gives rms VLBI interscan post-fit delay residuals when WVR line-of-sight wet path delay estimates were applied as calibration These estimates use two-channel (20 7- and 31 4-GHz) retrievals for the J-WVR and one-channel (31 4-GHz) retrievals for the D-WVR Other combinations were also tried but gave inferior results As discussed below, the D2 channel-1 data were apparently corrupted by instrument pointing problems The WVR calibrations reduced the post-fit residuals for all three sessions

Table 3 VLBI interscan rms residuals without mean zenith troposphere estimate

Session	No WVR calibration, ps	Dual channel for J3, channel 2 for D2, ps
4	80 0	77 2
5	22 6	16 3
6	24 2	23 3

The VLBI scan-averaged residual phase delays (i e , after the least-squares fits in MODEST) and WVR station-differenced path delays for sessions 5 and 6 are shown in Fig 1 The MODEST VLBI solution used for this figure included the estimation and subtraction of a mean tropospheric zenith delay but did not include WVR calibration The line-of-sight residual delays (one for each scan) have all been mapped to the zenith, using the factor $\sin\theta$, where θ is elevation angle The mean zenith delay has been removed from the WVR delays This process allows a more valid comparison with the VLBI residual delays,

Table 4. VLBI interscan rms residuals with mean zenith troposphere estimate.

Session	No WVR calibration, ps	Dual channel for J3, channel 2 for D2, ps
4	80 0	77 2
5	14 4	12 1
6	23 5	23 0

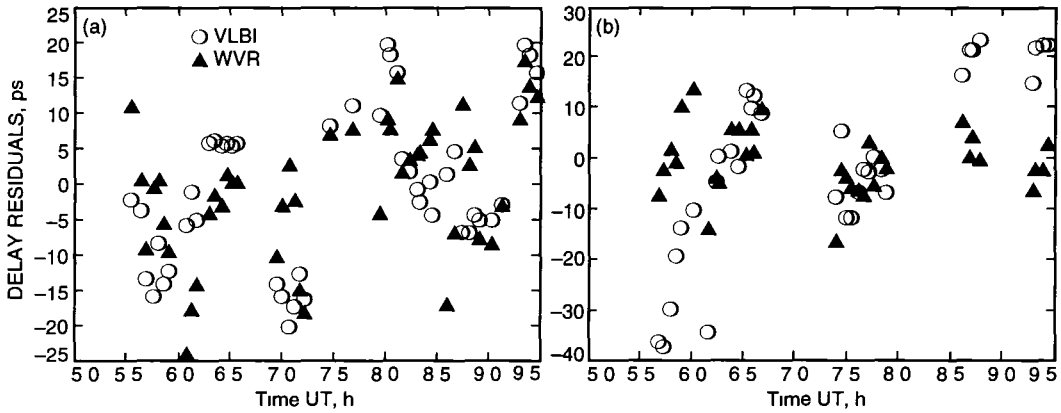

Fig 1 VLBI interscan phase delay residuals and WVR delay estimates (a) session 5 and (b) session 6 A mean tropospheric zenith delay has been subtracted from both the VLBI and the WVR data A constant delay (clock offset) has been subtracted from the VLBI data

which have also had a linear delay fitted and subtracted Examination of Fig 1 shows good correlation between the VLBI and WVR delay changes during some limited time intervals However, there are large systematic differences at other times In order to understand those differences, we examined the VLBI and WVR delay variations in several ways

The standard deviations of the zenith residuals for VLBI and for single-site and site-differenced WVR zenith delays are given in Table 5 The VLBI values correspond to those plotted in Figs 1(a) and 1(b) line-of-sight values with a clock and mean zenith troposphere removed, and the delays then mapped to zenith The WVR values had a constant offset removed from the zenith delay values As in Tables 3 and 4, the WVR results for D2 are based on channel 2 only If the VLBI interscan residuals were dominated by the troposphere, we would expect the WVR site-differenced residuals to be at least as large as the VLBI residuals (equal if the WVR measurement errors were much smaller than the troposphere, and larger otherwise) The scatter in the site-differenced WVR delays was significantly less than in the VLBI delays for session 5 and especially for session 6 Over the duration of a session, either the WVRs underestimated the tropospheric variations or the VLBI measurements had some significant noise source in addition to the troposphere

Because the sites at DSS 13 and DSS 15 were nearby and similar, we would expect the individual-site WVR standard deviations to be comparable The fact that the D2 residual rms values were substantially larger than the J3 residuals suggests that D2 instrument errors contributed significantly to the D2 residuals The mechanical design of the D-WVRs makes them more susceptible to pointing errors than J-WVRs An elevation angle offset for each D2 channel was estimated from tip curves 0 9 deg for channel 1 and 0 5 deg for channel 2 However, because all tip curves during our observations were performed along one azimuth, there was no way to determine the azimuth dependence of these offsets With an unknown azimuth dependence for both channels, the pointing error for channel 1 was expected

Table 5 VLBI and WVR interscan rms zenith delay residuals

Session	VLBI, ps	WVR site differenced, ps	J3, ps	D2, ps
5	10 7	9 5	7 0	8 7
6	10 3	6 4	7 4	10 0

to be larger than for channel 2 An elevation error of 0 5 deg in channel 2 at a 30-deg elevation angle would cause a fractional error of 2 percent, or ≈6 ps for the conditions during these observations

B. Intrascan Delay Variability

In order to analyze the delay variations on short (≤700-s) time scales, we calculated structure functions from WVR line-of-sight delays and from residual VLBI phase delays within individual scans (i e , intrascan residuals) For a delay τ measured at time t, the structure function $D_\tau(\Delta t)$ for a time interval Δt is $D_\tau(\Delta t) \equiv \langle [\tau(t) - \tau(t + \Delta t)]^2 \rangle$ We used long (≥300-s) scans in this comparison, because these scans provided the largest possible logarithmic range of time interval

For each of sessions 5 and 6, WVR structure functions (using individual 5- to 6-s integrations) were calculated for all long scans, mapped to a reference elevation angle (described below), and averaged There were four such scans in session 5 and thirteen in session 6 The mapping between elevation angles (for both WVR and VLBI structure functions) was determined from numerical integration of the Treuhaft–Lanyi model, it was $\approx \sin\theta_{obs} / \sin\theta_{ref}$, where θ_{obs} is the elevation angle where the structure function was measured and θ_{ref} is the reference elevation angle The averaged structure function for each WVR was then multiplied by 2, because each was derived from single-station data and the VLBI structure functions were derived from station-differenced data

All long scans in sessions 5 and 6 had VLBI elevation angles θ_{VLBI} >37 deg or <20 deg For VLBI structure functions, the low elevation angle (<20 deg) scans could not be used At these low elevation angles, sidereal tracking causes a significant nonlinear air mass change with time Combined with imperfectly modeled zenith delays (i e , the static troposphere), this effect corrupted the measurement of actual fluctuations (Because the WVRs did not move during observations, their structure functions did not suffer from this problem) The structure functions (based on residual $\tau_{ph}(S/X)$ values for 2-s integrations) from all long scans with $\theta_{VLBI} > 37$ deg (three in session 5 and one in session 6) were mapped to θ_{ref} and averaged The reference elevation angle θ_{ref} was the mean VLBI elevation angle for these scans in each session ($\theta_{ref} = 38\ 5$ deg in session 5 and $\theta_{ref} = 40\ 3$ deg in session 6)

The WVR and VLBI structure functions are shown in Fig 2(a) for session 5 and Fig 2(b) for session 6 In Fig 2(a), the curve labeled "VLBI (AVG)" is the average of the VLBI structure functions for the three long (≥ 600-s) scans at elevation angles >30 deg The curves labeled "J3 (AVG)" and D2 (AVG)" are the averages of the J3 and D2 WVR structure functions for all four long scans All structure functions have been scaled to a constant elevation angle, 38 5 deg, before averaging The WVR structure functions have been multiplied by 2 for comparison with the two-station VLBI structure functions At time scales less than ~100 s, the WVR structure functions (especially for J3) are dominated by thermal noise The VLBI structure function is not shown for time scales >300 s, because the least-squares delay rate fitting performed on the data (by FIT) has suppressed the structure function in this regime For session 6, Fig 2(b), there was only one long VLBI scan at elevation angle >30 deg, and 13 WVR scans The WVR structure functions were mapped to the VLBI elevation angle of 40 3 deg before averaging Because only one WVR scan was longer than 300 s, the WVR structure functions are only shown for 0 to 300 s Except at time scales <100 s, where thermal noise dominates the WVR structure functions, the VLBI and WVR structure functions in Fig 2 show a qualitative agreement

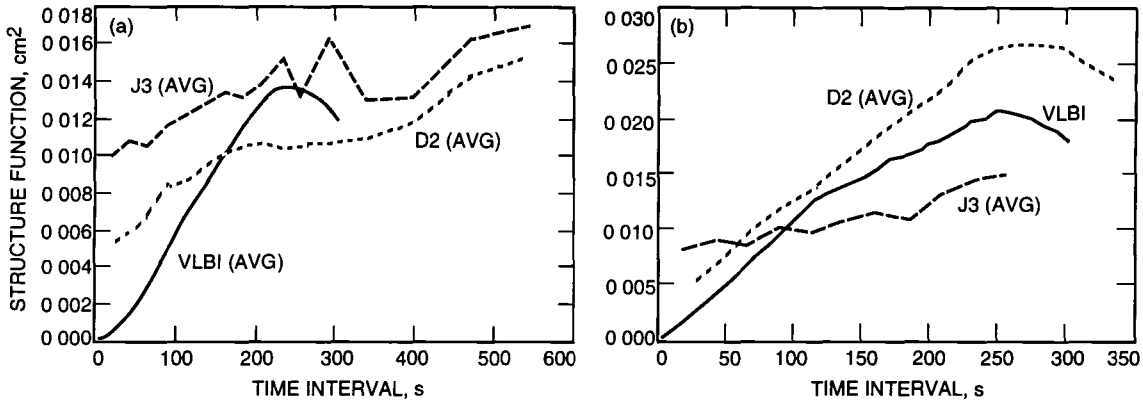

Fig 2 VLBI and WVR intrascan structure functions, shown on a linear scale. (a) session 5 and (b) session 6

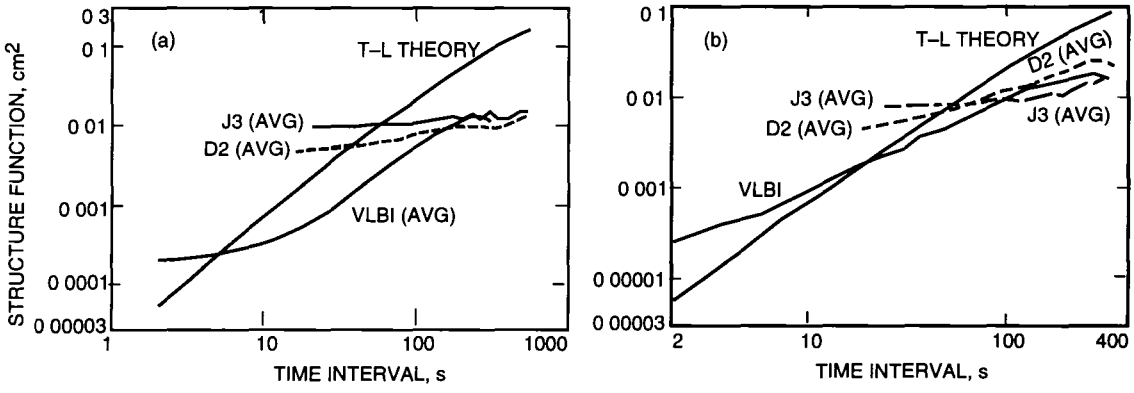

Fig 3 VLBI and WVR structure functions shown on a log scale (a) session 5 and (b) session 6 The theoretical Treuhaft–Lanyi structure function for average Goldstone tropospheric conditions ($C\chi = 7 \times 10^{-8}$ $m^{-1/3}$) is shown for comparison The VLBI structure function is dominated by thermal noise on time scales less than ~10 s

In Figs 3(a) and 3(b), the VLBI and WVR structure functions are shown on a logarithmic scale Also shown for comparison is the theoretical Treuhaft–Lanyi structure function for θ_{ref} under typical Goldstone conditions ($C_\chi = 7 \times 10^{-8}$ $m^{-1/3}$, the mean Goldstone value derived from intercontinental DSN VLBI observations, 8 m/s wind velocity) The thermal noise floor in both the WVR and VLBI structure functions can clearly be seen At time scales >100 s (i e , where thermal noise is not important), the measured structure functions (for both VLBI and WVRs) are a factor of 2 to 4 smaller than expected for normal conditions

C. Session Average VLBI Structure Functions

In order to quantify the average level of tropospheric activity for each session, high SNR scans were used to determine the VLBI structure function The measured VLBI D_τ values were compared to theoretical structure functions, based upon the model of [15], and the results are presented in Table 6 The parameters in the model include elevation angle (chosen to be the same as in the individual VLBI scans), vector wind velocity, tropospheric slab height (chosen to be 2 km, the mean wet tropospheric scale height), and the structure constant C_χ (7×10^{-8} $m^{-1/3}$) Vector wind velocities as a function of height were measured by optical tracking of our radiosondes at DSS 13, with launches every 6 hours The vector wind velocities used in the structure function calculations were linear interpolations (in time) of the values measured by radiosonde tracking

Table 6 Measured and theoretical delay structure functions

Session	Scan	Δt used for D_τ, s	$\sqrt{\frac{D_\tau(measured)}{D_\tau(theory)}}$	Mean value	Predicted interscan line-of-sight rms residual, ps
4	11	16	0 48		
	35	16	0 80		
	145	16	0 54		
	160	16	0 40		
	199	16	0 16		
	212	16	0 29		
	237	16	0 17		
	276	16	0 23		
	309	16	0 28		
				0 37	9 7
5	2	50	0 32		
	12	16	0 26		
	27	16	0 30		
	33	50	0 27		
	40	16	0 48		
	60	16	0 51		
	65	50	0 32		
				0 35	8 1
6	4	50	0 48		
	8	16	0 34		
	20	16	0 48		
	35	16	0 37		
	38	50	0 95		
	54	16	0 34		
	59	50	0 20		
				0 45	10 2

For each scan, the square root of the ratio of measured to theoretical value of D_τ is given in column 4 of Table 6 The value of Δt used to determine this ratio was 50 s for 700- to 800-s scans and 16 s for 100- to 150-s scans, as indicated in column 3 These Δt values were chosen to be large enough to yield negligible contribution from thermal noise, yet short enough that D_τ was not significantly reduced by the linear delay rate subtraction done by FIT The quantity in column 4 varies linearly with C_χ Column 5 gives the mean of the column 4 values for each session As was evident from Figs 3(a) and 3(b), the magnitude of water vapor fluctuations during this experiment was significantly less than normal for Goldstone

For each session, a corrected value of C_χ was obtained by multiplying the nominal value (7×10^{-8} m$^{-1/3}$) by the mean $\sqrt{D_\tau(measured)/D_\tau(theory)}$ value The corrected C_χ value represented the mean tropospheric activity, as measured from the intrascan residuals This C_χ value was used to calculate the tropospheric delay standard deviation $\sigma(T)$ expected for the entire session (i e , the interscan rms residual) The variance $\sigma^2(T)$ of a random process over an interval T can be expressed in terms of the structure function as [15]

$$\sigma^2(T) = \frac{1}{T^2}\int_0^T (T-t)D_{\tau_{2stn}}(t)dt \tag{9}$$

In Eq (9), $D_{\tau_{2stn}}(t)$ is the two-station delay structure function, the expected square of the line-of-sight delay difference at the two sites (DSS 13 and DSS 15) Using a frozen flow model, separations in space and time are related through the vector wind velocity $\vec{v}_w$ Thus, for a time interval Δt, the vector used for the calculations of $D_{\tau_{2stn}}(t)$ is $\vec{v}_w\Delta t + (\vec{x}_{15} - \vec{x}_{13})$, where $\vec{x}_{15}$ and $\vec{x}_{13}$ are the locations of DSS 15 and DSS 13 For time scales much less than the wind crossing time of the interferometer (i e , $\Delta t << \|\vec{x}_{15} - \vec{x}_{13}\|/v_w$), variations at the two sites are uncorrelated, and $D_{\tau_{2stn}}(t) \approx 2D_{\tau_{1stn}}(t)$, where $D_{\tau_{1stn}}(t)$ is the single-station delay structure function This approximation was used for the calculations in Sections V A and V B The time scale used in evaluating Eq (9) was the length of a session, and the wind velocity was the mean value measured at a 1-km height during that session Because the scans in each session had a reasonably uniform distribution over any one quadrant of the sky, a source-wind azimuth of 45 deg was used in these calculations The dependence of calculated tropospheric effects upon wind velocity is fairly weak Use of the default wind velocity of 8 m/s changed the estimated tropospheric interscan rms by <20 percent For the elevation angle in the model, we used the mean air mass-weighted elevation angle for all VLBI scans in a session that had high-quality WVR data at both stations 42 deg for session 4, 47 deg for session 5, and 50 deg for session 6 The results of these calculations are given in column 6 of Table 6

D. Implications of the Model Predictions of Interscan VLBI Residuals

A comparison of VLBI-measured and the model-predicted interscan residuals is given in Table 7 For each session, the predicted delay rms due to the troposphere, based on the VLBI intrascan structure functions (column 6 of Table 6), is shown in column 2 The measured VLBI rms, with a solution for a mean troposphere but without WVR calibration (column 2 of Table 4), is given in column 3 The discrepancy between the values in columns 2 and 3 indicates that nontropospheric (i e , instrumental) errors were the major source of the VLBI interscan delay residuals

Table 7 Comparison of expected and actual VLBI residual delay improvement from WVR calibration

Session	Predicted tropospheric interscan rms, ps	Actual VLBI rms, ps	Expected rms reduction from perfect tropospheric calibration, %	Actual rms reduction from WVR calibration, %
4	9 7	80 0	1	4
5	8 1	14 4	17	16
6	10 2	23 5	10	2

Significant instrumental delay variations at DSS 13 could have remained uncalibrated Table 8 gives the rms phase delay variation (with respect to a least-squares linear fit in time) for the instrumental phase calibration measurements at each station for sessions 4 through 6, at both S- and X-band The instrumental delay variations at DSS 13 were significantly larger than for DSS 15 during all three sessions If the phase calibration had worked perfectly, even the larger DSS-13 variations would not pose a problem However, the DSS-13 phase calibration system was not able to measure delay changes on the transmission from the control room up to the antenna focus We suspect that these instrumental delay changes constituted the nontropospheric component of our interscan rms Instrumental delay changes due to mechanical motion of the antenna would likely be much smaller during sidereal tracking than when the

antenna slewed from one source to another Instrumental changes due to thermal variations are likely to be important only over time scales longer than approximately an hour, when significant temperature changes can accumulate

Table 8 RMS phase delays (one delay per scan) from phase calibration

Session	DSS-13 S-band, ps	DSS-13 X-band, ps	DSS-15 S-band, ps	DSS-15 X-band, ps
4	181	167	8	9
5	10	11	4	4
6	29	30	7	4

As a further test of the nature of the VLBI residuals, their elevation angle dependence was examined For the case where WVR calibration was not applied, the VLBI residuals for some low elevation angle scans were large When there was a long antenna slew after several scans in a small area of the sky, there was often a substantial change in the residuals Both of these effects went away when WVR calibration was applied, suggesting that tropospheric effects (largest at low elevation angles or when comparing two regions that are far apart on the sky) had been largely removed The signature of the VLBI residuals *with* WVR calibration was a systematic variation on time scales >1 h, with no obvious elevation angle dependence We suspect that thermal variations in the DSS-13 antenna or receiver system were the most likely cause of the largest component of the long-term (interscan) residuals

If the troposphere model calculations are correct, perfect line-of-sight tropospheric delay calibrations would reduce (in quadrature) the total rms (column 3 in Table 7) by the amount in column 2 This "perfect calibration" interscan rms improvement, Δ_{cal}, is given in column 4

$$\Delta_{cal} \equiv 1 - \sqrt{\frac{\sigma^2_{VLBI} - \sigma^2_{Trop}}{\sigma^2_{VLBI}}}$$

Here the total rms and the tropospheric rms are represented by σ_{VLBI} and σ_{Trop}, respectively The measured improvement from WVR calibration (derived from values in Table 4) is given in column 5 of Table 7 Except for session 6, the improvement from WVR calibration is a large fraction of the calculated maximum improvement This shows that WVR measurements were able to calibrate the majority of the wet tropospheric fluctuations

VI. Conclusions

Application of WVR calibration resulted in a definite but minor (2- to 16-percent) reduction in the VLBI interscan rms residual delays and is consistent with our understanding of the relative amounts of instrumental and atmospheric fluctuations We conclude that, over the duration of an observing session, the VLBI residual delays had a larger instrumental component than a tropospheric component, and that the WVR calibration removed most of the tropospheric component of these delays This conclusion is based upon the following evidence

(1) Within scans, the WVRs and VLBI measured similar levels of delay variations (intrascan residuals), as shown by the agreement in their structure functions (Figs 2 and 3) On longer time scales, the VLBI delay residuals were larger than the WVR residuals (Table 5)

(2) The VLBI residual values *within* and *between* scans are not consistent The level of intrascan residuals implies that the interscan residuals should be a factor of 1 8 to 8 smaller than was actually measured This is most easily explained by a nontropospheric component to the long time-scale VLBI residuals

(3) WVR calibration of VLBI delays reduced the interscan residuals for all three sessions For sessions 4 and 5, the reduction was nearly equal to the amount calculated as being due to the troposphere

(4) The WVR site-differenced zenith rms delays were substantially smaller than the VLBI residual rms delay

Our test of the wet delay calibration ability of WVRs was hindered by the quiet nature of the troposphere during these observations Future tests should be conducted during times (e g , summer afternoons) when convection-driven atmospheric turbulence is common

Acknowledgments

We thank the DSS-13 staff for a large effort in reinstalling the S-band receiver at DSS 13 and making the station operational for VLBI We are grateful to D Mischel, B Gaudian, C Goodson, G Hall, and the rest of the DSN staff for miscellaneous arrangements during the observations R Denning, R Swindlehurst, and G Hoover provided much useful assistance with field operations J Wilcox assisted with the VLBI observations B Gary provided helpful consulting during data reductions

References

[1] R N Treuhaft and S T Lowe, "A Measurement of Planetary Relativistic Deflection," *The Astronomical Journal*, vol 102, no 5, pp 1879–1888, November 1991

[2] G Elgered, "Tropospheric Radio Path Delay From Ground-Based Microwave Radiometry," Chapter 5, *Atmospheric Remote Sensing by Microwave Radiometry*, edited by M Janssen, New York Wiley & Sons, 1993

[3] G D Thayer, "An Improved Equation for the Radio Refractive Index of Air," *Radio Science*, vol 9, no 10, pp 803–807, October 1974

[4] J C Owens, "Optical Refractive Index of Air Dependence on Pressure, Temperature, and Composition," *Applied Optics*, vol 6, pp 51–58, 1967

[5] G Boudouris, "On the Index of Refraction of Air, the Absorption and Dispersion of Centimeter Waves by Gases," *J Res Natl Bur Stand , Sect D*, vol 69D, no 6, pp 631–684, 1963

[6] R J Hill, R S Lawrence, and J T Priestly, "Theoretical and Calculational Aspects of the Radio Refractive Index of Water Vapor," *Radio Science*, vol 17, no 5, pp 1251–1257, September–October 1982

[7] S Chandrasekhar, *Radiative Transfer*, Chicago University of Chicago Press, 1950

[8] E R Westwater, J B Snider, and M J Falls, "Ground-Based Radiometric Observations of Atmospheric Emission and Attenuation at 20 6, 31 65, and 90 0 GHz—A Comparison of Measurements and Theory," *IEEE Trans Antennas Propag* , vol 38, no 10, pp 1569–1580, October 1990

[9] M N England, F J Schmidlin, and M M Johansson, "Atmospheric Moisture Measurements A Microwave Radiometer—Radiosonde Comparison," *IEEE Trans Geoscience and Remote Sensing*, vol 31, no 2, pp 389–398, March 1993

[10] S M Lichten, "Precise Estimation of Tropospheric Path Delays with GPS Techniques," *The Telecommunications and Data Acquisition Progress Report 42–100, October–December 1989*, Jet Propulsion Laboratory, Pasadena, California, pp 1–12, February 15, 1990

[11] D M Tralli and S M Lichten, "Stochastic Estimation of Tropospheric Path Delays in Global Positioning System Geodetic Measurements," *Bull Geod* , vol 64, pp 127–159, 1990

[12] B L Gary, S J Keihm, and M A Janssen, "Optimum Strategies and Performance for the Remote Sensing of Path-Delay Using Ground-Based Microwave Radiometry," *IEEE Trans Geoscience and Remote Sensing*, vol GE-23, no 4, pp 479–484, July 1985

[13] G M Resch, D E Hogg, and P J Napier, "Radiometric Correction of Atmospheric Path Length Fluctuations in Interferometric Experiments," *Radio Science*, vol 19, no 1, pp 411–422, January–February 1984

[14] S J Keihm, *Proceedings of a Specialist Meeting on Microwave Radiometry and Remote Sensing Applications*, edited by E R Westwater, Boulder, Colorado, pp 211–218, 1992

[15] R N Treuhaft and G E Lanyi, "The Effect of the Dynamic Wet Troposphere on Radio Interferometric Measurements," *Radio Science*, vol 22, no 2, pp 251–265, March–April 1987

[16] R P Linfield and J Z Wilcox, "Radio Metric Errors Due to Mismatch and Offset Between a DSN Antenna Beam and the Beam of a Troposphere Calibration Instrument," *The Telecommunications and Data Acquisition Progress Report 42–114, April–June 1993*, Jet Propulsion Laboratory, Pasadena, California, pp 1–9, August 15, 1993

[17] R F Denning, S L Guidero, G S Parks, and B L Gary, "Instrument Description of the Airborne Microwave Temperature Profiler," *J Geophys Res* , vol 94, no D14, pp 16,757–16,765, November 30, 1989

[18] E R Westwater, "Ground-Based Microwave Remote Sensing of Meteorological Variables," Chapter 4, *Atmospheric Remote Sensing by Microwave Radiometry*, edited by M Janssen, New York Wiley & Sons, 1993

[19] A E E Rogers, R J Cappallo, H F Hinteregger, J I Levine, E F Nesman, J C Webber, A R Whitney, T A Clark, C Ma, J Ryan, B E Corey, C C Counselman, T A Herring, I I Shapiro, C A Knight, D B Shaffer, N R Vandenberg, R Lacasse, R Mauzy, B Rahrer, B Schupler, and J C Pigg, "Very-Long-Baseline Radio Interferometry The Mark III System for Geodesy, Astrometry, and Aperture Synthesis," *Science*, vol 219, no 4580, pp 51–53, January 7, 1983

[20] C D Edwards, D H Rogstad, D N Fort, L White, and B Iijima, "The Goldstone Real-Time Connected Element Interferometer," *The Telecommunications and Data Acquisition Progress Report 42–110, April–June 1992*, Jet Propulsion Laboratory, Pasadena, California, pp 52–62, August 15, 1992

[21] S T Lowe, *Theory of Post-Block II VLBI Observable Extraction*, JPL Publication 92-7, Jet Propulsion Laboratory, Pasadena, California, 1992

[22] E H Sigman, "Phase Calibration Generator," *The Telecommunications and Data Acquisition Progress Report 42-92, October–December 1987*, Jet Propulsion Laboratory, Pasadena, California, pp 89–104, February 15, 1988

[23] M A Janssen, "A New Instrument for the Determination of Radio Path Delay Due to Atmospheric Water Vapor," *IEEE Trans Geoscience and Remote Sensing*, vol GE-23, no 4, pp 485–490, July 1985

[24] O J Sovers, *Observation Model and Parameter Partials for the JPL VLBI Parameter Estimation Software 'MODEST' — 1991*, JPL Publication 83-39, Rev 4, Jet Propulsion Laboratory, Pasadena, California, 1991

A Novel Photonic Oscillator

X S Yao and L Maleki
Tracking Systems and Applications Section

We report a novel oscillator for photonic RF systems This oscillator is capable of generating high-frequency signals up to 70 GHz in both electrical and optical domains and is a special voltage-controlled oscillator with an optical output port It can be used to make a phase-locked loop (PLL) and perform all functions that a PLL is capable of for photonic systems It can be synchronized to a reference source by means of optical injection locking, electrical injection locking, and PLL It can also be self-phase locked and self-injection locked to generate a high-stability photonic RF reference Its applications include high-frequency reference regeneration and distribution, high-gain frequency multiplication, comb-frequency and square-wave generation, carrier recovery, and clock recovery We anticipate that such photonic voltage-controlled oscillators (VCOs) will be as important to photonic RF systems as electrical VCOs are to electrical RF systems

I. Introduction

RF oscillators, especially voltage controlled oscillators (VCOs), are essential to RF communication, broadcasting, and receiving systems Their functions include generating, tracking, cleaning, amplifying, and distributing RF carriers The VCOs in a phase-locked loop configuration can also be used for clock recovery, carrier recovery, signal modulation and demodulation, and frequency synthesizing

Photonic RF systems [1–3] embed photonic technology into the traditional RF systems In particular, in a photonic RF system, optical waves are used as a carrier to transport RF signals through optical fiber to remote locations In addition, some of the RF signal-processing functions, such as signal mixing [4], antenna beam steering [5,6], and signal filtering [7,8] can also be accomplished optically The photonic technology offers the advantages of low loss, light weight, high frequency, high security, remoting capability, and immunity to electromagnetic interference and, therefore, is desirable in many RF systems

Traditional RF oscillators cannot meet all the requirements of photonic RF systems Because photonic RF systems involve RF signals in both optical and electrical domains, an ideal oscillator for the photonic systems should be able to generate RF signals in both optical and electrical domains In addition, it should be possible to synchronize or control the oscillator by both electrical and optical references or signals

Presently, generating a high-frequency RF signal in the optical domain is usually done by modulating a diode laser or an external electro-optical (E/O) modulator using a high-frequency stable electrical signal from a local oscillator (LO) Such an LO signal is generally obtained by multiplying a low-frequency reference (e g , a quartz oscillator) to the required high frequency, say 32 GHz, with several stages of

multipliers and amplifiers Consequently, the resulting system is bulky, complicated, inefficient, and costly An alternative way to generate photonic RF carriers is to mix two lasers with different optical frequencies [9] However, the resulting bandwidth of the signal is wide (limited by the spectral width of the lasers, typically greater than tens of kilohertz) and the frequency stability of the beat signal is poor, caused by the drift of the optical frequency of the two lasers

We report here a novel photonic oscillator [10] that meets the special requirements for the photonic RF systems This oscillator is capable of generating stable signals at frequencies up to 70 GHz (limited by the speed of the E/O modulator and photoreceiver) in both electrical and optical domains We show that the photonic oscillator is a special VCO with both optical and electrical outputs It can be used to make a phase-locked loop (PLL) and perform all functions that a PLL is capable of for photonic systems It can also be phase locked to a remote reference through optical injection and, thus, is useful for high-frequency reference regeneration and distribution We have also demonstrated carrier recovery, clock recovery, high-gain frequency multiplication, and comb-frequency and square-wave generation using the photonic oscillator By using self-phase-locked loop and self-injection-locking techniques we have developed, high-stability photonic millwave references can be generated with the photonic oscillator We anticipate that such photonic VCOs will be as important to photonic RF systems as electrical VCOs are to electrical RF systems

II. Device Description

In a photonic oscillator [10], light from one of the output ports of the E/O modulator is detected by the photodetector and is then amplified, filtered, and fed back to the electrical input port of the modulator, as shown in Fig 1(a) If the modulator is properly biased and the open-loop gain of the feedback loop is properly chosen, self-electro-optic oscillation will be sustained Because both optical and electrical processes are involved in the oscillation, both the optical subcarrier and the electrical signal will be generated simultaneously Note that this ring oscillator is inherently unidirectional, immune to the back reflections in the loop, and therefore generically stable

The photonic oscillator can be represented by a simple functional block diagram, shown in Fig 1(b) It is a six-port device with both optical and electrical injection ports, both optical and electrical output ports, and two voltage-controlling ports One of the controlling ports is simply the bias port of the E/O modulator, and the other one is connected to a fiber stretcher for controlling the loop length As will be shown below, the two injection ports can be used to injection lock the photonic oscillator to a reference source either optically or electrically The two output ports provide outputs with an RF carrier in both optical and electrical forms Finally, the two controlling ports can be used to tune the oscillation frequency and to make the photonic oscillator a VCO The six ports collectively make interfacing the oscillator and a photonic RF system much simpler

We have built several such photonic oscillators using different modulators and have generated optical subcarriers as high as 9 2 GHz, using a diode-pumped YAG laser at 1310 nm Figure 2(a) shows the generated RF signal at 9 2 GHz, and Fig 2(b) shows the generated signal at 100 MHz In both cases, the photonic oscillators were free running and no effort was made to reduce the noise For comparison, signal from a Hewlett Packard (HP)8656A signal generator is also shown in Fig 2(b), and the photonic oscillator clearly has higher spectral purity than the HP8656A

III. Steady-State Characteristics

A. Oscillation Threshold

To start oscillation from noise, the open-loop gain of the photonic oscillator must be larger than 1 The open-loop gain of the photonic oscillator is simply the RF power gain of an externally modulated photonic link and is given by [11]

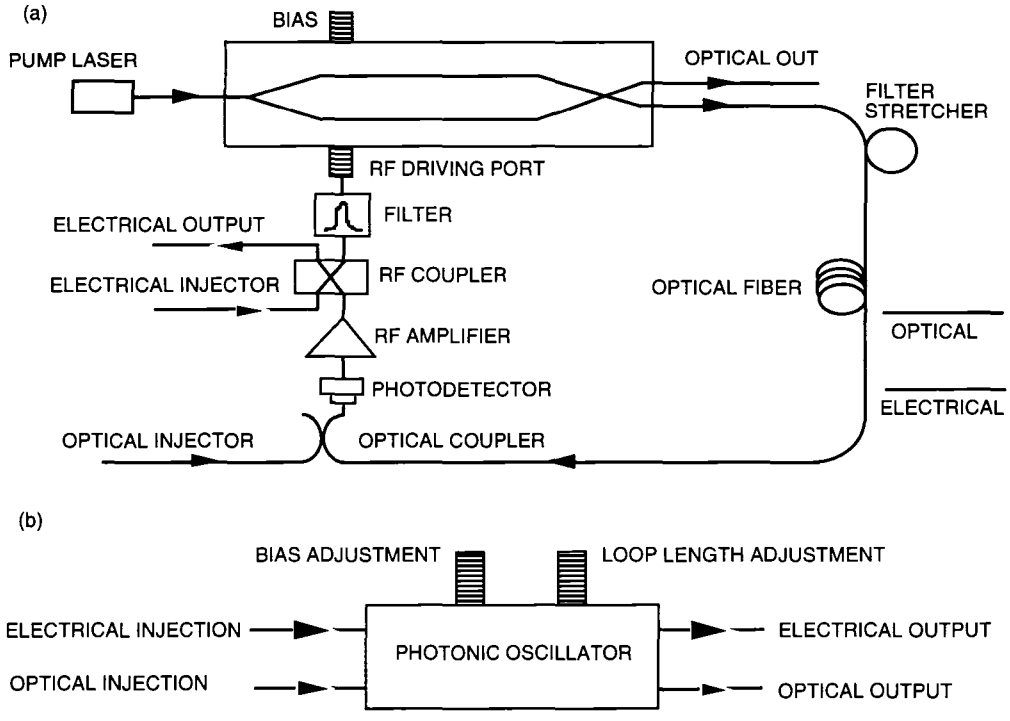

Fig 1 Device description of the photonic oscillator (a) device construction and (b) functional diagram

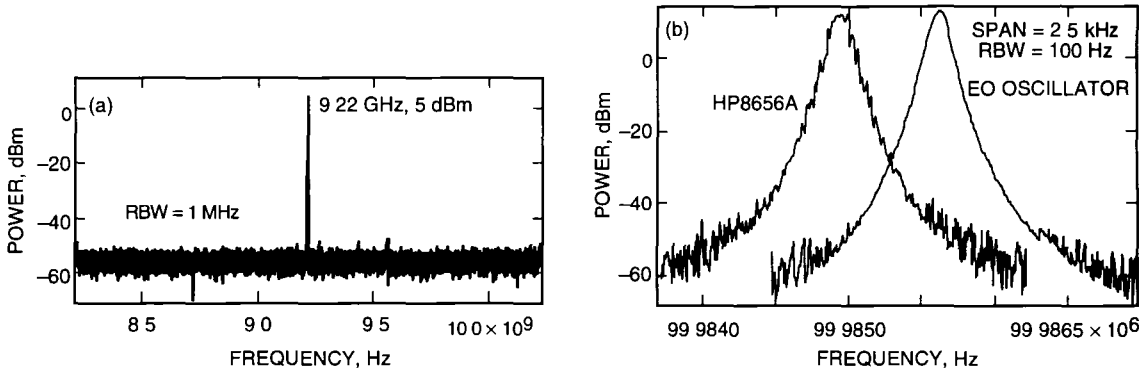

Fig 2 Spectra of free-running photonic oscillators, oscillation at (a) 9 22 GHz and (b) 100 MHz

$$G_{open}^2 = G_{amp}^2 \pi^2 \frac{I_{ph}^2 R_L}{V_\pi^2 / R_m} \tag{1}$$

where G_{open} is the open-loop voltage gain, I_{ph} is the photocurrent in the receiver, R_L is the load resistance of the receiver, R_m is the input impedance of the modulator, V_π is the half-wave voltage of the modulator, and G_{amp} is the voltage gain of the amplifier following the photoreceiver In Eq (1), the modulator is assumed to be of a Mach–Zehnder type and is biased at quadrature The oscillation condition of the photonic oscillator is, thus, $G_{open} \geq 1$ For $R_L = R_m \equiv R$, this condition becomes

$$I_{ph}RG_{amp} \geq \frac{V_\pi}{\pi} \tag{2}$$

It is important to notice that the amplifier in the loop is not a necessary condition for oscillation So long as $I_{ph}R \geq V_\pi/\pi$ is satisfied, no amplifier is needed ($G_{amp} = 1$) It is the optical power from the pump laser that actually supplies the necessary energy for the photonic oscillator This property is significant because it enables the photonic oscillator to be powered remotely using an optical fiber In addition, the elimination of the amplifier in the loop also eliminates the amplifier noise, resulting in a more stable oscillator For a modulator with a V_π of 3 14 V and an impedance R of 50 Ω, a photocurrent of 20 mA is required for sustaining the photonic oscillation without an amplifier This corresponds to an optical power of 25 mW, taking the responsivity ρ of the photodetector to be 0 8 A/W

B. Oscillation Amplitude

The optical power from the output port that forms the loop is related to an applied voltage $V(t)$ by [11]

$$P(t) = \frac{\alpha P_o}{2}\left\{1 - \eta \sin \pi \frac{V(t) + V_B}{V_\pi}\right\} \tag{3}$$

where α is the fractional insertion loss of the modulator, V_B is the bias voltage, and η relates to the extinction ratio of the modulator by $(1 + \eta)/(1 - \eta)$ If $P(t)$ has a positive slope as a function of driving voltage $V(t)$, the modulator is said to be positively biased, otherwise it is negatively biased Consequently, if the value of V_B is chosen such that $V_B = 0$, the modulator is biased at negative quadrature, while when $V_B = V_\pi$, the modulator is biased at positive quadrature Note that in most externally modulated photonic links, the E/O modulators can be biased at either positive or negative quadrature without affecting their performance However, as will be seen next, the biasing polarity will have an important effect on the operation of the photonic oscillator

For the photonic oscillator, the applied voltage $V(t)$ is just the photovoltage after the filter in the loop $V(t) = \rho RG_{amp}P(t)$, where ρ is the responsivity of the detector, R is the loop impedance, and G_{amp} is the amplifier voltage gain The recurrence relation of the oscillating signal in the loop can be easily obtained from Eq (3)

$$u(t) = u_o\left\{1 - \eta \sin \pi\left[u(t - \tau) + u_B\right]\right\} \tag{4}$$

where τ is the loop delay time and u_o, u_B, and $u(t)$ are the normalized photovoltage, normalized bias voltage, and normalized oscillation voltage, respectively They are defined as

$$u_o \equiv \frac{I_{ph}RG_{amp}}{V_\pi} \tag{5}$$

$$u_B = \frac{V_B}{V_\pi} \tag{6}$$

$$u(t) \equiv \frac{V(t)}{V_\pi} \tag{7}$$

In Eq (5), $I_{ph} = \alpha\rho P_o/2$ Equation (4) simply relates the oscillation voltage at t with that of an earlier time, $t - \tau$

At steady state, the oscillating voltage should repeat itself after a round trip in the loop, that is, $u(t) = u(t - \tau)$ This is the self-consistent condition For the case when only one frequency ω_o is allowed to oscillate by putting a filter in the loop, the solution to Eq (4) has the form

$$u(t) = a \sin(\omega_o t + \phi_o) \tag{8}$$

where a is the normalized oscillation amplitude and ϕ_o is the phase Note that in writing down Eq (8) this way, the observation point of the field is chosen to be right after the filter Substituting Eq (8) in Eq (4) and using the self-consistent condition, we obtain

$$a \sin(\omega_o t + \phi_o) = u_o \{1 - \eta \sin \pi \{a \sin [\omega_o(t - \tau) + \phi_o] + u_B\}\} \tag{9}$$

Expanding the right-hand side of Eq (9) using the Bessel function and picking out the term with the fundamental frequency component, we obtain

$$a \sin(\omega_o t + \phi_o) = -2u_o \eta J_1(\pi a) \cos \pi u_B \sin(\omega_o t + \phi_o - \omega_o \tau) \tag{10}$$

To simplify the discussion, we will restrict ourselves to the case when $J_1(\pi a) \geq 0$ or $a \equiv V_{osc}/V_\pi \leq 1\ 21$, since in the majority of cases, the oscillation amplitude V_{osc} of the oscillator is much less than V_π With this restriction, we obtain form Eq (10) the following relations for determining the oscillation amplitude and frequency

$$J_1(\pi a) = \frac{\pi a}{2G_{open}} \tag{11}$$

$$f_o = \frac{k + (1/2)}{\tau} \quad \text{for } \cos \pi u_B > 0 \tag{12a}$$

$$f_o = \frac{k}{\tau} \quad \text{for } \cos \pi u_B < 0 \tag{12b}$$

where $f_o = \omega_o/2\pi$ and k is an integer It is interesting to notice from Eq (12) that the oscillation frequency depends on the biasing polarity of the modulator For negative biasing ($\cos \pi u_B > 0$), the fundamental frequency is $1/(2\tau)$, while for positive biasing ($\cos \pi u_B < 0$), the fundamental frequency is doubled to $1/\tau$

In Eq (11), G_{open} is the open-loop voltage gain of the oscillator and is defined as

$$G_{open} \equiv \frac{\pi I_{ph} R G_{amp} \eta |\cos \pi u_B|}{V_\pi} \tag{13}$$

For the ideal case when $\eta = 1$ and $|\cos \pi u_B| = 1$, it is the same as that given in Eq (1) The amplitude of the oscillation can be obtained by solving Eq (11) graphically, and the result is shown in Fig 3(a)

Equation (9) can also be solved by expanding its right-hand side into a Taylor series, and the resulting normalized oscillation amplitude is

$$a \equiv \frac{V_{osc}}{V_\pi} = \frac{2\sqrt{2}}{\pi}\sqrt{1 - \frac{1}{G_{open}}} \qquad \text{third order expansion} \tag{14a}$$

$$a \equiv \frac{V_{osc}}{V_\pi} = \frac{2\sqrt{3}}{\pi}\left(1 - \frac{1}{\sqrt{3}}\sqrt{\frac{4}{G_{open}} - 1}\right)^{1/2} \qquad \text{fifth order expansion} \tag{14b}$$

From Eq (14), one can easily see that the threshold condition for the oscillation is $G_{open} \geq 1$ or $I_{ph}RG_{amp}\eta|\cos u_B| \geq V_\pi/\pi$ The oscillation frequency obtained using this procedure is the same as Eq (12)

Figure 3(a) shows the normalized oscillation amplitude as a function of G_{open} obtained from Eq (11), Eq (14a) and Eq (14b), respectively Comparing the three theoretical curves, one can see that, for $G_{open} \leq 1\ 57$, the third-order expansion result is a good approximation For $G_{open} \leq 3\ 14$, the fifth-order expansion result is a good approximation Figure 3(b) shows the experimental data, and they are in good agreement with the theoretical results of Eq (14a)

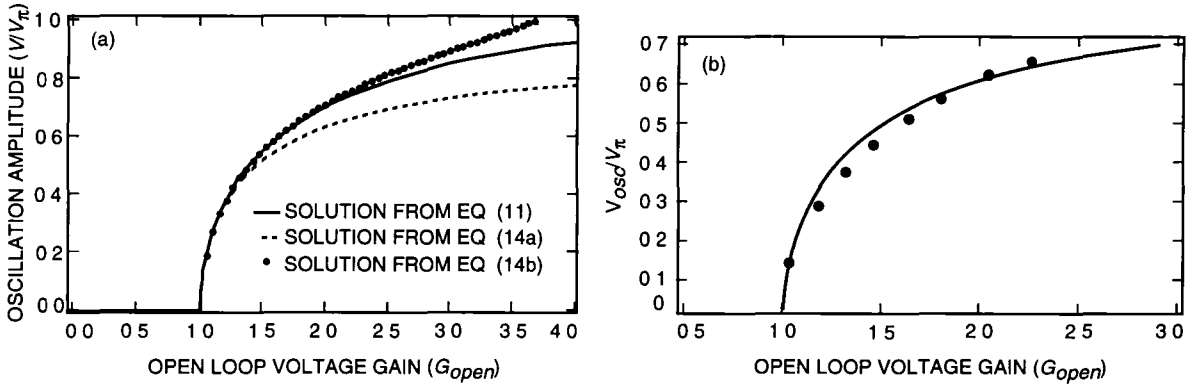

Fig 3 Oscillation amplitude as a function of photovoltage (a) theoretical curves and (b) experimental data

IV. Voltage-Controlled Oscillator Functions

As mentioned above, the oscillation frequency of the photonic oscillator can be tuned by changing the loop length using a piezoelectric stretcher The frequency change Δf is given by $\Delta f = -f_o\Delta L/L$, where L is the loop length, ΔL is the loop-length change, and f_o is the nominal oscillation frequency However, the tuning sensitivity (Hz/V) is expected to be small

The oscillation frequency can also be tuned by changing the bias voltage of the E/O modulator Figure 4(a) shows that the frequency detuning of the oscillator is linearly proportional to the bias voltage, with a slope of 38 8 kHz/V The output power of the oscillator remains relatively unchanged in a wide voltage range, as shown in Fig 4(b) This result is significant because it provided a simple way to tune the oscillation frequency with high sensitivity and is instrumental in realizing PLL using the novel photonic oscillator, as will be discussed next

V. Synchronization and Stabilization

A. Injection Locking

Injection locking [12,13] is a commonly used technique for synchronizing an oscillator with a reference frequency A unique aspect of the photonic oscillator is that it can be injection locked by either an optical

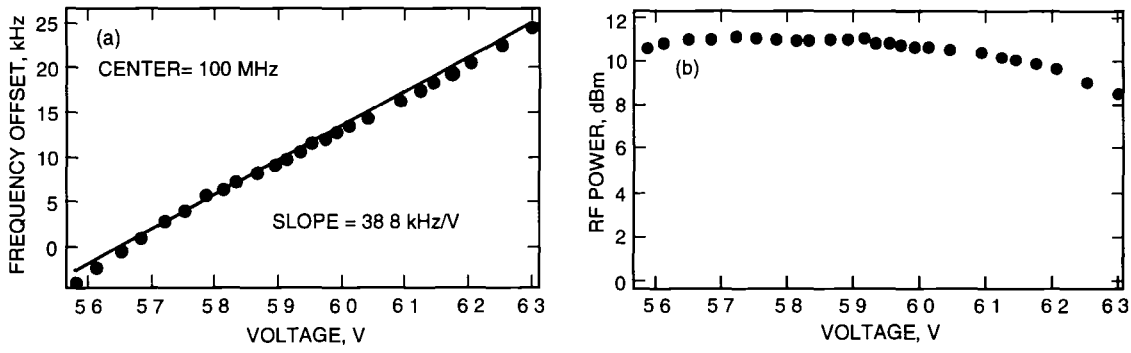

Fig 4 Demonstration of the capability of tuning the photonic oscillator's frequency by controlling the bias voltage of the photonic modulator (a) frequency versus bias voltage and (b) oscillation power versus bias voltage

signal or an electrical signal, as shown in Fig 1(b) Being able to injection lock an oscillator optically is important because it allows remote synchronization [14,15] This function is critical for high-frequency RF systems that require many oscillators locked to a single master, as in a phased-array radar Another advantage of optical injection locking is that the locking oscillator is electrically isolated from the locked oscillator, eliminating the need for impedance matching between the oscillators

Figure 5(a) shows the experimental results of injection locking the photonic oscillator with a maser reference at 100 MHz through the electrical injection port Similar results are expected for optical injection since the optical injection signal will first be converted to an electrical signal by an internal photodetector in the loop before affecting the E/O modulator As shown in Fig 5, with an injection power of −5 dBm, the phase noise of the photonic oscillator was almost identical to that of the injecting maser signal Note that the output RF power of the photonic oscillator was 13 dBm, resulting in a gain of 18 dB As the injection power decreased, the phase noise of the photonic oscillator increased somewhat However, the output RF power remained the same and, therefore, the gain was effectively increased In the experiments, we were able to injection lock the photonic oscillator to a maser reference with an injection power as low as −50 dBm Figure 5(b) shows the experimental result of the locking range as a function of injection power As expected, the locking range is linearly proportional to the square root of the injection power, agreeing well with Adler's injection-locking theory [12]

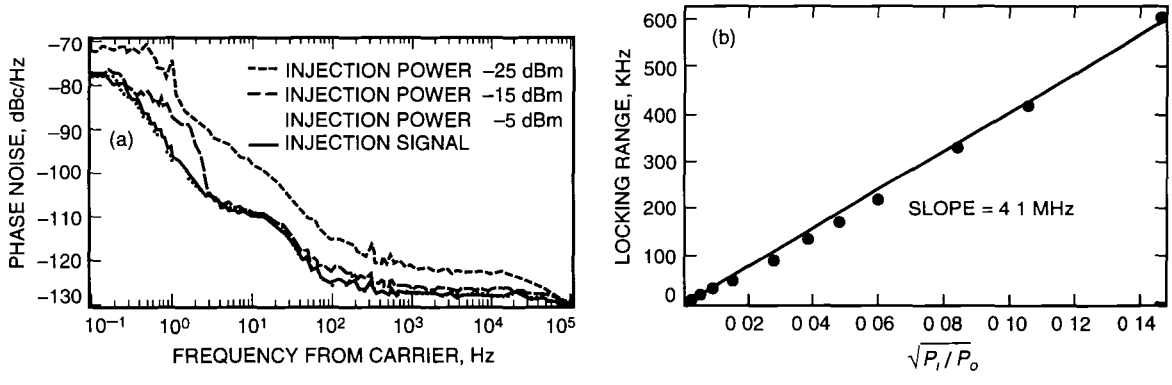

Fig 5 Demonstration of injection locking the photonic oscillator (a) phase noise measurement of the injection-locked oscillator and (b) locking range as a function of the square root of the injection power

B. Self-Injection Locking

Although injection locking is an effective means of synchronizing and stabilizing oscillators, it requires a low-noise and high-stability source to begin with Making a high-frequency and high-stability source

itself is a difficult task By using a novel scheme called self-injection locking to stabilize the photonic oscillator, the photonic oscillator may be made as the frequency reference, as illustrated in Fig 6(a) In this scheme, we derive a small portion of the output optical signal from the photonic oscillator and send it through a long fiber delay line The output from the fiber delay line is then converted to electric signal and is fed back to the RF driving port of the E/O modulator Note that the open-loop gain of this feedback loop should be kept much below unity so that no self-oscillation can be started Basically, what we do here is to inject a delayed replica of the photonic oscillator's output back to the oscillator and force the oscillator to lock to its "past " This will prevent the oscillator from changing its frequency and phase and, hence, reduce the frequency and phase fluctuations The frequency stability of the oscillator then is expected to be proportional to the length fluctuation $\Delta L/L$ of the fiber delay line

Figure 6(b) presents the experimental results, showing the effectiveness of the self-injection technique in reducing the frequency noise of the photonic oscillator The length of the delay line used in the experiment is 12 km, and the feedback injection RF power is -19 23 dBm It is evident that self-injection locking greatly reduced the frequency fluctuations of the photonic oscillator Further noise reduction is expected if we reduce the length fluctuation of the fiber delay line by placing it in a temperature-controlled environment and isolating it from acoustic vibrations More experiments are under way to further reduce the noise of the self-injection locked photonic oscillator

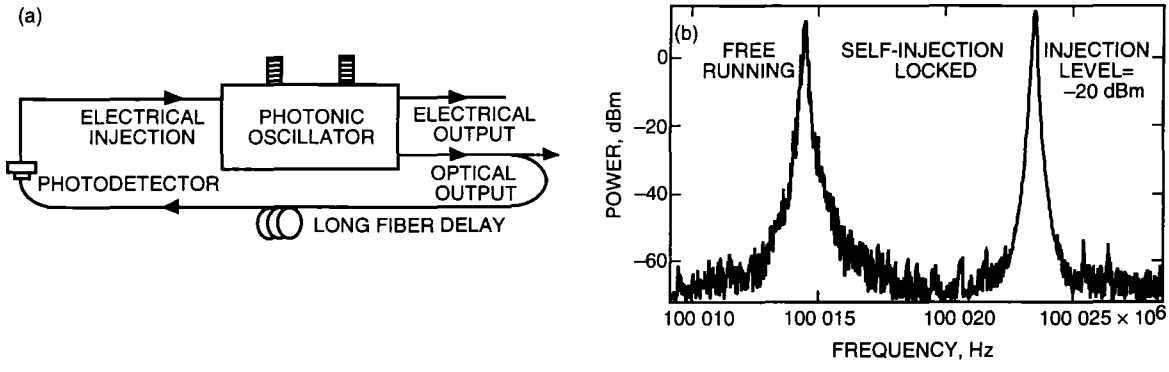

Fig 6 Demonstration of self-injection locking (a) the self-injection locking concept and (b) experimental result

C. Phase-Locked Loop

Because the photonic oscillator is also a VCO, it can be synchronized to a reference source via a phase-locked loop [16], as shown in Fig 7(a) Currently, experiments are under way for evaluating the performance of such a photonic phase-locked loop

D. Self-Phase Locking

One unique property of the photonic oscillator is that it has an optical output With this optical output, we can make a self-phase-locked loop to stabilize the photonic oscillator, as shown in Fig 7(b) Similar to self-injection locking described earlier, a self-phase-locked loop forces the oscillator to be locked to its past and prevents it from fluctuating

Using the delay-line discriminator technique to stabilize an oscillator is well known To effectively stabilize an oscillator, a delay of many kilometers is needed and was, therefore, considered impractical before the emergence of the photonic technology In our laboratory, Logan et al [17] previously demonstrated using a fiber-optic delay line to stabilize a traditional VCO and obtained excellent results However, in that setup, the fiber-optic delay line included a laser transmitter to convert the VCO's electrical output into optical signal and then transmit the optical signal through a few kilometers of fiber Since the photonic oscillator automatically contains an optical output, it is ideal for using the fiber delay line technique

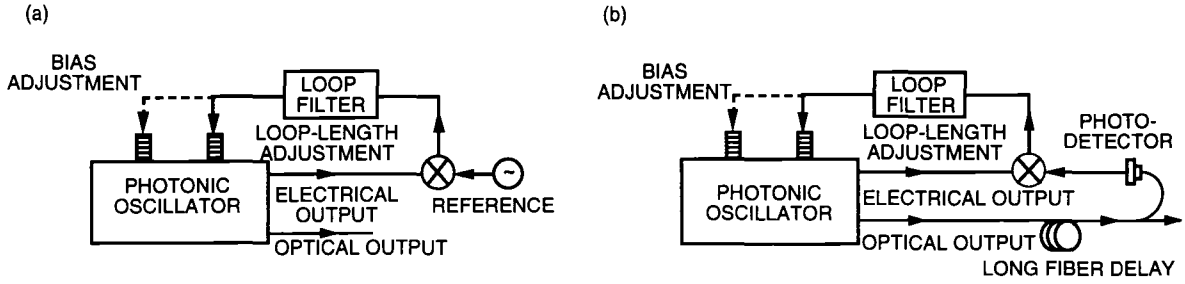

Fig 7 Illustrations of phase locking the photonic oscillator using a phase-locked loop (a) phase locking to a reference source and (b) phase locking to its past or self-phase locking

to stabilize itself without the need of electrical-to-optical signal conversion Consequently, the device is simple, low loss, and less expensive

VI. Applications

Voltage Controlled Oscillator As mentioned earlier, the photonic oscillator is a special VCO with optical output Therefore, it can perform all functions that a VCO is capable of for photonic RF systems These functions include generating, tracking, cleaning, amplifying, and distributing RF carriers [16] The photonic VCOs in a phase-locked loop configuration can also be used for clock recovery, carrier recovery, signal modulation and demodulation, and frequency synthesis

Photonic Signal Mixing The photonic oscillator can also be used for photonic signal up/down conversion, as shown in Fig 8 For such an application, a stable optical RF LO, or a modulated optical signal at an RF frequency, is required The photonic oscillator can accomplish just that, since one of its outputs gives the RF oscillation in optical domain

Carrier Distribution Because the photonic oscillator can be injection locked by a remote optical signal, it can be used for high-frequency RF carrier regeneration, amplification, and distribution, as shown in Fig 9 Such a capability is important in large photonic RF systems

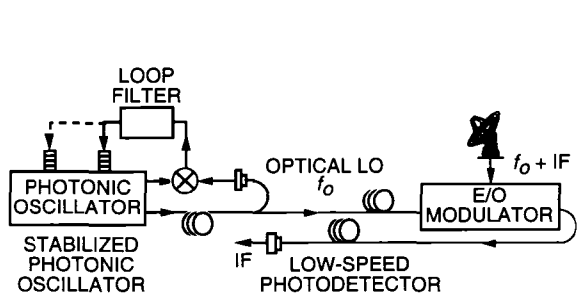

Fig 8 Using the photonic oscillator for photonic downconversion

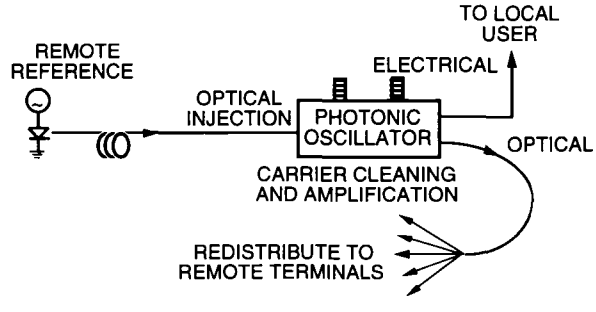

Fig 9 Using the photonic oscillator for reference regeneration and distribution

Frequency Multiplication The injection-locking property of the photonic oscillator can also be used for high-gain frequency multiplication In the first scheme, as shown in Fig 10(a), the nonlinearity of the modulator is used and the photonic oscillator is injection locked to an external signal that is a subharmonic of the oscillator's operating frequency This is the so-called subharmonic injection locking [18] We have demonstrated phase locking the oscillator operating at 300 MHz to a 100-MHz reference of 4 dBm The output of the oscillator is 15 dBm, resulting in a gain of 11 dB and a frequency multiplication factor of 3

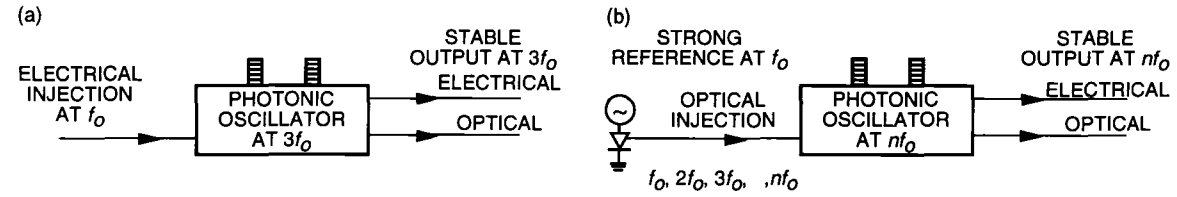

Fig 10 Using the photonic oscillator for frequency multiplication (a) using the photonic oscillator's nonlinearity and (b) using the laser diode's nonlinearity

In the second scheme, the nonlinearity of a laser diode [14] is used, as shown in Fig 10(b) If the laser is biased properly and is driven hard enough, its output will contain many harmonics of the driving signal The photonic oscillator is tuned to operate at a nominal frequency close to the nth harmonic of the reference signal driving the laser diode Upon the injection of the laser's output, the photonic oscillator will be locked to the nth harmonic This scheme offers remote frequency multiplication capability [19] and may be useful for many photonic RF systems

Comb-Frequency and Square-Wave Generation The photonic oscillator can also be used to generate frequency combs and square waves, as shown in Fig 11 For this application, the photonic oscillator is chosen to operate with multimodes A sinusoidal signal with a frequency equal to the mode spacing or a multiple of mode spacings is injected into the oscillator Just like laser mode locking, this injected signal will force all modes to oscillate in phase Consequently, we obtain a comb of frequencies that are in phase In the time domain, the output signal is a square wave

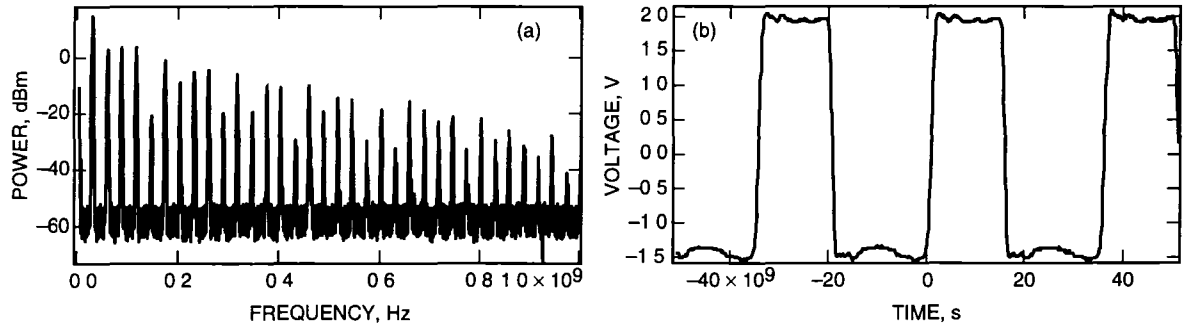

Fig 11 Using the photonic oscillator for (a) comb-frequency generation and (b) square-wave generation

Clock and Carrier Recovery In high-speed fiber-optic communication systems, the ability to recover the clock from the incoming random data is essential [20,21] The same injection-locking property of the photonic oscillator can also be used for clock and carrier recovery The incoming data are injected into the photonic oscillator either optically or electrically The free-running photonic oscillator is tuned to oscillate at a nominal frequency equal to the clock frequency of the incoming data With the injection of the data, the photonic oscillator will be quickly phase locked to the clock frequency of the data stream while rejecting other frequency components (harmonics and subharmonics) associated with the data Consequently, the output of the locked photonic oscillator is a continuous periodic wave synchronized with the incoming data, or simply the recovered clock As can be seen, the device has both electrical and optical inputs and both electrical and optical outputs

We have demonstrated clock recovery from both return-to-zero (RZ) and nonreturn-to-zero (NRZ) data at 100 Mb/s and have obtained excellent results [22] Data rates up to 70 Gb/s can also be recovered using the injection-locking technique with a photonic oscillator operating at 70 GHz Note that the data rates at one-half of this value are impossible to achieve with the current electronic clock recovery techniques

Another important feature of the photonic oscillator technique is that the clock can be recovered directly from data just out of a fiber-optic transmission line, without the need of optical-to-electrical conversion In addition, the recovered clock signal has both optical and electrical forms and is easy to interface with a fiber-optic communication system

Similar to clock recovery, a carrier buried in noise can also be recovered by the photonic oscillator To do so, we simply inject the spoiled carrier into a photonic oscillator that has a free-running frequency close to the carrier and an output power level $N(N >> 1)$ dB higher than the carrier The injected carrier forces the photonic oscillator to be locked with the carrier and results in an equivalent carrier gain of N dB Because the open-loop gain of the photonic oscillator is only n dB ($n \sim 1$), the noise of the input is only amplified by n dB, and the signal-to-noise ratio of the carrier is then increase by $(N - n)$ dB We have also demonstrated the recovery of carrier from noise and increased the carrier-to-noise ratio by 50 dB [22]

VII. Summary

In summary, we have reported a novel photonic oscillator This device is capable of generating stable signals at frequencies up to 70 GHz and is a special VCO with both optical and electrical output It can be used to make a phase-locked loop (PLL) and to perform all functions that a PLL is capable of for photonic systems It can be synchronized to a reference source by means of optical injection locking, electrical injection locking, and PLL It can also be self-phase locked and self-injection locked to generate high-stability photonic RF reference Its applications include high-frequency reference regeneration and distribution, high-gain frequency multiplication, comb-frequency and square-wave generation, carrier recovery, and clock recovery We anticipate that such photonic VCOs will be as important to photonic RF systems as electrical VCOs are to electrical RF systems

Acknowledgments

We thank G Lutes and M Calhoun for many technical discussions and for their assistance

References

[1] H Ogawa, D Polifko, and S Banba, "Millimeter-Wave Fiber Optics Systems for Personal Radio Communication," *IEEE Trans Microwave Theory Techn*, vol 40, no 12, pp 2285–2293, 1992

[2] P Herczfeld and A Daryoush, "Fiber Optic Feed Network for Large Aperture Phased Array Antennas," *Microwave Journal*, pp 160–166, August 1987

[3] X S Yao, G Lutes, R Logan, and L Maleki, "Field Demonstration of X-Band Photonic Antenna Remoting in the Deep Space Network," *The Telecommunications and Data Acquisition Progress Report 42-117, January–March 1994*, Jet Propulsion Laboratory, Pasadena, California, pp 29–34, May 15, 1994

[4] G K Gopalakrishnan, W K Burns, and C H Bulmer, "Microwave-Optical Mixing in $LiNbO_3$ Modulators," *IEEE Trans Microwave Theory Techn*, vol 41, no 12, pp 2383–2391, 1993

[5] E Toughlian and H Zmuda, "A Photonic Variable RF Delay Line for Phased Array Antennas," *J of Lightwave Technology*, vol 8, pp 1824–1828, 1990

[6] X S Yao and L Maleki, "A Novel 2-D Programmable Photonic Time-Delay Device for Millimeter-Wave Signal Processing Applications," *IEEE Photonic Techn Lett*, vol 6, no 12, pp 1463–1465, 1994

[7] D Nortton, S Johns, and R Soref, "Tunable Wideband Microwave Transversal Filter Using High Dispersive Fiber Delay Lines," *Proceedings of the 4th Biennial Department of Defense Fiber Optics and Photonics Conference*, McLean, Virginia, pp 297–301, 1994

[8] B Moslehi, K Chau, and J Goodman, "Fiber-Optic Signal Processors With Optical Gain and Reconfigurable Weights," *Proceedings of the 4th Biennial Department of Defense Fiber Optics and Photonics Conference*, McLean, Virginia, pp 303–309, 1994

[9] *Introduction to Diode-Pumped Solid-State Lasers*, Lightwave Electronics Corp , Technical Information No 1, Mountain View, California, 1993

[10] X S Yao and L Maleki, "High Frequency Optical Subcarrier Generator," *Electron Lett* , vol 30, no 18, pp 1525–1526, 1994

[11] X S Yao and L Maleki, "Influence of an Externally Modulated Photonic Link on a Microwave Communications System," *The Telecommunications and Data Acquisition Progress Report 42-117, January–March 1994*, Jet Propulsion Laboratory, Pasadena, California, pp 16–28, May 15, 1994

[12] R Adler, "A Study of Locking Phenomena in Oscillators," *Proc IRE*, vol 34, pp 351–357, 1946

[13] K Kurokawa, "Injection Locking of Microwave Solid-State Oscillators," *Proceedings of the IEEE*, vol 61, no 10, pp 1386–1410, 1973

[14] A Daryoush, "Optical Synchronization of Millimeter-Wave Oscillators for Distributed Architectures," *IEEE Trans Microwave Theory Techn* , vol 38, no 5, pp 467–476, 1990

[15] L Goldberg, C Rauscher, J F Weller, and H F Taylor, "Optical Injection Locking of X-Band FET Oscillator Using Coherent Mixing of GaAs Lasers," *Electron Lett* , vol 19, no 20, pp 848–849, 1983

[16] D Wolaver, *Phase-Locked Loop Circuit Design*, Englewood Cliffs, New Jersey Prentice Hall, 1991

[17] R Logan, L Maleki, and M Shadaram, "Stabilization of Oscillator Phase Using a Fiber Optic Delay Line," *Proceedings of the 45th Annual Symposium on Frequency Control*, IEEE Ultrasonic Ferroelectric and Frequency Control Society, Los Angeles, California, May 29–31, 1991

[18] X Zhang, X Zhou, and A Daryoush, "A Theoretical Study of the Noise Behavior of Subharmonically Injection Locked Local Oscillators," *IEEE Trans Microwave Theory Techn* , vol 40, no 5, pp 895–902, 1992

[19] A Daryoush, P Herczfeld, Z Turski, and P Kahi, "Comparison of Indirect Optical Injection Locking Techniques of Multiple X-Band Oscillators," *IEEE Trans Microwave Theory Techn* , vol MTT-34, no 12, pp 1363–1369, 1986

[20] P E Barnsley, H J Wickes, G E Wickens, and D M Spirit, "All-Optical Clock Recovery From 5 Gb/s Data Using a Self-Pulsation 1 56 mm Laser Diode," *IEEE Photonic Techn Lett* , vol 3, no 10, pp 942–945, 1991

[21] D M Patrick and R J Manning, "20 Gbit/s All-Optical Clock Recovery Using Semiconductor Nonlinearity," *Electron Lett* , vol 30, no 2, pp 151–152, 1994

[22] X S Yao and G Lutes, "A High-Speed Photonic Clock and Carrier Regenerator," *The Telecommunications and Data Acquisition Progress Report 42-121, January–March 1995*, Jet Propulsion Laboratory, Pasadena, California, pp 202–210, May 15, 1995

Transfer Function Bounds on the Performance of Turbo Codes

D Divsalar, S Dolinar, and F Pollara
Communications Systems and Research Section

R J McEliece
California Institute of Technology
and
Communications Systems and Research Section

In this article, we apply transfer function bounding techniques to obtain upper bounds on the bit-error rate for maximum-likelihood decoding of turbo codes constructed with random permutations These techniques are applied to two turbo codes with constraint length 3 and later extended to other codes The performance predicted by these bounds is compared with simulation results The bounds are useful in estimating the "error floor" that is difficult to measure by simulation, and they provide insight on how to lower this floor More refined bounds are needed for accurate performance measures at lower signal-to-noise ratios

I. Introduction

Simulations have shown that turbo codes can produce low error rates at astonishingly low signal-to-noise ratios if the information block is large and the permutations are selected randomly [3,4] In addition to simulations, it is also useful to have theoretical bounds that establish decoder performance in the range where obtaining sufficient data from simulations is impractical

In this article, we apply transfer function bounding techniques to obtain upper bounds on the bit-error rate for maximum-likelihood decoding of turbo codes constructed with random permutations The premise for these bounds is the same as for the usual transfer function bounds applied to standard convolutional codes [7] The error probability is upper bounded by a union bound that sums contributions from error paths of different encoded weights The state diagram of the code is used to enumerate the paths of each possible weight

The transfer function bounds for turbo codes differ from the usual transfer function bounds for convolutional codes in several respects For turbo codes, these bounds require a term-by-term joint enumerator for all possible combinations of input weights and output weights of error events, even for bounds on the word error rate Second, because turbo codes are block codes, it is crucial to accurately enumerate "compound" error events that can include more than one excursion from the all-zero state during the fixed block length, as shown in Fig 1 Third, since explicit results are intractable for any particular randomly chosen permutation, the bound is developed as a random coding bound Finally, the bounds are derived as upper bounds on the bit-error rate of a maximum-likelihood decoder operating on

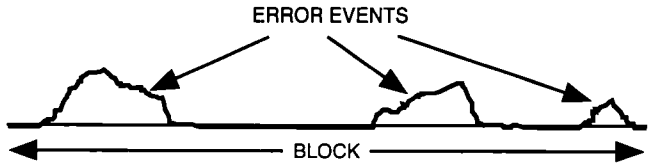

Fig 1 Example of "compound" error events

turbo-encoded data, whereas the iterative turbo-decoding procedure is not guaranteed to converge to the maximum-likelihood codeword On the other hand, since the turbo decoder attempts to minimize the bit-error rate rather than the word-error rate, it can in some circumstances yield a slightly lower bit-error rate than a maximum-likelihood decoder

Transfer function bounds for turbo codes were first published by Benedetto and Montorsi [1,2], but our computation method allows for more accurate numerical results Our algorithm uses a short recursion formula to calculate the necessary transfer function coefficients efficiently for large block lengths We have found that the bound "diverges" (i e , becomes useless) at low E_b/N_0, as does the corresponding type of bound for standard convolutional codes

Our approach in this article is first to explicitly develop the bounds for two exemplary turbo codes with constraint length 3 One code is the same reported in [2] The second code should be superior to the first according to the heuristic arguments of [5], it is presented to underscore the reasons why one code should outperform the other Only after developing the two examples in detail do we extend the theory to additional codes

II. Turbo Code Examples

In this section, we introduce the two particular turbo codes that will be used throughout this article to develop the bounds

A. Encoder Diagrams

Figures 2(a) and 2(b) depict the two exemplary turbo encoders Both encoders produce one uncoded output stream $\mathbf{x}_0$ and two encoded parity streams $\mathbf{x}_1, \mathbf{x}_2$, for an overall code rate of 1/3 The parity streams come from simple recursive convolutional encoders with constraint length $K = 3$ (i e , memory $m = 2$) For the first code, the parity sequences both correspond to a ratio of generator polynomials g_a/g_b, where $g_a(D) = 1 + D + D^2$ and $g_b(D) = 1 + D^2$ For the second code, the parity sequences both correspond to g_b/g_a Representing g_a as octal 7 and g_b as octal 5, the two codes are denoted by (1, 7/5, 7/5) and (1, 5/7, 5/7), respectively The notation explicitly shows the method of generating each of the three output streams, one uncoded and two parity We refer to these three separate rate-1 components of the code as *code fragments* The turbo code is a *parallel concatenation* of its code fragments By parallel concatenation, we simply mean adjoining several pieces of a codeword to form the full codeword

Figures 2(a) and 2(b) show each code fragment preceded by a permutation, π_0, π_1, or π_2 This seemingly needless complication is introduced here for symmetry and to facilitate random coding arguments presented later For these two examples, the only permutation relevant to the construction of the overall turbo code is the *relative* permutation $\pi_1^{-1}\pi_2$ or $\pi_2^{-1}\pi_1$ between the inputs $\mathbf{u}_1$ and $\mathbf{u}_2$ In practice, the permutations π_0 and π_1 are identities (i e , no permutation) Each of the encoders in Figs 2(a) and 2(b) is used to generate a $(3(N+2), N)$ block code, where N is the information block length Following the information bits, an additional 2 "tail bits" are appended in order to drive the encoder to the all-zero state at the end of the block The termination method described in [3] can be used

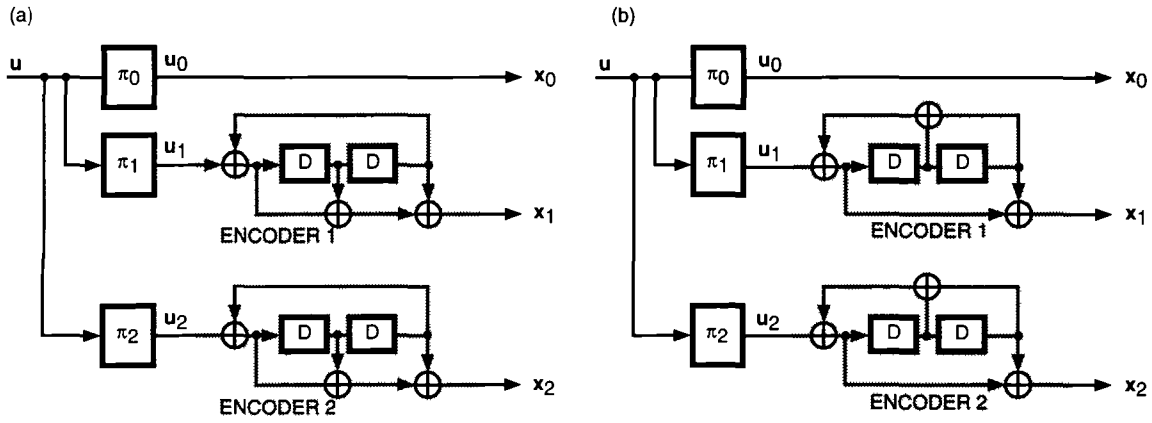

Fig 2 Two examples of turbo encoders (a) the (1, 7/5, 7/5) code and (b) the (1, 5/7, 5/7) code

B. State Diagrams

Each of the two exemplary turbo encoders is a four-state device Figures 3(a) and 3(b) show the state transition diagrams for the nontrivial code fragments, (g_a/g_b) and (g_b/g_a), respectively In this diagram, each transition between states is labeled by the input information bit and the corresponding output encoded bit It is convenient to replace each edge label in Figs 3(a) and 3(b) with a monomial $L^l I^i D^d$, where l is always equal to 1, and i and d are either 0 or 1, depending on whether the corresponding input and output bits are 0 or 1, respectively Then the information in the state transition diagrams can be summarized by state transition matrices $\mathbf{A}(L, I, D)$, where

$$\mathbf{A}_{7/5}(L, I, D) = \begin{pmatrix} L & LID & 0 & 0 \\ 0 & 0 & LD & LI \\ LID & L & 0 & 0 \\ 0 & 0 & LI & LD \end{pmatrix} \tag{1}$$

for the (7/5) code fragment, and

$$\mathbf{A}_{5/7}(L, I, D) = \begin{pmatrix} L & LID & 0 & 0 \\ 0 & 0 & LI & LD \\ LID & L & 0 & 0 \\ 0 & 0 & LD & LI \end{pmatrix} \tag{2}$$

for the (5/7) code fragment

C. Input–Output Weight Enumerator

For a given code fragment, defined by a state diagram with 2^m states as in Section II B, denote by $t(l, i, d)$ the number of paths of length l, input weight i, and output weight d, starting and ending in state 0^m, with the proviso that the last m edges in the path are "termination" edges and have neither length nor input weight The corresponding transfer function (generating function) is defined by

$$T(L, I, D) = \sum_{l \geq 0} \sum_{i \geq 0} \sum_{d \geq 0} L^l I^i D^d t(l, i, d) \tag{3}$$

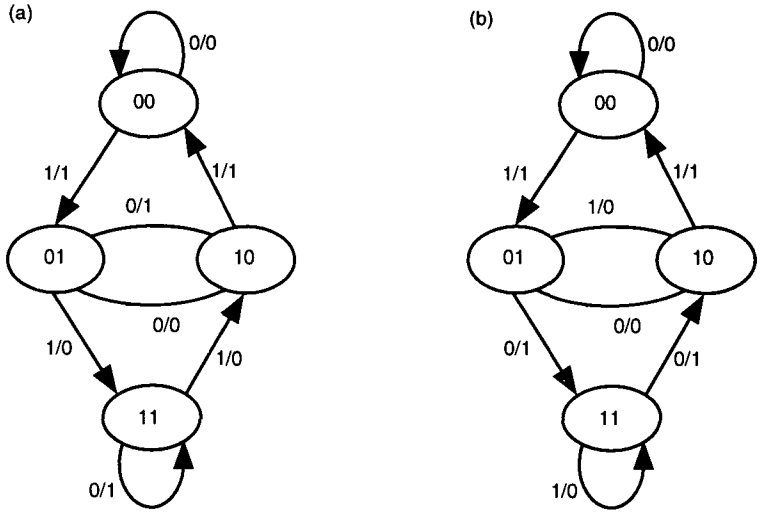

Fig 3 State diagrams of two code fragments (a) the (7/5) code fragment and (b) the (5/7) code fragment

Using the method described in Section 4 7 of [8], we find that $T(L, I, D)$ is the $(0^m, 0^m)$ entry in the matrix

$$(\mathbf{I} + \mathbf{A}(L, I, D) + \mathbf{A}(L, I, D)^2 + \mathbf{A}(L, I, D)^3 + \quad)\mathbf{A}(1, 1, D)^m \tag{4}$$

The factor $\mathbf{A}(1, 1, D)^m$ takes care of the termination edges Since $\mathbf{I} + \mathbf{A} + \mathbf{A}^2 + \mathbf{A}^3 + \quad = (\mathbf{I} - \mathbf{A})^{-1}$, it follows from Eq (4) that

$$T(L, I, D) = \left[(\mathbf{I} - \mathbf{A}(L, I, D))^{-1} \quad \mathbf{A}(1, 1, D)^m\right]_{0^m, 0^m} \tag{5}$$

Using Eq (5) (approximately, by omitting the termination factor $\mathbf{A}(1, 1, D)^m$), we find that the transfer functions for the (7/5) and (5/7) code fragments are

$$T_{7/5}(L, I, D) \approx \frac{1 - LD - L^2D + L^3\left(D^2 - I^2\right)}{1 - L(1 + D) + L^3\left(D + D^2 - I^2 - I^2D^3\right) - L^4\left(D^2 - I^2 - I^2D^4 + I^4D^2\right)} \tag{6}$$

and

$$T_{5/7}(L, I, D) \approx \frac{1 - LI - L^2I - L^3\left(D^2 - I^2\right)}{1 - L(1 + I) - L^3\left(D^2 - I - I^2 + I^3D^2\right) + L^4\left(D^2 - I^2 - I^2D^4 + I^4D^2\right)} \tag{7}$$

respectively Note that, in this approximation, $T_{7/5}(L, I, D) = T_{5/7}(L, D, I)$, i e , the roles of input weight i and output weight d are reversed for the two code fragments

If we multiply both sides of Eq (6) by the denominator of the right-hand side, and take the coefficient of $t(l, i, d)$ of both sides of the resulting equation, we obtain the following recursion determining $t_{7/5}(l, i, d)$ for the (7/5) code fragment, for $l \geq 0, i \geq 0, d \geq 0$

$$
\begin{aligned}
t(l,i,d) &= t(l-1,i,d-1) + t(l-1,i,d) \\
&\quad + t(l-3,i-2,d-3) + t(l-3,i-2,d) - t(l-3,i,d-2) - t(l-3,i,d-1) \\
&\quad + t(l-4,i-4,d-2) - t(l-4,i-2,d-4) - t(l-4,i-2,d) + t(l-4,i,d-2) \\
&\quad + \delta(l,i,d) - \delta(l-1,i,d-1) - \delta(l-2,i,d-1) + \delta(l-3,i,d-2) - \delta(l-3,i-2,d)
\end{aligned}
$$

where $\delta(l,i,d) = 1$ if $l = i = d = 0$ and $\delta(l,i,d) = 0$ otherwise, and with the initial conditions that $t(l,i,d) = 0$ if any index is negative

Similarly, $t_{5/7}(l,i,d)$ for the (5/7) code fragment can be evaluated by the recursion

$$
\begin{aligned}
t(l,i,d) &= t(l-1,i-1,d) + t(l-1,i,d) \\
&\quad + t(l-3,i-3,d-2) - t(l-3,i-2,d) - t(l-3,i-1,d) + t(l-3,i,d-2) \\
&\quad - t(l-4,i-4,d-2) + t(l-4,i-2,d-4) + t(l-4,i-2,d) - t(l-4,i,d-2) \\
&\quad + \delta(l,i,d) - \delta(l-1,i-1,d) - \delta(l-2,i-1,d) - \delta(l-3,i,d-2) + \delta(l-3,i-2,d)
\end{aligned}
$$

again with the understanding that $t(l,i,d) = 0$ if any index is negative

III. Union Bounds on Word and Bit-Error Probabilities

In this section, we use the input–output weight enumerators $t(l,i,d)$ for the various code fragments to obtain a union bound on the probabilities of word error and bit error, assuming an additive white Gaussian noise channel with channel symbol signal-to-noise ratio E_s/N_0

A. Derivation of the Bound

As depicted in Figs 2(a) and 2(b), the turbo code is constructed as a parallel concatenation of its three code fragments, each preceded by a random permutation of the input information bits $\mathbf{u}$ The randomly chosen permutations π_0, π_1, and π_2 transform the input sequence $\mathbf{u}$ into three permuted sequences $\mathbf{u}_0$, $\mathbf{u}_1$, and $\mathbf{u}_2$, each having the same Hamming weight as the original sequence $\mathbf{u}$ Since the turbo code has block length N, there are $t_{7/5}(N,i,d)$ codeword fragments of input weight i and output weight d from the two (7/5) code fragments of the (1, 7/5, 7/5) code, and $t_{5/7}(N,i,d)$ codeword fragments of input weight i and output weight d from the two (5/7) code fragments of the (1, 5/7, 5/7) code

Denote by $p(d|i)$ the conditional probability of producing a codeword fragment of weight d given a randomly selected input sequence of weight i Then[1]

$$
p(d|i) = \frac{t(N,i,d)}{\sum_{d'} t(N,i,d')} = \frac{t(N,i,d)}{\binom{N}{i}}
$$

[1] The summation $\sum_d t(N,i,d)$ equals the total number of codewords of information weight i, $\binom{N}{i}$ However, this is not exact if $t(N,i,d)$ is computed according to the approximation that does not account for the termination edges

The conditional probability distributions $p_{7/5}(d|i)$ and $p_{5/7}(d|i)$ are plotted in Figs 4(a) and 4(b) for the two code fragments (7/5) and (5/7), for block length $N = 100$ For the uncoded fragment, $p_1(d|i) = \delta(i, d)$

Note from Figs 4(a) and 4(b) that the (7/5) code fragment admits only even input weights i, while the (5/7) code fragment has only even output weights d The vertical scale of Fig 4(b) is twice that of Fig 4(a) to reflect the concentration of probability into even-only output weights for the (5/7) fragment The figures also show for reference a binomial probability distribution for 100 trials with probability 1/2 (in the case of Fig 4(b), the reference "binomial" distribution is twice the binomial probability for even weights only)

In both Figs 4(a) and 4(b), the conditional probability distribution $p(d|i)$ approaches the binomial reference for moderate to large values of input weight i, indicating a more or less random distribution of output weights d In contrast, the skewed distributions for low values of i are what differentiate the two code fragments from each other and the corresponding overall turbo codes from purely random codes In particular, notice how the $p(d|i)$ distribution for input weight $i = 2$ is more skewed toward lower output weights d for the (7/5) fragment than for the (5/7) fragment

If the permutations are selected randomly and independently, the probability $\tilde{p}(d_0, d_1, d_2|i)$ that any input sequence $\mathbf{u}$ of weight i will be mapped into codeword fragments of weights d_0, d_1, and d_2 is

$$\tilde{p}(d_0, d_1, d_2|i) = p_1(d_0|i)p_{7/5}(d_1|i)p_{7/5}(d_2|i)$$

for the (1, 7/5, 7/5) code and

$$\tilde{p}(d_0, d_1, d_2|i) = p_1(d_0|i)p_{5/7}(d_1|i)p_{5/7}(d_2|i)$$

for the (1, 5/7, 5/7) code The conditional probability that a maximum-likelihood decoder will prefer a particular codeword of total weight $d = d_0 + d_1 + d_2$ to the all-zero codeword is $Q(\sqrt{2dE_s/N_0})$, where $Q(\,)$ is the complementary unit variance Gaussian distribution function Thus, the codeword error probability P_w is upper bounded as follows

$$P_w = \sum_{i=1}^{N} \text{Prob [error event of weight } i] \leq \sum_{i=1}^{N} \binom{N}{i} \mathrm{E}_{d|i} \left\{ Q\left(\sqrt{\frac{2dE_s}{N_0}} \right) \right\} \tag{8}$$

where the conditional expectation $\mathrm{E}_{d|i}\{\ \}$ is over the probability distribution $\tilde{p}(d_0, d_1, d_2|i)$ Similarly, the information bit-error probability P_b is upper bounded by

$$P_b = \sum_{i=1}^{N} \frac{i}{N} \text{Prob [error event of weight } i] \leq \sum_{i=1}^{N} \frac{i}{N} \binom{N}{i} \mathrm{E}_{d|i} \left\{ Q\left(\sqrt{\frac{2dE_s}{N_0}} \right) \right\} \tag{9}$$

The error probabilities P_w and P_b bounded in Eqs (8) and (9) are averages (over randomly chosen permutations) of the word and bit error probabilities achieved by any particular turbo code with specified permutations π_0, π_1, π_2

B. Evaluation of the Bound for the Examples

Figures 5(a) and 5(b) show the bounds on P_b for the (1, 7/5, 7/5) code and the (1, 5/7, 5/7) code for various block lengths N Note that the transition from a well-behaved, useful, low P_b bound into

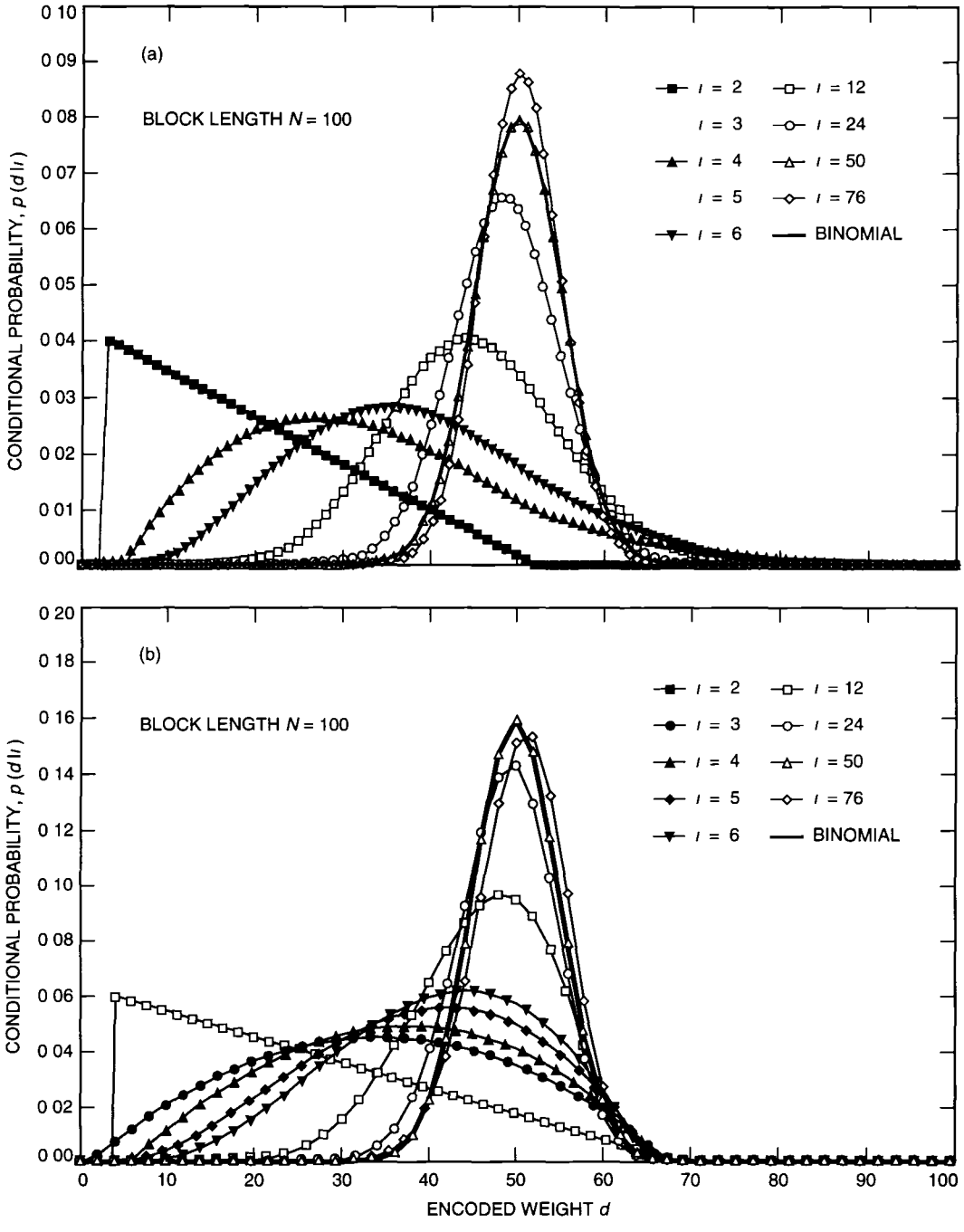

Fig 4 Conditional probability distribution $p(d \mid i)$ for output weight d given input weight i (a) code fragment (7/5) and (b) code fragment (5/7)

a diverged, useless bound greater than 1 occurs very abruptly if the block length N (i e , permutation length) is large The abrupt transition occurs roughly when the information bit signal-to-noise ratio E_b/N_0 drops below the threshold determined by the computational cutoff rate R_0, i e , when $E_s/N_0 = rE_b/N_0 < -\ln(2^{1-r} - 1)$ for a code with rate r [9] This behavior mimics that of similar bounds applied to totally random codes, which turbo codes resemble

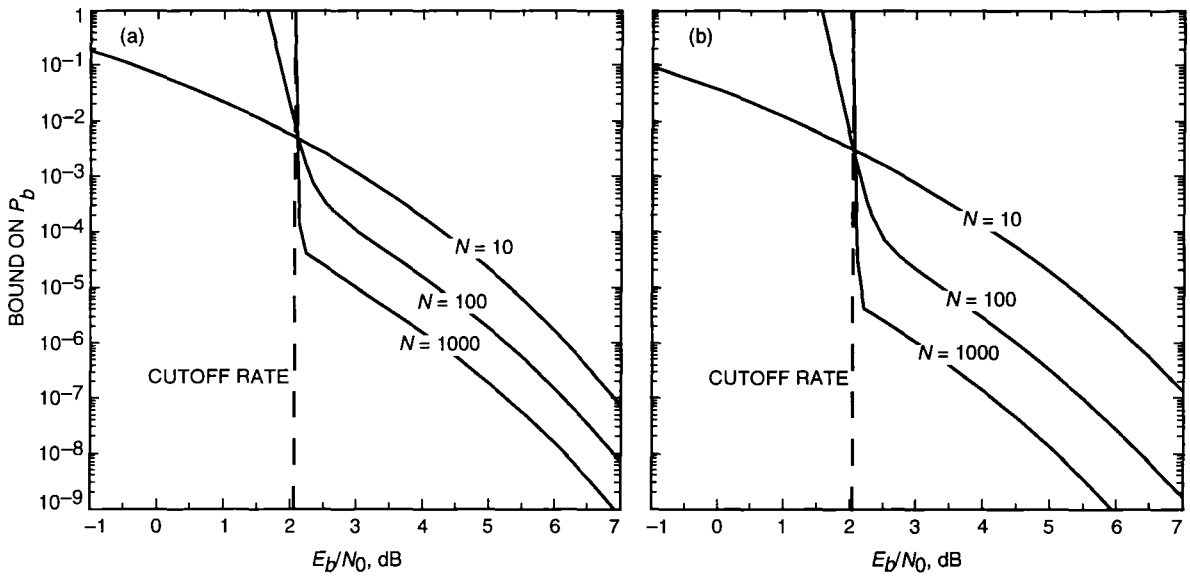

Fig 5 Bounds on P_b for various block lengths N (a) the (1, 7/5, 7/5) code and (b) the (1, 5/7, 5/7) code

In computing these bounds, we discovered and overcame two distinct types of pitfalls First, there is an inherent numerical precision problem that we have solved for block lengths up to about 1000 Second, for low E_b/N_0, there is a sinister "false convergence" region where the bound seems to have converged to an unchanging value, but after remaining at this constant value for many terms, it suddenly diverges to a useless probability bound greater than 1 Figure 6 illustrates this false convergence behavior For this figure, the summation in the union bound expression in Eq (9) is truncated after i^+ terms on the assumption that higher-order terms in i will not contribute to the sum For large block lengths (e g , $N = 400$ or $N = 1000$ in the figure), this assumption seems to be validated because the cumulative summation becomes almost totally flat after a small fraction i^+/N of all the terms However, when i^+/N reaches about 0 2, the cumulative summation starts increasing rapidly before saturating at a much higher level than the first plateau This illustration of the false convergence behavior is for $E_b/N_0 =$ 2 00 dB, which is just barely below the R_0 threshold of 2 03 dB for rate 1/3 codes The effect is even more dramatic if E_b/N_0 is decreased further On the other hand, when E_b/N_0 is above the R_0 threshold, false convergence is not a problem Figure 7 shows how quickly and truly the summation converges when $E_b/N_0 =$ 2 50 dB The curves in Fig 7 are also plotted versus the fraction i^+/N in order to show the full range of i^+ for all values of N simultaneously This demonstrates that the second plateau observed in Fig 6 is absent at the higher value of E_b/N_0 However, it is apparent from Fig 7 that only a handful of terms (roughly $i \leq 10$) are needed for convergence in this case, and this is almost independent of the value of N

When we first attempted to evaluate these bounds, we were fooled by the false convergence region and were computing error rates low enough to contradict Shannon's limit! After we learned how to properly evaluate the bounds, we found that other researchers (e g , [2]) were unaware of the intricacies of the divergence and had computed the bounds inaccurately at low E_b/N_0 However, in the next section, we will see that this divergence is an artifact of the bound, the error rate from an actual turbo decoder does not diverge at the R_0 threshold

C. Comparison of the Bounds With Turbo Decoder Simulation Results

Figure 8 compares the computed bounds for the (1, 7/5, 7/5) and (1, 5/7, 5/7) turbo codes with simulated turbo decoder bit-error rates We observe that, above the R_0 threshold of 2 03 dB, the simulated turbo decoder bit-error rate closely matches the error rate predicted by the bound Below this threshold,

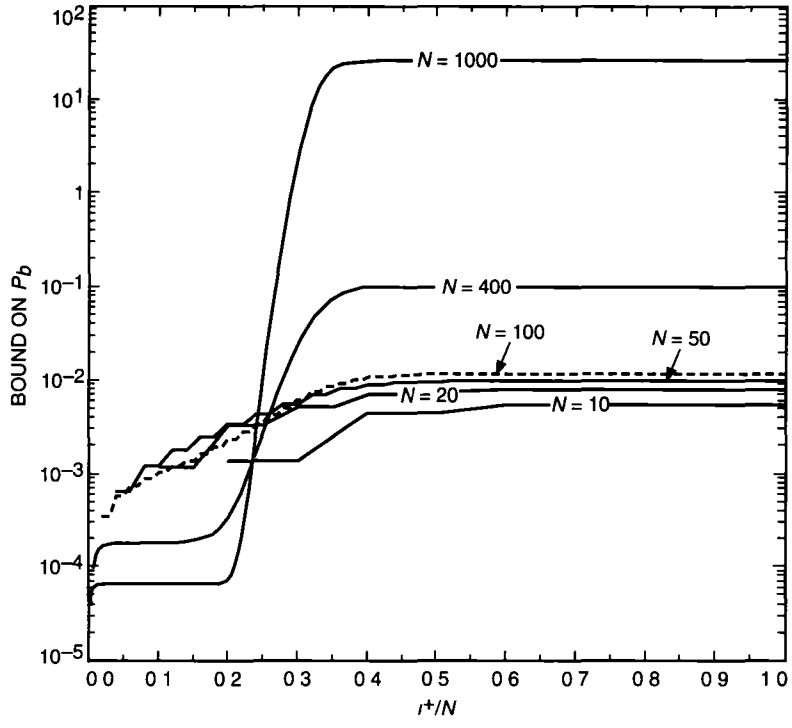

Fig 6 False convergence behavior at E_b/N_0 = 2 00 dB (just below the R_0 threshold of 2 03 dB)

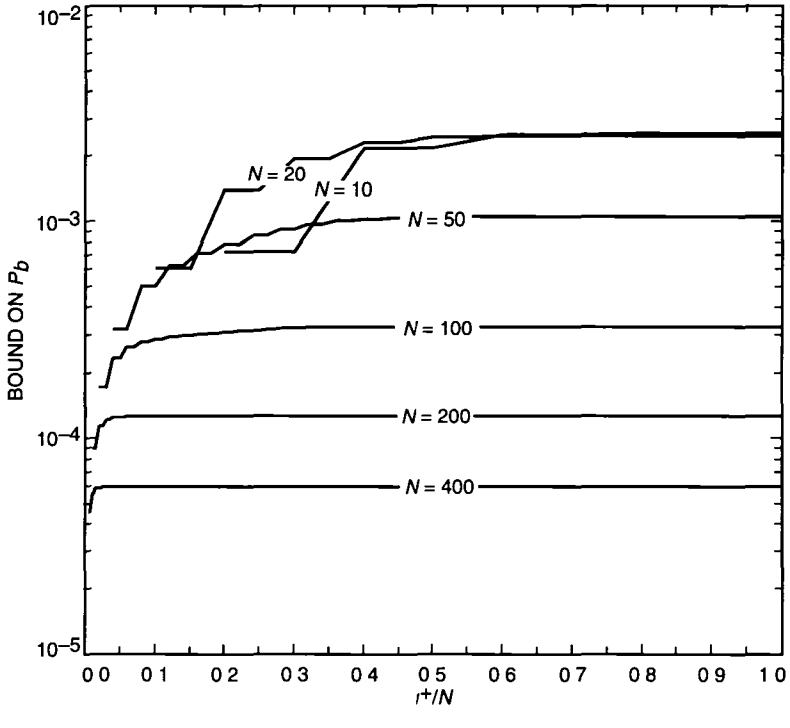

Fig 7 Convergence at E_b/N_0 = 2 50 dB (comfortably above the R_0 threshold of 2 03 dB)

the turbo decoder experiences its own region of "divergence" wherein its performance deteriorates rapidly because its iterative decoding algorithm frequently fails to converge However, this "divergence" is far less steep than that experienced by the bound, and it occurs well below the R_0 threshold, allowing turbo decoders to operate in the region between the limit determined by channel capacity and that determined by R_0

We observe in Fig 8 the relative performance of the two exemplary turbo codes and the relative performance of the same codes with different block lengths The (1, 5/7, 5/7) code is clearly superior to the (1, 7/5, 7/5) code in the region where the bound accurately predicts turbo decoder performance This is consistent with the heuristic arguments presented in [5] However, when E_b/N_0 is low enough that the decoder's iterative algorithm stops being effective, the two codes perform similarly, and the heuristic arguments do not apply By comparing the results for block lengths $N = 100$ and $N = 1000$, we also see how the performance of turbo decoders at high E_b/N_0 is dramatically improved by increasing the length of the random permutation

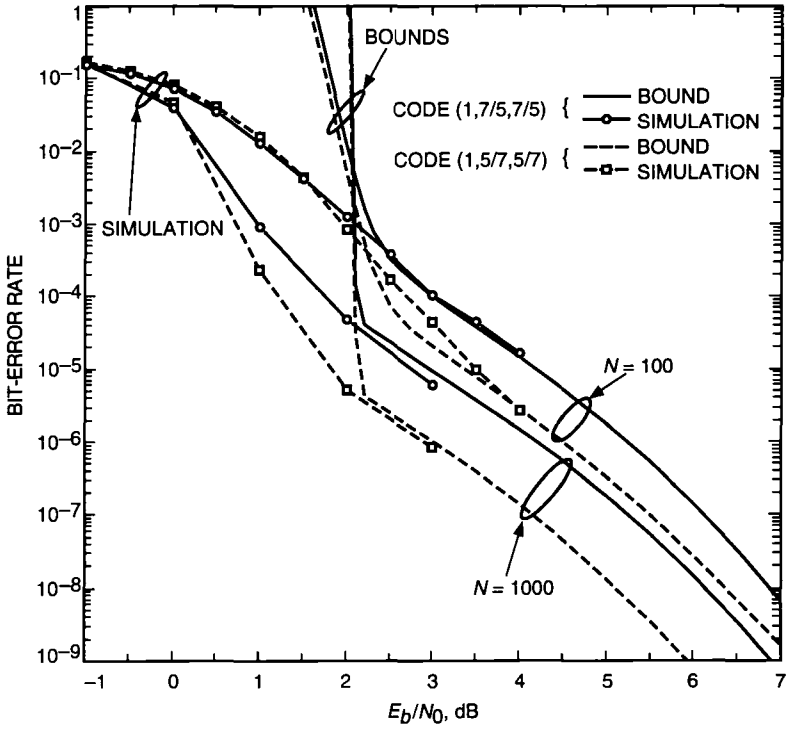

Fig 8 Transfer function bound versus simulated bit-error rates for the (1, 7/5, 7/5) and (1, 5/7, 5/7) codes

D. The Turbo Decoder Error Floor

Unfortunately, the region where turbo codes have offered astounding performance is below the computational cutoff rate threshold, so at first glance the bounds appear to be of dubious utility Nevertheless, our work has some immediate applications and suggests some refinements For E_b/N_0 above the computational cutoff rate threshold, we believe that the bound is not only meaningful but that it essentially tells the whole story, i e , the bit-error rate predicted by the bound is accurately achieved both by a maximum-likelihood decoder and by a turbo decoder This is demonstrated by the confluence of the simulation and bound performance curves in Fig 8 at high E_b/N_0 In this region, evaluation of the bound requires only a few terms in the summation, and its behavior is predictable from the more heuristic analysis about the relationships of weight distributions, permutations, and the number of codes reported

in [5] This low-slope region of the bound establishes the elusive "error floor" that several researchers, including ourselves, have noted but have had difficulty establishing clearly via simulations, because the error floor for large block-length turbo codes is too low to simulate accurately

The error floor is actually not flat, but instead is a low-slope region of the performance curve, wherein the turbo decoder's error rate decreases very slowly with increasing E_b/N_0 The slope of the error floor is limited by the weakness of the turbo code's simple constituent codes, but the position of the error floor can be lowered by increasing the permutation length N Empirically, the error floor appears to be extrapolatable backwards through the computational cutoff rate barrier to some (as yet undetermined) lower E_b/N_0 where it finally stops being an accurate predictor of turbo code performance Furthermore, the extrapolated error floor in this region appears to be computable as the "false convergence" plateau we noted earlier Thus, we surmise that, for some values of E_b/N_0 below the R_0 threshold, the false convergence region of the bound actually corresponds to a true convergence region for predicting turbo decoder performance even though the bound diverges, the portion of the bound based only on low-weight input sequences is still a useful predictor of performance

IV. Results for Other Codes

Our results thus far have been developed with respect to the two exemplary turbo codes for concreteness The theory obviously generalizes to arbitrary turbo codes constructed as parallel concatenations of code fragments The enumerators $t(l, i, d)$ must be evaluated for each code fragment, and the union bound is obtained as a summation over products of independent enumerators Some results for rate 1/3 and 1/4 codes with constraint lengths 3 and 4 are shown in Fig 9 comparing the bounds with the Shannon limits for these rates

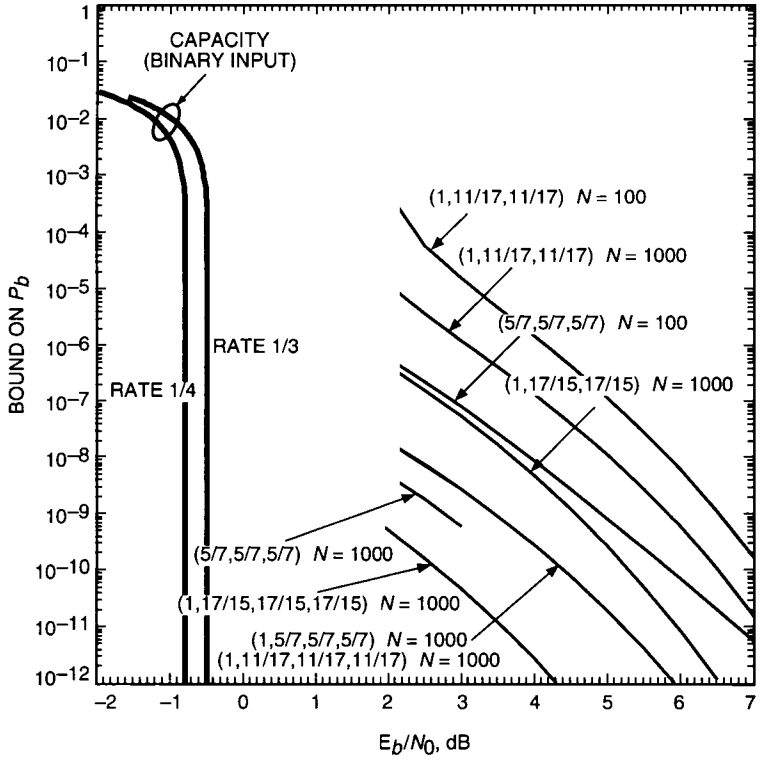

Fig 9 Transfer function bounds for other codes

V. Conclusion and Further Work

One of the most important lessons we have learned is that the divergence properties of these bounds for turbo codes appear to be the same as those of similar bounds applied to random codes This observation leads us to try to adapt known bounding techniques that diverge at capacity, rather than the computational cutoff rate, when applied to random codes Foremost among the candidate techniques we propose to evaluate are the Gallager bound and the bound based on the "code geometry function" [6] Preliminary work is encouraging, but is currently limited by extreme numerical computation barriers when the block length is large However, we are developing analytical approximations that are valid asymptotically as the block length gets larger

References

[1] S Benedetto and G Montorsi, "Average Performance of Parallel Concatenated Block Codes," *Electronics Letters*, vol 31, no 3, pp 156–158, February 2, 1995

[2] S Benedetto and G Montorsi, "Performance Evaluation of Turbo-Codes," *Electronics Letters*, vol 31, no 3, pp 163–165, February 2, 1995

[3] D Divsalar and F Pollara, "Turbo Codes for Deep-Space Communications," *The Telecommunications and Data Acquisition Progress Report 42-120, October–December 1994*, Jet Propulsion Laboratory, Pasadena, California, pp 29–39, February 15, 1995

[4] D Divsalar and F Pollara, "Multiple Turbo Codes for Deep-Space Communications," *The Telecommunications and Data Acquisition Progress Report 42-121, January–March 1995*, Jet Propulsion Laboratory, Pasadena, California, pp 66–77, May 15, 1995

[5] S Dolinar and D Divsalar, "Weight Distributions for Turbo Codes Using Random and Nonrandom Permutations," *The Telecommunications and Data Acquisition Progress Report 42-122, April–June 1995*, Jet Propulsion Laboratory, Pasadena, California, pp 56–65, August 15, 1995

[6] S Dolinar, L Ekroot, and F Pollara, "Improvements on Probability of Error Bounds for Block Codes on the Gaussian Channel," *Proceedings 1994 International Symposium on Information Theory*, Trondheim, Norway, p 243, June 27–July 1, 1994

[7] A J Viterbi and J K Omura, *Principles of Digital Communication and Coding*, New York McGraw-Hill, 1979

[8] R P Stanley, *Enumerative Combinatorics*, Monterey, California Wadsworth & Brooks/Cole, 1986

[9] S Benedetto, E Biglieri, and V Castellani, *Digital Transmission Theory*, Englewood Cliffs, New Jersey Prentice-Hall, Inc , 1987

Weight Distributions for Turbo Codes Using Random and Nonrandom Permutations

S Dolinar and D Divsalar
Communications Systems and Research Section

This article takes a preliminary look at the weight distributions achievable for turbo codes using random, nonrandom, and semirandom permutations Due to the recursiveness of the encoders, it is important to distinguish between self-terminating and non-self-terminating input sequences The non-self-terminating sequences have little effect on decoder performance, because they accumulate high encoded weight until they are artificially terminated at the end of the block From probabilistic arguments based on selecting the permutations randomly, it is concluded that the self-terminating weight-2 data sequences are the most important consideration in the design of the constituent codes, higher-weight self-terminating sequences have successively decreasing importance Also, increasing the number of codes and, correspondingly, the number of permutations makes it more and more likely that the bad input sequences will be broken up by one or more of the permuters

It is possible to design nonrandom permutations that ensure that the minimum distance due to weight-2 input sequences grows roughly as $\sqrt{2N}$, where N is the block length However, these nonrandom permutations amplify the bad effects of higher-weight inputs, and as a result they are inferior in performance to randomly selected permutations But there are "semirandom" permutations that perform nearly as well as the designed nonrandom permutations with respect to weight-2 input sequences and are not as susceptible to being foiled by higher-weight inputs

I. Introduction

Turbo codes are constructed by applying two or more simple-to-decode codes to differently permuted versions of the same information sequence The corresponding turbo decoding algorithm iterates the outputs of simple decoders acting on each component code Recent work in this area by researchers all over the world (e g , [1–5]) has shown that low bit-error rates can be achieved by turbo decoders at astonishingly low bit signal-to-noise ratios (SNRs) if the information block is large and the permutations are selected randomly In this article, we also consider turbo code structures based on nonrandom and semirandom permutations

Good turbo codes have been constructed using short constraint length, infinite impulse response (IIR) convolutional codes as components instead of the more familiar finite impulse response (FIR) convolutional codes These IIR convolutional codes are also referred to as recursive convolutional codes, because previously encoded information bits are continually fed back to the encoder's input For both IIR and

FIR encoders, a single isolated information-bit error will produce the same convolutionally encoded sequence (i.e., the encoder's "impulse response") no matter where it is permuted within the information sequence. For an IIR encoder, this impulse response has infinite weight (for a never-ending information stream), while for an FIR encoder, the weight of its response to a single isolated bit error cannot be much larger than the code's free distance. Thus, the IIR property is important for building turbo codes, because it avoids low-weight encodings that are impervious to the action of the permuters.

In contrast to single bit-error inputs, two or more bit errors in an information sequence can be permuted into different bit patterns whose encoded output bears no resemblance to the encoding of the unpermuted information. The trick in turbo coding is to match low-weight encodings of one permutation with high-weight encodings of the other(s), thus producing total weights significantly higher than the low weights that are possible from each of the simple component codes individually. In this article, we take a preliminary look at the weight distributions achievable for turbo codes using random, nonrandom, and semirandom permutations. Some of this material was included in [5] but is repeated here for a coherent presentation.

II. Turbo Code Structure

Figure 1 shows a particular example of a turbo code using three component codes that will be used throughout this article to illustrate some fundamental concepts. This is the same example used in [5], which derives the iterative algorithm for decoding such a code and evaluates the resulting performance of the iterative decoder. The figure shows three simple recursive convolutional encoders with constraint length $K = 3$ (i.e., memory $M = 2$). The overall code is a rate $1/4$ code with four output streams. One of the output streams is the information sequence (uncoded). The other three output streams in this example are parity sequences corresponding to a ratio of generator polynomials g_b/g_a, where $g_a(D) = 1 + D + D^2$ and $g_b(D) = 1 + D^2$. These three parity streams would be identical if no permutations π_1, π_2 were used.

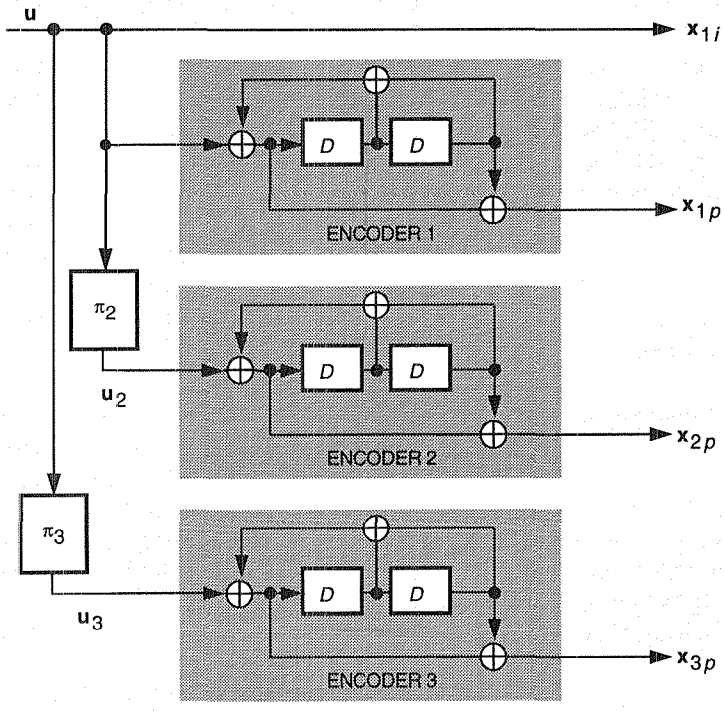

Fig. 1. Example of turbo encoder with three codes.

The encoder in Fig 1 is used to generate an $(n(N+M), N)$ block code, where N is the information block size Following the information bits, an additional M tail bits are appended in order to drive the encoder to the all-zero state at the end of the block Due to the encoders' recursiveness, the required M tail bits cannot be predetermined, but they can be automatically computed at the encoders using a trick suggested in [4] This action of returning the encoders to the all-zero state is called trellis termination

Some input data sequences of length N are *self-terminating*, because the encoders are already in the all-zero state after encoding N information bits before any tail bits are appended All M tail bits are zero for a self-terminating input sequence Non-self-terminating input sequences require one or more nonzero tail bits for proper trellis termination

III. Weight Distributions for Turbo Codes

The weight distribution for the codewords produced by the turbo decoder depends on how the codewords from one of the simple component encoders are teamed with codewords from the other encoder(s) In the example of Fig 1, the component codes have minimum distances 5, 2, and 2 If the codes were not recursive (but used the same generator polynomials g_a, g_b), the minimum weight word for all three encoders would be generated by the weight-1 input sequence (00 0000100 00) with a single "1 " This will produce a minimum distance of 9 for the overall turbo code because the weight-1 input sequence will always appear again in the other encoders regardless of the choice of permutations This motivates the use of recursive encoders, where the key ingredient is the recursiveness and not the fact that the encoders are systematic For the recursive encoder in Fig 1, the weight-1 input sequence generates the code's infinite impulse response, and the output encoded weight is kept finite only due to the trellis termination at the end of the block In the recursive case, the minimum weight word for all three encoders is generated by the weight-3 input sequence (00 000011100 00) with three consecutive 1's However, after random permutations, a pattern of three consecutive 1's is not likely to appear again at the input to the second and third encoders, so it is unlikely that all three encoders will simultaneously emit minimum-weight words In this case, the minimum distance will be higher than 9 for the turbo code structure in Fig 1

Recursive encoders do not modify the output weight distributions of the individual component codes They only change the mapping between the input data sequences and the output encoded sequences As the previous example illustrates, having the same output sequence mapped from a weight-3 input sequence instead of a weight-1 input sequence gives the permuters a chance to break up the offending input before feeding it to the second and third encoders An encoder whose low output weights come from high input weights is generally undesirable for conventional use where the goal is minimizing the decoded bit-error rate However, it is precisely this characteristic that makes an encoder very desirable for use as a component of a turbo code structure! The next section gives a more detailed examination of the link between the weight of the input sequence and the ability of the permuters to disperse it into a sequence with higher output weight

Now let us consider another input sequence that produces fairly low weights at the outputs of each of the encoders in Fig 1, the weight-2 sequence (00 00100100 00) This sequence is self-terminating, i e , it forces the encoder back to the all-zero state without any help from the trellis termination scheme applied at the end of the block The four output streams that are encoded from this input are of the form (00 00100100 00) and (00 00111100 00), with the latter sequence repeated three times In this case, the nonzero portion of the output has a duration of four bit times, the same as the nonzero portion of the input If the permuters do not "break" this sequence before the input to the second and third encoders, the resulting total encoded weight will be 14

For comparison, let us examine the weight-2 sequence (00 0010100 00) This sequence is not self-terminating because the encoder never returns to the all-zero state until it is forced to do so at the end of the block Now the parity sequence (repeated three times) is of the form (00 001111), and the

sequence of all 1's continues until the trellis is terminated This sequence accumulates a very large weight unless it starts near the end of the block If the permuters could map all self-terminating sequences into non-self-terminating sequences, the turbo code could have a minimum weight that grows linearly with block size N

For a nonrecursive encoder, nearly all low-weight input sequences are self-terminating The only non-self-terminating sequences are those whose last 1 occurs near the end of the block As a result, the output weight is very strongly correlated with the input weight for all possible input sequences For instance, there are no weight-2 sequences that produce a very large output weight, in contradistinction to the previous example for the recursive encoders in Fig 1

The weight-2 input sequence (00 00100100 00) is not the only self-terminating weight-2 sequence for the recursive encoders in Fig 1 In general, weight-2 sequences with their 1's separated by $d = 3\delta$ bit positions, where $\delta = 1, 2,$, are also self-terminating unless the last 1 occurs near the end of the block However, the weight of the encoded output increases linearly with the separation The total encoded weight of such a sequence would be $14 + 6\delta$ if there were no permutations With permutations before the second and third encoders, a weight-2 sequence with its 1's separated by $d_1 = 3\delta_1$ bit positions will be permuted into two other weight-2 sequences with 1's separated by $d_i = 3\delta_i$ bit positions, $i = 2, 3$, where each δ_i is defined as a multiple of $1/3$ If any δ_i is not an integer, the corresponding encoded output will have a high weight because then the convolutional code output is non-self-terminating If all δ_i's are integers, the total encoded weight will be $14 + 2\sum_{i=1}^{3} \delta_i$ This weight grows linearly with the separation between the 1's in the input sequences (after permutations) When the 1's are far apart, the encoded sequence looks like the code's infinite impulse response up to the point where the second strategically placed 1 terminates the further accumulation of weight

The coefficient "2" in the expression for the total encoded weight of the self-terminating weight-2 sequences is a characteristic of the particular codes chosen in Fig 1 It measures the rate of growth of the weight of each encoder's output as a function of the separation between the two 1's in the input sequence This coefficient cannot be made any larger than 2 using constraint-length-3 codes as in Fig 1 It can, however, be made smaller, and the result is an inferior turbo code To illustrate this, we consider the same encoder structure in Fig 1, except with the roles of g_a and g_b reversed Now the minimum distances of the three component codes are 5, 3, and 3, producing an overall minimum distance of 11 for the total code without any permutations This is apparently a better code, but it turns out to be inferior as a turbo code This paradox is explained by again considering the critical weight-2 data sequences For this code, weight-2 sequences with $d_1 = 2\delta_1$ bit positions separating the two 1's produce self-terminating output and, hence, low-weight encoded words if $\delta_1 = 1, 2,$ In the turbo encoder, such sequences will be permuted to have separations $d_i = 2\delta_i, i = 2, 3$, for the second and third encoders, where now each δ_i is defined as a multiple of $1/2$ But now the total encoded weight for integer triplets $(\delta_1, \delta_2, \delta_3)$ is $11 + \sum_{i=1}^{3} \delta_i$ Notice how this weight grows only half as fast with $\sum_{i=1}^{3} \delta_i$ (three-fourths as fast with $\sum_{i=1}^{3} d_i$) as the previously calculated weight for the original code Clearly, it is important to choose component codes that cause the overall weight to grow as fast as possible with the individual separations d_i or δ_i This consideration outweighs the criterion of selecting component codes that would produce the highest minimum distance if unpermuted

The summation $\sum_{i=1}^{3} \delta_i$ in the expression for the total encoded weight of the self-terminating weight-2 sequences depends mostly on the choice of permutations and less on the choice of code For a given set of permutations, this summation would be the same for any code whose self-terminating weight-2 sequences have separations $d = 3\delta$ between the 1's This approach provides a method to partially separate the problem of picking good permutations from the problem of picking good component codes If the weight-2 sequences are the only ones that matter, the permutations should be designed to avoid integer triplets $(\delta_1, \delta_2, \delta_3)$ that are simultaneously small in all three components In fact, it would be nice to design permutations to guarantee that the smallest value of $\sum_{i=1}^{3} \delta_i$ (for integer δ_i) grows with the block size N

Alas, things are never so simple There are also many weight-$n, n = 3, 4, 5,$, data sequences that produce self-terminating output and, hence, low encoded weight The criterion for optimally choosing the permutations also depends on similar expressions for the separations between the 1's of the higher-weight sequences Achieving a global optimum, by considering input sequences of all weights simultaneously, is still an unsolved problem

As argued in the next section, higher-weight input sequences are much more likely than weight-2 input sequences to be broken up by randomly chosen permuters If the block size is large, they are likely to produce non-self-terminating output from at least one of the encoders But a purely random permuter is also likely to reproduce a few of the weight-2 input sequences with the lowest output weights It is easy to design nonrandom permutations that combat the weight-2 sequences more effectively than random permutations, but such designs tend to unnaturally amplify the effects of higher-weight sequences Section IV explores these issues in more detail

IV. Choosing the Permutations

The performance of a turbo code depends on how effectively the data sequences that produce low encoded weights at the output of one encoder are matched with permutations of the same data sequence that yield higher encoded weights at the outputs of the others Random permutations do a very good job of teaming low weights with high weights for the vast majority of possible information sequences It has been demonstrated empirically that the performance of these codes is astonishingly good as compared to everyday convolutional codes that do not use any permuters In this section, we try to analyze why random permutations work so well and whether nonrandom or semirandom permutations can be designed to outperform them

If randomly chosen permutations perform well, then in principle it is possible to design deterministic permutations that work even better Unfortunately, this has proved to be an elusive goal To date, most deterministic permutation designs have produced turbo codes that do not match the decoded error rates of corresponding codes using random permutations In this section, we describe some suggested nonrandom permutations, and we try to develop design criteria that mimic or improve on the good features of random permutations

A. Random Permutations

Now we briefly examine the issue of whether one or more random permutations can avoid matching small separations between the 1's of a weight-2 data sequence with equally small separations between the 1's of its permuted version(s) Consider, for example, a particular self-terminating weight-2 data sequence (00 001001000 00) that corresponds to a low-weight codeword in each of the encoders of Fig 1 If we select one permutation at random, the probability that this sequence will be permuted into another sequence with the same distance 3 between its two 1's is roughly $2/N$ (assuming that N is large and ignoring minor edge effects) The probability that such an unfortunate pairing happens for at least one possible position of the original sequence (00 001001000 00) within the block of size N is approximately $1-(1-2/N)^N \approx 1-e^{-2}$ This implies that the minimum distance of a two-code turbo code constructed with a random permutation is not likely to be much higher than the encoded weight of such an unpermuted weight-2 data sequence, e g , 14 for the code in Fig 1 By contrast, if we use three codes and two different random permutations, the probability that a particular sequence (00 001001000 00) will be reproduced by both permuters is only $(2/N)^2$ Now the probability of finding such an unfortunate data sequence somewhere within the block of size N is roughly $1-\left[1-(2/N)^2\right]^N \approx 4/N$ Thus, it is not probable that the minimum distance of a three-code turbo code using two random permutations will be limited roughly by the lowest encoded weight of an unpermuted weight-2 data sequence This argument can be extended to account for other weight-2 data sequences that may also produce low-weight codewords, e g , (00 00100(000)$^\delta$1000 00), for the code in Fig 1

For comparison, let us consider a weight-3 data sequence such as (00 0011100 00) that, for our example, corresponds to the minimum distance of the code (using no permutations) The probability that this sequence is reproduced with one random permutation is roughly $6/N^2$, and the probability that some sequence of the form (00 0011100 00) is paired with another of the same form is $1-(1-6/N^2)^N \approx 6/N$ Thus, for large block sizes, the bad weight-3 data sequences have a small probability of being matched with bad weight-3 permuted data sequences, even in a two-code system For a turbo code using 3 codes and 2 random permutations, this probability is even smaller, $1-\left[1-(6/N^2)^2\right]^N \approx (36/N^3)$ This implies that the minimum-distance codeword of the turbo code in Fig 1 is more likely to result from a weight-2 data sequence of the form (00 001001000 00) than from the weight-3 sequence (00 0011100 00) that produces the minimum distance in the unpermuted version of the same code Higher-weight sequences have an even smaller probability of reproducing themselves after being passed through the random permuters These probabilistic arguments do not guarantee that all possible choices of permutations will increase the unpermuted code's minimum distance For the worst-case permutations, the minimum distance of the turbo code is still 9, but these permutations are highly unlikely if chosen randomly

For a turbo code using q codes and $q-1$ permutations, the probability that a weight-n data sequence will be reproduced somewhere within the block by all $q-1$ permutations is of the form $1-\left[1-(\beta/N^{n-1})^{q-1}\right]^N$, where β is a number that depends on the weight-n data sequence but does not increase with block size N For large N, this probability is proportional to $(1/N)^{nq-n-q}$, which falls off rapidly with N, when n and q are greater than 2 Furthermore, the symmetry of this expression indicates that increasing either the weight of the data sequence n or the number of codes q has roughly the same effect on lowering this probability

B. Designed Permutations

In the discussion of random permutations, we identified self-terminating weight-2 data sequences as the most likely to contribute low-weight codewords that might not be successfully permuted into sequences that contribute high weights for the other encoders Therefore, the first design criterion for a good permutation ought to be how well it breaks up the self-terminating weight-2 input sequences We have seen how the encoded weights of self-terminating weight-2 input sequences increase linearly with the distance between their two 1's, with a slope that depends on the characteristics of the constituent codes The first job of the permuter(s) then is to produce a good weight distribution for self-terminating weight-2 inputs For the example in Figure 1, this is accomplished by making sure that the sum $\sum_{i=1}^{3}\delta_i$ is never (or seldom) very small for integer values of δ_i

1. Nonrandom Permutations Based on Block Interleavers. One method for the design of nonrandom permutations is based on block interleavers Interleavers should be capable of spreading low-weight input sequences so that the resulting codeword has high weight Block interleavers, defined by a matrix with ν_r rows and ν_c columns such that $N=\nu_r\times\nu_c$, may fail to spread certain sequences For example, the weight-4 sequence shown in Fig 2 cannot be broken by a block interleaver Block interleavers are effective if the low-weight sequence is confined to one row If low-weight sequences (which can be regarded as the combination of lower-weight sequences) are confined to several consecutive rows, then the ν_c columns of the interleaver should be sent in a specified order to spread as much as possible the low-weight sequences A method for reordering the columns is given in [6] This method guarantees that for any number of columns $\nu_c=ab+r$ $(r\le a-1)$, the minimum separation between data entries is $b-1$, where a is the number of columns affected by a burst However, as can be observed in the example in Fig 2, the sequence (00 00100100 00) will still appear at the input of the encoders for any possible column permutation Only if we permute the rows of the interleaver in addition to its columns is it possible to break these weight-4 sequences The method in [6] can be used again for the permutation of rows Appropriate selection of a and b for rows and columns depends on the particular set of codes used and on the specific low-weight sequences that we would like to break

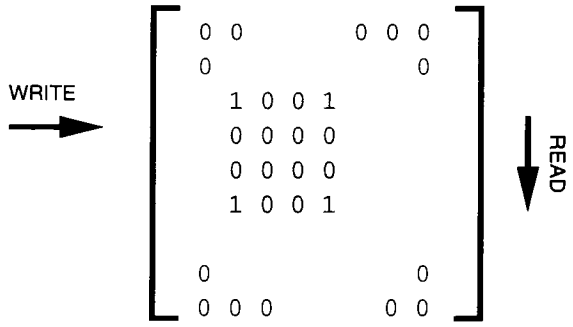

Fig 2 Example where a block interleaver fails to "break" the input sequence

2. Nonrandom Permutations Based on Circular Shifting. Another class of nonrandom permutations is derived from circular shifting The basic formula is

$$\pi(j) = (aj + r) \bmod N \tag{1}$$

where $r < N$ is an offset and $a < N$ is a step size that is relatively prime to N The choice of offset is unimportant if edge effects can be ignored Here we take $r = 0$ and concentrate on selecting the step size a For a concrete example, we take $N = 32$ and $a = 7$ This generates the following permutation

j	0	1	2	3	4	5	6	7	8	9	10	11	12	13	14	15
	16	17	18	19	20	21	22	23	24	25	26	27	28	29	30	31
$\pi(j)$	0	7	14	21	28	3	10	17	24	31	6	13	20	27	2	9
	16	23	30	5	12	19	26	1	8	15	22	29	4	11	18	25

Note that for consecutive values of j, the corresponding values of $\pi(j)$ are always separated by either 7 or 25 In other words, if the distance between a pair of 1's in an unpermuted weight-2 input sequence is $d_1 = 1$, then the corresponding distance after permutation by π is either $d_2 = 7$ or $d_2 = 25$ Similarly, if $d_1 = 2$, then either $d_2 = 14$ or $d_2 = 18$ Continuing in this way, we can verify that $d_1 + d_2 \geq 8$ for any possible combination of d_1 and d_2

If one tries to improve on this by using a larger step size, things do not always get better For example, consider the permutation generated by taking $a = 11$

j	0	1	2	3	4	5	6	7	8	9	10	11	12	13	14	15
	16	17	18	19	20	21	22	23	24	25	26	27	28	29	30	31
$\pi(j)$	0	11	22	1	12	23	2	13	24	3	14	25	4	15	26	5
	16	27	6	17	28	7	18	29	8	19	30	9	20	31	10	21

In this case, $d_1 + d_2 \geq 12$ whenever $d_1 = 1$ or $d_1 = 2$, but $d_1 + d_2 = 4$ when $d_1 = 3$

This example generalizes in the following manner when the block size N is half of a perfect square Take the step size $a = \sqrt{2N} - 1$ Then $d_1 + d_2 \geq \sqrt{2N}$ for all possible combinations of d_1 and d_2 The

step size a that achieves this inequality is not unique For example, $a = \ell\sqrt{2N} \pm 1$ also gives the same lower bound on $d_1 + d_2$ for positive integers $\ell < \sqrt{N/2}$ that are relatively prime to $\sqrt{N/2}$ When $\sqrt{2N}$ is not an integer, it can be demonstrated empirically that the same bound holds approximately, i e , for a properly optimized step size, $d_1 + d_2 \geq \nu$, where ν is only slightly smaller than $\sqrt{2N}$ Figure 3 shows the maximum over step sizes of the minimum value of $d_1 + d_2$ as a function of N

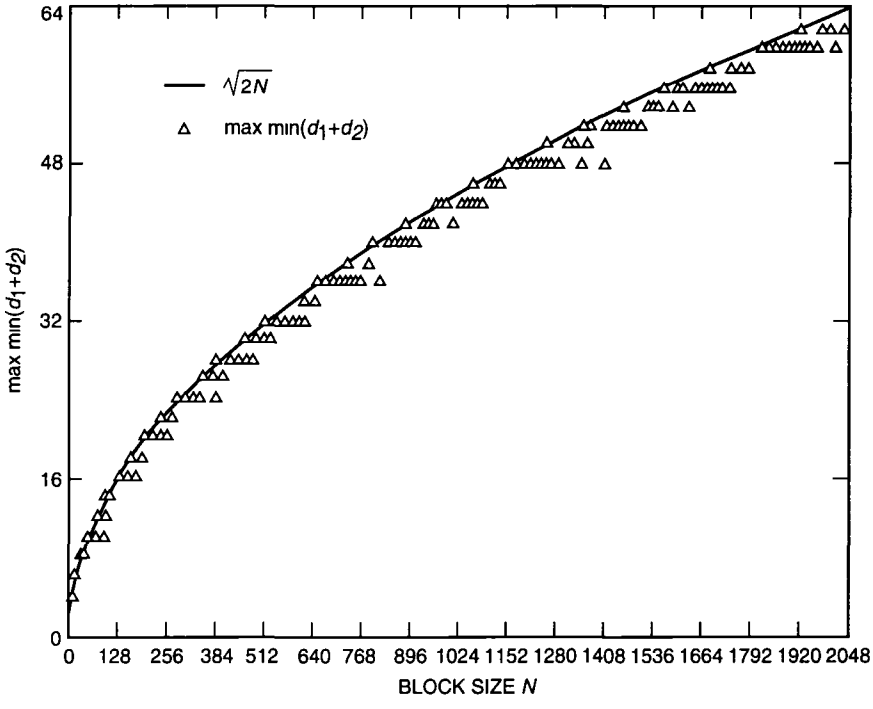

Fig 3 Maximum over step size of the minimum value of d_1+d_2, as a function of block size N, for nonrandom permutations based on circular shifting

Section III gave a rationale for trying to ensure that, for weight-2 data sequences, the sum of separations between the 1's induced by different permutations is as large as possible This correlates with our objective here of choosing a permutation to make the minimum value of $d_1 + d_2$ as large as possible In fact, we have just shown that a nonrandom permutation can be designed such that this minimum value increases without bound as N gets large But the relevant summation in Section III was $\sum_i \delta_i$, not $\sum_i d_i$, where $\delta_i = d_i/3$ for the code illustrated in Fig 1, and noninteger values of δ_i are of no consequence if N is large and edge effects can be ignored If the design criterion is to maximize the minimum value of $\delta_1 + \delta_2$ for integer δ_1, δ_2 only, then the permutation can be redefined to step in units of 3 instead of 1, if 3 and N are relatively prime But in this case, this gives the same permutation defined above The result is that $\delta_1 + \delta_2 \geq \sqrt{2N}$ if $\sqrt{2N}$ is an integer and an optimum step size is chosen as above For the example above with $N = 32$ and $a = 7$, we can see that the minimum value of $d_1 + d_2$ is 24 if the minimization is restricted to separations d_1, d_2 that are both integer multiples of 3, this corresponds to $\delta_1 + \delta_2 = 8 = \sqrt{2N}$

The permutation based on circular shifting does a very good job of permuting weight-2 data sequences with low encoded weights into weight-2 sequences with high encoded weights But this does not imply that we have found the ideal permutation for constructing turbo codes Indeed, this permutation has an Achilles heel similar to that of block interleavers For the example with $N = 32$ and $a = 7$, the weight-4 data sequence (10010100100000000000000000000000) is permuted into the sequence (10010000000000000000010010000000), and both of these sequences consist of two self-terminating weight-2 subsequences each characterized by $\delta = 1$ Adding the contributions from all four subsequences

gives $\sum_i \delta_i = 4$, which is only half as big as the minimum value of 8 optimized for weight-2 full sequences only

We have not yet explored how to modify the permutation based on circular shifting so as to combat weight-4 and higher-weight input sequences while not losing too much optimality with respect to weight-2 sequences Another open question is how to optimally select two or more different permutations when the turbo code has three or more constituent codes

3. Semirandom Permutations. The nonrandom permutations discussed in the previous section were based on a limited design objective, namely to attack the most problematical weight-2 input sequences According to the previous arguments for random permutations, it should be easy to break up input sequences with higher weights (if N is large) without even trying to optimize the permuter Unfortunately, the permutations designed to optimally break up the lowest-weight sequences possess so much regularity that the random permutation analysis is not applicable when considering the higher weights This regularity actually enhances the probability that the nonrandom permuter will reproduce bad sequences of weight-4 and higher

To circumvent this problem, one might try to design permutations to simultaneously break up all weights of input sequences in an optimum manner This is a formidable task that we have not yet attempted As an alternative, we propose to evaluate some semirandom permutations, constructed so as to satisfy a limited nonrandom design objective but retaining some degree of randomness to prevent too much regularity

We have designed one type of semirandom permutation by generating random integers i, $1 \le i \le N$, without replacement An "S-random" permutation is defined as follows Each randomly selected integer is compared to the S previously selected integers If the current selection is equal to any of the S previous selections within a distance of $\pm S$, then the current selection is rejected This process is repeated until all N integers are selected The searching time for this algorithm increases with S, and it is not guaranteed to finish successfully However, we have observed that choosing $S < \sqrt{N/2}$ usually produces a solution in reasonable time Note that for weight-2 input sequences the separations d_1, d_2 satisfy $d_1 + d_2 \ge S + 1$, so the S-random construction (if successful) ensures that the minimum value of $d_1 + d_2$ grows with the block size N If S is around $\sqrt{N/2}$, this growth rate is about half the growth rate achievable by the nonrandom permutation based on circular shifting At the other extreme, for $S = 1$, the S-random permutation reduces to a purely random permutation

V. Conclusion

We have taken a preliminary look at the weight distributions achievable for turbo codes using random, nonrandom, and semirandom permutations We first drew a distinction between self-terminating and non-self-terminating input sequences, noting that due to the recursiveness of the encoders the latter sequences continue to accumulate encoded weight until they are artificially terminated at the end of the block Using probabilistic arguments based on selecting the permutations randomly, we concluded that the self-terminating weight-2 data sequences are the most important consideration in the design of the component codes, and we argued that higher-weight sequences have successively decreasing importance Also, increasing the number of codes and, correspondingly, the number of permutations, makes it more and more likely that the bad input sequences will be broken up by one or more of the permuters

We have argued that the usual goal of minimizing the weight of the input data sequences associated with the lowest-weight output encoded sequences might be backwards in the case of turbo codes If the input weight of the most likely error sequences is maximized rather than minimized, the permuters will have a better chance to avoid matching low-weight outputs from each encoder We have discussed a partial separation of the problem of picking good permutations and that of picking good component

codes that arises from analyzing how fast the output weight grows as a function of the separation between the 1's of weight-2 input sequences

We have designed nonrandom permutations that ensure that the minimum distance due to weight-2 input sequences grows roughly as $\sqrt{2N}$, where N is the block size However, these nonrandom permutations amplify the bad effects of higher-weight inputs, and as a result they are inferior in performance to randomly selected permutations But we have proposed semirandom permutations that perform nearly as well as the designed nonrandom permutations with respect to weight-2 input sequences and are not as susceptible to being foiled by higher-weight inputs

References

[1] C Berrou, A Glavieux, and P Thitimajshima, "Near Shannon Limit Error-Correcting Coding Turbo Codes," *Proc 1993 IEEE International Conference on Communications*, Geneva, Switzerland, pp 1064–1070, May 1993

[2] J Hagenauer and P Robertson, "Iterative (Turbo) Decoding of Systematic Convolutional Codes With the MAP and SOVA Algorithms," *Proc of the ITG Source and Channel Coding Conference*, Frankfurt, Germany, pp 1–9, October 1994

[3] P Robertson, "Illuminating the Structure of Code and Decoder of Parallel Concatenated Recursive Systematic (Turbo) Codes," *Proceedings GLOBECOM '94*, San Francisco, California, pp 1298–1303, December 1994

[4] D Divsalar and F Pollara, "Turbo Codes for Deep-Space Communications," *The Telecommunications and Data Acquisition Progress Report 42-120, October–December 1994*, Jet Propulsion Laboratory, Pasadena, California, pp 29–39, February 15, 1995

[5] D Divsalar and F Pollara, "Multiple Turbo Codes for Deep-Space Communications," *The Telecommunications and Data Acquisition Progress Report 42-121, January–March 1995*, Jet Propulsion Laboratory, Pasadena, California, pp 66–77, May 15, 1995

[6] E Dunscombe and F C Piper, " Optimal Interleaving Scheme for Convolutional Codes," *Electronics Letters*, vol 25, no 22, pp 1517–1518, October 26, 1989

Analysis of Automatic Repeat Request Methods for Deep-Space Downlinks

F Pollara and L Ekroot
Communications Systems and Research Section

Automatic repeat request (ARQ) methods cannot increase the capacity of a memoryless channel However, they can be used to decrease the complexity of the channel-coding system to achieve essentially error-free transmission and to reduce link margins when the channel characteristics are poorly predictable This article considers ARQ methods on a power-limited channel (e g , the deep-space channel), where it is important to minimize the total power needed to transmit the data, as opposed to a bandwidth-limited channel (e g , terrestrial data links), where the spectral efficiency or the total required transmission time is the most relevant performance measure In the analysis, we compare the performance of three reference concatenated coded systems used in actual deep-space missions to that obtainable by ARQ methods using the same codes, in terms of required power, time to transmit with a given number of retransmissions, and achievable probability of word error The ultimate limits of ARQ with an arbitrary number of retransmissions are also derived

I. Introduction

A major concern in data communications is the control of transmission errors caused by channel noise so that error-free data can be delivered to the user Error control systems that rely only on a one-directional (forward) channel are called forward error correction (FEC) systems Systems that make use of a reverse or feedback channel are called automatic repeat request (ARQ) systems and are based on protocols that request retransmission of data blocks when errors are detected ARQ systems trade time for link margin and aim at returning *all* of the data reliably

It is well known [2, p 213] that the capacity of a memoryless channel cannot be increased by using a feedback channel [1] However, the implementation complexity for a given performance goal can be considerably reduced by using the feedback channel for requesting retransmission of data frames Situations where the probability of frame error needs to be virtually zero, such as for heavily compressed data, or where large link margins are imposed by poorly predictable channel impairments, are particularly suitable for retransmission schemes

[1] In this article, the feedback channel is assumed to be noiseless This is a realistic assumption since the uplink channel used for deep space typically operates at a high signal-to-noise ratio (SNR), includes powerful error detection capabilities, and already employs ARQ in the uplink direction

We consider the use of ARQ methods on the downlink channel of deep-space missions Some rudimentary forms of ARQ are already used in deep-space missions, where blocks of corrupted or lost data are isolated and requested again from the spacecraft Retransmission methods have been considered, particularly as a playback strategy to overcome weather outages We propose to use retransmission methods in a more systematic and automatic fashion, based on the error detection capability of existing codes This implies a wider use of the uplink channel, not only for commands, but as a true "reverse" channel representing an integral part of the communication system The effects of ARQ methods on the downlink performance must, therefore, be included in the link analysis This article considers ARQ methods on a power-limited channel (e g , the deep-space channel), where it is important to minimize the total power needed to transmit the data, as opposed to a bandwidth-limited channel (e g , terrestrial data links), where the spectral efficiency or the total required transmission time is the most relevant performance measure

We consider an interplanetary spacecraft transmitting frames of data to Earth The frame consists of at least one Reed–Solomon (RS) codeword and may have an identification header In this article, we limit the analysis to the case where a frame is one RS codeword The frame is convolutionally encoded before transmission Each RS codeword has redundancy, or parity symbols, that may be used for either error correction or error detection

An (n, k) RS code with minimum distance $d_{min} = n - k + 1$ can correct all received words containing c errors and e erasures within the constraint $2c + e < d_{min}$, when hard-decision decoding is used If the received word is within c errors and e erasures of a valid word, then the decoder will output the correct codeword If the selected codeword is not the transmitted one, then a decoder error has occurred If there is no codeword within c errors and e erasures, then a decoder failure is declared, and retransmission is requested A similar situation occurs when a soft-bounded distance decoder is used Given the decoding radius, we can calculate analytically the exact probability of decoder error and decoder failure for linear block codes [5]

An ARQ system must at least rely on error detection The system we will discuss here uses a convolutional code concatenated with a (255,223) RS code for FEC The convolutional codes considered here are constraint length $K = 7$ rate 1/2, $K = 15$ rate 1/4, and $K = 15$ rate 1/6 The RS code is used for both error correction and detection Such a system is in the category of type I hybrid ARQ [10, pp 393–423]

Section II describes the concatenated system at the heart of the ARQ system described in Section III More thorough coverage of the concatenated system without ARQ can be found in [1], [3], and [9] Section V describes features that are not examined in depth in this article, such as the effect of combining multiple copies of received words

We have not yet fully considered problems that may be encountered with errors in the frame header or with frames that contain more than one codeword Thus far, we have assumed a noiseless feedback channel, and we have ignored the effect of undetected errors, which occur with extremely low probability for the codes considered

II. The Reference System

The nominal system is a concatenated system without ARQ We consider a t-error-correcting (n, k) RS code on GF(2^8), with $n = 255$, $k = n - 2t = 223$, and $t = 16$ This means that the code sends k 8-bit symbols of information using n 8-bit symbols and that it can correct all patterns of t or fewer errors This code is used as the outer code of a concatenated system, as shown in Fig 1 We assume for this article that there is infinite interleaving between the RS encoder and the convolutional encoder, which implies that the errors at the input of the RS decoder can be modeled as independent This allows a simpler analysis that can be used to bound the performance of a more practical implementation

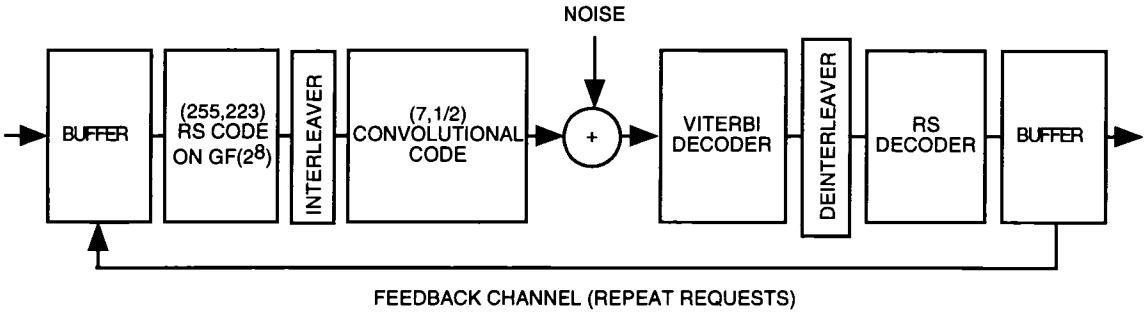

Fig 1 The ARQ system

For this system, there are several different SNRs that will be discussed There is an SNR for bits that are convolutionally encoded and decoded Let s_V be the SNR for the channel and inner (convolutional) code only The concatenated system uses more power-per-information bit because k symbols are sent using n coded symbols, increasing the signal power by a factor of n/k Let $s = (n/k)s_V$ denote the SNR of the concatenated system Since this concatenated RS and convolutional system is the nominal system in this article, s will be called the nominal SNR

We can measure the symbol error rate, $v_s(s)$, at the output of the Viterbi decoder by simulation Since errors at the RS decoder input may be assumed to be independent because of infinite interleaving, the probability of decoder failure and decoder error, i e , the probability that more than the correctable number of symbols are in error, is given by

$$p(s) = \sum_{i=t+1}^{n} \binom{n}{i} v_s(s)^i [1 - v_s(s)]^{n-i} \tag{1}$$

In this article, we use $p(s)$ to approximate the probability of decoding failure, and we ignore the probability of decoding error, since it is negligible for the (255,223) RS code Specifically, if more than $t = 16$ errors occur, the probability of decoder error is less than $1/t! \approx 4.8 \times 10^{-14}$ [8]

The simulated symbol error rate at the output of the Viterbi decoder for the (7,1/2) code and the calculated word error rate of the (255,223) RS code assuming infinite interleaving are shown in Table 1 [2] Similar simulated data for the (15,1/4) and (15,1/6) codes are given in Tables 2 and 3

Table 1 Simulated symbol error rate at the output of the Viterbi decoder (7,1/2) and the calculated word error rate of the (255,223) RS code assuming infinite interleaving

s_V, dB	s, dB	$v_s(s)$	$p(s)$
1 05	1 63	$8\,53 \times 10^{-2}$	$8\,83 \times 10^{-1}$
1 55	2 13	$3\,41 \times 10^{-2}$	$7\,11 \times 10^{-3}$
1 85	2 43	$1\,91 \times 10^{-2}$	$1\,08 \times 10^{-5}$
1 95	2 53	$1\,51 \times 10^{-2}$	$4\,90 \times 10^{-7}$
2 05	2 63	$1\,14 \times 10^{-2}$	$9\,48 \times 10^{-9}$
2 55	3 13	$3\,20 \times 10^{-3}$	$2\,50 \times 10^{-17}$

[2] F Pollara and S Dolinar, "Concatenated Codes Performance at Low Bit Error Rates," JPL Interoffice Memorandum 331-88 2-043 (internal document), Jet Propulsion Laboratory, Pasadena, California, July 13, 1988

Table 2. Simulated symbol error rate at the output of the Viterbi decoder (15,1/4) and the calculated word error rate of the (255,223) RS code assuming infinite interleaving

s_V, dB	s, dB	$v_s(s)$	$p(s)$
0 10	0 68	$4\ 22 \times 10^{-2}$	$4\ 397 \times 10^{-2}$
0 30	0 88	$2\ 24 \times 10^{-2}$	$7\ 735 \times 10^{-5}$
0 50	1 08	$1\ 08 \times 10^{-2}$	$4\ 327 \times 10^{-9}$

Table 3 Simulated symbol error rate at the output of the Viterbi decoder (15,1/6) and the calculated word error rate of the (255,223) RS code assuming infinite interleaving

s_V, dB	s, dB	$v_s(s)$	$p(s)$
0 10	0 68	$2\ 28 \times 10^{-2}$	$9\ 453 \times 10^{-5}$
0 30	0 88	$1\ 19 \times 10^{-2}$	$1\ 674 \times 10^{-8}$
0 50	1 08	$5\ 79 \times 10^{-3}$	$3\ 364 \times 10^{-13}$

Fitting a curve to the simulated Viterbi decoder symbol error rates give us the approximation $V_s(s) \approx v_s(s)$ The fit is of the form $V_s(s) = e^{a_0+a_1 s+a_2 s^2}$, where the coefficients in the exponent are given for each code in Table 4 [3] The comparisons of original data $v_s(s)$ and curve fits $V_s(s)$ for each code are shown in Fig 2 Using the curve fit $V_s(s)$ for $v_s(s)$ in Eq (1), we get an approximation for the probability of RS decoder failure $P(s)$

$$P(s) = \sum_{i=t+1}^{n} \binom{n}{i} V_s(s)^i [1 - V_s(s)]^{n-i}$$

The comparison of the probability of an undecodable word at the output of the RS decoder from both the simulated v_s and from the fit V_s is shown in Fig 3

III. The ARQ System

A. ARQ Protocols

The possible implementations of ARQ protocols fall into different categories, all of which include automatic requests for retransmission of data that are deemed unreliable by the receiver The performance of ARQ protocols is often measured by the accepted-packet error rate and the throughput, which is the average number of information bits accepted by the receiver per packet sent The variables of interest for deep-space applications are the required transmitter power for a given data rate, the required probability of block error, the time available for transmission, the number of retransmissions, the error detection capability of the code, and the round-trip delay These variables affect the onboard complexity and memory requirements and the ground operational complexity

[3] This fit is for s measured in dB, which yields a "quadratic" exponent instead of the more commonly used "linear" exponent for s not in dB reported, for example, in S Dolinar, "Empirical Formula for the Performance of the Recommended (15,1/6) Convolutional Code," JPL Interoffice Memorandum 331-90 2-060 (internal document), Jet Propulsion Laboratory, Pasadena, California, October 12, 1990

Table 4 Viterbi symbol error rate fits, where each $V_S(s)$ is of the form $e^{a_0+a_1 s+a_2 s^2}$ and s is in dB

Code	a_0	a_1	a_2
(7,1/2)	−0 993617	−0 235839	−0 409607
(15,1/4)	−1 731157	−1 291763	−1 201945
(15,1/6)	−2 095216	−1 882523	−0 877300

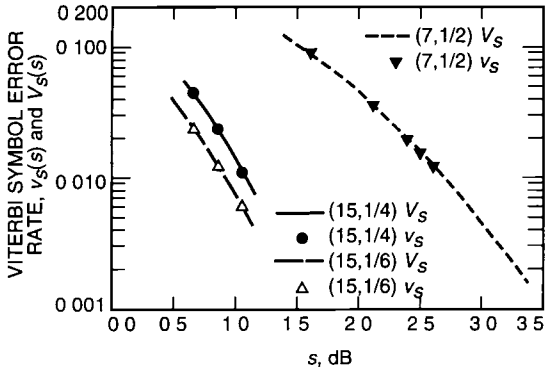

Fig 2 Original data $v_S(s)$ and curve fit $V_S(s)$

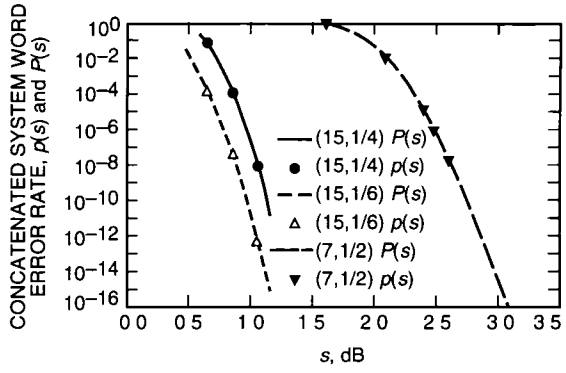

Fig 3 For the concatenated systems, the word error rates from the simulation $p(s)$ and from the fitted curves $P(s)$ are shown as a function of $s(E_b/N_0)$

The most appropriate protocols are based on selective repeat, where the transmitter retransmits only the packets requested by the receiver Here the throughput does not depend on the round-trip transmission delay [10, p 399] Other protocols that have a throughput depending on round-trip delay are described here for contrast

(1) The "stop and wait" ARQ protocol is one in which the transmitter sends one packet and waits for either an acknowledgment or a repeat request before sending either the next packet or the previous packet again Although this is simple to implement at both the transmitter and receiver, the throughput is very dependent on the round-trip transmission time For deep-space applications, this is not a practical protocol

(2) The "go back N" protocol is one in which the transmitter sends packets sequentially When the receiver is unable to decode a packet, it sends a repeat request and stops listening to the transmitter until the requested packet arrives When the transmitter receives the repeat request, it goes back N and starts sending sequentially again This version has a better throughput than the stop and wait protocol The throughput and N depend on the round-trip transmission time, but the effect of the round-trip transmission time is lower for a relatively noiseless channel than for a noisy one

In a selective repeat system, the transmitter must keep a buffer of what it has sent so that retransmission is possible The receiver may store unreliable frames and combine them with subsequent retransmissions to improve reliability, as we will discuss in Section V Let R be the number of retransmissions that are either allowed or that are necessary If some maximum number of retransmissions is allowed, then we ask what fraction of the data is received error free If it is essential to return all of the data, then we ask how many retransmissions are necessary to return the data The answer to both questions depends on the channel SNR

B Buffer Size On Board the Spacecraft

Using ARQ, every frame transmitted must be stored long enough for it to be received, processed, and (if necessary) for a repeat request to be received and processed by the spacecraft So, the buffer size on board the spacecraft needs to be large enough to store all the data transmitted in that amount of time The buffer size B is a function of the data rate D, the round-trip transmission time τ, and the on-ground processing time η Specifically,

$$B = D(\tau + \eta)$$

If we consider a Mars-Earth-Mars round-trip transmission time of approximately 25 min, a ground processing time of 1 min, and a data rate of 512 kb/s, the buffer size must be approximately 100 Mbytes The ground processing time is also an operations question since it depends on how often uplink transmissions are desired

C. ARQ Analysis

We consider the use of ARQ to transmit a large data set After the first transmission of the whole data set, subsequent retransmissions will repeat only the frames that were flagged as unreliable The average amount of data that must be sent after the Rth retransmission is the amount of data sent during the Rth retransmission times the probability of decoder failure If successive retransmissions of the same frame are decoded without reference to previous transmissions, then the fraction of data that is still in error after R retransmissions is $P(s)$ where s is the nominal SNR Thus, the fraction of the original data that is still in error after R retransmissions is

$$P_R(s) = P(s)^{R+1}$$

If previous copies of a retransmitted word are combined with the current copy, as explained in Section V, then $P_R(s)$ may be smaller

In this article, time refers to the amount of time the transmitter is actively sending coded data and, correspondingly, the amount of time the receiver is actively receiving data In this way, time relates well to the amount of transmitter energy used for sending data [4] For our purposes, references to time are normalized by the amount of time it takes to send the whole data set once Thus, a system with the same coding, but without ARQ, sends the data back in 1 time unit The average amount of time it takes to send the data set when R retransmissions are allowed is given by

$$t_R(s) = 1 + \sum_{i=0}^{R-1} P_i(s) = \sum_{i=0}^{R} P^i(s) = \frac{1 - P(s)^{R+1}}{1 - P(s)}$$

Note that a system that allows no more than R retransmissions of the data is done transmitting before $R+1$ units of time have past, i e , $t_R \leq R+1$ For high SNR, few transmissions are necessary, so $t_R \approx 1$ For low SNR, the maximum number of transmissions will almost always be used, so $t_R \approx R+1$ If the number of retransmissions is unlimited, the average amount of time is given by

[4] The amount of time between when the first and last bytes of data are received is different and depends on operations If the ground station cannot send and receive simultaneously, then there is a delay while a clump of data is being received and before a batch of repeat requests can be sent There may also be some delay on the ground for processing As a result, the amount of clock time it takes to send the data is different from the amount of time the transmitter is sending data

$$t_\infty(s) = \frac{1}{1 - P(s)}$$

Since, on average, each frame is transmitted $t_R > 1$ times, for a system that allows no more than R retransmissions, the effective SNR, $s_R(s)$, is larger than the nominal SNR, s

$$s_R(s) = st_R(s) = s\sum_{i=0}^{R} P^i(s) = s\frac{1 - P(s)^{R+1}}{1 - P(s)}$$

Note that $s_0(s) = s$ If the number of retransmissions is unlimited, the effective SNR is given by

$$s_\infty(s) = \frac{s}{1 - P(s)}$$

Performance for low SNRs is described in the Appendix, as it is primarily of academic interest The effective rate at which data are received is $r_R(s) = 1/t_R(s)$ Note that $t_\infty(s) = 1/r_\infty(s) = 1/[1 - P(s)]$

1. ARQ Performance Limits: Limiting Performance for Zero Error Probability. It is interesting to establish the performance limits of ARQ for a given coding system when the maximum number of retransmissions is arbitrary The minimum effective SNR at which the system can produce vanishingly small probability of word error for arbitrary R is given by

$$s^*_\infty = \min_s[s_\infty(s)] \tag{2}$$

Accordingly, $P_R(s) \to 0$ for large R, if $s_R(s) > s^*_\infty$ Conversely, if R and s are sufficiently small so that the effective SNR $s_R(s)$ is less than s^*_∞, then vanishingly small word error probability is impossible The minimum effective SNR s^*_∞ for a given ARQ coded system can be compared with the ultimate Shannon limit $[(2^{2r} - 1)/2r] < s^*_\infty$, where r is the rate of the concatenated system

2. ARQ Performance Limits: Limiting Performance for Nonzero Error Probability. If the required word error probability P_ϵ is nonzero, then one has to simultaneously optimize the required effective SNR, s_ϵ, and the number of retransmissions, R The limiting performance is given by the envelope of the curves for different R's (as shown later for the (7,1/2) code in Fig 7) or, equivalently, by the locus of the minimum effective SNRs for each R Since a given data volume can be transmitted reliably with power proportional to s^*_∞, a fraction $1 - P_\epsilon$ of the data volume can be transmitted with power proportional to $s_\epsilon = s^*_\infty(1 - P_\epsilon)$ Then the limiting ARQ performance is given by

$$P_\epsilon = 1 - \frac{s_\epsilon}{s^*_\infty}, \quad s_\epsilon \le s^*_\infty \tag{3}$$

It has been suggested[5] that Eq (3) can also be explained by considering the ARQ system as an erasure channel, whose capacity can be achieved by just retransmitting codewords until they get through Since RS codewords get through with probability $1 - P_\epsilon$, the capacity of the erasure channel is $C = 1 - P_\epsilon$, and we must have $r \le C$, i e , the rate is limited by capacity It can be verified[6] that $r = s_\epsilon/s^*_\infty$

[5] Personal communication with M Costa, Jet Propulsion Laboratory, Pasadena, California, August 1994

[6] Ibid

D. The (7,1/2) Convolutional Code

Three plots showing the pairwise relationships between nominal SNR, effective SNR, and probability of word error for the (7,1/2) convolutional code are shown in Fig 4 In designing the coding system, we start from a given available nominal SNR The effective SNR is then a measure of the average power actually used for transmission, including the penalty due to retransmissions For example, if we start out at a nominal SNR of 2 5 dB, we would have a resulting effective SNR also of 2 5 dB, as shown by point A in Figs 4(b) and 4(c), for $R = 1$ Point B in Figs 4(b) and 4(c) represents an anomalous operation of the system, where the given nominal SNR is insufficient for good performance, even though the effective SNR has the same value of 2 5 dB due to the retransmission overhead Note that, for $R = 1$, Fig 4(c) shows that, for high nominal SNR, the effective SNR is equal to the nominal SNR and, for low nominal SNR, the effective SNR is 3-dB more than (i e , double) the nominal SNR The latter follows from the fact that for finite R the data can be transmitted at most $R+1$ times (and at low SNR, the maximum number of retransmissions will almost always be used), so the effective SNR due to retransmissions is approximately $10\log_{10}(R+1) + s$ for low SNR This phenomenon at low SNR happens for all finite R, but not when the number of retransmissions is unrestricted This effect appears on all the curves, but is at such low nominal SNRs that discussion is deferred to the Appendix

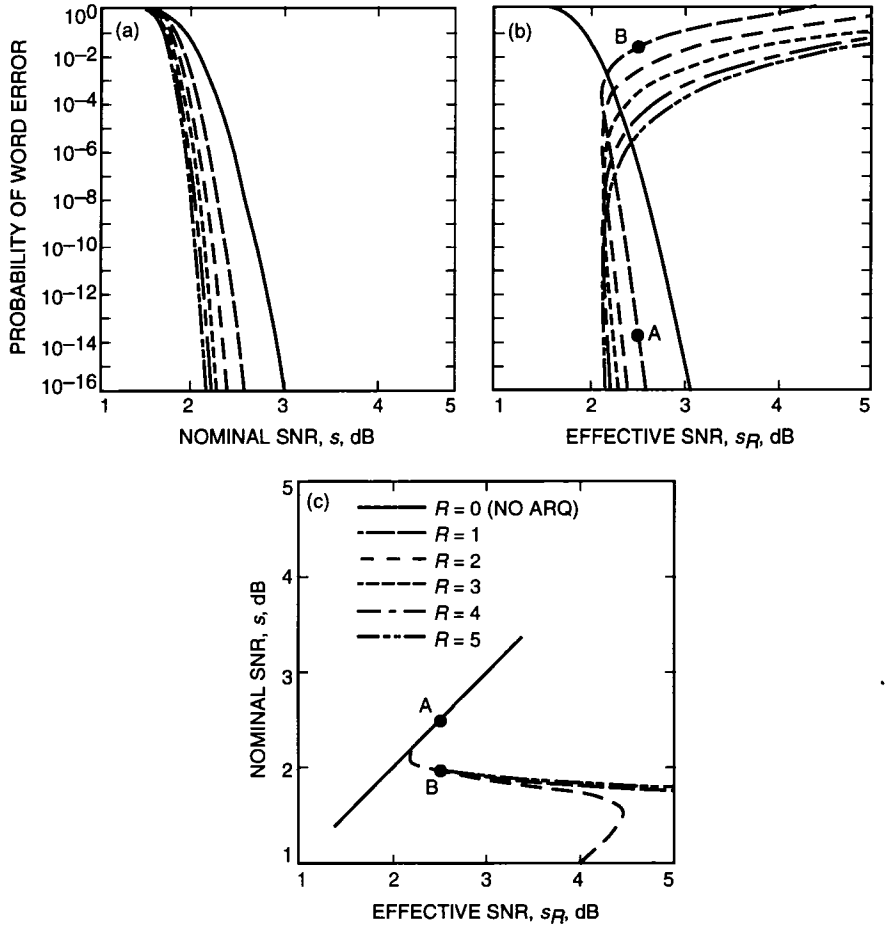

Fig 4 Pairwise relationships between (a) nominal SNR s, (b) effective SNR $s_R(s)$, and (c) probability of word error $P_R(s)$ for the (7,1/2) + (255,223) convolutional code.

A parametric plot of $s_R(s)$ versus $t_R(s)$ in Fig 5 shows a local minimum where the effective SNR is low and the average amount of time spent transmitting is close to 1 For the (7,1/2) code and $R > 1$, a nominal SNR $s = 2\ 109$ dB yields an effective SNR $s_R = 2\ 166$ dB, and the amount of time spent transmitting ($t_R = 1\ 013$) is only 1 3-percent more time than the time to transmit once For nominal SNR higher than 2 25 dB, the channel is relatively noiseless and few retransmissions are requested Thus, $s_R(s) \approx s$, and the ARQ system performance is comparable to the system without ARQ, as evidenced by t_R being nearly 1 As the nominal SNR gets lower than 2 1 dB, the amount of data transmitted increases and so the effective SNR s_R and time t_R also increase

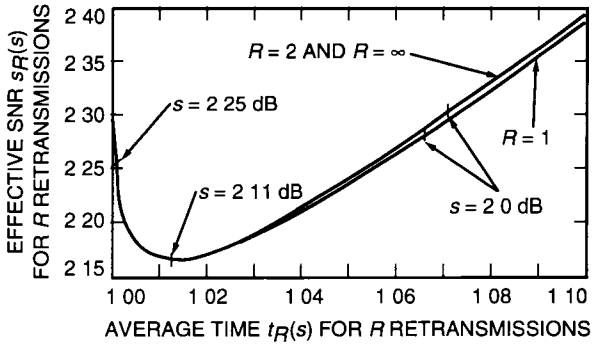

Fig 5 Effective SNR (s_R) plotted with the average time to transmit (t_R) using the (7,1/2) + (255,223) code

So, for an additional 0 057 dB = 2 166 dB − 2 109 dB of SNR (due to 1 3-percent more time required to transmit), the data will be delivered virtually error free, if an unlimited number of retransmissions is allowed, instead of with a probability of error of 0 013 for the same system without ARQ This is especially useful for compressed data where errors can propagate through the data Another advantage is that the link margin, for say a 10^{-6} word error rate, can be reduced by more than 0 3 dB, if retransmissions are used to combat unforeseen SNR reductions and 1 3-percent more time is allowed for transmission

The fraction of the total data volume that is accepted (successfully decoded) after R retransmissions, $1 - P^{R+1}$, versus the amount of time for R retransmissions is shown in Fig 6 for several values of nominal SNR

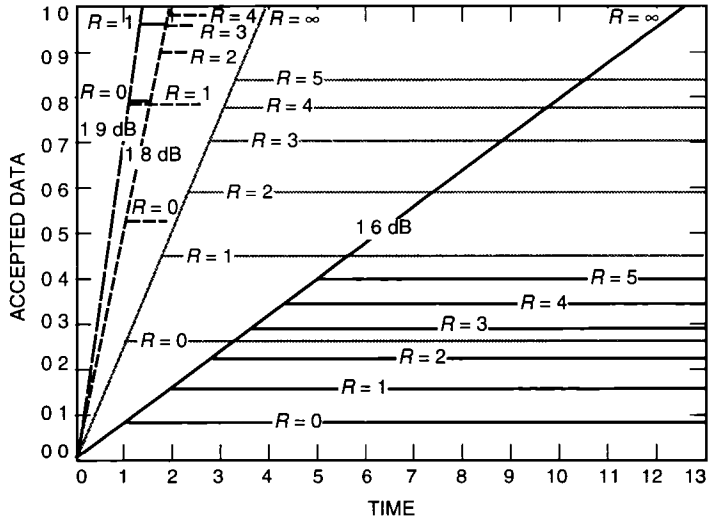

Fig 6 Decoded data volume versus time for the (7,1/2) + (255,223) code

For the concatenated system considered in this section, the minimum effective SNR [see Eq (2)] is $s^*_\infty = 2\ 166$ dB, where this minimum is achieved at nominal SNR $s^* = 2\ 109$ dB This limiting SNR value of s^*_∞ is still significantly higher than the Shannon limit $(2^{2r} - 1)/2r = -0\ 209$ dB, where $r = (1/2)\ (223/255)$ We can compute the limiting time and rate at nominal SNR s^* to be

$$t^*_\infty = t_\infty(s^*) = 1\ 013$$

$$r^*_\infty = r_\infty(s^*) = 0\ 987$$

The limiting performance curve [see Eq (3)] is shown in Fig 7, and it coincides with the envelope of the parametric curves of $s_R(s)$ and $P_R(s)$ for finite R

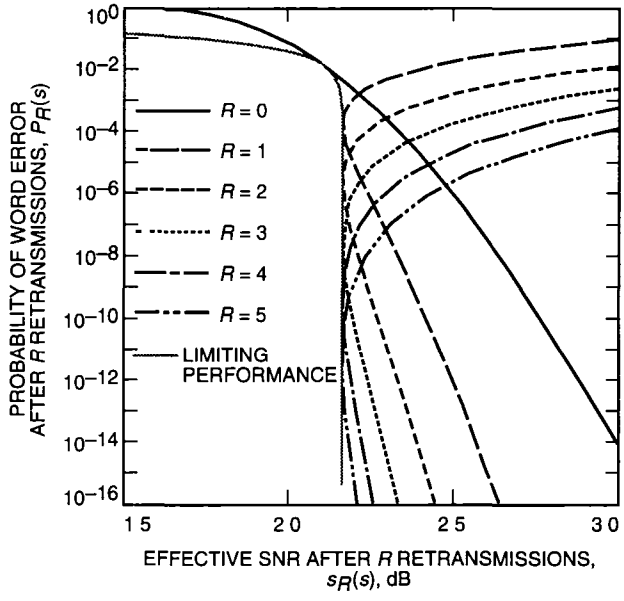

Fig 7 $P_R(s)$ versus $s_R(s)$, (7,1/2) + (255,223) code

E. The (15,1/4) Convolutional Code

Three plots showing the pairwise relationships between nominal SNR, effective SNR, and probability of word error for the (15,1/4) convolutional code are shown in Fig 8 In Fig 9, a parametric plot of effective SNR versus time shows a local minimum where the effective SNR is low and the average amount of time spent transmitting is close to 1 For the (15,1/4) code, a nominal SNR $s = 0\ 747$ dB yields an effective SNR $s_R = 0\ 782$ dB, and the amount of time spent transmitting ($t_R = 1\ 008$) is only 0 8-percent more time than transmitting once For nominal SNR higher than 0 8 dB, the channel is essentially noiseless and few retransmissions are requested As the nominal SNR gets lower than 0 740 dB, the amount of data transmitted increases and so the effective SNR s_R and time t_R also increase

So, for an additional 0 035 dB = 0 782 dB − 0 747 dB of SNR (due to 0 795-percent more time to transmit), the data will be delivered without detected errors, if an unlimited number of retransmissions are allowed, instead of with a probability of error of 0 0079 for the same system without ARQ The fraction of the total data volume that is accepted after R retransmissions, $1 - P^{R+1}$, versus the amount of time for R retransmissions is shown in Fig 10

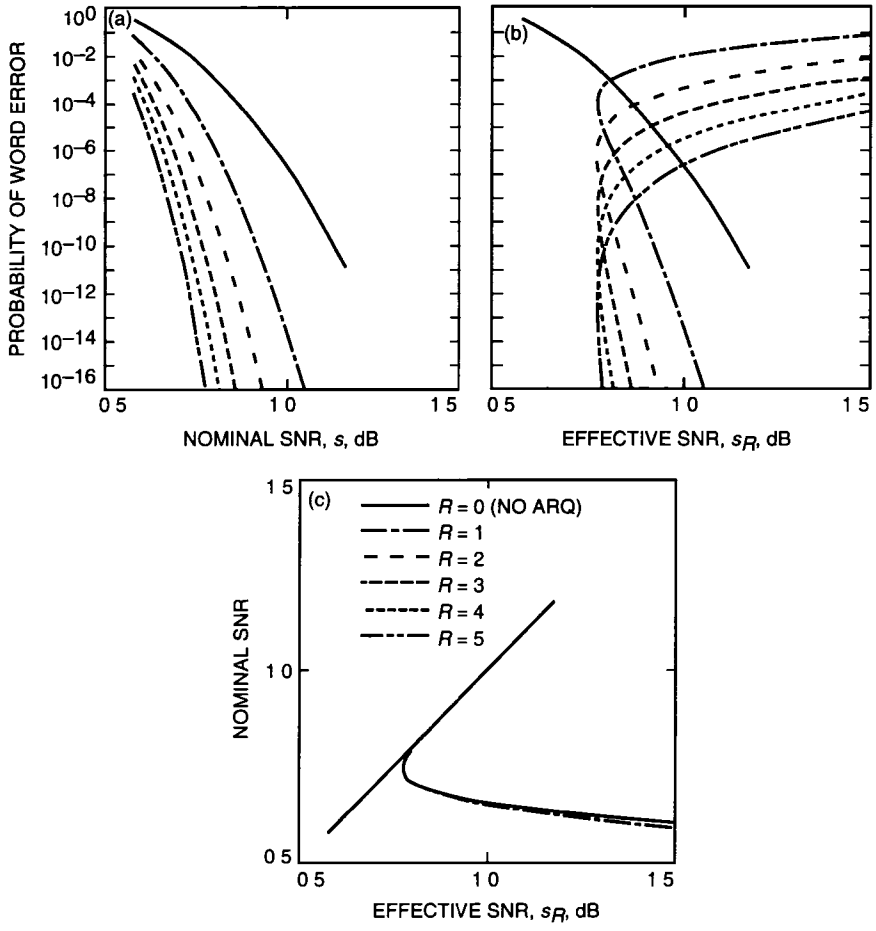

Fig 8 Pairwise relationships between (a) nominal SNR s, (b) effective SNR $s_R(s)$, and (c) probability of word error $P_R(s)$ for the (15,1/4) + (255,223) convolutional code

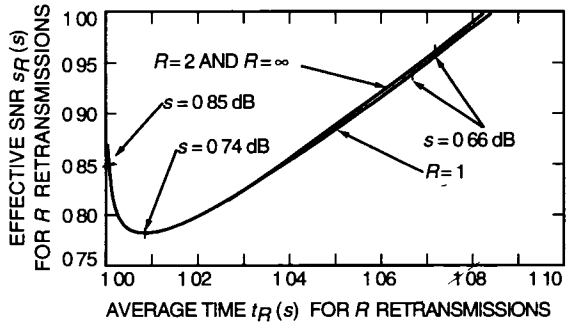

Fig 9 Effective SNR, s_R, plotted with the average time to transmit, t_R, using the (15,1/4) + (255,223) code

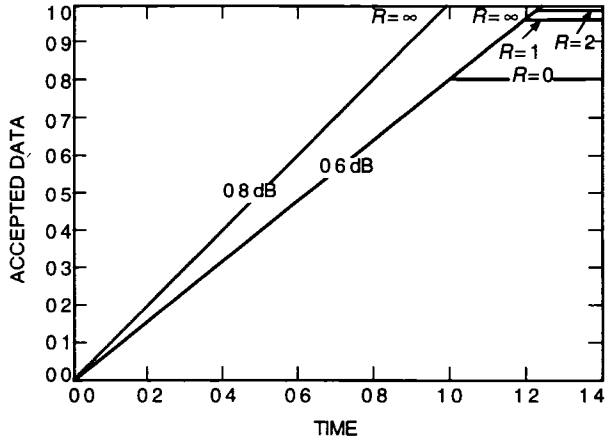

Fig 10 Decoded data volume versus time for the (15,1/4) + (255,223) code

For the concatenated system considered in this section, we have $s^*_\infty = 0.782$ dB, where the minimum is achieved at $s^* = 0.747$ dB. This limiting SNR value of s^*_∞ is still significantly higher than the Shannon limit $> (2^{2r} - 1)/(2r) = -0.917$ dB, where $r = (1/4)\ (223/255)$. We can compute the limiting time and rate at the channel SNR s^* to be

$$t^*_\infty = t_\infty(s^*) = 1.008$$

$$r^*_\infty = r_\infty(s^*) = 0.992$$

The limiting performance curve is shown in Fig. 11 as the envelope of the parametric curves of $s_R(s)$ and $P_R(s)$ for finite R.

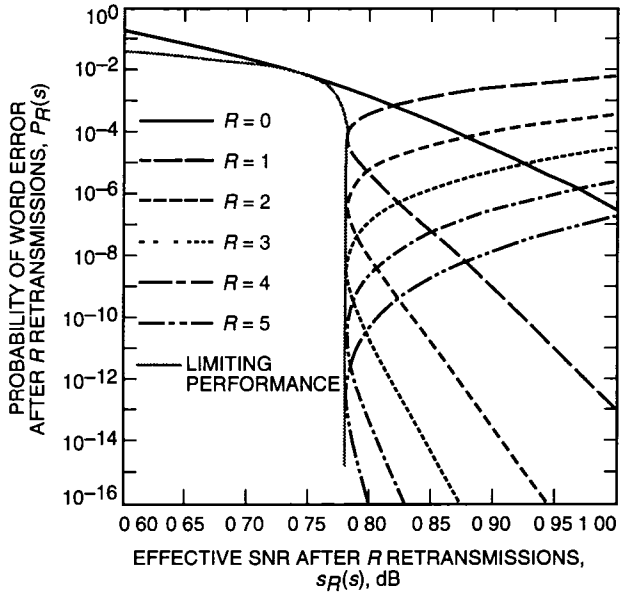

Fig. 11 $P_R(s)$ versus $s_R(s)$, (15,1/4) + (255,223) code

F. The (15,1/6) Convolutional Code

Three plots showing the pairwise relationships between nominal SNR, effective SNR, and probability of word error for the (15,1/6) convolutional code are shown in Fig. 12.

In Fig. 13, a parametric plot of effective SNR versus time shows a local minimum where the effective SNR is low and the average amount of time spent transmitting is close to 1. For the (15,1/6) code, a nominal SNR $s = 0.536$ dB yields an effective SNR $s_R = 0.574$ dB, and the amount of time spent transmitting ($t_R = 1.009$) is only 0.9-percent more time than transmitting once. For nominal SNR higher than 0.6 dB, the channel is essentially noiseless and few retransmissions are requested. As the nominal SNR gets lower than 0.53 dB, the amount of data transmitted increases and so the effective SNR s_R and time t_R also increase. The amount that they can increase is limited because the number of retransmissions is limited to R.

So, for an additional 0.038 dB = 0.574 dB − 0.536 dB of SNR (due to 0.88-percent more time to transmit), the data will be delivered without detected errors, if an unlimited number of retransmissions is allowed, instead of with a probability of error of 0.0087 for the same system without ARQ. The fraction

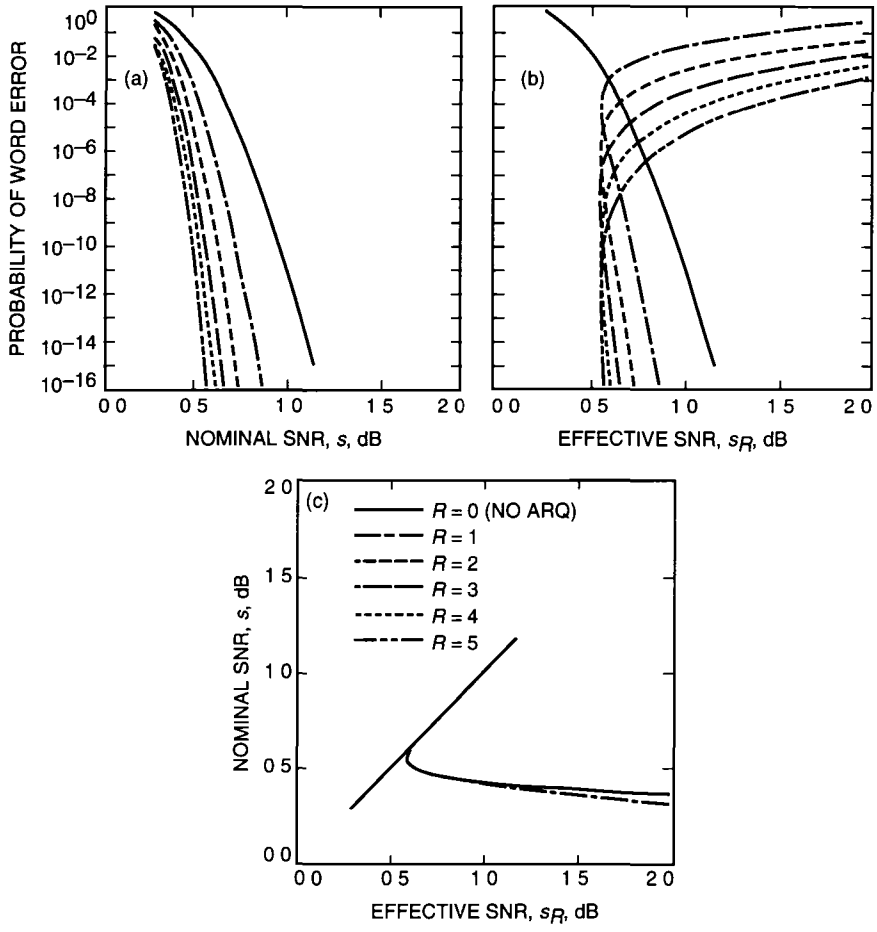

Fig 12 Pairwise relationships between (a) nominal SNR s, (b) effective SNR $s_R(s)$, and (c) probability of word error $P_R(s)$ for the (15,1/6) + (255,223) convolutional code

of the total data volume that is accepted after R retransmissions, $1 - P^{R+1}$, versus the amount of time for R retransmissions is shown in Fig 14

For the concatenated system considered in this section, we have $s^*_\infty = 0\ 574$ dB, where the minimum is achieved at $s^* = 0\ 536$ dB This limiting SNR value of s^*_∞ is still significantly higher than the Shannon limit $(2^{2r} - 1)/(2r) = -1\ 15$ dB, where $r = (1/6)\ (223/255)$ We can compute the limiting time and rate at the channel SNR s^* to be

$$t^*_\infty = t_\infty(s^*) = 1\ 009$$

$$r^*_\infty = r_\infty(s^*) = 0\ 991$$

The limiting performance curve is shown in Fig 15 as the envelope of the parametric curves of $s_R(s)$ and $P_R(s)$ for finite R

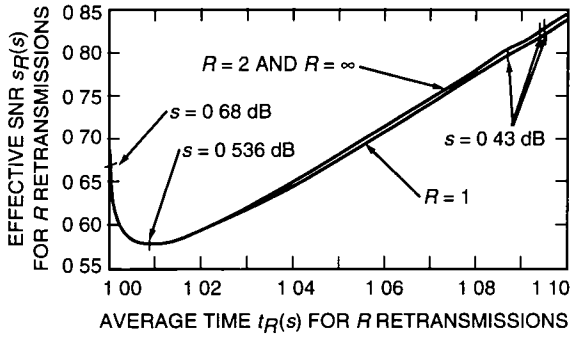

Fig 13 Effective SNR, s_5, plotted with the average time to transmit, t_5, for five allowed retransmissions using the (15,1/6) + (255,223) code This represents the performance for nominal SNRs above 0 480 dB

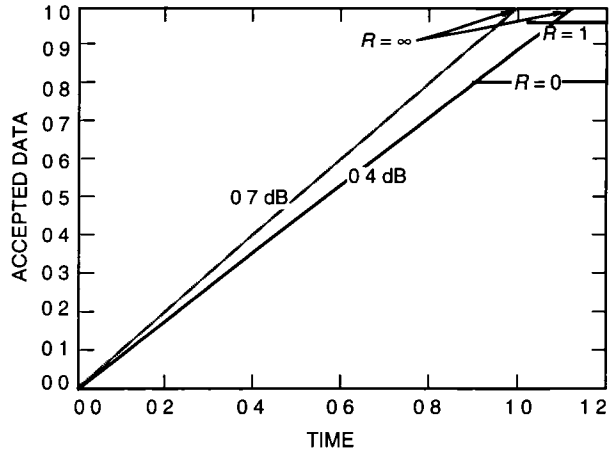

Fig 14 Decoded data volume versus time for the (15,1/6) + (255,223) code

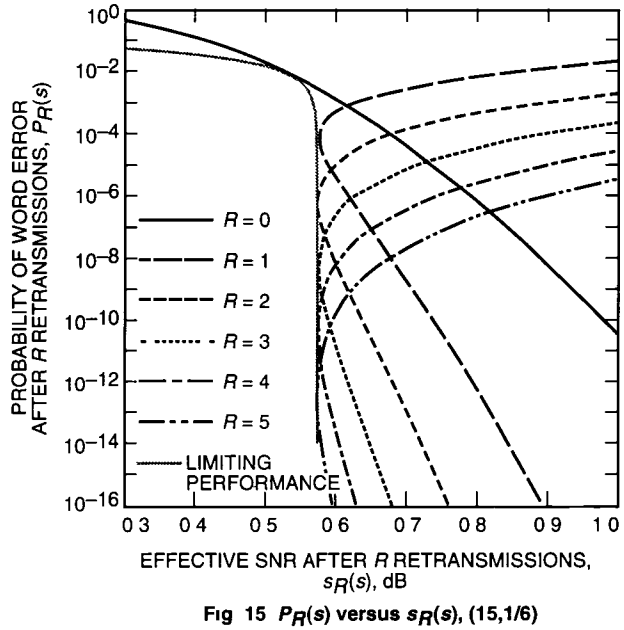

Fig 15 $P_R(s)$ versus $s_R(s)$, (15,1/6) + (255,223) code

IV. Conclusions

We have compared the performance of three reference concatenated coded systems used in actual deep-space missions to that obtainable by ARQ methods using the same codes, in terms of required power, time to transmit with a given number of retransmissions, and achievable probability of word error We have established the ultimate limits of ARQ with an arbitrary number of retransmissions

For an additional 0 035 to 0 057 dB of average power, the retransmission scheme can deliver virtually error-free data to the user This is important when just a few residual errors may disrupt the operation of subsequent data processing stages, e g , the decompression of source encoded data ARQ schemes are also attractive when the available SNR is poorly predictable, since they allow one to trade time for link margin The disadvantages are the need for large onboard storage and for heavier usage of the uplink channel

V. Topics for Future Investigation

Frame Identification If the identification headers are not in every frame, there may be questions about whether the frame requested for repeat can be accurately identified in the request This may depend on the usage of onboard memory or on how consistent the round-trip delay is If there is a sequential log of data that was coded and transmitted, and the periodic header information is associated with the right frames, the repeat request should be able to accurately identify the data to be re-sent

Packet Combining Traditionally, ARQ systems decode retransmitted frames without consideration of the information contained in earlier noisy versions of frames already received By combining subsequent transmissions of the same word/packet, the effect is that the probability of correctly decoding increases There are two ways to do this One is to concatenate the many received versions of the word, forming a longer, lower-rate codeword This is called code combining The other is to combine symbols of the received versions of the word, forming a word of the same length but with stronger symbols This is called diversity combining

Kallel and Leung [7] describe the performance, in terms of throughput, of several schemes with different techniques for combining different numbers and combinations of copies of received words They run the comparisons for a binary symmetric channel, a nonfading and a Rayleigh fading channel with additive white Gaussian noise, as well as for schemes with and without forward error correction (in the form of rate 1/2 and rate 7/8 convolutional coding) Their focus is on systems with finite receiver buffers Kallel [6] shows some significant performance improvements for systems using code combining

Either of these techniques may be able to be translated into an improved SNR Let s_i denote the improved SNR for a word transmitted i times The effect of considering this new SNR is that the lines in Fig 6 would have a steeper slope with each retransmission One can view this as a multiple rate adaptive coding system, since the system runs at the highest rate, while the channel is relatively noiseless and effectively decreases the rate when the channel quality drops The fraction of words that were retransmitted i times that must be retransmitted again is on average $P(s_R)$ The fraction of data that is still in error after i retransmissions is

$$P_i(s) = \prod_{j=0}^{i} P(s_j)$$

It follows that the amount of time it takes for i retransmissions is

$$t_i(s) = 1 + \sum_{m=0}^{i-1} P_m(s) = 1 + \sum_{m=0}^{i-1} \prod_{j=0}^{m} P(s_j)$$

This leads to an effective SNR of

$$s_i(s) = s \left(1 + \sum_{m=0}^{i-1} \prod_{j=0}^{m} P(s_j) \right)$$

Incremental Redundancy An ARQ system using incremental redundancy is one in which the transmitter sends more parity when requested by the receiver While packet combining is strictly a strategy for improving the receiver without altering the transmission process, it is also equivalent to the incremental redundancy strategy when a repetition code is used Incremental redundancy methods have the potential

for achieving the best possible ARQ performance, but their implementation is more complicated Parallel concatenated codes (turbo codes) have been recently proposed for deep-space applications [4] and seem to be particularly suited for incremental redundancy ARQ schemes

Acknowledgments

The authors are grateful to A Kiely and L Swanson for several helpful comments during the preparation of this article

References

[1] S A Butman, L J Deutsch, and R L Miller, "Performance of Concatenated Codes for Deep Space Missions," *The Telecommunications and Data Acquisition Progress Report 42-63, March–April 1981*, Jet Propulsion Laboratory, Pasadena, California, pp 33–39, June 15, 1981

[2] T M Cover and J A Thomas, *Elements of Information Theory*, New York Wiley, 1991

[3] D Divsalar and J H Yuen, "Performance of Concatenated Reed-Solomon/ Viterbi Channel Coding," *The Telecommunications and Data Acquisition Progress Report 42-71, July–September 1982*, Jet Propulsion Laboratory, Pasadena, California, pp 81–94, November 15, 1982

[4] D Divsalar and F Pollara, "Multiple Turbo Codes for Deep-Space Communications," *The Telecommunications and Data Acquisition Progress Report 42-121, January–March 1995*, Jet Propulsion Laboratory, Pasadena, California, pp 66–77, May 15, 1995

[5] S Dolinar, L Ekroot, and F Pollara, "Improvements on Probability of Error Bounds for Block Codes on the Gaussian Channel," *1994 IEEE International Symposium on Information Theory*, Trondheim, Norway, 1994

[6] S Kallel, "Analysis of a Type II Hybrid ARQ Scheme With Code Combining," *IEEE Transactions on Communications*, vol 38, no 8, pp 1133–1137, August 1992

[7] S Kallel and C Leung, "Efficient ARQ Schemes With Multiple Copy Decoding," *IEEE Transactions on Communications*, vol 40, no 3, pp 642–650, March 1992

[8] R J McEliece and L Swanson, "On the Decoder Error Probability for Reed–Solomon Codes," *The Telecommunications and Data Acquisition Progress Report 42-84, October–December 1985*, Jet Propulsion Laboratory, Pasadena, California, February 15, 1986

[9] F Pollara, and K -M Cheung, "Performance of Concatenated Codes Using 8-Bit and 10-Bit Reed-Solomon Codes," *The Telecommunications and Data Acquisition Progress Report 42-97, January–March 1989*, Jet Propulsion Laboratory, Pasadena, California, pp 194–201, May 15, 1989

[10] S B Wicker, *Error Control Systems for Digital Communication and Storage*, New Jersey, Prentice Hall 1995

Appendix
Low Nominal SNRs

When an ARQ system is limited in the number of retransmissions R, at low SNRs, the effects of R being finite are apparent This appendix describes the effects at low SNR although, as we shall see, the system should not be designed to operate in this region To illustrate the effects, we will consider the system with concatenated RS and (7,1/2) codes, though the results hold for all three concatenated systems described in this article

We describe an ARQ system as having three performance regions that depend on the nominal SNR At high SNRs the system behaves as if no ARQ is present, at mid SNRs, the system behaves like an ARQ system with an unlimited number of repeat requests, and at low SNRs, the system behaves like $R+1$ repeats are being used The transitions between these regions are smooth and follow the equations in Section III C The plot of effective SNR versus time in Fig A-1 illustrates the three regions for three different values of R The system performance for SNRs ranging from high through mid range is the focus of the main portion of this article Here they will be discussed at an intuitive level for comparison to the low-SNR regions

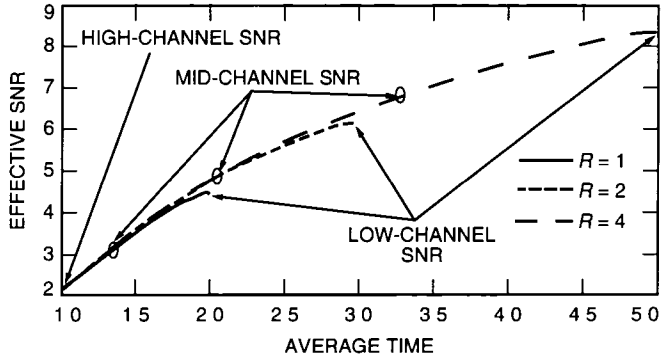

Fig A-1 Average time versus effective SNR for the (7,1/2) + (255,223) code and varying nominal SNR

As we have seen in Section III C, at high SNR the system performs much like a system without ARQ The data are almost always delivered reliably by the first transmission So, for high SNRs, the probability of word error, amount of time to transmit, and effective SNR are indistinguishable from a system without ARQ As such, there also are no effects of a finite R on the performance For mid-range SNRs, repeat requests are being made with some frequency, but the SNR is sufficiently high that correct decoding almost always occurs within the limited number of retransmissions In this region, performance is approximately that of a system with an unlimited number of retransmissions For low SNRs, the system is frequently retransmitting all R times The amount of time it takes to transmit is nearly $R+1$ The effective SNR, $s_R(s)$, is approximately $10\log_{10}(R+1)$ more than the nominal SNR, s The probability of word error is near 1, and the system is performing as though it is using a $R+1$ repeat on a very noisy channel (this is, in fact, what it is doing most of the time) The transition from mid-to-low SNRs produces a "hook" in all of the curves The behavior is similar for different R, so $R=1$ will be used to show the mid-to-low SNR transitions for the different performance curves in Fig A-2

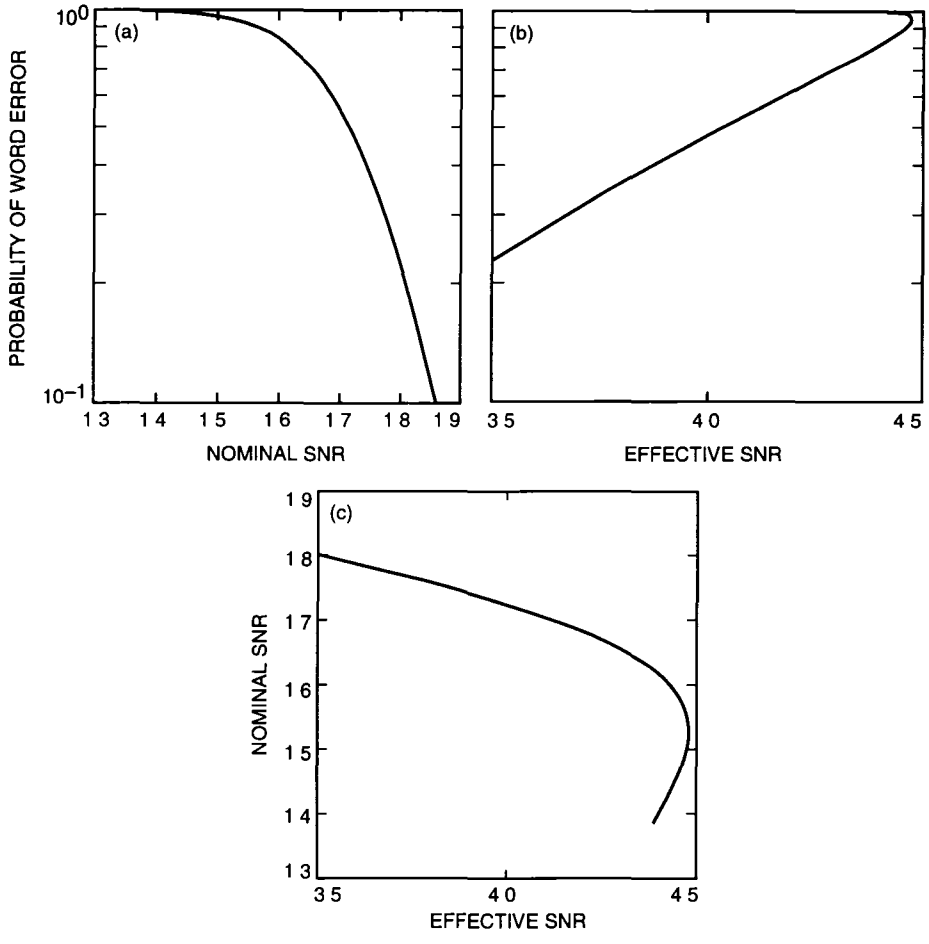

Fig A-2 Parametric plot of probability of word error versus effective SNR with curves showing relations between (a) nominal SNR and probability of both (b) word error and (c) effective SNR

Noncausal Telemetry Data Recovery Techniques

H Tsou, R Lee, A Mileant, and S Hinedi
Communications Systems and Research Section

Cost efficiency is becoming a major driver in future space missions Because of the constraints on total cost, including design, implementation, and operation, future spacecraft are limited in terms of their size, power, and complexity Consequently, it is expected that future missions will operate on marginal space-to-ground communication links that, in turn, can pose an additional risk on the successful scientific data return of these missions For low data-rate and low downlink-margin missions, the buffering of the telemetry signal for further signal processing to improve data return is a possible strategy, it has been adopted for the Galileo S-band mission This article describes techniques used for postprocessing of buffered telemetry signal segments (called gaps) to recover data lost during acquisition and resynchronization Two methods, one for a closed-loop and the other one for an open-loop configuration, are discussed in this article Both of them can be used in either forward or backward processing of signal segments, depending on where a gap is specifically situated in a pass

I. Introduction

With all the budget cuts under way, cost efficiency is becoming a major driver in future space missions Because of the constraints on total cost, including design, implementation, and operation, future spacecraft are limited in terms of their size, power, and complexity Consequently, it is expected that future missions will operate on marginal space-to-ground communication links As a result, data compression techniques aboard the spacecraft and other advanced signal-processing techniques on the ground are important for providing alternatives in order to increase the scientific data return of a mission by improving the communication link margin One adopted concept is buffering the telemetry signal for further signal processing to improve data return for low data-rate and low downlink-margin missions This has been implemented first in the buffered telemetry demodulator (BTD) to support NASA's Galileo Mission [1] In this mission, because of a malfunctioning high-gain antenna, the Galileo spacecraft has to rely on its low-gain antenna to transmit data from Jupiter back to Earth The mission operation can only support very low symbol signal-to-noise ratios (SNRs) (ranging from -10 to -6 dB) at low symbol rates (up to 640 symbols per second) For such a low SNR range, it is estimated that the signal acquisition (including carrier, subcarrier, and symbol) can take up to 10 minutes when a single ground antenna is used Furthermore, in order to maximize the data return, several data rate changes intending to take advantage of all the available antenna apertures on the ground can occur in a pass, and each may require reacquisition of the signal, depending upon the availability of exact knowledge of phase and timing at the rate change The combination of the above two conditions can result in significant data loss if the signal is not buffered

With the data buffered, various nonreal-time (noncausal) signal-processing techniques can be performed to reduce the data loss due to acquisition, resynchronization, and loss of lock For example, the

use of different loop bandwidths and/or different quadrature windowing may realize better acquisition performance [2] In this article, we will focus on techniques used for reprocessing segments of buffered telemetry signal (called gaps), by using checkpoint information obtained from the real-time processing of signal segments next to the gap (called pads), to recover the lost data These techniques, being able to greatly reduce telemetry data loss under low-SNR scenarios, present a unique opportunity to employ non-causal signal-processing techniques for the purpose of signal demodulation and detection In Section II, a brief description of the BTD and the nature of gaps is given Two methods, one for a closed-loop and the other one for an open-loop configuration, are discussed in Sections III and IV, respectively Both of them can be used for either forward or backward gap processing, depending on where a gap is specifically situated in a pass The overall gap-processing strategy is then discussed in Section V Finally, the loop initialization technique associated with closed-loop gap closure processing can be found in the Appendix

II. Buffered Telemetry Demodulator and Gaps

The BTD is a software receiver implemented on a general-purpose, multiple central-processing unit (CPU) workstation It performs acquisition and tracking functions for the carrier, subcarrier, and symbol as well as providing miscellaneous monitoring functions, such as lock indicators, symbol SNR estimators, etc It is designed to take advantage of multiple CPUs in simultaneously doing several processes on different segments of digitally sampled and recorded signal For example, it can process real-time samples forward (in terms of time) and reprocess any other segment of samples in the past at the same time The necessity to reprocess a segment of samples arises from the following two scenarios (1) the out-of-lock indication is detected in any of the loops in the BTD and (2) the succeeding decoder fails to extract valid information from the BTD output symbols Both situations indicate that demodulation was not successfully performed for that segment of samples, which is called a gap Typically, gaps are caused by either acquisition/reacquisition or cycle slip in one of the three loops Gaps due to acquisition/reacquisition can be found in the beginning of each pass and at the instants of data rate change However, gaps due to cycle slips are usually accompanied by the drop of loop SNR and can occur randomly in a pass In rare cases, a gap may happen as demodulated symbols are mishandled in the data flow between the BTD and the succeeding decoder The processing of a gap to extract any valid information not available when that segment of signal samples was first processed is referred to as gap closure processing (GCP)

Along its demodulation process, the BTD keeps a record of its internal states, including the lock indicator states, the state variables inside the loop filter, and the numerically controlled oscillator (NCO) for all three loops These state variables are recorded at fixed intervals and are stored as checkpoints The checkpoint information will serve as a reference when a gap closure process is necessary For a gap situated inside a pass, it is possible to perform the GCP by using the available checkpoint information either prior to or after the gap The former is referred to as forward gap closure processing (FGCP) because it loads in the checkpoint information prior to the gap and starts to process the gap from the beginning toward the end, the latter is referred to as backward gap closure processing (BGCP) since the gap is processed in the order of reversed time Obviously, only the FGCP can be performed when the gap is at the end of a pass, and only the BGCP can be performed when the gap is at the beginning of a pass There is no essential difference between FGCP and BGCP except that the order of signal samples processed is reversed The exclusion of either one depends solely on the availability of sufficient checkpoint information Since every state variable of each checkpoint is a random variable, it is necessary to take more than one checkpoint to make a good estimation of states at the start of GCP A pad is referred to a segment of signal samples from which all the checkpoints used for a GCP are derived Since reliable checkpoint information is essential to a successful GCP, it is always true that the receiver remains in lock throughout a pad while performing real-time signal processing It will be clear that the pad-to-gap size ratio is an important factor in determining the strategy of GCP

The concept of FGCP and BGCP is simply illustrated in Fig 1, where two gaps, two pads, and associated GCPs are given The gap #1 is caused by initial acquisition at the start of a pass It can be

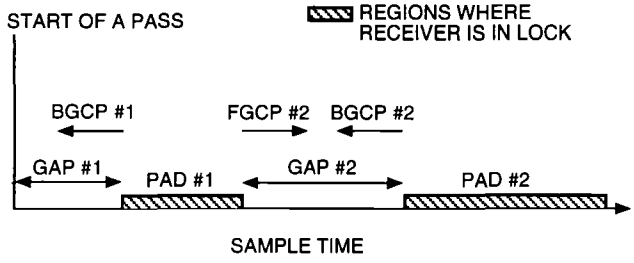

Fig 1 Conceptual illustration of gap closure processing

recovered by the BGCP #1 using checkpoint information obtained from pad #1 The same checkpoint information can also support the FGCP #2 in reprocessing gap #2, where it is inside a pass and probably caused by a data rate change or an unexpected drop of loop SNR Of course, BGCP #2, using checkpoint information obtained from pad #2, is an alternative for the GCP of gap #2

III. Closed-Loop Gap Closure Configuration

The most straightforward way to reprocess a gap is to run the same receiver over that segment of sampled signal with some new a priori information pertinent to the starting point The a priori information is typically obtained by estimates of the state prior to the gap (in the case of FGCP) or after the gap (in the case of BGCP) in segments when the receiver is in lock Then, a loop-filter coefficients initialization method [3] that was first proposed to reduce the transient response of a digital phase-locked loop (DPLL) can be used to set up the loop using the estimated state information As shown in the Appendix, a baseband equivalent phase-locked loop can be augmented by including additional loop parameters for the purpose of phase, frequency, and frequency rate initialization For example, a typical third-order DPLL for deep-space applications, given in Fig 2, can track a signal with third-order Doppler effect, whose phase can be expresssed as

$$\theta(t) = \theta_0 + \theta_1 t + \frac{\theta_2}{2!}t^2 + \frac{\theta_3}{3!}t^3 \tag{1}$$

The loop transient state can be eliminated by setting the parameters C_0, C_1, and C_2 as follows

$$C_0 = \theta_0 - \frac{\theta_3 T_u^2}{G_3} \tag{2a}$$

$$C_1 = \theta_1 + \theta_2 T_u - \frac{G_1}{G_3}\theta_3 T_u^2 + \frac{1}{2}\theta_3 T_u^2 \tag{2b}$$

$$C_2 = \frac{T_u}{G_3}\left[\theta_2 + \frac{1}{2}\theta_3 T_u - \frac{G_2}{G_3}\theta_3 T_u\right] \tag{2c}$$

where $G_i, i \in \{1, 2, 3\}$ are internal gain factors of the loop filter and T_u is the loop filter update interval With good a priori knowledge on θ_0, θ_1, θ_2, and θ_3 as checkpoint information available right before a gap, Eqs (2a), (2b), and (2c) can be used for FGCP

Besides the required checkpoint information obtained right after the end of a gap, the BGCP needs another slight modification in these coefficient settings by changing the sign in front of the terms containing

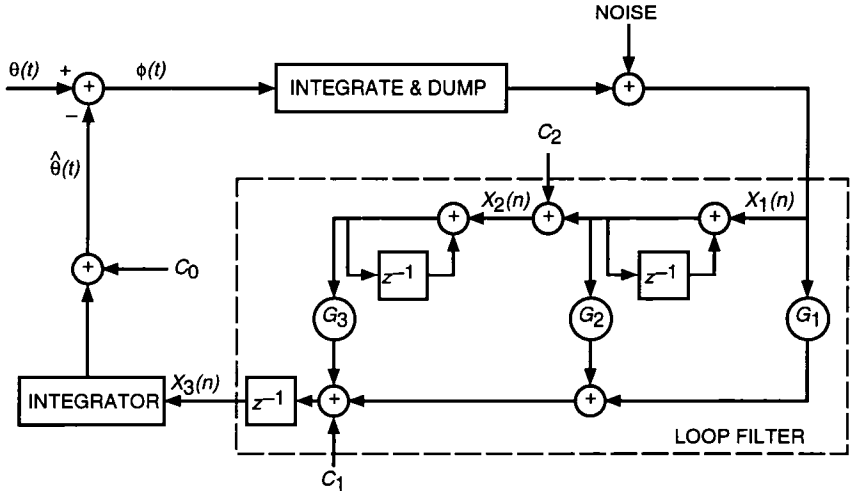

Fig 2 Augmented third-order digital phase-locked loop

θ_i, where i is a positive even integer In the above example, C_0 remains unchanged but C_1 and C_2 need to be changed so that

$$C_0 = \theta_0 - \frac{\theta_3 T_u^2}{G_3} \tag{3a}$$

$$C_1 = \theta_1 - \theta_2 T_u - \frac{G_1}{G_3}\theta_3 T_u^2 + \frac{1}{2}\theta_3 T_u^2 \tag{3b}$$

$$C_2 = \frac{T_u}{G_3}\left[-\theta_2 + \frac{1}{2}\theta_3 T_u - \frac{G_2}{G_3}\theta_3 T_u\right] \tag{3c}$$

The reason for this modification is that the odd-order derivatives of a phase process do not need a sign change as the time is reversed, however, the even-order derivatives do need one This can be explained by a simple example, as follows The frequency for a periodic movement at a rate of $2\pi/s$ is always 1 Hz, whether its associated phasor is described as rotating clockwise or counterclockwise On the other hand, a frequency ramp increasing (positive slope) with time will be decreasing (negative slope) when the time is reversed

Similar results for a second-order DPLL can be readily given, by setting $G_3 = \theta_3 = 0$ in the derivation of third-order DPLL results shown before, as follows for FGCP

$$C_0 = \theta_0 - \frac{\theta_2 T_u}{G_2} \tag{4a}$$

$$C_1 = \theta_1 + \theta_2 T_u - \left(\frac{G_1}{G_2}\right)\theta_2 T_u \tag{4b}$$

and for BGCP

$$C_0 = \theta_0 + \frac{\theta_2 T_u}{G_2} \tag{5a}$$

$$C_1 = \theta_1 - \theta_2 T_u + \left(\frac{G_1}{G_2}\right)\theta_2 T_u \tag{5b}$$

IV. Open-Loop Gap Closure Configuration

A gap can be reprocessed without the use of a PLL to adaptively estimate the signal phase, provided that the signal phase is reasonably stable or slowly varying in that gap The open-loop gap closure configuration uses an estimated phase profile to serve as the reference phase The estimated phase profile can be obtained from the phase observation over an adjoint region where phase has been successfully tracked

It is assumed that the measurements at the output of the NCO can be modeled as

$$y(k) = \theta(k) + \nu(k) = \theta_0 + \theta_1(kT) + \frac{\theta_2(kT)^2}{2} + \nu(k) \tag{6}$$

where $\theta(k)$ is the input phase process sampled at interval T and $\nu(k)$ is a zero-mean Gaussian random variable with variance σ_y^2 Given m noisy correlated samples of $y(k)$, the least-squared estimate of the input phase parameters, namely, θ_0, θ_1, and θ_2, is easily shown as [4]

$$\underline{\hat{\theta}} = \left[H^T H\right]^{-1} H^T \underline{y} \tag{7}$$

where $\underline{\hat{\theta}}$ is the estimation vector and $\underline{y}$ is the measurement vector, given as

$$\underline{\hat{\theta}} = \begin{bmatrix} \hat{\theta}_0 \\ \hat{\theta}_1 \\ \hat{\theta}_2 \end{bmatrix} \quad \text{and} \quad \underline{y} = \begin{bmatrix} y(1) \\ y(2) \\ \\ y(m) \end{bmatrix}$$

and the transpose of the observation matrix H is given as

$$H^T = \begin{bmatrix} 1 & 1 & 1 \\ T & 2T & mT \\ \dfrac{T^2}{2} & \dfrac{(2T)^2}{2} & \dfrac{(mT)^2}{2} \end{bmatrix}$$

Therefore, the estimated phase at time t will be

$$\hat{\theta}(t) = \hat{\theta}_0 + \hat{\theta}_1 t + \frac{\hat{\theta}_2 t^2}{2} \tag{8}$$

which is an unbiased estimate with variance

$$\sigma_{\hat{\theta}}^2(t) = \sigma_y^2 \left[p_{11} + p_{22}t^2 + \frac{p_{33}t^4}{4} + 2\left(p_{12}t + \frac{p_{13}t^2}{2} + \frac{p_{23}t^3}{2}\right)\right] \tag{9}$$

where p_{ij} is the (i,j)th component of the covariance matrix

$$P = \left[H^T H\right]^{-1} H^T R H \left[H^T H\right]^{-1}$$

with $R = E\{\underline{\nu\nu}^T\}$ being the covariance matrix of the NCO output, determined by sampling the correlation function of the phase process given in [5]

It is interesting to note that the normalized variance of the open-loop, least-squared estimated phase, defined as the ratio of $\sigma_{\hat{\theta}}^2(t)/\sigma_y^2$, serves as an important indicator showing whether the open-loop configuration outperforms the closed-loop configuration or not A ratio smaller than 1 actually implies that the open-loop estimated phase has smaller variance than the NCO output phase derived from the closed-loop configuration Figure 3 gives a typical example of the performance of the least-squares smoother/predictor versus the sample number, in which the observation window consists of 2000 samples starting from the sample one Note that the region where normalized variance is less than unity extends both sides symmetrically beyond the observation window The ratio of the single-sided extension size to the observation window size, denoted as $\eta(m, B_L T)$, is listed in Table 1 for various m, the number of observed samples, and $B_L T$, the product of the loop bandwidth of the counterpart closed-loop configuration and the sampling interval For example, as listed in Table 1 and also shown in Fig 3, the open-loop configuration should outperform the closed-loop configuration over any gap with a size up to 133 percent of the available observation size $m = 2000$ and $B_L T = 1\ 0$

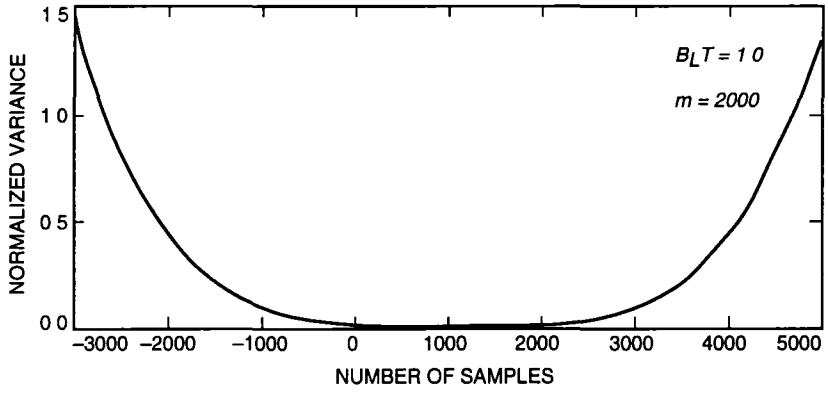

Fig 3 Performance of the least-squares smoother/predictor

Table 1 The $\eta(m, B_L T)$ values

m	$B_L T$				
	1 0, %	0 2, %	0 1, %	0 05, %	0 01, %
100	38 00	14 00	5 00	0 00	0 00
500	80 80	43 60	29 60	18 20	0 00
1000	105 00	60 40	43 80	29 80	6 20
2000	133 85	80 55	60 65	43 90	15 05
5000	180 62	113 32	88 12	66 84	29 94
10,000	223 91	143 71	113 64	88 17	43 92
15,000	252 95	164 12	130 79	102 57	53 41
20,000	275 43	179 92	144 07	113 72	60 76

V. Overall Gap Closure Strategy

It has been shown that open-loop configuration can simply outperform the closed-loop configuration for a certain length of time into a gap, and then its performance deteriorates rapidly when further into the gap Based upon this phenomenon, the overall gap closure strategy that optimizes the GCP performance is depicted as the flow chart of Fig 4

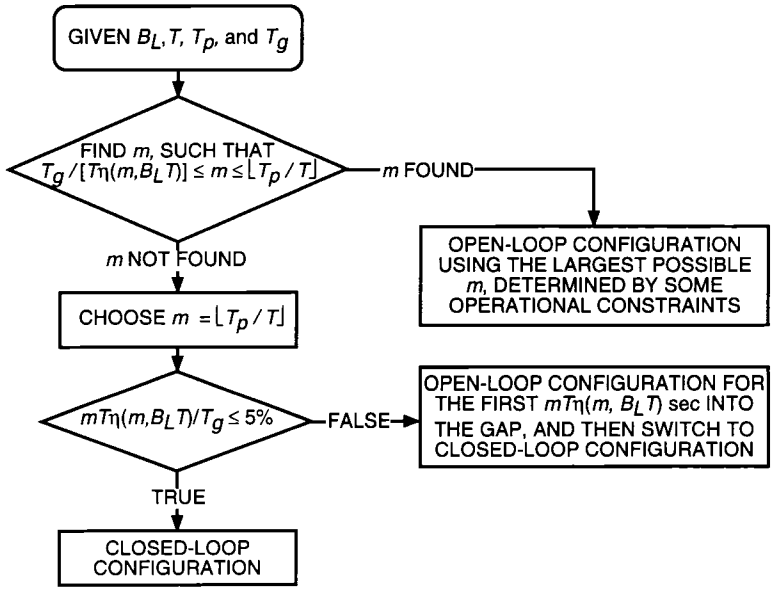

Fig 4 The overall gap closure strategy

For a given loop bandwidth B_L, checkpoint interval T, gap size T_g, and available pad size T_p, the open-loop configuration is able to process the complete gap with better performance, only if there exists at least an integer number of checkpoints, denoted as m, which satisfies

$$\frac{T_g}{T \ \eta(m, B_L T)} \le m \le \left\lfloor \frac{T_p}{T} \right\rfloor \tag{10}$$

The upper limit of Eq (10) is the number of available checkpoints from the given pad, and the lower limit is the number of required checkpoints to open loop cover the whole gap When such m exists, the largest possible m, determined by some operational constraints, is chosen to ensure the best open-loop gap closure performance When no such m can be found to satisfy Eq (10), it is still possible to use open-loop configuration up to the point where the open-loop performance is going to be worse than the closed-loop performance, namely the first $mT \ \eta(m, B_L T)$ seconds into the gap, and then close the loop for the rest of the gap A decision needs to be made here whether the benefit justifies including an additional switching mechanism from open-loop to closed-loop configuration Typically, the break point is arbitrarily set as

$$\frac{mT \ \eta(m, B_L T)}{T_g} = 5\%$$

Figure 5 shows the result from gap closure processing of a gap in the real Galileo telemetry data received at DSS 14 The received signal has a predicted P_T/N_0 ratio around 16 dB-Hz with its carrier

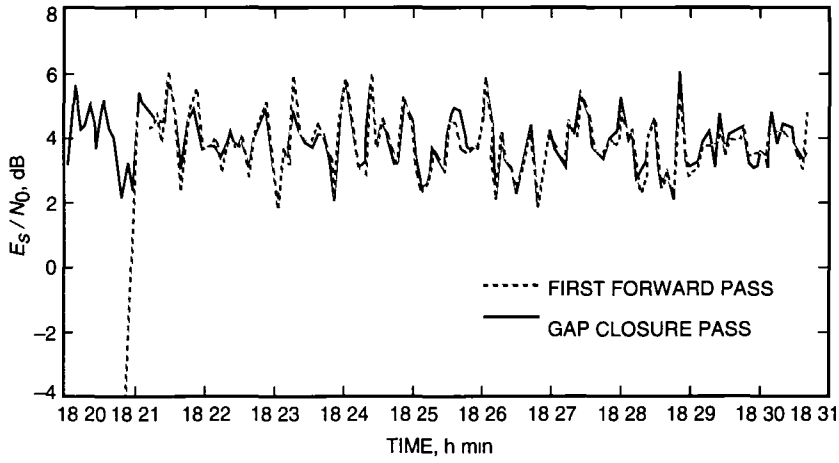

Fig 5 The estimated symbol SNR versus time

component being fully suppressed The symbol rate is 20 symbols per second, which is translated to the predicted symbol SNR, denoted as E_s/N_0, at the 3-dB level The gap, characterized by the below-average estimated SNR of demodulated symbols from the BTD in Fig 5, happens at the beginning of the first forward pass and lasts about 1 minute (from 18 20 to 18 21) After this initial acquisition effort, the BTD maintains its lock on the signal, and the demodulated symbol SNR is stabilized around its predicted level During BGCP, the telemetry data in this gap are successfully recovered as the estimated symbol SNR remains at its normal level until the beginning of the data pass is reached

VI. Conclusion

Techniques used to recover data loss from buffered telemetry signal during acquisition/reacquisition, data rate changes, and cycle slips are presented in this article Two different configurations—one a simple least-squares phase estimator used for the open-loop gap closure processing and the other involving loop filter initialization for the closed-loop gap closure processing—can be chosen to recover lost data, depending upon the size of a gap and the size of its surrounding pad(s) Both methods have the flexibility to be used in either forward or backward processing, which helps to cover gaps at various positions, especially at the beginning of each pass where initial acquisition is always required The overall strategy that optimizes the gap closure-processing performance is also presented With the ease of implementation on general-purpose workstations and the flexibility to work on the reversed time order, these techniques should be crucial to the future low-cost space missions, since the expected very low downlink communication margin is a threat to the scientific data return

Besides the techniques presented in this article, other techniques, including Kalman filters and the use of both the past and future information jointly to perform the gap closure processing, have also been studied The performance comparison will be addressed later

Acknowledgments

The authors would like to thank Ms K Simpson and Mr T Dry for their efforts in implementing the gap closure techniques in the BTD The authors are also grateful to Mr T Pham for his valuable comments on this work The various discussions held with Mr J Statman are greatly appreciated

References

[1] H Tsou, B Shah, and S Hinedi, "A Functional Description of the Buffered Telemetry Demodulator," *SUPERCOM/ICC'94*, New Orleans, Louisiana, May 1994

[2] M Aung, W J Hurd, C M Buu, and J B Berner, "The Block V Receiver Fast Acquisition Algorithm for the Galileo S-Band Mission," *The Telecommunications and Data Acquisition Progress Report 42-118, April–June 1994*, Jet Propulsion Laboratory, Pasadena, California, pp 83–114, August 15, 1994

[3] S A Stephens and J B Thomas, "Controlled-Root Formulation for Digital Phase-Locked Loops," *IEEE Trans on Aerospace and Electronic Systems*, vol 31, no 1, pp 78–95, January 1995

[4] H W Sorenson, *Parameter Estimation*, New York M Dekker, 1985

[5] A Mileant and S Hinedi, "Lock Detection in Costas Loops," *IEEE Trans on Communications*, vol 40, no 3, pp 480–483, March 1992

Appendix

Loop Initialization of the Augmented Digital Phase-Locked Loop

Figure 2 shows an augmented baseband-equivalent DPLL used for deep-space applications, in which the loop filter coefficients can be initialized to reduce the transient response It is assumed that the phase detector and the NCO are updated at a much higher rate—usually the sampling rate—as compared to the loop update rate with which the rest of the loop is operating Therefore, in this baseband-equivalent model, the NCO is treated as an integrator in the continuous-time domain, and the loop filter remains in the discrete-time domain The loop filter z-domain transfer function is given as

$$F(z) = G_1 + \frac{G_2}{1 - z^{-1}} + \frac{G_3}{(1 - z^{-1})^2} \tag{A-1}$$

where

$$G_1 = \frac{rd}{T_u} \tag{A-2a}$$

$$G_2 = \frac{rd^2}{T_u} \tag{A-2b}$$

$$G_3 = \frac{krd^3}{T_u} \tag{A-2c}$$

and

$$d = \frac{4B_L T_u (r-k)}{r(r-k+1)} \tag{A-2d}$$

with T_u as the loop update interval, B_L as the designed loop bandwidth, r being equal to 4ξ where ξ is the damping ratio, and k as a third-order loop gain parameter ($k = 0$ for a second-order loop) This augmented baseband-equivalent model includes three constant parameters, C_0, C_1, and C_2, which can be used to initialize the loop, as described later

The estimated phase for this loop can be derived as follows

$$\hat{\theta}(t) = C_0 + \int_0^t X_3(\tau) d\tau \tag{A-3}$$

where

$$X_3(k) \triangleq \left.\frac{d\hat{\theta}(t)}{dt}\right|_{t=kT_u} = C_1 + G_1 X_1(k-1) + G_2 \sum_{i=1}^{k-1} X_1(i) + G_3 \left[C_2(k-1) + \sum_{i=1}^{k-1} \sum_{j=1}^{i} X_1(j) \right] \tag{A-4}$$

is the loop filter output representing the discrete-time estimated frequency process updated at the loop update rate The first-order difference of $X_3(k)$ can be found as

$$\begin{aligned} \Delta X_3(k) &\triangleq X_3(k) - X_3(k-1) \\ &= G_1 [X_1(k-1) - X_1(k-2)] + G_2 X_1(k-1) + G_3 \left[C_2 + \sum_{j=1}^{k-1} X_1(j) \right] \end{aligned} \tag{A-5}$$

and the second-order difference of $X_3(k)$ can be found as

$$\begin{aligned} \Delta^2 X_3(k) &\triangleq \Delta X_3(k) - \Delta X_3(k-1) \\ &= G_1 [X_1(k-1) - 2X_1(k-2) + X_1(k-3)] + G_2 [X_1(k-1) - X_1(k-2)] + G_3 X_1(k-1) \end{aligned} \tag{A-6}$$

The phase process of the incoming signal can be approximated by the following Taylor series expansion

$$\theta(t) = \theta_0 + \theta_1 t + \frac{\theta_2}{2!} t^2 + \quad + \frac{\theta_m}{m!} t^m \tag{A-7}$$

A third-order phase-locked loop can track $\theta(t)$ with $m \leq 3$, while a second-order loop can only track $\theta(t)$ with $m \leq 2$ In the following, we will describe the loop initialization for both second-order and third-order DPLLs, with the third-order DPLL discussed first and the second-order loop discussed as a simplified case from the previous one

I. The Third-Order DPLL

Let us consider a third-order input phase process given as follows

$$\theta(t) = \theta_0 + \theta_1 t + \frac{\theta_2}{2!}t^2 + \frac{\theta_3}{3!}t^3 \tag{A-8}$$

We can find the sampled phase derivative process $X(n)$ as

$$X(n) \triangleq \left.\frac{d\theta(t)}{dt}\right|_{t=nT_u} = \theta_1 + \theta_2(nT_u) + \frac{\theta_3}{2}(nT_u)^2 \tag{A-9a}$$

and its associated first and second-order differences as follows

$$\Delta X(n) = \theta_2 T_u + \left(n - \frac{1}{2}\right)\theta_3 T_u^2 \tag{A-9b}$$

$$\Delta^2 X(n) = \theta_3 T_u^2 \tag{A-9c}$$

When the augmented third-order DPLL is used to track this input phase in a noiseless environment, the loop will eventually reach a steady state in which

$$\theta(t) - \hat{\theta}(t) = \phi_{ss} \tag{A-10}$$

where ϕ_{ss} is called the steady-state phase error Let us assume that the loop has reached its steady state at time instance $t = nT_u$, so that the loop filter input becomes the steady-state phase error

$$X_1(k) = \phi_{ss} \tag{A-11}$$

for k being in the vicinity of n In this case, Eqs (A-4), (A-5), and (A-6) can be further simplified as

$$X_3(n) = C_1 + G_1\phi_{ss} + G_2\sum_{i=1}^{n-1} X_1(i) + G_3\left[C_2(n-1) + \sum_{i=1}^{n-1}\sum_{j=1}^{i} X_1(j)\right] \tag{A-12a}$$

$$\Delta X_3(n) = G_2\phi_{ss} + G_3\left[C_2 + \sum_{j=1}^{n-1} X_1(j)\right] \tag{A-12b}$$

$$\Delta^2 X_3(n) = G_3\phi_{ss} \tag{A-12c}$$

Note that the summations in the above equations involve the history of the $X_1(k)$ that should trace back to the beginning of loop operation, including any possible transient state

Equation (A-10) suggests that, in the steady state, all the corresponding phase derivatives of the input phase process and the estimated phase process should be equal By equating Eq (A-9c) and Eq (A-12c), we find the steady-state phase error is

$$\phi_{ss} = \frac{\theta_3 T_u^2}{G_3} \tag{A-13}$$

Using Eq (A-13), we can solve for C_1 and C_2 by equating Eq (A-9a) with Eq (A-12a) and Eq (A-9b) with Eq (A-12b) It can be found that

$$\begin{aligned} C_1 &= \theta_1 + \theta_2 T_u - \frac{G_1}{G_3}\theta_3 T_u^2 + (n-1)\frac{G_2}{G_3}\theta_3 T_u^2 - \frac{1}{2}(n^2 - 3n + 1)\theta_3 T_u^2 \\ &\quad - G_2 \sum_{j=1}^{n-1} X_1(j) + (n-1)G_3 \sum_{j=1}^{n-1} X_1(j) - G_3 \sum_{i=1}^{n-1}\sum_{j=1}^{i} X_1(j) \end{aligned} \tag{A-14}$$

$$C_2 = \frac{T_u}{G_3}\left[\theta_2 + \left(n - \frac{1}{2}\right)\theta_3 T_u - \frac{G_2}{G_3}\theta_3 T_u\right] - \sum_{j=1}^{n-1} X_1(j) \tag{A-15}$$

Also, from Eqs (A-10) and (A-13), it is clear that

$$C_0 = \theta_0 - \frac{\theta_3 T_u^2}{G_3} \tag{A-16}$$

Ideally, the transient state can be eliminated by properly setting the parameters C_0, C_1, and C_2 so that, immediately as the loop begins its operation, the loop is in the steady state, namely,

$$X_1(k) = \phi_{ss} \quad \text{for every} \quad k \geq 0 \tag{A-17}$$

Equation (A-17) suggests that the loop can be initialized so that it starts with its steady state by setting C_0 as given in Eq (A-16) and, based on Eqs (A-14) and (A-15),

$$C_1 = \theta_1 + \theta_2 T_u - \frac{G_1}{G_3}\theta_3 T_u^2 + \frac{1}{2}\theta_3 T_u^2 \tag{A-18}$$

$$C_2 = \frac{T_u}{G_3}\left[\theta_2 + \frac{1}{2}\theta_3 T_u - \frac{G_2}{G_3}\theta_3 T_u\right] \tag{A-19}$$

II. The Second-Order DPLL

As mentioned previously, the second-order DPLL is exactly the same as the third-order DPLL except that one of the loop filter branch gains, i e , G_3, is set to be 0 Therefore, the augmented second-order DPLL has only two parameters, C_0 and C_1, to be set in the loop initialization Accordingly, a second-order input phase process that can be tracked by a second-order DPLL has $\theta_3 = 0$

Following the same argument about the steady state of the loop as given before, the second-order DPLL steady-state phase error can be found by equating Eq (A-9b) with Eq (A-12b) and setting both G_3 and θ_3 to be 0, as

$$\phi_{ss} = \frac{\theta_2 T_u}{G_2} \tag{A-20}$$

Thus, C_1 can be solved by equating Eq (A-9a) with Eq (A-12a) and using Eq (A-20) as

$$C_1 = \theta_1 + n\theta_2 T_u - \frac{G_1}{G_2}\theta_2 T_u - G_2 \sum_{i=1}^{n-1} X_1(i) \tag{A-21}$$

and C_0 is found from Eqs (A-10) and (A-20) as

$$C_0 = \theta_0 - \frac{\theta_2 T_u}{G_2} \tag{A-22}$$

This loop can be initialized so that it starts with its steady state by setting C_0 as given in Eq (A-22) and

$$C_1 = \theta_1 + \theta_2 T_u - \frac{G_1}{G_2}\theta_2 T_u \tag{A-23}$$

Carrier Arraying—Revisited

M K Simon
Communications Systems and Research Section

Depending on the basis used for comparison, it is possible to predict different gains when applying carrier arraying to a conventional coherent receiver In the past, the specific performance comparisons were made between the arrayed and nonarrayed cases assuming a fixed carrier-tracking closed-loop bandwidth While the notion of loop bandwidth for the nonarrayed loop with a single input is well defined and meaningful, the comparable notion for an arrayed loop with multiple inputs is not uniquely defined since it depends on the knowledge of the statistical relation, e g , degree of correlation, among the various antenna inputs To circumvent the need for such knowledge, which is often not completely available, we suggest in this article an alternate criterion for comparing arrayed and nonarrayed loops, namely, fixed steady-state phase error, which, in the arrayed case, is independent of the statistical relation among the antenna inputs We show that, in this case, the gain derived from carrier arraying is quite different from that obtained under the assumption of fixed-loop bandwidth, which suggests that one should exercise care when comparing arrayed and unarrayed loops in that the criterion used for comparison should be directly applicable to the situation at hand

I. Introduction

Carrier arraying is a technique for automatically aligning the phases of a multitude (say N) of received carriers possibly at geographically separated locations so as to allow them to be coherently combined, thereby improving the overall signal-to-noise ratio (SNR) performance of the system Previous analysis [1] of such a carrier-arraying system focused on the tracking performance of the first receiver (where the carrier arraying is performed) as measured by its closed-loop rms phase jitter and radio loss associated with the data detection process It was shown in [1] that when the loop bandwidths of stations 2, 3, , N are much narrower than that of the first station, then carrier arraying could offer a significant enhancement in station 1's loop SNR, thereby reducing its rms phase jitter and associated radio loss relative to the no carrier-arraying case

The specific performance comparisons made in [1] between the arrayed and nonarrayed cases assumed a fixed carrier-tracking closed-loop bandwidth As such, the authors of [1] first evaluated station 1's loop bandwidth after carrier arraying and then computed the loop SNR enhancement (reduction in rms phase jitter) with this bandwidth set equal to this same quantity prior to arraying While the latter notion of loop bandwidth (i e , for the nonarrayed loop with a single input) is well defined and meaningful (see any standard text on phase-locked loop (PLL) theory, e g , [2]), the former notion of loop bandwidth (i e , for an arrayed loop with multiple inputs) is not uniquely defined since it depends on the statistical relation among the antenna inputs Thus, the performance comparisons derived and illustrated in [1] depend on

the particular definition of loop bandwidth in the presence of carrier arraying assumed in that reference In what follows, we shall expand on this notion, starting out with an interpretation of the comparisons made in [1] Following that, we shall suggest an alternate criterion for comparing arrayed and nonarrayed loops that has the advantage of being independent of the definition of loop bandwidth applied We shall see that, in this case, the gain derived from carrier arraying is quite different from that obtained under the assumption of fixed-loop bandwidth This suggests that one should exercise care when comparing arrayed and unarrayed loops in that the criterion used for comparison should be directly applicable to the situation at hand

Although our results will be presented in a form that allows for any order loops, to keep matters simple and allow for comparisons that are easy to comprehend, we shall specifically consider the case of first-order loops

II. Stochastic Differential Equation of Operation

Illustrated in Fig 1 is the carrier-arraying system identified in [1] and in Fig 2 its equivalent block diagram based on linear loop operation for all station receivers The stochastic differential equation of operation of station 1's carrier-tracking loop (the one that is arrayed) is (see Eq (A-2) of [1] with $\theta_m = 0$)[1]

$$\hat{\theta}_1 = \frac{K_1 F_1(p)}{p}\left[\sqrt{P_1}\beta_1\left(\theta_1 - \hat{\theta}_1\right) + \sum_{i=2}^{N}\sqrt{P_i}\beta_i\left(\theta_i - \hat{\theta}_i - \theta_1\right) + \sum_{i=2}^{N}\beta_i N_i\right] \tag{1}$$

where P_i is the signal power of the received signal at station i, N_i is a zero-mean, variance $N_{0i}/2$ Gaussian random variable representing the additive noise in station i's receiver, K_1 is the total loop gain of station 1's carrier-tracking loop (prior to arraying), and $F_1(p)$ is the transfer function of the loop filter with p denoting the Heaviside operator Similarly, the stochastic differential equation of loop operation for the remaining station receivers is given by (see Eq (A-4) of [1] with $\theta_m = 0$)

$$\hat{\theta}_i = \frac{K_i F_i(p)}{p}\left[\sqrt{P_i}\left(\theta_i - \hat{\theta}_i - \theta_1\right) + N_i\right], \quad i = 2, 3, \quad , N \tag{2}$$

Substituting Eq (2) into Eq (1) and defining the gain ratio $\gamma_i = \sqrt{P_i/P_1}$, it is straightforward to show that

$$\hat{\theta}_1 = H_1(p)\left\{\theta_1 + \frac{N_1}{\sqrt{P_1}} + \sum_{i=2}^{N}\left(\frac{\beta_i}{\beta_1}\right)\gamma_i\left(1 - H_i(p)\right)\left[\left(\theta_i - \hat{\theta}_1\right) + \frac{N_i}{\sqrt{P_i}}\right]\right\} \tag{3}$$

where

$$\left.\begin{aligned} H_1(p) &= \frac{K_1\sqrt{P_1}F_1(p)\beta_1}{p + K_1\sqrt{P_1}F_1(p)\beta_1} \\ H_i(p) &= \frac{K_1\sqrt{P_i}F_i(p)}{p + K_i\sqrt{P_i}F_i(p)} \end{aligned}\right\} \tag{4}$$

[1] To keep the normalization of the loop gains completely general, we do at this point set the combining weight β_1 equal to 1, as was done in [1]

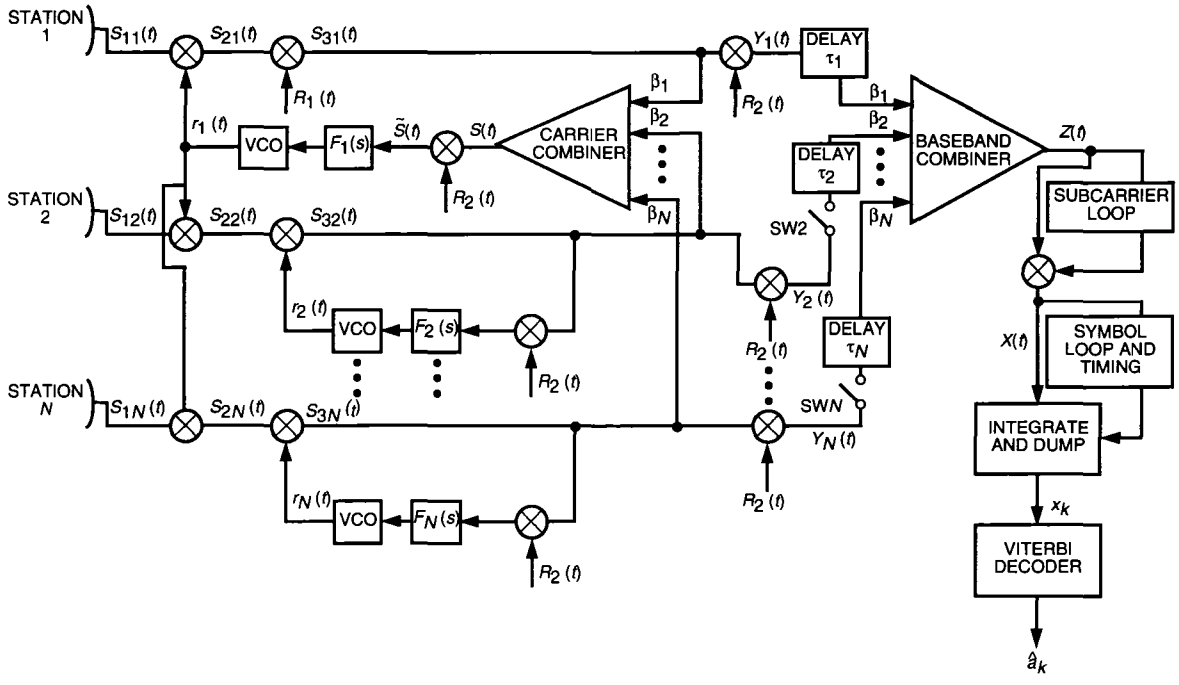

Fig 1 Configuration for arrayed network with carrier and baseband arraying

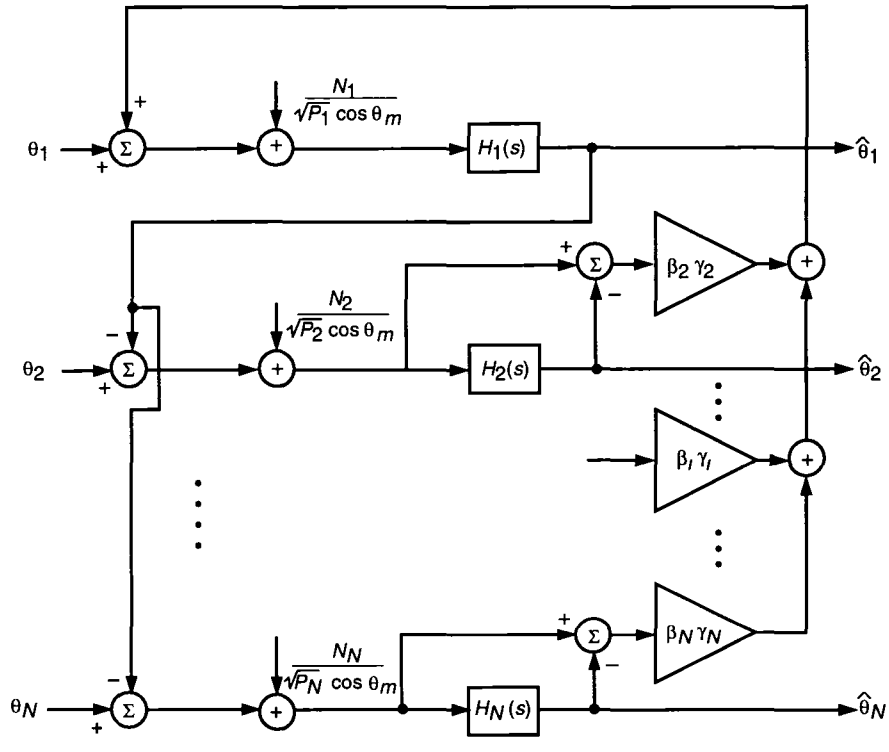

Fig 2 An equivalent linear representation of carrier arraying system for phase jitter analysis

For the special case of two antennas ($N = 2$) with equal powers ($P_1 = P_2 = P$ or $\gamma_2 = 1$), Eq (3) simplifies to

$$\hat{\theta}_1 = H_1(p)\left\{\theta_1 + \frac{N_1}{\sqrt{P}} + \left(\frac{\beta_2}{\beta_1}\right)(1 - H_2(p))\left[\left(\theta_2 - \hat{\theta}_1\right) + \frac{N_2}{\sqrt{P}}\right]\right\} \tag{5}$$

Without loss in generality, we shall focus the remainder of our discussion on this special case since it is sufficient to illustrate the points that need to be made

III. Defining the Loop Bandwidth

For a carrier-tracking loop with a single input, θ, and a single output, $\hat{\theta}$, the single-sided loop noise bandwidth, B_L, is defined by

$$2B_L \triangleq \frac{1}{2\pi j}\int_{-j\infty}^{j\infty} |H(s)|^2 ds \tag{6}$$

where

$$H(s) \triangleq \frac{\hat{\theta}(s)}{\theta(s)} \tag{7}$$

with s denoting the LaPlace transform operator For a first-order loop with $F(s) = 1$, Eq (6) evaluates to the well-known result [2]

$$B_L = \frac{K\sqrt{P}}{4} \tag{8}$$

whereas for a second-order loop with imperfect integrating loop filter, $F(s) = (1 + s\tau_2)/(1 + s\tau_1)$, the result is

$$\begin{aligned} B_l &= \frac{r+1}{4\tau_2\left(\dfrac{1+\tau_2}{r\tau_1}\right)} \cong \frac{r+1}{4\tau_2} \\ r &= \frac{K\sqrt{P}\tau_2^2}{\tau_1} \end{aligned} \tag{9}$$

where the approximation is valid for the usual case $r\tau_2 >> \tau_1$

In the carrier-arraying case, we are dealing with an arrayed loop (station 1) that has a single output, $\hat{\theta}_1$, and, in general, *multiple* inputs, i e , $\theta_1, \theta_2, \quad , \theta_N$ For such a system, the definition of loop bandwidth

for station 1's receiver is not uniquely defined since it indeed depends on the relation of the other receiver inputs, $\theta_2, \quad , \theta_N$, to its own input, θ_1 In the simplest scenario with just two antennas, the received signals at antenna 1 and antenna 2 differ only in a constant delay, $\tau = \Delta\theta/\omega_c$, between them, where ω_c is the radian carrier frequency common to both Thus, for this scenario, we would have $\theta_2 = \theta_1 + \Delta\theta$, i e , $\theta_1$and θ_2 are totally correlated, in which case Eq (5) becomes

$$\hat{\theta}_1 = H_1(p)\left\{\theta_1 + \frac{N_1}{\sqrt{P}} + \left(\frac{\beta_2}{\beta_1}\right)(1 - H_2(p))\left[\theta_1 + \Delta\theta - \hat{\theta}_1 + \frac{N_2}{\sqrt{P}}\right]\right\} \tag{10}$$

or equivalently,

$$\hat{\theta}_1 = \left[\frac{H_1(p)\left[1 + \left(\frac{\beta_2}{\beta_1}\right)(1 - H_2(p))\right]}{1 + \left(\frac{\beta_2}{\beta_1}\right)H_1(p)(1 - H_2(p))}\right]\theta_1 + \left[\frac{H_1(p)\left(\frac{\beta_2}{\beta_1}\right)(1 - H_2(p))}{1 + \left(\frac{\beta_2}{\beta_1}\right)H_1(p)(1 - H_2(p))}\right]\Delta\theta \tag{11}$$

Even for this assumption of totally correlated θ_1 and θ_2, the definition of loop bandwidth is not well defined since, in general, it depends on the value of $\Delta\theta$

If one makes the assumption that $\Delta\theta = 0$ (corresponding to the case of perfect delay compensation), then in accordance with Eq (7), the loop bandwidth would be given by

$$2B_{L1} = \frac{1}{2\pi j}\int_{-j\infty}^{j\infty}\left|\frac{H_1(s)\left[1 + \left(\frac{\beta_2}{\beta_1}\right)(1 - H_2(s))\right]}{1 + \left(\frac{\beta_2}{\beta_1}\right)H_1(s)(1 - H_2(s))}\right|^2 ds \tag{12}$$

For first-order loops, Eq (12) evaluates to

$$\begin{aligned} B_{L1} &= \frac{K_1'\left[\beta_1^2 K_2' + K_1'\beta_1(\beta_1 + \beta_2)^2\right]}{4\left(\beta_1 K_2' + K_1'\beta_1(\beta_1 + \beta_2)\right)} \\ K_i' &\triangleq K_i\sqrt{P} \end{aligned} \tag{13}$$

which for $K_2' << K_1'\beta_1$, i e , station 2's loop narrowband with respect to station 1's loop prior to arraying, simplifies to

$$B_{L1} = \frac{K_1\sqrt{P}\beta_1}{4}\left(1 + \frac{\beta_2}{\beta_1}\right) = (B_{L1})_0\left(1 + \frac{\beta_2}{\beta_1}\right) \tag{14a}$$

where $(B_{L1})_0 \triangleq K_1'\beta_1/4 = K_1\sqrt{P}\beta_1/4$ denotes the loop bandwidth of station 1's receiver prior to arraying (i e , with $\beta_2 = 0$)

For second-order loops with imperfect integrating loop filters $F_i(s) = (1 + s\tau_{2i})/(1 + s\tau_{1i})$, $i = 1, 2$, and the same assumption regarding station 2's loop being narrowband with respect to that of station 1 prior to arraying, Eq (12) evaluates to

$$B_{L1} = (B_{L1})_0 \left[\frac{1 + r_1 \left(1 + \dfrac{\beta_2}{\beta_1}\right)}{1 + r_1} \right] \tag{14b}$$

$$r_1 = \frac{\sqrt{P} K_1 \beta_1 \tau_{21}^2}{\tau_{11}}$$

Although not explicitly stated, the definition of loop bandwidth given in Eq (14) corresponding to $\Delta\theta = 0$ is the case assumed in [1] (compare Eq (14b) with Eq (23) of [1])

When $\Delta\theta \neq 0$ but constant, then one can argue that, under the assumption of station 2's loop being narrowband with respect to station 1's loop prior to arraying, the $1 - H_2(p)$ factor in the numerator of the second term in Eq (11) will for all practical purposes filter out the dc component due to $\Delta\theta$ Hence, the dynamics of the output, $\hat{\theta}_1$, are dominated by the input, θ_1, and to a first approximation the loop bandwidth after arraying would be the same as in the previous case where $\Delta\theta = 0$ was assumed In other situations, $\Delta\theta$ may not be constant, i e , θ_1 and θ_2 may not be totally correlated and, hence, the loop bandwidth will depend on the statistical properties of $\Delta\theta$

In summary then, the definition of loop bandwidth applied in a multiple input system such as a carrier-arrayed loop is dependent on the relation assumed among its inputs In what follows, we suggest an alternate basis for comparing arrayed and unarrayed performances that has the advantage that it does not depend on $\Delta\theta$, hence, one does not have to make any assumption regarding its statistical properties More generally, we suggest an alternate normalization of the problem wherein the relation between the other receiver inputs, $\theta_2, \theta_3, \quad , \theta_N$, and that corresponding to the receiver being arrayed, i e , θ_1, is inconsequential Before presenting this alternate formulation, we briefly review the performance comparison in terms of rms phase jitter made in [1] using the criterion of equal loop bandwidths prior to and after arraying, which *strictly speaking* is only proper when $\Delta\theta = 0$ This is done so that it can later be contrasted to the analogous performance comparison using the suggested alternate basis

IV. Evaluation of Phase Jitter Variance

Letting $\phi_1 \triangleq \theta_1 - \hat{\theta}_1$ denote the phase error in station 1's carrier-tracking loop, then it is straightforward to show that Eq (11) can be written in the form

$$\phi_1 = \left[\frac{1 - H_1(p)}{1 + \left(\dfrac{\beta_2}{\beta_1}\right) H_1(p)(1 - H_2(p))} \right] \theta_1 - \left[\frac{H_1(p) \left(\dfrac{\beta_2}{\beta_1}\right) (1 - H_2(p))}{1 + \left(\dfrac{\beta_2}{\beta_1}\right) H_1(p)(1 - H_2(p))} \right] \Delta\theta$$

$$- \left[\frac{H_1(p)}{1 + \left(\dfrac{\beta_2}{\beta_1}\right) H_1(p)(1 - H_2(p))} \right] \left(\frac{N_1}{\sqrt{p}}\right) - \left[\frac{H_1(p) \left(\dfrac{\beta_2}{\beta_1}\right) (1 - H_2(p))}{1 + \left(\dfrac{\beta_2}{\beta_1}\right) H_1(p)(1 - H_2(p))} \right] \left(\frac{N_2}{\sqrt{P}}\right) \tag{15}$$

Denoting variances of the Gaussian noise random variables by $\sigma_{N_i}^2 = N_{0i}/2, i = 1, 2$, then the variance of the phase jitter in station 1's carrier-tracking loop in the presence of arraying would be

$$\sigma_{\phi 1}^2 = \left(\frac{N_{01}}{2P}\right) \frac{1}{2\pi j} \int_{-j\infty}^{j\infty} \left| \frac{H_1(s)}{1 + \left(\frac{\beta_2}{\beta_1}\right) H_1(s)(1 - H_2(s))} \right|^2 ds$$

$$+ \left(\frac{N_{02}}{2P}\right) \frac{1}{2\pi j} \int_{-j\infty}^{j\infty} \left| \frac{H_1(s)\left(\frac{\beta_2}{\beta_1}\right)(1 - H_2(s))}{1 + \left(\frac{\beta_2}{\beta_1}\right) H_1(s)(1 - H_2(s))} \right|^2 ds \tag{16}$$

Evaluating Eq (16) for first-order loops gives

$$\sigma_{\phi 1}^2 = \left(\frac{N_{01}(B_{L1})_0}{P}\right) \left(\frac{\beta_1 + \frac{K_2'}{K_1'}}{\beta_1 + \beta_2 + \frac{K_2'}{K_1'}} \right) + \left(\frac{N_{02}(B_{L1})_0}{P}\right) \left[\left(\frac{\beta_2}{\beta_1}\right)^2 \left(\frac{\beta_1}{\beta_1 + \beta_2 + \frac{K_2'}{K_1'}} \right) \right] \tag{17}$$

which for $K_2' << K_1'\beta_1$ and $N_{01} = N_{02} = N_0$ simplifies to

$$\sigma_{\phi 1}^2 = \left(\frac{N_0(B_{L1})_0}{P}\right) \left(\frac{1 + \left(\frac{\beta_2}{\beta_1}\right)^2}{1 + \frac{\beta_2}{\beta_1}} \right) \tag{18}$$

If we now write Eq (18) in terms of the definition of loop bandwidth given in Eq (14a), then we obtain

$$\sigma_{\phi 1}^2 = \left(\frac{N_0 B_{L1}}{P}\right) \left(\frac{1 + \left(\frac{\beta_2}{\beta_1}\right)^2}{\left(1 + \frac{\beta_2}{\beta_1}\right)^2} \right) \tag{19}$$

If using this definition of loop bandwidth, we hold the loop bandwidth fixed prior to and after arraying, then since $\sigma_{\phi 1}^2 = N_0 B_{L1}/P$ represents the variance of the phase jitter prior to arraying, the arraying gain (loop SNR improvement factor) is given by

$$G \triangleq \frac{\left(1 + \frac{\beta_2}{\beta_1}\right)^2}{1 + \left(\frac{\beta_2}{\beta_1}\right)^2} \tag{20}$$

which when optimized with respect to the combining weight ratio β_2/β_1 yields $(\beta_2/\beta_1)_{opt} = 1$ and, hence, $G_{opt} = 2$, i e , *a 3-dB gain!* This result is what would be predicted by the results in [1] if two first-order loops and equal power-to-noise ratios at both antennas, i e , $P_1/N_{01} = P_2/N_{02} \triangleq P/N_0$ were assumed Also, in order to realize the gain predicted by Eq (20), i e , to hold the loop bandwidth fixed, station 1's total loop gain, K_1', must be renormalized (divided by) the factor $1 + \beta_2/\beta_1$, which, for the optimum design, implies division of K_1' by a factor of 2 This can be accomplished by including a 1/2 gain factor in series with the loop filter $F_1(s)$

V. Computation of Arraying Gain Based on Fixed Steady-State Phase Error

It is well known that when a frequency offset exists in the received signal to a carrier-tracking loop, then a steady-state phase error, ϕ_{ss}, will exist If the loop input phase is modeled as $\theta(t) = \theta + \Omega t$, then for a first-order loop, ϕ_{ss} is given by

$$\phi_{ss} = \frac{\Omega}{K\sqrt{p}} = \frac{\Omega}{4B_L} \tag{21}$$

whereas for a second-order loop with imperfect integrating loop filter $F(s) = (1 + s\tau_2)/(1 + s\tau_1)$, the result is

$$\phi_{ss} = \frac{\Omega}{r\tau_1/\tau_2^2} \cong \frac{\Omega}{r\tau_1/\tau_2}\left(\frac{r+1}{4B_L}\right) \tag{22}$$

where the approximation is in the same sense as that used in Eq (9) Since from Eq (21) or Eq (22) we see that ϕ_{ss} is inversely proportional to B_L, then for the carrier-arraying application, keeping ϕ_{ss} fixed prior to and after arraying can be construed as maintaining a fixed-loop bandwidth The importance of this normalization in terms of fixed ϕ_{ss} is that, as we shall soon see, the value of ϕ_{ss} in station 1's carrier-tracking loop is unaffected by the presence of the arraying, provided that the same frequency offset is present at the input of the other receivers, e g , for the two-antenna case, assuming as before that the inputs to the two antennas only differ by a fixed delay $(\theta_2 - \theta_1 = \Delta\theta)$

Setting N_1 and N_2 equal to zero in Eq (15), we have

$$\begin{aligned}\phi_{ss_1} &= \lim_{t\to\infty}\phi_1(t) = \lim_{s\to 0} s\Phi_1(s) \\ &= \lim_{s\to 0}\left[\frac{s(1 - H_1(s))}{1 + \left(\frac{\beta_2}{\beta_1}\right)H_1(s)(1 - H_2(s))}\right]\left(\frac{\theta_1}{s} + \frac{\Omega_1}{s^2}\right) - \lim_{s\to 0}\left[\frac{sH_1(s)\left(\frac{\beta_2}{\beta_1}\right)(1 - H_2(s))}{1 + \left(\frac{\beta_2}{\beta_1}\right)H_1(s)(1 - H_2(s))}\right]\left(\frac{\Delta\theta}{s}\right)\end{aligned} \tag{23}$$

For first-order loops, Eq (23) becomes

$$\phi_{ss_1} = \lim_{s\to 0}\left[\frac{s^2(s+K_2')}{s^2+s\left[K_1'\beta_1\left(1+\frac{\beta_2}{\beta_1}\right)+K_2'\right]+K_1'\beta_1K_2'}\right]\left(\frac{\theta_1}{s}+\frac{\Omega_1}{s^2}\right)$$

$$-\lim_{s\to 0}\left[\frac{\left(\frac{\beta_2}{\beta_1}\right)s^2K_1'\beta_1}{s^2+s\left[K_1'\beta_1\left(1+\frac{\beta_2}{\beta_1}\right)+K_2'\right]+K_1'\beta_1K_2'}\right]\left(\frac{\Delta\theta}{s}\right)=\frac{\Omega}{K_1'\beta_1}=\frac{\Omega}{K_1\sqrt{P}\beta_1}=\frac{\Omega}{4(B_{L1})_0} \tag{24}$$

independent of $\Delta\theta$ *and* β_2 Thus, as previously predicted, the steady-state error in station 1's carrier-tracking loop is unchanged when carrier arraying is added to the receiver A similar conclusion is reached for second-order loops, namely, the steady-state phase error in station 1's carrier-tracking loop, with or without arraying, is given by [see Eq (22)]

$$\phi_{ss_1}=\frac{\Omega_1}{r_1\tau_{11}/\tau_{21}^2}\cong\frac{\Omega}{r_1\tau_{11}/\tau_{21}}\left(\frac{r_1+1}{4(B_{L1})_0}\right) \tag{25}$$

The upshot of the above is that in order to maintain a fixed steady-state phase error when carrier arraying is employed in a receiver, *the total loop gain should not be renormalized at all!* Hence, the phase jitter variance is given by Eq (18) with no renormalization of the loop bandwidth and, thus, the arraying gain using fixed ϕ_{ss_1} as a basis of comparison with the unarrayed case is

$$G\triangleq\frac{\left(1+\frac{\beta_2}{\beta_1}\right)}{1+\left(\frac{\beta_2}{\beta_1}\right)^2} \tag{26}$$

which when optimized with respect to β_2/β_1 yields $(\beta_2/\beta_1)_{opt}=\sqrt{2}-1=0\ 414$ and, hence, $G_{opt}=1\ 207$, i e , *only a 0 82-dB gain!* This result has been confirmed by computer simulation

VI. Conclusions

What has been shown here is that, depending on the basis used for comparison, it is possible to predict different gains when applying carrier arraying to a conventional coherent receiver Thus, it is concluded that one should exercise caution when attempting to compare the performance of a coherent receiver before and after carrier arraying in that one should have a complete knowledge of the relative phase and frequency conditions of the signals being received at the various antenna inputs

Acknowledgments

The author would like to acknowledge Sami Hinedi, Biren Shah, and Bill Hurd for many useful discussions related to an understanding of the subject of carrier arraying Also, the author would like to further acknowledge Biren Shah for computer simulation support in verifying all of the above analytically obtained results

References

[1] D Divsalar and J H Yuen, "Improved Carrier Tracking Performance With Coupled Phase-Locked Loops," *The Telecommunications and Data Acquisition Progress Report 42-66, September–October 1981*, Jet Propulsion Laboratory, Pasadena, California, pp 148–171, December 15, 1981

[2] W C Lindsey, *Synchronization Systems in Communication and Control*, Englewood Cliffs, New Jersey Prentice-Hall, Inc , 1972

Estimating Errors in Least-Squares Fitting

P H Richter
Communications Systems and Research Section

While least-squares fitting procedures are commonly used in data analysis and are extensively discussed in the literature devoted to this subject, the proper assessment of errors resulting from such fits has received relatively little attention The present work considers statistical errors in the fitted parameters, as well as in the values of the fitted function itself, resulting from random errors in the data Expressions are derived for the standard error of the fit, as a function of the independent variable, for the general nonlinear and linear fitting problems Additionally, closed-form expressions are derived for some examples commonly encountered in the scientific and engineering fields, namely, ordinary polynomial and Gaussian fitting functions These results have direct application to the assessment of antenna gain and system temperature characteristics, in addition to a broad range of problems in data analysis The effects of the nature of the data and the choice of fitting function on the ability to accurately model the system under study are discussed, and some general rules are deduced to assist workers intent on maximizing the amount of information obtained from a given set of measurements

I. Summary

The fitting of data of the form $(x_i, y_i), i = 1, 2, \quad , N$ by a function $y(x, a_1, \quad , a_M) \equiv y(x, \mathbf{a})$, depending on M coefficients, a_j, and the independent variable x, is common in scientific and engineering work The procedure most often used for optimizing the coefficients in order to obtain the best fit is the least-squares method, in which the quantity

$$\chi^2(\mathbf{a}) = \sum_{i=1}^{N} \frac{[y_i - y(x_i, \mathbf{a})]^2}{\sigma_i^2}$$

is minimized, where σ_i is the standard deviation of the random errors of y_i, which we assume to be normally distributed

The result of such a fitting procedure is the function $y(x, \mathbf{a}_0)$, where $\mathbf{a}_0$ is the coefficient vector that minimizes $\chi^2(\mathbf{a})$, and the question arises as to what standard error to associate with the values of this resulting fit Standard references on statistics and data analysis give the well-known result that the variances of the coefficients, a_j, are given by the diagonal elements of the covariance matrix, $\mathbf{C}$, i e , $\sigma_{a_j}^2 = C_{jj}$, where $\mathbf{C}$ is the inverse of the matrix $\mathbf{H}$, variously referred to as the curvature or Hessian matrix While it is often useful to know what the parameter errors are, especially if the parameters

themselves are related to some underlying physical model of the process under study, this does not tell one directly what the error is in the values of the fitting function itself, and a knowledge of this error, which is a function of the independent variable, is frequently of value in characterizing the system performance

Lacking a general discussion of this in the literature, it seems that various workers assume a mean error equal to either the rms value of the data errors or $1/\sqrt{N}$ times this It is shown in the present work, however, that for the general least-squares fit, the weighted mean value of the variance of the fit, averaged over the data points $x = x_i$, is given by

$$\frac{1}{N}\sum_{i=1}^{N}\frac{\sigma_y^2(x_i)}{\sigma_i^2} = \frac{M}{N}$$

so that for constant data errors,

$$\overline{\sigma_y^2} = \frac{1}{N}\sum_{i=1}^{N}\sigma_y^2(x_i) = \frac{M}{N}\sigma^2$$

Thus, the mean standard error depends on the order of the fit, increasing as the square root of this value

The error in the value of the fitted function, however, always depends on x, even when the standard deviations of the data errors, σ_i, are all the same, independent of x An analysis of these errors leads to the general result that the variance of the value of the fitted function, resulting from the random data errors, is given by

$$\sigma_y^2(x) = \sum_{j=1}^{M}\sum_{k=1}^{M} C_{jk}d_j(x)d_k(x) = \mathbf{d}(x)^T\mathbf{C}\ \mathbf{d}(x)$$

where $[\mathbf{d}(x)]_j \equiv d_j(x) = [\partial y(x,\mathbf{a})/\partial a_j]|_{\mathbf{a}_0}$ and T implies matrix transpose For the special case of linear fitting, where $y(x,\mathbf{a}) = \sum_{j=1}^{M} a_j X_j(x)$, this becomes

$$\sigma_y^2(x) = \sum_{j=1}^{M}\sum_{k=1}^{M} C_{jk}X_j(x)X_k(x) = \mathbf{x}(x)^T\mathbf{C}\ \mathbf{x}(x)$$

where $\mathbf{x}(x)$ is a column vector whose elements are $X_j(x)$ An example of the application of this result to a set of antenna aperture efficiency versus elevation data is shown in Figs 1 through 4

For the important class of basis functions corresponding to ordinary polynomials, $X_j(x) = x^{j-1}$, it is shown that if the data are uniformly distributed along the x-axis and the data standard errors are constant, $\sigma_i = \sigma$, then simple, closed-form expressions can be derived for $\sigma_y^2(x)$ Thus, we find

$$\eta^2 = \sum_{j=0}^{M-1} A_{2j}^{(M-1)}(N)\xi^{2j}$$

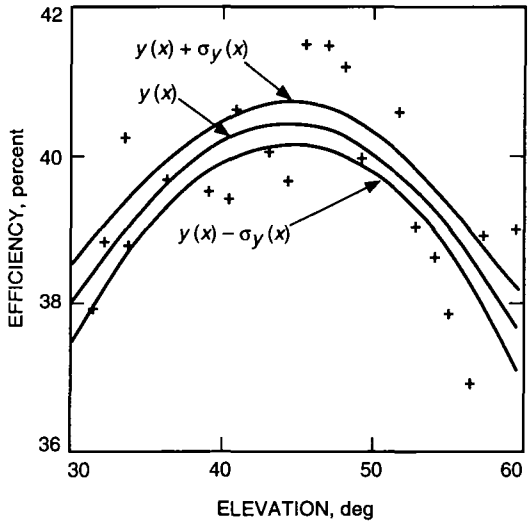

Fig. 1 Quadratic fit to antenna aperture efficiency versus elevation data showing the confidence limits corresponding to 68 3 percent ($\pm\sigma_y(x)$) The data standard errors were constant and equal to 0 91 efficiency percent, and the computed reduced χ^2 was 1 06

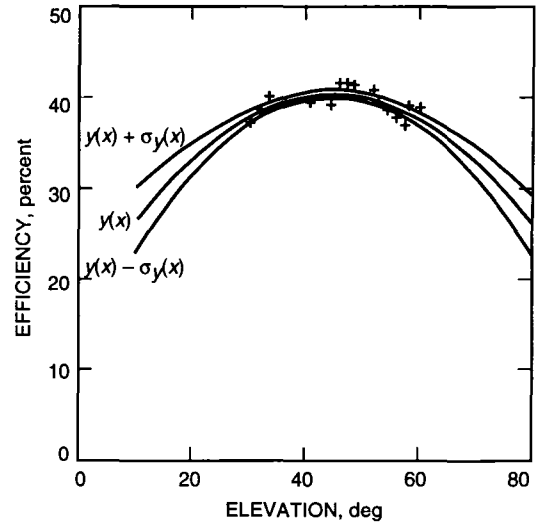

Fig 2 The same as Fig 1 except the fit and limits are extended beyond the existing data to illustrate the effect of the rapid increase in the error of the fit

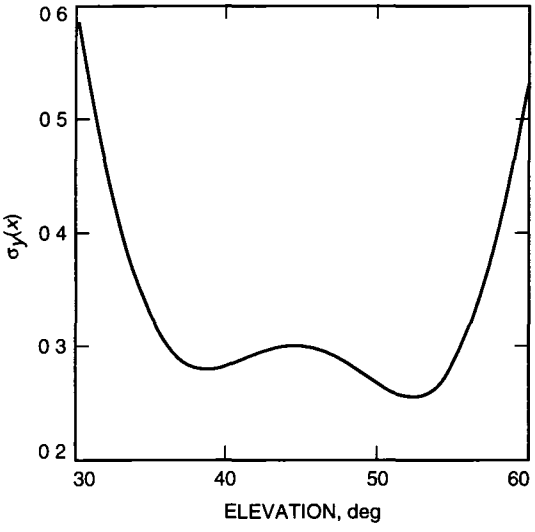

Fig 3 The standard error of the fit corresponding to Fig 1 for the range of elevation over which the data exist

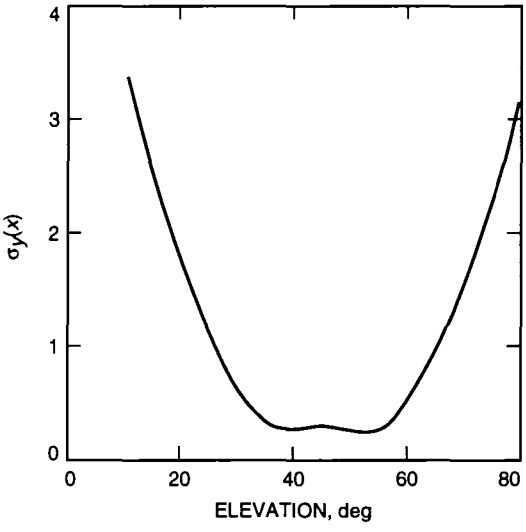

Fig 4 The same as Fig 3 except the range of elevation is extended beyond the existing data

where $\eta = \sqrt{N}([\sigma_y(x)]/\sigma)$, $\xi = [(x-\overline{x})/\sigma_x]$, $\overline{x} = (1/N)\sum_{i=1}^{N} x_i$, $\sigma_x^2 = (1/N)\sum_{i=1}^{N} x_i^2 - (1/N^2)(\sum_{i=1}^{N} x_i)^2$, and the coefficients $A_{2j}^{(M-1)}N$ are listed in Table 1 for the cases $M = 2, 3, 4$, corresponding to straight-line, quadratic, and cubic fits For the straight-line fit, the coefficients appearing in the above expression are independent of the number of data points, N, while for the quadratic and cubic cases they become independent for reasonable values of N, say, $N > 10$ These results are summarized graphically with the set of universal error curves shown in Fig 5

Table 1 The coefficients in the equation for the squared normalized standard error of the fit for straight-line, quadratic, and cubic fits [a]

$M-1$	A_0	A_2	A_4	A_6
1	1	1	0	0
2	$\frac{3(3N^2-7)}{4(N^2-4)}$ $\left[\frac{9}{4}\right]$	$-\frac{6(N^2+1)}{4(N^2-4)}$ $\left[-\frac{3}{2}\right]$	$\frac{5(N^2-1)}{4(N^2-4)}$ $\left[\frac{5}{4}\right]$	0
3	$\frac{3(3N^2-7)}{4(N^2-4)}$ $\left[\frac{9}{4}\right]$	$\frac{5}{12}\,\frac{9N^4-12N^2-61}{(N^2-4)(N^2-9)}$ $\left[\frac{15}{4}\right]$	$-\frac{5}{36}\,\frac{33N^4-23N^2-226}{(N^2-4)(N^2-9)}$ $\left[-\frac{55}{12}\right]$	$\frac{175}{108}\,\frac{(N^2-1)^2}{(N^2-4)(N^2-9)}$ $\left[\frac{175}{108}\right]$

[a] The values for $N \to \infty$ are shown in brackets

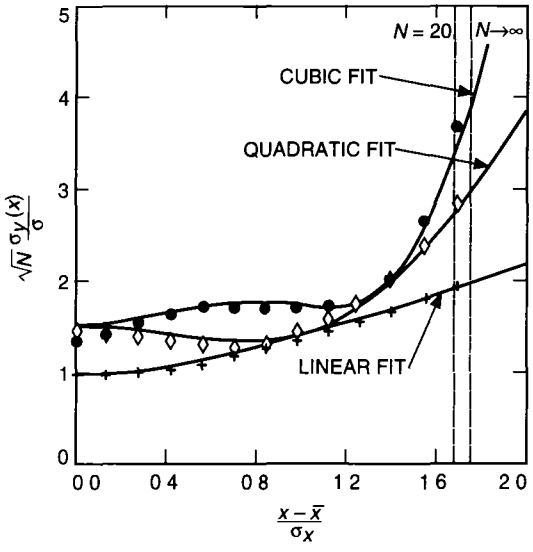

Fig 5 Universal, normalized error curves for straight-line, quadratic, and cubic fits for constant, normally distributed data errors, $\sigma_i = \sigma$, with N uniformly distributed data points The symbols associated with each curve correspond to the results of Monte Carlo calculations carried out as a check (see Appendix for details)

As an example of a similar development for nonlinear fitting, the case of a Gaussian function given by

$$y(x, \mathbf{a}) = a_1 \exp\left[\frac{-(x-a_2)^2}{2a_3^2}\right]$$

is treated exactly, and it is shown that for uniformly distributed data points located symmetrically relative to the peak, and constant data errors,

$$\eta^2 = \sqrt{\frac{3}{\pi}}\sigma_t e^{-(\xi\sigma_t)^2}\left(3 + 4\sigma_t^4\xi^4\right)$$

where $\sigma_t = (\sigma_x/a_3)$, while if the data errors are proportional to the value of the function, $\sigma(x) \propto y(x, \mathbf{a})$, one finds

$$\eta^2 = N\left[\frac{\sigma_y(x)}{\sigma(x)}\right]^2 = \frac{9}{4} - \frac{3}{2}\xi^2 + \frac{5}{4}\xi^4$$

where in both cases it is assumed that the number of data points, N, is reasonably large, of the order of 20 or more, and in the former case, it is also assumed that the spread of the data points, L, is greater than about $\pm 2a_3$ These results are shown graphically in Figs 6 and 7

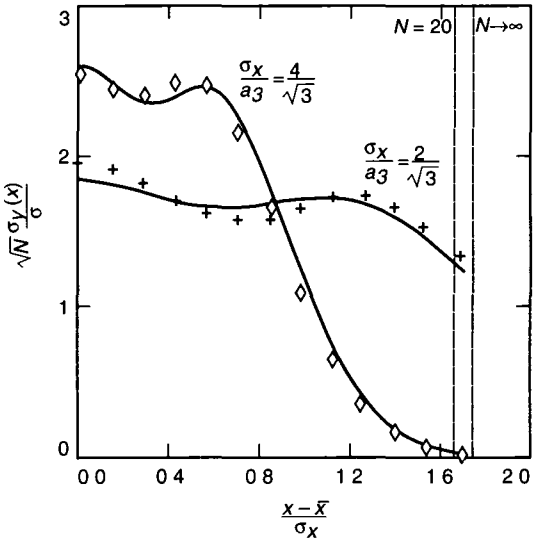

Fig 6 Universal, normalized error curves for the general Gaussian function $y(x,a) = a_1 \exp[-(x-a_2)^2/2a_3]$ for constant, normally distributed data errors, $\sigma_i = \sigma$, with N uniformly distributed data points centered on the peak of the Gaussian The symbols associated with each curve correspond to the results of Monte Carlo calculations carried out as a check (see Appendix for details)

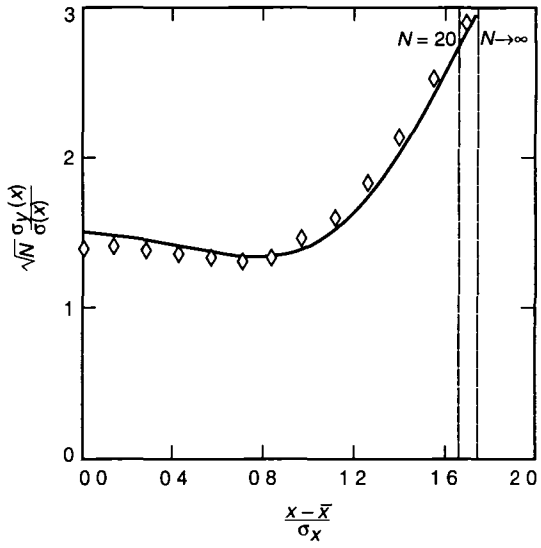

Fig 7 The same as Fig 6 except that the data errors are now proportional to the function, $\sigma_i = \sigma(x_i) \propto y(x_i;a)$ The symbols associated with each curve correspond to the results of Monte Carlo calculations carried out as a check (see Appendix for details)

Another important aspect of the general least-squares fitting problem is the optimization of the sampling during the taking of data, e g , what spacing should one use along the x-axis and how many points should one use in order to reduce the parameter errors to acceptable levels? Since the parameter errors for the case of polynomial fits depend sensitively on the location of the origin of the x-scale, and in any event the coefficients themselves are unlikely to have a fundamental significance in terms of an underlying physical model of the process under study, we restrict ourselves to a consideration of Gaussian fits as an example of some practical importance

Thus, for uniformly and symmetrically distributed data points, we find the following For constant data errors $\sigma_i = \sigma$,

$$N\frac{\sigma_{a_1}^2}{\sigma^2} = \frac{NS_4}{(2S_0+1)S_4 - 2S_2^2}$$

$$N\frac{(\sigma_{a_2}/a_3)^2}{(\sigma/a_1)^2} = \frac{1}{2}\frac{N}{\delta_t^2 S_2}$$

$$N\frac{(\sigma_{a_3}/a_3)^2}{(\sigma/a_1)^2} = \frac{1}{2}\frac{N(2S_0+1)}{\delta_t^4[(2S_0+1) - 2S_2^2]}$$

where the sums S_0, S_2, and S_4 are given by Eq (A-7) of the Appendix and $\delta_t^2 = [12/(N^2-1)](\sigma_x^2/a_3^2) = [12/(N^2-1)]\sigma_t^2$ The normalized errors $\sqrt{N}(\sigma_{a_1}/\sigma)$, $\sqrt{N}[(\sigma_{a_2}/a_3)/(\sigma/a_1)]$, and $\sqrt{N}[(\sigma_{a_3}/a_3)/(\sigma/a_1)]$ are plotted as functions of the variable L/a_3 for selected values of the number of data points, N, in Fig 8 In the limit $N \to \infty$ and $L/a_3 \geq 4$, the above normalized standard errors become

$$N\frac{\sigma_{a_1}^2}{\sigma^2} = \frac{3}{2\sqrt{\pi}}\frac{L}{a_3}$$

$$N\frac{(\sigma_{a_2}/a_3)^2}{(\sigma/a_1)^2} = \frac{2}{\sqrt{\pi}}\frac{L}{a_3}$$

$$N\frac{(\sigma_{a_3}/a_3)^2}{(\sigma/a_1)^2} = \frac{2}{\sqrt{\pi}}\frac{L}{a_3}$$

For data errors proportional to the function, $\sigma_i = \beta y(x, \mathbf{a})$,

$$N\frac{\sigma_{a_1}^2}{a_1^2} = \beta^2 A_0^{(2)}(N) = \beta^2\frac{3(3N^2-7)}{4(N^2-4)} \to \frac{9}{4}\beta^2$$

as $N \to \infty$,

$$N\frac{\sigma_{a_2}^2}{a_3^2} = \frac{\beta^2}{\sigma_t^2}$$

independent of N, and

$$N\frac{\sigma_{a_2}^2}{a_3^2} = \frac{\beta^2}{\sigma_t^4}A_4^{(2)}(N) = \frac{\beta^2}{\sigma_t^4}\frac{5(N^2-1)}{4(N^2-4)} \to \frac{5}{4}\frac{\beta^2}{\sigma_t^4}$$

as $N \to \infty$

II. Introduction

If one measures a single quantity N times in the presence of normally distributed, random errors, then it is well known that the variance of the mean of these measurements is equal to the variance of the measurements themselves divided by N, and in the absence of systematic errors, the mean value approaches the true value of the quantity as the number of measurements increases without limit

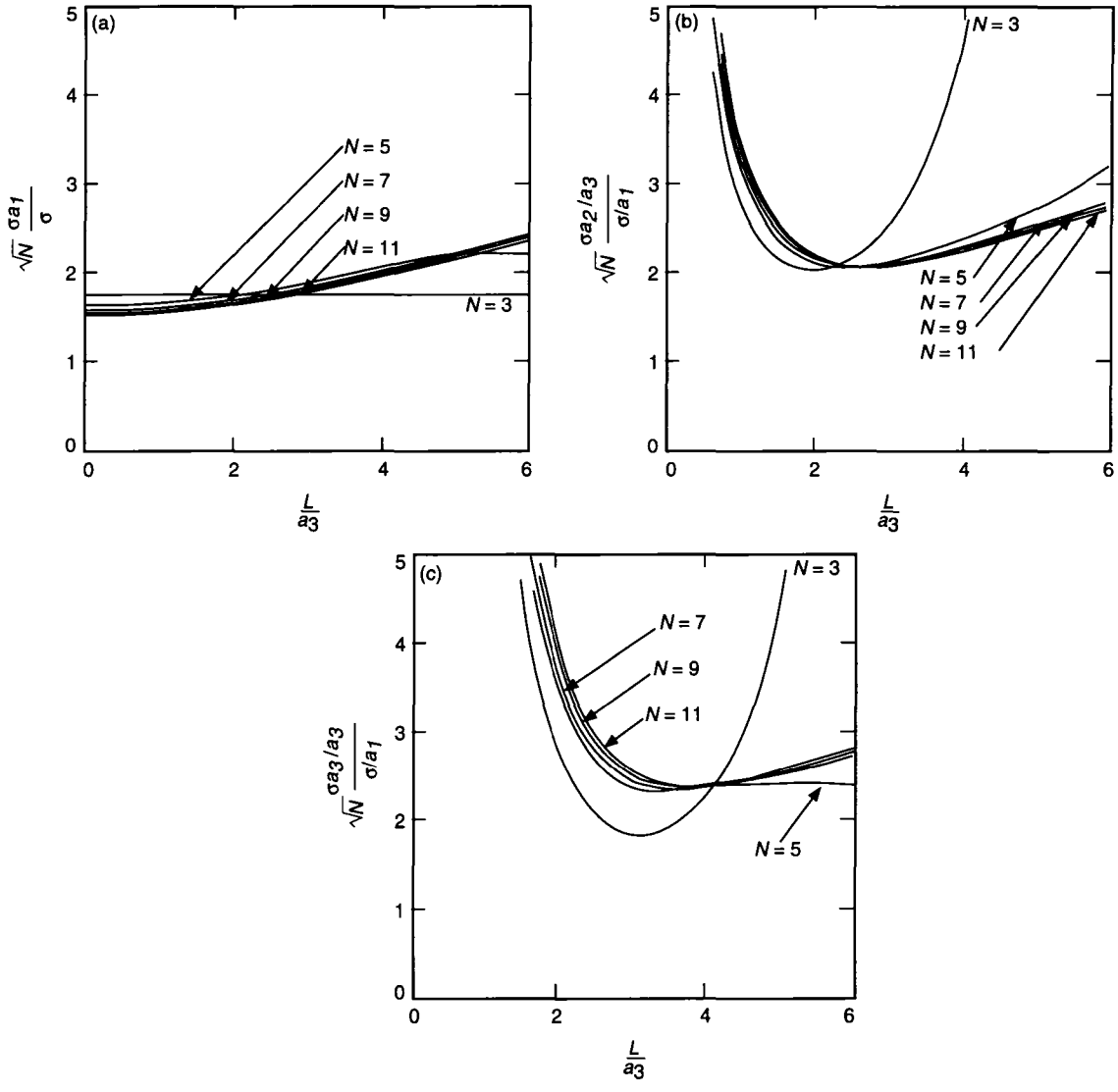

Fig 8 Universal, normalized error curves for the three parameters of a Gaussian fit for constant data errors, $\sigma_i = \sigma$, as a function of the normalized x-axis interval L/a_3 for various values of the number of data points, N (a) a_1, (b) a_2, and (c) a_3

In the case of least-squares fitting of a given function to a given set of data that are likewise subject to normally distributed, random errors, the resulting fit is the mean function corresponding to the data, and the question arises as to what variance to assign to the errors of the values of this function Here, two related concerns arise First, the fitting function will contain a certain number of parameters, M, and one or more of these may be of interest in relation to a physical quantity whose value is sought For example, system noise temperatures may have been recorded as an antenna is scanned through a point source of radiation, and one may be interested in the peak value or the half-width of the antenna pattern or both Or, one may have determined a series of system noise temperatures at different elevations and wish to know what the maximum system noise temperature is and at what elevation it occurs In each case, an appropriate fitting function could be chosen so that one or more of the parameters involved corresponds to the quantity or quantities of interest, and one would like to know, therefore, what standard error to assign to the quantities so determined Alternatively, one may want to know what the standard error is

as a function of the independent variable, say declination or elevation in the two examples cited above In the remainder of this article, we will refer to this standard error of the value of the fitted function as the error of the fit and designate it by the symbol $\sigma_y(x)$

The first instance considered above, namely, determining the error of one or more fitting parameters, has a straightforward answer given in terms of the diagonal elements of the covariance matrix of the fit, and is well known Less well known, however, particularly among nonmathematicians, is the relationship between this matrix and the error of the fit as a function of the independent variable Some insight into this problem can be obtained by examining Fig 9, where we show the results of sequentially fitting straight lines to a series of data sets generated by the same linear function, $y = a_1 + a_2 x$, but with different random errors, corresponding, however, to the same normal distribution, i e , having the same constant standard deviation, σ Since each of these lines could have resulted from the same underlying function, albeit with different probability, the ensemble of all possible lines defines the error statistics of the particular fit actually obtained with the particular set of errors present during the data gathering, i e , the data errors actually obtained correspond to but one of the infinite number of sets that could have resulted from the measurements In the case shown in Fig 9, one can see that the error of the fit tends to be smaller toward the centroid of the data points and larger at the extremes In fact, it is shown below that the error curve in this case is actually a hyperbola and that the same general behavior is found for higher-degree polynomials, albeit with differing functional dependence The standard error of the fit, $\sigma_y(x)$, derived below is shown superimposed on the ensemble of straight lines in Fig 9

It is the purpose of this article to discuss the above errors and, in particular, to present results that will permit one to determine the standard error of the fit as a function of the independent variable, as well as to establish confidence limits for these errors

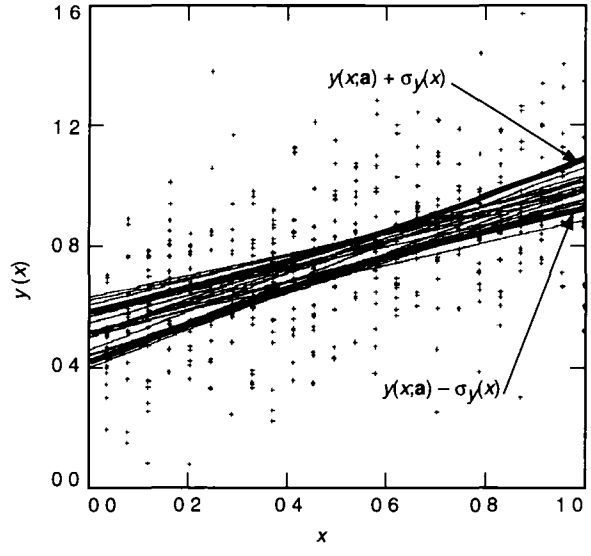

Fig 9 Plot of 20 straight lines resulting from fits to data generated from the same parent straight line but with different random, normally distributed errors having the same statistics

III. Least-Squares Fitting

The fitting of data of the form $(x_i, y_i), i = 1, 2, \quad , N$ by a function $y(x, a_1, \quad , a_M) \equiv y(x, \mathbf{a})$ depending on M coefficients, a_j, and the independent variable x is frequently used in scientific and engineering

work, either to determine the most likely values of the fitting coefficients, which may relate to some physically reasonable model of the process under study, or simply to permit the prediction of the most likely value of the dependent variable y for a given value of x, including those values where no data exist

While many techniques for finding optimum values of the fitting coefficients exist, the one most commonly used is the least-squares method, where the coefficients are determined by minimizing the quantity χ^2, given by

$$\chi^2(\mathbf{a}) \equiv \sum_{i=1}^{N} \frac{[y_i - y(x_i, \mathbf{a})]^2}{\sigma_i^2} \tag{1}$$

The variances σ_i^2 of the data values y_i are assumed known, either from a knowledge of the experimental errors involved in the measurements or from analysis of the data itself, and it is assumed that the errors themselves are normally distributed While this latter requirement is not essential for the derivations that follow, it is nonetheless a common assumption, valid for most measurements, and permits one to establish confidence limits, as discussed below

This approach, also called the method of maximum likelihood, is described in numerous publications and is the basis of many curve-fitting programs available in various software packages devoted to data analysis However, in spite of its widespread use, there are a number of aspects of the least-squares fitting problem that are not often discussed in the literature on the subject, especially those having to do with the proper evaluation and interpretation of errors In the following section, the general linear, least-squares problem, in which the fitting coefficients a_j enter into the fitting function $y(x, \mathbf{a})$ in a linear manner, is formulated, and the solution for the coefficients is obtained The purpose here is to establish the notation and display the main results, rather than to provide a detailed derivation [1] This is followed by an analysis of standard errors for the various quantities encountered and a section devoted to illustration of the main ideas through consideration of some simple examples Next, the general nonlinear, least-squares fitting problem, in which the coefficients a_j enter into the fitting function $y(x, \mathbf{a})$ in a nonlinear way, is discussed, and the standard errors once again analyzed Two final sections provide a discussion of a related problem involving errors of the difference between a function at two values of the argument and a general discussion of the significance of the results

IV. The Linear Least-Squares Problem

For the linear, least-squares problem, the fitting function $y(x, \mathbf{a})$ may be written

$$y(x, \mathbf{a}) \equiv \sum_{j=1}^{M} a_j X_j(x) \tag{2}$$

where $X_j(x)$ are arbitrary basis functions of the independent variable, x, and the M coefficients, a_j, are to be determined by minimizing χ^2, as given by Eq (1) This problem is most often framed in the language of linear algebra, where the fitting function $y(x_i, \mathbf{a})$ is taken as an N-element column vector, the coefficients a_j as an M-element column vector, and the basis functions $X_j(x_i)$ are represented by an $N \times M$ matrix X_{ij}, so that letting $x = x_i$, Eq (2) may be written

$$y(x_i, \mathbf{a}) = \sum_{j=1}^{M} X_{ij} a_j, \quad i = 1, 2, \quad , N$$

[1] The latter may be found in numerous sources, such as [1], which has been used as a guide to define the notation

or, in the matrix equation form, $\mathbf{y} = \mathbf{Xa}$

Similarly, by defining the column vector $b_i \equiv (y_i/\sigma_i)$ and the matrix $A_{ij} \equiv (X_{ij}/\sigma_i)$, Eq (1) may be written

$$\chi^2 = (\mathbf{b} - \mathbf{Aa})^T(\mathbf{b} - \mathbf{Aa}) \tag{3}$$

where T implies matrix transpose Thus, the extremum condition for the coefficients,

$$\frac{\partial}{\partial a_j}(\chi^2) = 0$$

results in the matrix equation

$$(\mathbf{A}^T\mathbf{A})\,\mathbf{a} = \mathbf{A}^T\mathbf{b}$$

having the solution

$$\mathbf{a} = \left(\mathbf{A}^T\mathbf{A}\right)^{-1}\mathbf{A}^T\mathbf{b} = \mathbf{C}\mathbf{A}^T\mathbf{b} \tag{4a}$$

In the above, we have defined the matrix, $\mathbf{H} \equiv \mathbf{A}^T\mathbf{A}$, and its inverse, $\mathbf{C}$ The symmetric $M \times M$ matrix $\mathbf{C} = \mathbf{H}^{-1}$ is called the covariance matrix and is central to the determination of standard errors, as discussed below In component form, Eq (4a) may be written

$$a_j = a_j(y_1, \quad , y_N) = \sum_{k=1}^{M} C_{jk} \sum_{i=1}^{N} y_i \frac{X_k(x_i)}{\sigma_i^2} \tag{4b}$$

where the dependence of the coefficients on the measured data has been made explicit in the notation

Before proceeding with a discussion of errors and their evaluation, the question of the suitability of the set of basis functions chosen at the outset should be addressed It is shown in various treatises on statistics and data analysis that the resulting fit to the function $y(x, \mathbf{a})$ is meaningful if χ^2, as given by Eq (1), is of the order of $N - M \equiv \nu$, referred to as the number of degrees of freedom for the system [2] Since the quantity χ^2 should be reasonably close to ν for a good fit, the related quantity $\chi_\nu \equiv \chi/\nu$, called the reduced χ^2, is often used as a measure of the suitability of the chosen basis functions for fitting to the given data, i e , the condition $\chi_\nu^2 \approx 1$ is taken to indicate that the fit is meaningful For $\nu >> 1$, χ^2, and hence the reduced χ^2, is normally distributed, with the latter having a mean of 1 and a standard deviation of $\sqrt{2/\nu}$

Figure 10 illustrates the significance of the quantity χ_ν^2 for the simple case of a polynomial fit In Fig 10(a), the data clearly show a quadratic dependence on the independent variable, but an attempt has been made to obtain a fit with a straight line The formal application of Eq (4a) results in the computation of two coefficients for the line, but since at least three coefficients are obviously required to give a reasonable fit to the given data, these coefficients are meaningless, both in terms of providing a decent fit and in terms of the model used to represent the data, and this is manifest in the large value of χ_ν^2 resulting from the fit On the other hand, increasing the degree of the polynomial to 2 by adding a quadratic term results in a much more reasonable-looking fit and a value of χ_ν^2 close to 1

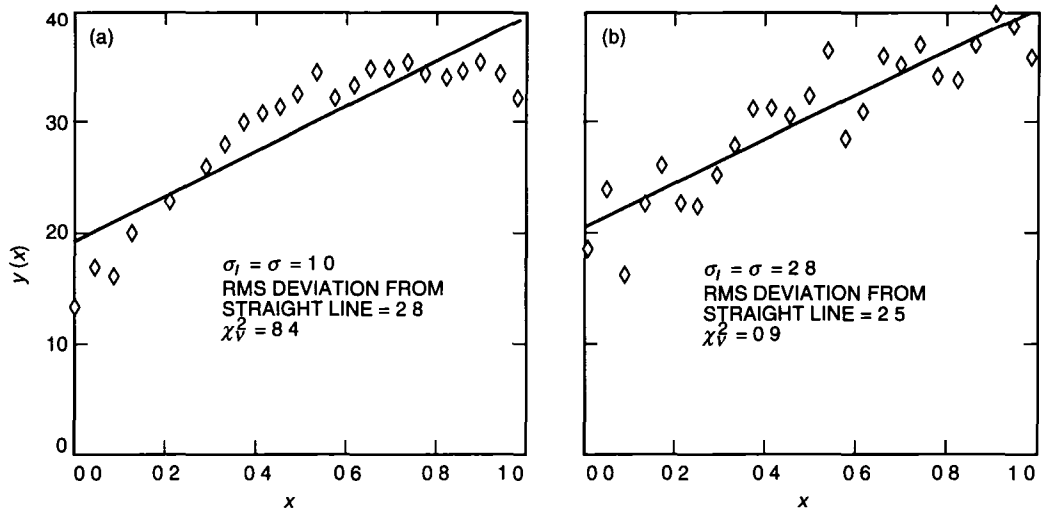

Fig 10 The significance of the quantity χ^2_ν for a polynomial fit (a) a straight-line fit to data having a quadratic dependence on the independent variable, illustrating the increase in χ^2_ν resulting from a poor fit to the data, and (b) a straight-line fit to straight-line data In each case, the constant standard deviation of the data errors, σ, is relative to the parent curve, a quadratic for Fig 10(a) and a straight line for Fig 10(b) (see Section IV for discussion)

It must be pointed out, however, that the value of χ^2_ν that one obtains with a given fitting function depends not only on the suitability of the function chosen but also on the values of the data errors assumed, as is evident from the definition given by Eq (1) Thus, in Fig 10(b), where a straight-line fit has been obtained for straight-line data, an accurate knowledge of the data errors, σ_i, leads to a reduced χ^2 of 0 9 However, had the data errors in Fig 10(a) been overestimated, as could result with an overly cautious experimenter, for example, then the calculated χ^2_ν would be smaller than it should be, so that one might end up with a value close to 1 as the result of a relatively poor fit and excessively large σ_i's This points up the importance of properly assessing the data errors, a subject we will return to in a later section

V. Standard Errors

Since the coefficient values a_j depend on the data values y_i, as given by Eq (4b), or its matrix equivalent, Eq (4a), the uncertainties in the coefficients depend on the uncertainties in the data values Thus,

$$\delta a_j = \sum_{i=1}^{N} \frac{\partial a_j}{\partial y_i} \delta y_i = \sum_{i=1}^{N} \sum_{k=1}^{M} C_{jk} \frac{X_k(x_i)}{\sigma_i^2} \delta y_i$$

or, in matrix form,

$$\delta \mathbf{a} = \mathbf{C}\mathbf{A}^T \delta \mathbf{b}$$

so that the covariance of a_j and a_k is given by

$$\sigma^2_{\mathbf{a}_{jk}} \equiv \langle \delta a_j \delta a_k \rangle = \sum_{n=1}^{M} \sum_{m=1}^{M} C_{jn} C_{km} \sum_{i=1}^{N} \frac{X_n(x_i)}{\sigma_i^2} \sum_{l=1}^{N} \frac{X_m(x_l)}{\sigma_l^2} \langle \delta y_i \delta y_l \rangle \tag{5a}$$

where $\langle\ \rangle$ indicates an ensemble average, giving the expectation value of the quantity in parenthesis In matrix form,

$$\sigma_{\mathbf{a}}^2 \equiv \left\langle \delta\mathbf{a}\delta\mathbf{a}^T \right\rangle = \left\langle \mathbf{C}\left(\mathbf{A}^T\delta\mathbf{b}\right)\left(\mathbf{A}^T\delta\mathbf{b}\right)^T\mathbf{C}^T \right\rangle = \mathbf{C}\mathbf{A}^T\left\langle \delta\mathbf{b}\delta\mathbf{b}^T \right\rangle \mathbf{A}\mathbf{C}^T \tag{5b}$$

where use has been made of the relation $(\mathbf{A}^T\delta\mathbf{b})^T = \delta\mathbf{b}^T\mathbf{A}$ Since the data errors δy_i are assumed to be statistically uncorrelated, $\langle \delta y_i \delta y_l \rangle = \delta_{il}\sigma_i^2$, where δ_{il} is the Kronecker delta

Thus, $\langle \delta\mathbf{b}\delta\mathbf{b}^T \rangle = \mathbf{I}$, the identity matrix, so that Eq (5b) becomes

$$\sigma_{\mathbf{a}}^2 = \mathbf{C}(\mathbf{A}^T\mathbf{A})\mathbf{C}^T = \mathbf{C} \tag{6a}$$

where the definition of the matrix $\mathbf{C} = (\mathbf{A}^T\mathbf{A})^{-1}$ [see Eq (4a)] and its symmetry have been used In component form,

$$\sigma_{\mathbf{a}_{jk}}^2 = C_{jk} \tag{6b}$$

so that, unlike the data errors, the resulting errors in the coefficients are correlated, i e , the off-diagonal terms of the matrix $\mathbf{C}$ do not, in general, vanish The diagonal elements give the variances of the coefficients,

$$\sigma_{a_j}^2 = C_{jj} \tag{6c}$$

We are now in a position to determine the error in the value of the fitted function $y(x)$ that results from the errors in the coefficients a_j

From Eq (2),

$$\delta y(x, \mathbf{a}) = \sum_{j=1}^{M} \delta a_j X_j(x)$$

so that the covariance $\sigma_y^2(x, x') \equiv \langle \delta y(x)\delta y(x') \rangle$ is given by

$$\sigma_y^2(x, x') = \sum_{j=1}^{M}\sum_{k=1}^{M} \langle \delta a_j \delta a_k \rangle X_j(x)X_k(x') = \sum_{j=1}^{M}\sum_{k=1}^{M} C_{jk}X_j(x)X_k(x') \tag{7}$$

We note that this holds for any two values of the independent variable, not just the data points, and that it is independent of the parameter values, a_j

For the special case $x' = x$, we have the variance

$$\sigma_y^2(x) = \sum_{j=1}^{M}\sum_{k=1}^{M} C_{jk}X_j(x)X_k(x) = \mathbf{x}(x)^T\mathbf{C}\ \mathbf{x}(x) \tag{8}$$

where $\mathbf{x}(x)$ is a column vector whose elements are $X_j(x)$ Since the above expression for $\sigma_y^2(x, x')$ does not, in general, vanish for $x' \neq x$, the errors in $y(x, \mathbf{a})$ at two different values of x are correlated, unlike the data errors Some insight into the significance of the result given by Eq (8) can be obtained by considering the weighted mean value of $\sigma_y^2(x)$ averaged over all data points $x = x_i$

$$\frac{1}{N}\sum_{i=1}^{N}\frac{\sigma_y^2(x_i)}{\sigma_i^2} = \frac{1}{N}\sum_{j=1}^{M}\sum_{k=1}^{M}C_{jk}\sum_{i=1}^{N}\frac{X_{ij}}{\sigma_i}\,\frac{X_{ik}}{\sigma_i}$$

From the definition of the matrix $\mathbf{A}$, $(X_{ij}/\sigma_i) \equiv A_{ij}$, and hence the sum over i is just $(\mathbf{A}^T\mathbf{A})_{kj} = h_{kj} = (\mathbf{C}^{-1})_{kj}$, thus giving us

$$\frac{1}{N}\sum_{i=1}^{N}\frac{\sigma_y^2(x_i)}{\sigma_i^2} = \frac{1}{N}\sum_{j=1}^{M}\sum_{k=1}^{M}C_{jk}(\mathbf{C}^{-1})_{jk} = \frac{1}{N}\sum_{j=1}^{M}I_{jj} = \frac{M}{N} \tag{9}$$

For the special case of constant data errors, independent of the value of x, $\sigma_i = \sigma =$ constant, so that we obtain

$$\overline{\sigma_y^2} = \frac{1}{N}\sum_{i=1}^{N}\sigma_y^2(x_i) = \frac{M}{N}\sigma^2 \tag{10}$$

This result is analogous to the variance of the mean for the case of one value of x, where $M = 1$ Thus, we see that, as a result of fitting to the function $y(x)$, the variance of y, averaged over the data points, is reduced by the ratio M/N relative to the constant data variance This implies that the higher the order of the fit required by the data to reduce χ_ν^2 to a value close to 1, the larger will be the resulting errors of the values of the fitted function

In the following section, we examine these results for the simple case of a straight-line fit to the data, where an exact analysis enables one to bring out some of the more important consequences of the general theory

VI. Illustrative Examples

A. Fitting to a Straight Line

In order to illustrate some of the main consequences of the theory developed above, we first consider the simplest linear, least-squares fitting problem, that of a straight line [3], for which $M = 2$ Then, the basis functions are given by $X_{ij} = x_i^{j-1}, j = 1, 2$, and the fitting function by

$$y(x_i, \mathbf{a}) = \sum_{j=1}^{2} a_j x_i^{j-1} = a_1 + a_2 x_i$$

The matrix $\mathbf{H}$ is, thus,

$$\mathbf{H} = \begin{bmatrix} h_{11} & h_{12} \\ h_{21} & h_{22} \end{bmatrix} = \begin{bmatrix} \sum_{i=1}^{N}\frac{1}{\sigma_i^2} & \sum_{i=1}^{N}\frac{x_i}{\sigma_i^2} \\ \sum_{i=1}^{N}\frac{x_i}{\sigma_i^2} & \sum_{i=1}^{N}\frac{x_i^2}{\sigma_i^2} \end{bmatrix} \tag{11}$$

while its inverse, $\mathbf{C}$, is

$$\mathbf{C} = \frac{1}{\Delta}\begin{bmatrix} h_{22} & -h_{12} \\ -h_{21} & h_{11} \end{bmatrix}$$

In the above, $\Delta = h_{11}h_{22} - h_{12}^2$ and $h_{12} = h_{21}$, thus demonstrating the general result that both $\mathbf{H}$ and $\mathbf{C}$ are symmetric

For the special case where the data variances are independent of x, the diagonal terms of the latter, which correspond to the variances of the constant and the linear coefficient, are given by

$$C_{11} = \sigma_{a_1}^2 = \frac{\sigma^2}{N - \left(\sum_{i=1}^N x_i\right)^2 / \sum_{i=1}^N x_i^2}$$

$$C_{22} = \sigma_{a_2}^2 = \frac{\sigma^2}{\sum_{i=1}^N x_i^2 - \left(\sum_{i=1}^N x_i\right)^2 / N}$$

The variance of the data points is[2]

$$\sigma_x^2 = \frac{1}{N}\sum_{i=1}^N x_i^2 - \frac{1}{N^2}\left(\sum_{i=1}^N x_i\right)^2$$

and if we choose the origin of the x-scale symmetrically, then the sum over x_i vanishes so that we may write the above in the simplified form

$$C_{11} = \sigma_{a_1}^2 = \frac{\sigma^2}{N}$$

$$C_{22} = \sigma_{a_2}^2 = \frac{1}{N}\,\frac{\sigma^2}{\sigma_x^2}$$

These results agree with our intuition in that the variance of the constant term is just the variance of the mean of the data values, while the variance of the slope decreases from this as the spread of the data points increases From Eq (8), the variance of the value of the fitted function, in this case a straight line, becomes

$$\begin{aligned} \sigma_y^2(x) &= \sum_{j=1}^2 \sum_{k=1}^2 C_{jk} x^{j+k-2} \\ &= C_{11} + 2C_{12}x + C_{22}x^2 \\ &= \frac{1}{\Delta}\left(h_{22} - 2h_{12}x + h_{11}x^2\right) \end{aligned} \tag{12}$$

[2] For convenience, we are using a definition involving $1/N$ rather than $1/(N-1)$

This is the equation of a conic section, for which the characteristic is

$$B^2 - 4AC = \frac{4h_{11}}{\Delta}$$

where $h_{11} = \sum_{i=1}^{N} (1/\sigma_i^2)$ and $\Delta = \sum_{i=1}^{N} (1/\sigma_i^2) \sum_{l=1}^{N} (x_l^2/\sigma_l^2) - \left(\sum_{i=1}^{N} [x_i/\sigma_i]\right)^2$ Letting $1/\sigma_i = a_i$ and $x_i/\sigma_i = b_i$, in the latter, and applying the Cauchy–Schwarz inequality,

$$\sum_{i=l}^{N} a_i^2 \sum_{l=1}^{N} b_l^2 \geq \left(\sum_{i=1}^{N} a_i b_i\right)^2$$

we see that $B^2 - 4AC \geq 0$, so that the equation for $\sigma_y(x)$ is that of a hyperbola Similarly, the discriminant of the quadratic on the right-hand side of Eq (12) is $b^2 - 4ac = -(4/\Delta) \leq 0$, so that the roots of the equation $\sigma_y^2(x) = 0$ are complex, i e , the hyperbola is symmetric about the x-axis The minimum value of $\sigma_y^2(x)$ occurs at $x_{min} = h_{12}/h_{11}$, for which the variance is $\sigma_y^2|_{min} = 1/h_{11}$ For constant data variances, $\sigma_i = \sigma$, $x_{min} = (1/N) \sum_{i=1}^{N} x_i = \overline{x}$, and $\sigma_y^2|_{min} = (1/h_{11}) = (\sigma^2/N)$, while at $x = \overline{x} \pm \sigma_x$,

$$\sigma_y^2 (\overline{x} \pm \sigma_x) = \frac{2}{h_{11}} = 2\frac{\sigma^2}{N} = \overline{\sigma_y^2} \tag{13}$$

showing that the mean value of $\sigma_y^2(x)$ occurs at one standard deviation from the mean value of x

If the values of the matrix elements h_{jk} given by Eq (11) are substituted into Eq (12) for the special case $\sigma_i = \sigma$, it may be transformed into the simple dimensionless form

$$\eta^2 = 1 + \xi^2 \tag{14}$$

where $\eta = \sqrt{N}([\sigma_y(x)]/\sigma), \xi = ([x - \overline{x}]/\sigma_x)$ The universal error curve represented by Eq (14) is plotted, along with the higher-degree polynomial error curves discussed below, in Fig 5

B. More General Fits

The case of a general polynomial fit may be treated by the same methods used above, but the algebra becomes progressively more difficult for $M > 2$ However, one can see that for higher-degree polynomial fits, the general behavior illustrated by the straight-line case dealt with above is also found For example, since the highest power present in the expansion for $\sigma_y^2(x)$ is $2(M - 1)$ while the fit itself is of degree $M - 1$, the equation for $\sigma_y(x)$ corresponds to a double-branched function whose asymptotic behavior for $|x - \overline{x}| >> \sigma_x$ follows the same power law as the fit itself Thus, a quadratic fit yields an error that increases asymptotically as the second power of $|x - \overline{x}|$, a cubic as the third power, etc The implication of this is that higher-degree fits become less reliable than ones of lower degree as one moves away from the center of the given data

It is shown in the Appendix that if the data variances are constant, and the data points are uniformly distributed along the x-axis, then the variance of the fitted function $\sigma_y^2(x)$ is a symmetric function of $x - \overline{x}$, i e , $\sigma_y(\overline{x} + \Delta x) = \sigma_y(\overline{x} - \Delta x)$ Furthermore, it is possible to express $\sigma_y^2(x)$ in the same dimensionless form as for the straight-line case for the higher-degree polynomial fits Thus, for the general polynomial of degree $M - 1$, a set of universal, normalized error curves exists, the square of which is given by

$$\eta^2 = \sum_{j=0}^{M-1} A_{2j}^{(M-1)}(N)\xi^{2j}$$

where

$$\eta = \sqrt{N}\frac{\sigma_y(x)}{\sigma}$$

$$\xi = \frac{x - \overline{x}}{\sigma_x}$$

$$\overline{x} = \frac{1}{N}\sum_{i=1}^{N} x_i$$

$$\sigma_x^2 = \frac{1}{N}\sum_{i=1}^{N} x_i^2 - \frac{1}{N^2}\left(\sum_{i=1}^{N} x_i\right)^2$$

While the coefficients appearing in the above expression generally depend on the number of data points, N, they do not for the straight-line case Furthermore, for values of N exceeding that required for a given fit by some reasonable number, say 5, they become essentially constant for polynomial fits of all degrees These results are summarized in Table 1, which lists the coefficients $A_{2j}^{(M-1)}(N)$, including their limiting values for $N \to \infty$, for straight-line, quadratic, and cubic fits, corresponding to $M = 2, 3$, and 4 The corresponding normalized standard deviations of the fit, η, are plotted in Fig 5

In the general case where the basis functions are not polynomials, the standard errors are not constant, or the data points are not uniformly distributed, one must use Eq (8) to determine the behavior of the error as a function of the independent variable, so that this equation takes on fundamental importance in determining confidence limits resulting from a given fit to a given set of data An example of the direct use of this equation is shown in Figs 1 through 4, where a set of antenna aperture efficiency data has been fitted to a quadratic function The figures illustrate the behavior of the standard error of the fit over a wide range of elevation angles, including those beyond the existing data We have assumed from the outset that the data errors are normally distributed, and under these circumstances, it may be shown that the errors in the coefficients and, consequently, also in the fitting function $y(x)$ are also normally distributed, so that Gaussian statistics may be used to determine these limits

As a final comment, it should be observed that the above analysis assumes that the fit is meaningful, i e , that $\chi_\nu^2 \approx 1$, and this is crucial to a proper interpretation of the fitting errors If the fitting function has been improperly chosen, one may not assume that the errors follow Eq (8) and, equally important, if the data errors have been incorrectly estimated, one may not assume that the fit is meaningful even if $\chi_\nu^2 \approx 1$, since these errors appear directly in the expression for χ^2 [Eq (1)] It is, therefore, of the utmost importance to have a reasonably accurate estimate of the actual data errors if one is to have reasonable estimates of the resulting fitting errors

VII. The Nonlinear Least-Squares Problem

The linear, least-squares problem is characterized by Eqs (2) and (3), which, respectively, express the fitting function $y(x, \mathbf{a})$ as a linear and χ^2 as a quadratic function of the coefficients a_j, thus allowing an explicit solution to be obtained for the latter, as shown in Section IV In the nonlinear case, no such

simple formulation is possible, and one is led to an iterative procedure for the solution that starts with an assumed solution vector $\underline{\mathbf{a}}$ and evolves so as to produce values closer and closer to the value $\underline{\mathbf{a}_0}$, which minimizes χ^2 The iteration is based on the assumption that if $\underline{\mathbf{a}}$ is sufficiently close to $\underline{\mathbf{a}_0}$, then $y(x, \mathbf{a})$ may still be expressed as a linear and χ^2 as a quadratic function of the coefficients This assumption rests on using Taylor expansions for these quantities and retaining only the leading terms Thus, for $\underline{\mathbf{a}}$ near $\underline{\mathbf{a}_0}$, we may write

$$\begin{aligned} y(x, \mathbf{a}) &= y(x, \mathbf{a}_0) + \sum_{j=1}^{M} \left. \frac{\partial y(x, \mathbf{a})}{\partial a_j} \right|_{\mathbf{a}_0} (a_j - a_{0j}) \\ &= y(x, \mathbf{a}_0) + (\mathbf{a} - \mathbf{a}_0)^T \mathbf{d}(x, \mathbf{a}_0) \end{aligned} \tag{15}$$

where $[\mathbf{d}(x, \mathbf{a}_0)]_j \equiv d_j(x, \mathbf{a}_0) = (\partial y(x, \mathbf{a})/\partial a_j)|_{\mathbf{a}_0}$ Similarly,

$$\begin{aligned} \chi^2(\mathbf{a}) &= \chi^2_{min} + \frac{1}{2} \sum_{j=1}^{M} \sum_{k=1}^{M} \left. \frac{\partial^2 \chi^2(\mathbf{a})}{\partial a_j \partial a_k} \right|_{\mathbf{a}_0} (a_j - a_{0j})(a_k - a_{0k}) \\ &= \chi^2_{min} + (\mathbf{a} - \mathbf{a}_0)^T \mathbf{H}(\mathbf{a}_0)(\mathbf{a} - \mathbf{a}_0) \end{aligned} \tag{16}$$

where $\chi^2_{min} = \chi^2(\mathbf{a}_0)$, and

$$h_{jk}(\mathbf{a}_0) = \frac{1}{2} \left. \frac{\partial^2 \chi^2(\mathbf{a})}{\partial a_j \partial a_k} \right|_{\mathbf{a}_0} = \sum_{i=1}^{N} \frac{1}{\sigma_i^2} \left. \frac{\partial y(x_i, \mathbf{a})}{\partial a_j} \right|_{\mathbf{a}_0} \left. \frac{\partial y(x_i, \mathbf{a})}{\partial a_k} \right|_{\mathbf{a}_0}$$

Note that the gradient term vanishes in the above expression for $\chi^2(\mathbf{a})$ since it is evaluated at the minimum Also, the final expression for $h_{jk}(\mathbf{a}_0)$ involves only first derivatives because of the assumed form for $y(x, \mathbf{a})$ given by Eq (15) If we now define

$$A_{ij}(\mathbf{a}_0) = \frac{1}{\sigma_i} \left. \frac{\partial y(x_i, \mathbf{a})}{\partial a_j} \right|_{\mathbf{a}_0} = \frac{d_{ij}(\mathbf{a}_0)}{\sigma_i}$$

then $\mathbf{H}(\mathbf{a}_0) = \mathbf{A}^T \mathbf{A}$ just as in the linear case and, hence, the derivation leading up to Eq (6) carries through just as before, giving us

$$\sigma_a^2(\mathbf{a}_0) = \mathbf{C}(\mathbf{a}_0) = \mathbf{H}^{-1}(\mathbf{a}_0)$$

Also, the derivation leading up to Eq (8) follows through as before when $d_j(x, \mathbf{a}_0)$ is substituted for $X_j(x)$, giving the result

$$\sigma_y^2(x, \mathbf{a}_0) = \sum_{j=1}^{M} \sum_{k=1}^{M} C_{jk}(\mathbf{a}_0) d_j(x, \mathbf{a}_0) d_k(x, \mathbf{a}_0)$$

$$= \mathbf{d}(x, \mathbf{a}_0)^T \mathbf{C}(\mathbf{a}_0) \mathbf{d}(x, \mathbf{a}_0)$$

as does that leading up to Eqs (9) and (10)

Thus, the results

$$\frac{1}{N} \sum_{i=1}^{N} \frac{\sigma_y^2(x_i)}{\sigma_i^2} = \frac{M}{N}$$

and

$$\overline{\sigma_y^2} = \frac{1}{N} \sum_{i=1}^{M} \sigma_y^2(x_i) = \frac{M}{N} \sigma^2$$

continue to hold in the general, nonlinear case so that with the appropriate definitions for the quantities involved, the nonlinear and linear, least-squares problems lead to the same formal results Note, however, that all of the quantities now explicitly depend on the solution vector, $\underline{\mathbf{a}_0}$

Furthermore, within the assumptions made in writing down Eqs (15) and (16), i e , assuming that the deviations δa_j are not so large as to invalidate the linear and quadratic approximations involved, one may assume that all of the distributions are normal and, hence, that the usual confidence limits derived from such distributions hold Thus, the limits for a confidence level of 68 3 percent are $\pm\sigma_X$, those for 95 4 percent $\pm 2\sigma_X$, for 99 73 percent $\pm 3\sigma_X$, etc , where X corresponds to either $\underline{\mathbf{a}}$ or y As an example of the application of the above theory to a specific case, the nonlinear fitting problem for the Gaussian function

$$y(x, \mathbf{a}) = a_1 \exp\left[\frac{-(x - a_2)^2}{2a_3^2}\right]$$

is treated in the Appendix, where it is shown that the normalized variance of the fit for the case of constant data errors is given by

$$\eta^2 = \sqrt{\frac{3}{\pi}} \sigma_t e^{-(\xi\sigma_t)^2} \left(3 + 4\sigma_t^4 \xi^4\right)$$

under the assumptions that the number of data points is reasonably large, say 20 or more, that they are uniformly and symmetrically distributed about the peak $x = a_2$, and that they extend out to a distance of $x - a_2 = \pm 2a_3$ or more In the above expression,

$$\eta = \sqrt{N} \frac{\sigma_y(x)}{\sigma}$$

and

$$\sigma_t = \frac{\sigma_x}{a_3}$$

where $\sigma_x^2 = (1/N)\sum_{i=1}^{N} x_i^2 - (1/N^2)(\sum_{i=1}^{N} x_i)^2$, as before This equation is plotted in Fig 6 for $\sigma_t = 2/\sqrt{3}$ and $4/\sqrt{3}$, corresponding to $L/a_3 = 4$ and 8, where L is the full range of the data points

If the data errors, instead of being constant, are proportional to the value of the function, $\sigma_i = \sigma(x_i) \propto y(x_i, \mathbf{a})$, then the normalized error of the fit is given by

$$\eta^2 = A_0^{(2)}(N) + A_2^{(2)}(N)\xi^2 + A_4^{(2)}(N)\xi^4$$

where now $\eta = \sqrt{N}\sigma_y(x)/\sigma(x)$ and the only restriction on the data points is that they be uniformly and symmetrically distributed relative to the peak The coefficients $A_{2j}^{(2)}(N)$ appearing in the above expression are the same as those found for the quadratic polynomial fit, and their values, including those for $N \to \infty$, are give in Table 1 The equation is plotted in Fig 7

The functional dependence of the parameter errors, σ_{a_j}, on the data interval, L, and the number of points, N, is frequently of importance in determining an optimum sampling strategy, and this is derived in Section V of the Appendix, with the results for constant data errors plotted in Fig 8

VIII. A Related Problem

It is sometimes of interest to determine the variance of the difference of the fit at two points x_1 and $x_2, \Delta y(x_1, x_2) = y(x_1, \mathbf{a}) - y(x_2, \mathbf{a})$ Thus, from Eq (13), we have

$$\begin{aligned} \delta\left[\Delta y(x_1, x_2)\right] &= \delta y(x_1, \mathbf{a}) - \delta y(x_2, \mathbf{a}) \\ &= \sum_{j=1}^{M} \left[d_j(x_1) - d_j(x_2)\right] \delta a_j \end{aligned}$$

so that

$$\begin{aligned} \sigma_{\Delta_{1\,2}}^2 \equiv \left\langle \left\{\delta\left[\Delta y(x_1, x_2)\right]\right\}^2 \right\rangle &= \sum_{j=1}^{M}\sum_{k=1}^{M} \langle \delta a_j \delta a_k \rangle (d_{1j} - d_{2j})(d_{1k} - d_{2k}) \\ &= \sum_{j=1}^{M}\sum_{k=1}^{M} C_{jk}(d_{1j} - d_{2j})(d_{1k} - d_{2k}) \end{aligned}$$

For the case of a polynomial expansion, $d_{ij} = X_{ij} = x_i^{j-1}$, so

$$\sigma_{\Delta_{1\,2}}^2 = \sum_{j=1}^{M}\sum_{k=1}^{M} C_{jk}\left(x_1^{j-1} - x_2^{j-1}\right)\left(x_1^{k-1} - x_2^{k-1}\right)$$

and, hence, using the results of Section VI, we obtain

$$\sigma^2_{\Delta_{1\,2}} = C_{22}(x_1 - x_2)^2 = \sigma^2_{a_2}(x_1 - x_2)^2$$

for a straight-line fit For constant data errors,

$$\sigma^2_{\Delta_{1\,2}} = \frac{1}{N}\,\frac{\sigma^2}{\sigma_x^2}(x_1 - x_2)^2$$

IX. Discussion

In applying the above results, it is important to be aware that the variances of the fit obtained in Eq (8) and related equations are valid only if one is reasonably confident of the fit itself If the fitting function being considered does not accurately represent the data, then one must find one that does before attempting to assign appropriate errors, and the best test for this is the value of the reduced χ^2 In this connection, it is worth mentioning that while fits using ordinary polynomials are often used for convenience and simplicity, they seldom correspond to physical reality They may approximate a given physical process reasonably well over a limited range of the independent variable x, but one should exercise care when attempting to go beyond this, because the hallmark of these functions is that they diverge for large absolute values of x, and the variances of the fit derived for the polynomials in the Appendix and discussed in Section VI offer a warning of this by doing likewise in the region beyond the existing data

Clearly, one is better off with a fitting function that reflects the underlying physics reasonably well, but of course it is not always possible to find such a function, especially if the system being studied has a large number of basic processes going on at the same time, some of which may be unknown to the observer A good example is trying to determine the microwave spectrum of a complex astrophysical source of radiation, such as a galaxy, or even a planet, where not only is the physics not known with certainty, but also the data have typically been gathered by many different workers using different measuring systems with different accuracies at different frequencies Under such circumstances, one cannot be sure that some hidden absorption or emission feature has not gone undetected because of a gap in the measurements and knowledge, over some small range of frequencies, possibly at one of the extremes of the existing measurements A case in point is the HII region DR21, where early measurements by workers identified the basic radiation process as thermal bremsstrahlung and, on that basis, predicted its microwave spectrum out to frequencies of 100 GHz, unaware of the fact that the region was surrounded by a dust cloud that converted intense visible and ultraviolet radiation to near-infrared radiation, which resulted in significant departure from the predicted spectrum at frequencies as low as 85 GHz The existing measurements of the time did not extend beyond 31 4 GHz, so considerable extrapolation was involved, even on a logarithmic scale

Spectral determinations are particularly treacherous, especially at the extremes of the data, because, in principle, the range of the independent variable, frequency, is open at both ends, thus precluding a knowledge of the asymptotic behavior At the opposite extreme, however, one may be dealing with a relatively uncomplicated situation involving a finite and known range for the independent variable and a system that can reliably be modeled in a fairly simple manner In such a case, it pays to determine the errors as accurately as one can, i e , to make maximum use of the given data by applying the variance of the fit theory discussed above

The question of how best to determine the actual data errors is not an easy one If the measuring system and the system under study are simple, it may be possible to determine these from first principles, combined with the performance data for the instrumentation used, and it might further be possible to check this by a series of measurements on a known system Often, however, one does not have such a simple circumstance to deal with, nor does one have the time to make the requisite test measurements

In this case, one might obtain a reasonable estimate of the data errors by breaking up the range of the independent variable into a small number of segments over each of which the functional dependence may be reasonably well approximated by a quadratic, and fitting each of these restricted data sets by a quadratic assuming $\sigma = 1$ Then, $\chi^2_\nu(\sigma = 1) = (1/\nu)\sum_{i=1}^{N}[y_i - y(x_i)]^2$ and $\chi^2_\nu(\sigma) = (1/\nu\sigma^2)\sum_{i=1}^{N}[y_i - y(x_i)]^2 \approx 1$ so that $\sigma^2 \approx \chi^2_\nu(\sigma = 1)$ A plot of the resulting values of σ as a function of the mean value of the independent variable for each segment would then provide an estimate for $\sigma(x)$, which would in turn permit an assignment of the appropriate values for the σ_i's for the final overall fit In the final analysis, as always, common sense and experience must be the ultimate guide in determining how best to proceed

Acknowledgments

I would like to express my thanks to Charles Lawson for many useful comments, Charles Stelzried for forcing me to examine Gaussian parameter errors more closely, Stephen Slobin for urging me to present the essential results in a more easily digestible form, and last, but not least, Shervin Shambayati for carrying out the Monte Carlo calculations and creating the figures

References

[1] W H Press, B P Flannery, S A Teukolsky, and W T Vetterling, *Numerical Recipes* Chapter 14, New York Cambridge University Press, 1992

[2] P R Bevington, *Data Reduction and Error Analysis for the Physical Sciences*, New York McGraw-Hill, 1969

[3] F S Acton, *Analysis of Straight-Line Data*, New York John Wiley & Sons, 1959

[4] I S Gradshteyn and I M Ryzhik, *Table of Integrals, Series, and Products*, Corrected and Enlarged Edition, New York Academic Press, 1980

Appendix
Mathematical Details

I. Symmetry Considerations in Polynomial Fits

If the basis functions chosen are the ordinary polynomials and constant data errors are assumed, the curvature matrix elements are given by

$$h_{jk} = \frac{1}{\sigma^2} \sum_{i=1}^{N} x_i^{j+k-2}$$

Furthermore, if the data points are uniformly distributed, we may choose our y-axis so that $\sum_{i=1}^{N} x_i^{j+k} = 0$ for $j + k =$ odd integer [3] Then, the curvature matrix has the general appearance

$$\mathbf{H} = \begin{bmatrix} h_{11} & 0 & h_{13} & 0 \\ 0 & h_{22} & 0 & h_{24} \\ h_{13} & 0 & h_{33} & 0 \\ 0 & h_{24} & 0 & h_{44} \end{bmatrix} \tag{A-1}$$

where the symmetry has been explicitly indicated, i e , $h_{jk} = h_{kj}$ The elements of the covariance matrix are given by

$$C_{jk} = \frac{1}{\Delta} \times \text{cofactor}(h_{jk})$$

where $\Delta = \det \mathbf{H}$ and use has been made of the symmetry of $\mathbf{H}$ By an inductive process, one can show that if $j + k$ is an odd integer, then the cofactor matrix will, for a given rank of the curvature matrix, have $n + 1$ rows of identical sequences of zero and nonzero elements, where the number of the latter in a given such row is n Thus, if the rank of $\mathbf{H}$ is 4 or 5, $n = 1$, if it is 6 or 7, $n = 2$, etc In view of this structure of the cofactor matrix, one may perform a Gauss elimination on these rows and thereby end up with one row consisting of nothing but zeroes, in consequence of which the corresponding cofactor and, hence, also the covariance matrix element, C_{jk}, vanish for $j + k$ equal to an odd integer The covariance matrix, therefore, has the same structure as the curvature matrix, so that Eq (8) for the variance of the fit becomes $\sigma_y^2(x) = \sum_{j=1}^{M} \sum_{k=1}^{M} C_{jk} x^{j+k-2}$ for $j + k =$ even integer Hence, $\sigma_y^2(x)$ is an even function of x, i e , the variance of the fit for polynomials is symmetric about the mean of the data points if these are uniformly distributed and the data errors are constant

II. Polynomial Fits for *M* = 2, 3, and 4 With Constant Data Errors and Uniformly Distributed Data Points

A. Straight-Line Fits

While straight-line fits have already been dealt with in Section VI, the simplicity of this case makes it a useful starting point for discussion of the above ideas Thus, assuming constant data errors and

[3] The y-axis location affects the covariance matrix, but not the variance of the fit

uniformly distributed data points, we may introduce the variable $x' = x - \overline{x}$, where $\overline{x} = (1/N)\sum_{i=1}^{n} x_i$, in terms of which the curvature and covariance matrices have the sparse form shown in Eq (A-1) above Then, for $M = 2$, we have

$$\mathbf{H} = \begin{bmatrix} h_{11} & 0 \\ 0 & h_{22} \end{bmatrix}$$

so that $\Delta = \det \mathbf{H} = h_{11}h_{22}$, and

$$\mathbf{C} = \begin{bmatrix} \frac{1}{h_{11}} & 0 \\ 0 & \frac{1}{h_{22}} \end{bmatrix} = \frac{\sigma^2}{N}\begin{bmatrix} 1 & 0 \\ 0 & \frac{1}{\sigma_x^2} \end{bmatrix}$$

where $\sigma_x^2 = (1/N)\sum_{i=1}^{N}(x_i - \overline{x})^2 = (1/N)\sum_{i=1}^{N} x_i'^2$ Substituting into Eq (8), we thus have

$$\sigma_y^2(x) = \frac{\sigma^2}{N}[1 \;\; x']\begin{bmatrix} 1 & 0 \\ 0 & \frac{1}{\sigma_x^2} \end{bmatrix}\begin{bmatrix} 1 \\ x' \end{bmatrix} = \frac{\sigma^2}{N}\left[1 + \left(\frac{x'}{\sigma_x}\right)^2\right]$$

This may be written in the normalized form

$$\eta^2 = 1 + \left(\frac{x'}{\sigma_x}\right)^2 = 1 + \xi^2 \tag{A-2}$$

where $\eta = \sqrt{N}([\sigma_y(x)]/\sigma)$ and $\xi = ([x - \overline{x}]/\sigma_x)$, in agreement with the results of Section VI A [Eq (14)]

Note that while the above symmetric result has been obtained under the restrictive condition that the data points are uniformly distributed, no such assumption was made in the original derivation given in Section VI, i e , as long as the data variances are constant, the data points can be distributed in any manner and the result of Eq (A-2) still holds As we shall see in what follows, this is a special feature of the straight-line fit that does not carry over to polynomial fits of higher degree

B. Quadratic Fits

The general form for the variance of the fit for the quadratic case is

$$\sigma_y^2(x) = [1 \;\; x' \;\; x'^2]\begin{bmatrix} C_{11} & 0 & C_{13} \\ 0 & C_{22} & 0 \\ C_{13} & 0 & C_{33} \end{bmatrix}\begin{bmatrix} 1 \\ x' \\ x'^2 \end{bmatrix} \tag{A-3}$$

where $x' = x - \overline{x}$ as before, and

$$\mathbf{H} = \begin{bmatrix} h_{11} & 0 & h_{13} \\ 0 & h_{22} & 0 \\ h_{13} & 0 & h_{33} \end{bmatrix}$$

Inverting this, the matrix elements of $\mathbf{C}$ are

$$\left.\begin{aligned} C_{11} &= \frac{h_{33}}{h_{11}h_{33} - h_{13}^2} \\ C_{13} &= -\frac{h_{13}}{h_{11}h_{33} - h_{13}^2} \\ C_{22} &= \frac{1}{h_{22}} \\ C_{33} &= \frac{h_{11}}{h_{11}h_{33} - h_{13}^2} \end{aligned}\right\} \tag{A-4}$$

where $h_{11} = N/\sigma^2, h_{13} = h_{22} = (1/\sigma^2)\sum_{i=1}^{N} x_i'^2 = N(\sigma_x^2/\sigma^2)$, and $h_{33} = (1/\sigma^2)\sum_{i=1}^{N} x_i'^4$ The last term may be evaluated by making use of the uniformity of the distribution of the points Thus, designating the spacing between adjacent points by δ, we have

$$\sum_{i=1}^{N} x_i'^4 = 2\delta^4 \sum_{n=1}^{(N-1)/2} n^4 = \frac{\delta^4 N}{240}(N^2 - 1)(3N^2 - 7)$$

where the last step has used the relation

$$\sum_{k=1}^{n} k^4 = \frac{1}{30}n(n+1)(2n+1)(3n^2 + 3n - 1)$$

from [4, Eq (0 121 4)], and for definiteness we have assumed an odd number of points [4] Similarly, applying the relation $\sum_{k=1}^{n} k^2 = (1/6)n(n+1)(2n+1)$ to the expression for h_{22} above, we obtain the following relationship between the point spacing, δ, and the standard deviation of the data points, σ_x

$$\delta^2 = \frac{12}{N^2 - 1}\sigma_x^2$$

so that we may write h_{33} in the form

$$h_{33} = \frac{3(3N^2 - 7)}{5(N^2 - 1)}\left(N\frac{\sigma_x^4}{\sigma^2}\right)$$

Substituting these results into Eq (A-3), we finally obtain

$$\begin{aligned} \eta^2 &= \frac{1}{4(N^2 - 4)}\left[3(3N^2 - 7) - 6(N^2 + 1)\xi^2 + 5(N^2 - 1)\xi^4\right] \\ &= A_0^{(2)}(N) + A_2^{(2)}(N)\xi^2 + A_4^{(2)}(N)\xi^4 \end{aligned}$$

[4] The results obtained do not depend on whether N is even or odd

where $\xi = ([x - \overline{x}]/\sigma_x)$, as before In the limit as $N \to \infty$, and this limit is approached quite rapidly as N increases, this reduces to the simple fourth-degree polynomial

$$\eta^2 = \frac{9}{4} - \frac{3}{2}\xi^2 + \frac{5}{4}\xi^4$$

C. Cubic Fits

For the cubic case, the variance of the fit has the form

$$\sigma_y^2(x) = [1 \quad x'^2 \quad x'^4 \quad x'^6] \begin{bmatrix} C_{11} & 0 & C_{13} & 0 \\ 0 & C_{22} & 0 & C_{24} \\ C_{13} & 0 & C_{33} & 0 \\ 0 & C_{24} & 0 & C_{44} \end{bmatrix} \begin{bmatrix} 1 \\ x'^2 \\ x'^4 \\ x'^6 \end{bmatrix}$$

$$= C_{11} + (C_{22} + 2C_{13})x'^2 + (2C_{24} + C_{33})x'^4 + C_{44}x'^6 \tag{A-5}$$

and the curvature matrix is of the form

$$\mathbf{H} = \begin{bmatrix} h_{11} & 0 & h_{13} & 0 \\ 0 & h_{22} & 0 & h_{24} \\ h_{13} & 0 & h_{33} & 0 \\ 0 & h_{24} & 0 & h_{44} \end{bmatrix}$$

Inverting this, we have

$$C_{11} = \frac{h_{33}}{h_{11}h_{33} - h_{13}^2}$$

$$C_{13} = -\frac{h_{13}}{h_{11}h_{33} - h_{13}^2}$$

$$C_{22} = \frac{h_{44}}{h_{22}h_{44} - h_{24}^2}$$

$$C_{24} = -\frac{h_{24}}{h_{22}h_{44} - h_{24}^2}$$

$$C_{33} = \frac{h_{11}}{h_{11}h_{33} - h_{13}^2}$$

$$C_{44} = \frac{h_{22}}{h_{22}h_{44} - h_{24}^2}$$

where

$$h_{11} = \frac{N}{\sigma^2}$$

$$h_{13} = h_{22} = \frac{1}{\sigma^2}\sum_{i=1}^{N} x_i'^2 = N\frac{\sigma_x^2}{\sigma^2}$$

$$h_{24} = h_{33} = \frac{1}{\sigma^2}\sum_{i=1}^{N} x_i'^4 = \frac{3(3N^2-7)}{5(N^2-1)}N\frac{\sigma_x^4}{\sigma^2}$$

$$h_{44} = \frac{1}{\sigma^2}\sum_{i=1}^{N} x_i'^6 = \frac{9(3N^2-18N^2+31)}{7(N^2-1)^2}\ N\ \frac{\sigma_x^6}{\sigma^2}$$

and the last term has been evaluated with the use of the formula $\sum_{k=1}^{n} k^6 = (1/42)n(n+1)(2n+1)(3n^4 + 6n^3 - 3n + 1)$, taken from [4, Eq (0 121 6)]

Substituting these results into Eq (A-5), we obtain

$$\eta^2 = A_0^{(3)} + A_2^{(3)}\xi^2 + A_4^{(3)}\xi^4 + A_6^{(3)}\xi^6$$

where the coefficients are given by

$$A_0^{(3)} = \frac{3(3N^2-7)}{4(N^2-4)}$$

$$A_2^{(3)} = \frac{5}{12}\ \frac{9N^4-12N^2-61}{(N^2-4)(N^2-9)}$$

$$A_4^{(3)} = -\frac{5}{36}\ \frac{33N^4-23N^2-226}{(N^2-4)(N^2-9)}$$

$$A_6^{(3)} = \frac{175}{108}\ \frac{(N^2-1)^2}{(N^2-4)(N^2-9)}$$

thus giving us the limiting result $\eta^2 = (9/4) + (15/4)\xi^2 - (55/12)\xi^4 + (175/108)\xi^6$ as $N \to \infty$

III. Gaussian Fits

A. Constant Data Errors

The general Gaussian fitting function is given by

$$y(x, \mathbf{a}) = a_1 \exp\left[\frac{-(x-a_2)^2}{2a_3^2}\right] = a_1 \exp\left(\frac{-t^2}{2}\right)$$

where $t = (x - a_2)/a_3$ Thus, the required derivatives are

$$\left.\begin{aligned} d_1(x) &= \frac{\partial y}{\partial a_1} = \exp\frac{-t^2}{2} \\ d_2(x) &= \frac{\partial y}{\partial a_2} = \frac{a_1 t}{a_3}\exp\frac{-t^2}{2} \\ d_3(x) &= \frac{\partial y}{\partial a_3} = \frac{a_1 t^2}{a_3}\exp\frac{-t^2}{2} \end{aligned}\right\} \tag{A-6}$$

For σ = constant, $h_{jk} = \sum_{i=1}^{N} A_{ij}A_{ik} = (1/\sigma^2)\sum_{i=1}^{N} d_j(x_i)d_k(x_i)$, so the elements of the curvature matrix are given by

$$h_{11} = \frac{1}{\sigma^2}\sum_{i=1}^{N}\exp\left(-t_i^2\right)$$

$$h_{12} = \frac{r}{\sigma^2}\sum_{i=1}^{N} t_i\exp\left(-t_i^2\right)$$

$$h_{13} = \frac{r}{\sigma^2}\sum_{i=1}^{N} t_i^2\exp\left(-t_i^2\right)$$

$$h_{22} = \frac{r^2}{\sigma^2}\sum_{i=1}^{N} t_i^2\exp\left(-t_i^2\right)$$

$$h_{23} = \frac{r^2}{\sigma^2}\sum_{i=1}^{N} t_i^3\exp\left(-t_i^2\right)$$

$$h_{33} = \frac{r^2}{\sigma^2}\sum_{i=1}^{N} t_i^4\exp\left(-t_i^2\right)$$

where $r = a_1/a_3$

We see from this that unless the data points are located symmetrically relative to the peak of the Gaussian, all six matrix elements will be nonzero, and the resulting variance of the fit will be a function of the amount of offset Therefore, we consider only the simplest, and in fact most common, case where such a symmetry exists, at least approximately, and furthermore assume that the data points are uniformly distributed, as in the polynomial case Then $h_{12} = h_{23} = 0$, and the curvature and covariance matrices have the same form dealt with above [see Eq (A-1)] Thus, proceeding as in the polynomial case, we have

$$\left.\begin{aligned} h_{11} &= \frac{1}{\sigma^2}(2S_0+1) \\ h_{13} &= \frac{2}{\sigma^2}\delta_t^2 r S_2 \\ h_{22} &= \frac{2}{\sigma^2}\delta_t^2 r^2 S_2 \\ h_{33} &= \frac{2}{\sigma^2}\delta_t^4 r^2 S_4 \end{aligned}\right\} \tag{A-7}$$

where $S_0 = \sum_{i=1}^{(N-1)/2} \exp(-i^2\delta_t^2)$, $S_2 = \sum_{i=1}^{(N-1)/2} i^2 \exp(-i^2\delta_t^2)$, $S_4 = \sum_{i=1}^{(N-1)/2} i^4 \exp(-i^2\delta_t^2)$, and $\delta_t^2 = (12/[N^2-1])(\sigma_x^2/a_3^2) = (12/[N^2-1])\sigma_t^2$ is the spacing between points, normalized with respect to the standard deviation of the Gaussian function, a_3, and $\sigma_t = \sigma_x/a_3$

The above sums, which depend on δ_t, cannot be expressed in closed form in the general case, but in the limit as $N \to \infty$ and $\delta_t \to 0$, they may be expressed in terms of integrals Thus, if we further restrict ourselves to the most useful case where the data points extend out to at least two standard deviations of the Gaussian, i e , $L \geq 4a_3$, where L is the full width of the interval of the data points along the x-axis, then we find

$$\left.\begin{aligned} \lim_{N,\sigma_x\to\infty} \delta_t S_0 &= \frac{\sqrt{\pi}}{2} \\ \lim_{N,\sigma_x\to\infty} \delta_t^3 S_2 &= \frac{\sqrt{\pi}}{4} \\ \lim_{N,\sigma_x\to\infty} \delta_t^5 S_4 &= 3\frac{\sqrt{\pi}}{8} \end{aligned}\right\} \tag{A-8}$$

From the general form of the covariance matrix for symmetric data points with $M = 3$ [see Eq (A-3), for example] and the derivatives given by Eq (A-6), the variance of the fit becomes

$$\sigma_y^2(x) = \mathbf{d}^T(x)\mathbf{C}\mathbf{d}(x) = e^{-t^2}\begin{bmatrix}1 & rt & rt^2\end{bmatrix}\begin{bmatrix}C_{11} & 0 & C_{13}\\ 0 & C_{22} & 0\\ C_{13} & 0 & C_{33}\end{bmatrix}\begin{bmatrix}1\\ rt\\ rt^2\end{bmatrix}$$

$$= e^{-t^2}\left[C_{11} + (C_{22}r + 2C_{13})rt^2 + C_{33}r^2t^4\right]$$

Substituting Eqs (A-7) and (A-8) into Eq (A-4), we finally obtain

$$\eta^2 = \sqrt{\frac{3}{\pi}}\sigma_t e^{-(\xi\sigma_t)^2}\left(3 + 4\sigma_t^4\xi^4\right)$$

where $(L_\infty/a_3) \equiv \lim_{N\to\infty}(L/a_3) = \lim_{N\to\infty}(L/\sigma_x)\sigma_t = 2\sqrt{3}\sigma_t$ has been used

B. Data Errors Proportional to $y(x;\mathbf{a})$

When the dependent variable extends over a very large range, as in the case of the Gaussian function, it often happens that the measurement error scales with the measurement itself, at least in a piecewise sense, due to the changing of instrument ranges as the variable values change Thus, letting $\sigma_i = \beta y(x_i, \mathbf{a})$, the curvature matrix elements become

$$h_{jk} = \frac{1}{\beta^2} \sum_{i=1}^{N} \frac{d_j(x_i) d_k(x_i)}{y^2(x_i, \mathbf{a})}$$

and using Eq (A-6) for the derivatives, we have

$$\left.\begin{aligned}
h_{11} &= \frac{N}{(a_1\beta)^2} \\
h_{12} &= \frac{r}{(a_1\beta)^2} \sum_{i=1}^{N} t_i \\
h_{13} &= \frac{r}{(a_1\beta)^2} \sum_{i=1}^{N} t_i^2 \\
h_{22} &= \frac{r^2}{(a_1\beta)^2} \sum_{i=1}^{N} t_i^2 \\
h_{23} &= \frac{r^2}{(a_1\beta)^2} \sum_{i=1}^{N} t_i^3 \\
h_{33} &= \frac{r^2}{(a_1\beta)^2} \sum_{i=1}^{N} t_i^4
\end{aligned}\right\} \qquad \text{(A-9)}$$

These are of the same form as was found for the case of the quadratic fit, so the derivation follows through in much the same way, giving the result

$$\sigma_y^2(x) = \frac{(a_1\beta)^2}{N} e^{-t^2} \left[A_0^{(2)}(N) + A_2^{(2)}(N) \left(\frac{t}{\sigma_t}\right)^2 + A_4^{(2)}(N) \left(\frac{t}{\sigma_t}\right)^4 \right]$$

where we have again assumed symmetric data, and the coefficients that appear are the same ones appearing in the quadratic fit This may be simplified by noting that $a_1\beta = a_1\sigma_i / y(x_i, \mathbf{a}) = a_1\sigma(x)/y(x, \mathbf{a}) = \sigma(x)e^{t^2/2}$ so that we finally obtain $\eta^2 = A_0^{(2)}(N) + A_2^{(2)}(N)\xi^2 + A_4^{(2)}(N)\xi^4$, where $\eta = \sqrt{N}([\sigma_y(x)]/[\sigma(x)])$ and $t/\sigma_t = (x - \overline{x})/\sigma_x = \xi$, in exact agreement with the expression for the quadratic fit

IV. Monte Carlo Simulations

As a check on the above derivations, a series of Monte Carlo simulations has been carried out for the various cases treated by creating ensembles of data of the form $y_{ni} = y(x_i, \mathbf{a}) + r_n(x_i)$, where $r_n(x_i)$

is a zero-mean, normally distributed random variable having variance σ_i, fitting the function $y(x, \mathbf{a})$ to each of these to obtain an ensemble of fitted functions $y(x, \mathbf{a}_n)$, and computing the variance $\sigma_y^2(x_m) = (1/N_e)\sum_{n=1}^{N_e} y^2(x_m, \mathbf{a}_n) - [(1/N_e)\sum_{n=1}^{N_e} y(x_m, \mathbf{a}_n)]^2$ for a series of values of x_m, where N_e is the number of ensemble members, so that comparisons can be made with the theoretical results These are shown in Figs 5 through 7, and it can be seen that the agreement is excellent

V. Parameter Errors for Gaussian Fitting Functions

The results obtained above permit the calculation of standard errors for the parameters a_j appearing in the various cases treated, i e , $\sigma_{a_j}^2 = C_{jj}$ However, since these errors will depend on the location of the y-axis, the results are not of general interest unless the data are located symmetrically relative to the fitting function, as, for example, in the case of the Gaussian function This function is of sufficient interest to warrant a separate discussion, which we present below for the two cases considered earlier, namely, constant data errors and data errors proportional to the function

A. Constant Data Errors

When Eq (A-7) is substituted into Eq (A-4), the following expressions are obtained for the normalized standard errors

$$N\frac{\sigma_{a_1}^2}{\sigma^2} = \frac{NS_4}{(2S_0+1)S_4 - 2S_2^2}$$

$$N\frac{(\sigma_{a_2}/a_3)^2}{(\sigma/a_1)^2} = \frac{1}{2}\frac{N}{\delta_t^2 S_2}$$

$$N\frac{(\sigma_{a_3}/a_3)^2}{(\sigma/a_1)^2} = \frac{1}{2}\frac{N(2S_0+1)}{\delta_t^4[(2S_0+1) - 2S_2^2]}$$

where the sums S_0, S_2, and S_4 are given by Eq (A-7), and $\delta_t^2 = (12/[N^2-1])(\sigma_x^2/a_3^2) = (12/[N^2-1])\sigma_t^2$, as before These results are valid for any odd value of $N \geq 3$, and in Fig 8 we show the general behavior as a function of the variable $L/a_3 = (N-1)\delta_t$ for N =3, 5, 7, 9, and 11 In the limit $N \to \infty$ and $L/a_3 \geq 4$, the above normalized standard errors become

$$N\frac{\sigma_{a_1}^2}{\sigma^2} = \frac{3}{2\sqrt{\pi}}\frac{L}{a_3}$$

$$N\frac{(\sigma_{a_2}/a_3)^2}{(\sigma/a_1)^2} = \frac{2}{\sqrt{\pi}}\frac{L}{a_3}$$

$$N\frac{(\sigma_{a_3}/a_3)^2}{(\sigma/a_1)^2} = \frac{2}{\sqrt{\pi}}\frac{L}{a_3}$$

B. Proportional Data Errors

Substituting Eq (A-9) into Eq (A-4), we obtain the following normalized standard errors

$$N\frac{\sigma_{a_1}^2}{a_1^2} = \beta^2 A_0^{(2)}(N) = \beta^2 \frac{3(3N^2-7)}{4(N^2-4)} \to \frac{9}{4}\beta^2$$

as $N \to \infty$,

$$N\frac{\sigma_{a_2}^2}{a_3^2} = \frac{\beta^2}{\sigma_t^2}$$

independent of N, and

$$N\frac{\sigma_{a_2}^2}{a_3^2} = \frac{\beta^2}{\sigma_t^4} A_4^{(2)}(N) = \frac{\beta^2}{\sigma_t^4}\ \frac{5(N^2-1)}{4(N^2-4)} \to \frac{5}{4}\ \frac{\beta^2}{\sigma_t^4}$$

as $N \to \infty$, where β is the error proportionality constant, i e , $\sigma_i = \beta y(x_i, \mathbf{a})$

Novel Solutions to Low-Frequency Problems With Geometrically Designed Beam-Waveguide Systems

W A Imbriale, M S Esquivel, and F Manshadi
Communications Ground Systems Section

The poor low-frequency performance of geometrically designed beam-waveguide (BWG) antennas is shown to be caused by the diffraction phase centers being far from the geometrical optics mirror focus, resulting in substantial spillover and defocusing loss Two novel solutions are proposed (1) reposition the mirrors to focus low frequencies and redesign the high frequencies to utilize the new mirror positions and (2) redesign the input feed system to provide an optimum solution for the low frequency A novel use of the conjugate phase-matching technique is utilized to design the optimum low-frequency feed system, and the new feed system has been implemented in the JPL research and development BWG as part of a dual S-/X-band (2 3-GHz/8 45-GHz) feed system The new S-band feed system is shown to perform significantly better than the original geometrically designed system

I. Introduction

JPL has recently built a new 34-m beam-waveguide (BWG) antenna at Goldstone's Deep Space Station 13 site (DSS 13) The design of the center-fed BWG consists of a beam magnifier ellipse, in a pedestal room located below ground level, that transforms a 22-dB gain feedhorn into a high-gain 29-dB gain pattern for input to a standard four-mirror (two flat and two paraboloid) BWG system The design of the upper section of the BWG is based on geometrical optics (G O) criteria introduced by Mizusawa and Kitsuregawa in 1973 [1,2], which guarantees a perfect image from a reflector pair The system was initially designed (Phase 1) for operation at 8 45 GHz (X-band) and 32 GHz (Ka-band) and has less than 0 2-dB loss (determined by comparing the gain of a 29-dB gain horn feeding the dual-shaped reflector system with that obtained using the BWG system) [3,4] In Phase 2, S-band (2 3 GHz) is to be added

If a standard 22-dB S-band horn is placed at the input focus of the ellipse, the BWG loss is greater than 1 5 dB, primarily due to the fact that, for low frequencies, the diffraction phase centers are far from the G O mirror focus, resulting in a substantial spillover and defocusing loss This defocusing is especially a problem for the magnifier ellipse, where the S-band phase center at the output of the ellipse is 3 m from the G O focus If the input to the paraboloids were focused, the output defocusing would only cause a 0 3-dB loss One solution would be to move the high-frequency phase center at the ellipse output to the low-frequency phase center (accomplished at X-band by simultaneously increasing the gain of the input horn to 26 dB and moving the horn phase center 0 5-m below the input focus) and to reposition the phase centers to the input focus of the paraboloids This can be accomplished by leaving the ellipse

in its original position and increasing the spacing between the paraboloids With this arrangement, the BWG loss at S-band is only 0 4 dB and the loss at X-band is virtually unaffected This solution has the disadvantage, however, of necessitating a physical modification to the structure of the BWG system

A second solution is to redesign the horn to provide an optimum solution for S-band The question is how to determine the appropriate gain and location for this feed A straightforward design by analysis would prove cumbersome because of the large number of scattering surfaces required for the computation Rather, a unique application was made of the conjugate phase-matching techniques to obtain the desired solution A plane wave was used to illuminate the main reflector, and the fields from the currents induced on the subreflector were propagated through the BWG to a plane centered on the input focal point By taking the complex conjugate of the currents induced on the plane and applying the radiation integral, the far-field pattern was obtained for a theoretical horn that maximizes the antenna gain

To synthesize a horn quickly and inexpensively, the theoretical horn was matched as well as possible by an appropriately sized circular corrugated horn The corrugated horn performance was only 0 2-dB lower than the optimum theoretical horn but 1 4-dB above the standard 22-dB horn A system employing the corrugated horn was built and tested and installed in the 34-m BWG antenna as part of a simultaneous S-/X-band receiving system

II. The Problem

The basic design of the center-fed beam waveguide is shown in Fig 1 The shaped dual-reflector system (focal point f_1) is designed to provide uniform illumination with a 29 8-dB-gain horn at the input The upper four mirrors of the beam waveguide (from f_2 to f_1) are designed to image the input (at f_2) to the output (at f_1) Thus, to provide a 29 8-dB-pattern output at f_1 requires a 29 8-dB-gain pattern at the input, f_2 The 29 8-dB-gain pattern is generated by using a 22-dB-gain horn at f_3 (the input focus of the magnifier ellipse) to provide the required gain at the output focus of the ellipse, f_2 Figure 2 compares the input and output patterns from the BWG system with the 29-dB-gain horn at X-band Since the BWG project seeks to introduce S-band (2 3 GHz) into the antenna in the Phase 2 project, it is useful to inquire what happens when a 22-dB S-band horn is placed at the input focus of the ellipse Ignoring spillover past the BWG mirrors, the defocusing loss is 0 9 dB The BWG spillover loss is 0 5 dB, yielding a total BWG loss of 1 4 dB The principal cause of the defocusing loss is related to the fact that, for low frequencies, the diffraction phase center at the Cassegrain focus f_1 is far—3 56 m (140 in)—from the G O focus This loss is illustrated in Fig 3, where a plot of gain versus the z-displacement motion of the BWG assumes that the entire BWG is moved relative to the focal point of the dual-reflector system at f_1 Only the aperture illumination, phase efficiency, dual-reflector spillover, and center blockage loss are included in the calculation, BWG internal spillover is ignored for this comparison since it would be the same for each point of the curve in Fig 3 This defocusing is especially a problem for the magnifier ellipse, where the S-band phase center at the output of the ellipse is 3 05 m (120 in) from the G O focus at f_2 Thus, the input to the two-paraboloid section is defocused, causing the majority of the spillover loss and adding to the defocusing of the paraboloid output If the input to the upper BWG section were focused, the output would then be defocused by some 1 5 to 2 25 m However, this defocusing would cause only a 0 2- to 0 3-dB loss Efforts were made to determine if adjustment to the input pattern amplitude or phase would move the low-frequency diffraction phase center to the G O phase center at f_2 [5] It was determined that if the ellipsoidal mirror were large enough ($> 30\lambda$) it would be possible, but for smaller ellipsoids (18λ in this case), it was not possible to move the focus all the way to the G O phase center, f_2

III. Optics Redesign

To overcome the problem of the disparate phase centers (between X- and S-bands), it was found that, instead of moving the low-frequency phase center to the G O focus for the ellipse, the high-frequency

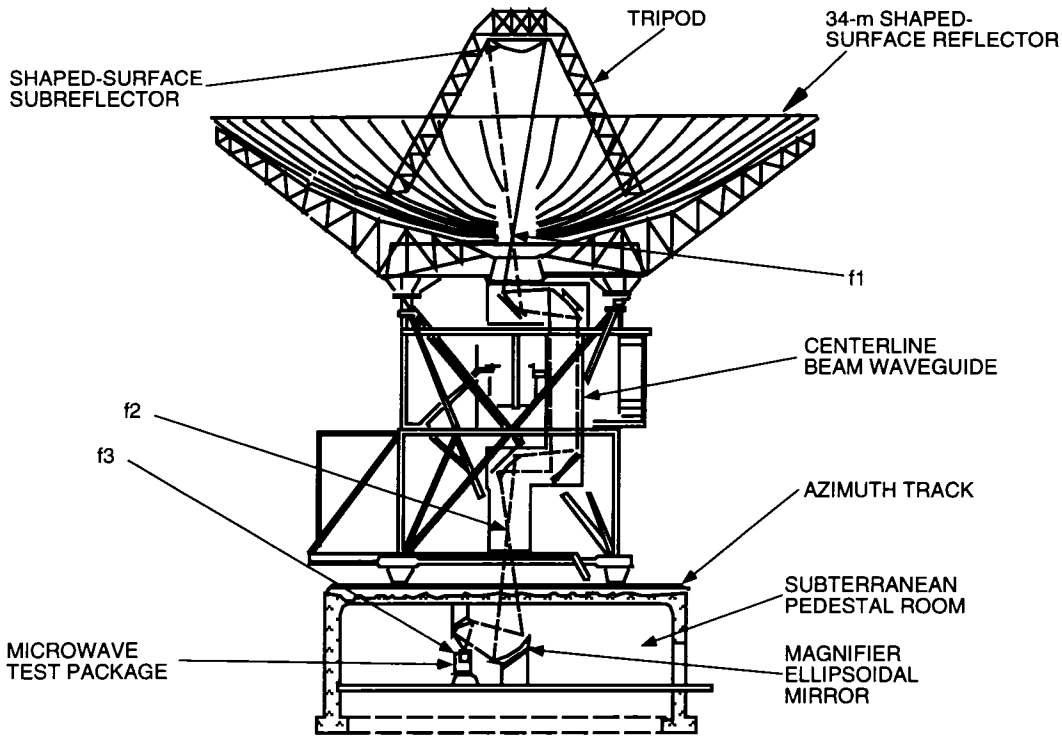

Fig 1 New NASA beam-waveguide antenna

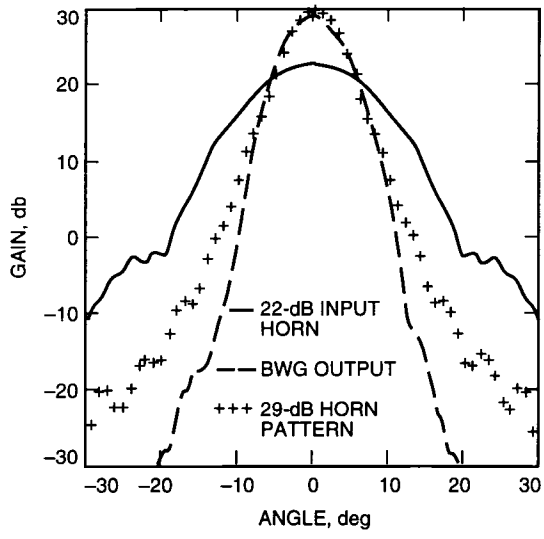

Fig 2 Beam-waveguide input and output radiation patterns at X-band

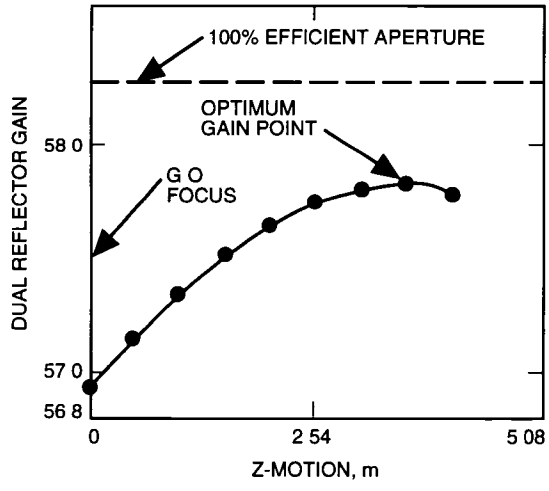

Fig 3 Beam-waveguide defocusing curve at S-band

phase center should be moved to the low-frequency phase center and the ellipse output repositioned to put these phase centers at the input focus of the paraboloids The motion of the X-band phase center can be accomplished by simultaneously increasing the gain of the X-band input horn to 26 dB and moving the horn phase center approximately 0 5-m below the input focus at f_3 Since the position of the pedestal room is fixed with respect to the reflector, and since there is insufficient room to move the output focal point of the ellipse the required distance upward, the separation of the parabolas is increased to effectively move the paraboloid input focus down to the phase centers (see Fig 4) Because the motion of the paraboloids

is in the path where the rays are parallel, and the increase in distance is not sufficient for the rays to diverge, there is very little effect on the BWG performance The distance selected was 2 03 m (80 in), to minimize the motion of the X-band phase center, so consequently a small S-band defocusing loss is retained With this arrangement, the BWG loss at S-band is only 0 4 dB, and the BWG loss at X-band is virtually unaffected Figure 5 compares the S- and X-band BWG output with the 29-dB horn and indicates that the modified design is an acceptable compromise

The analysis of the RF performance is calculated using physical optics (P O) on the BWG mirrors and subreflector [6] and the Jacobi–Bessel series [7] on the main reflector In these calculations, a feed radiation pattern was modeled as a set of spherical-wave expansion (SWE) coefficients expanded about f_3 [8] The coefficients were used to illuminate M_5, the BWG mirror in the pedestal room The induced currents on M_5 were cascaded by means of P O through M_4, M_3, M_2, M_1, the subreflectors, and the main reflectors The Jacobi–Bessel method was implemented at the main reflector to obtain the secondary pattern of the antenna

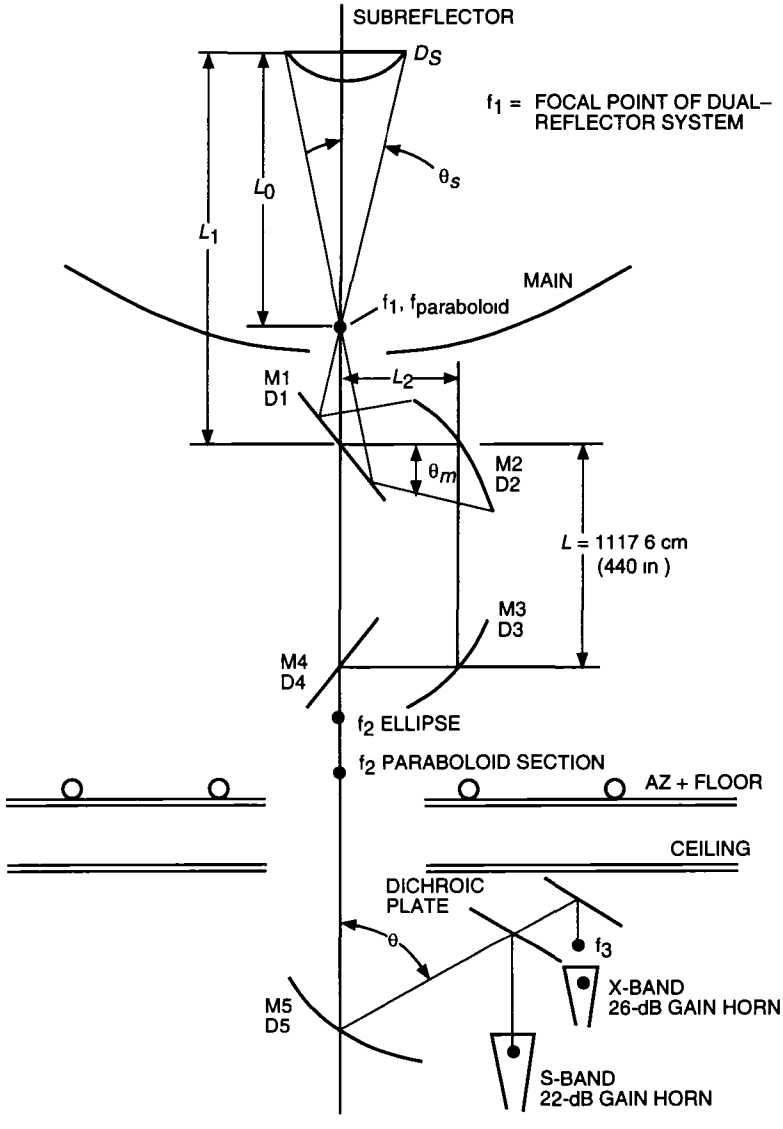

Fig 4 Modified design geometry

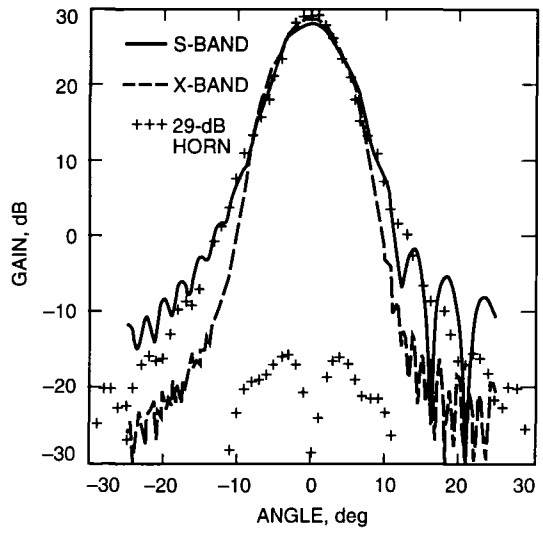

Fig 5 Modified design performance (output of BWG system)

Even though the mirrors are unaffected, this solution still requires a physical modification to the BWG structure and was deemed unacceptable, thus, another method that did not modify the BWG system itself was required

IV. Focal-Plane Method

The goal of the design was to maximize the gain over noise temperature (G/T) of the BWG antenna Since there are a large number of scattering surfaces (eight total), an optimization method that required repeated computation of the gain and noise temperature of the entire system would be rather time consuming Instead, a unique application of the conjugate phase-matching technique (called the focal-plane method) was tried In this method, a uniform plane wave was used to illuminate the main reflector, and the fields from the currents induced on the subreflector were propagated through the BWG, M_1, M_2, M_3, M_4, and M_5 Finally, the currents on a circular aperture with a 23λ diameter at the focal plane centered at f_3 (Fig 6) were computed By taking the complex conjugate of these currents and applying the radiation integral, the far-field pattern was obtained for a theoretical horn that should maximize the gain There was no a priori guarantee that the pattern produced by this method would be easily realized However, the pattern is nearly circularly symmetric, and the theoretical horn was able to be matched fairly well by a circular corrugated horn

Figure 7 shows the near-field E-plane patterns of the theoretical horn and a 19-dBi circular corrugated horn The agreement in amplitude and phase is quite good out to $\theta = 21$ deg, the angle subtended by M_5 The point of reference for the SWE coefficients used to generate the 19-dBi corrugated horn pattern was shifted until the radiation pattern matched the one of the theoretical horn centered at the focal plane f_3 By this method, the position of the 19-dBi corrugated horn in the antenna could be determined It turned out that the S-band corrugated horn's aperture position was 352 425 cm from the center of the magnifying ellipsoid M_5

The 19-dBi circular corrugated horn pattern was converted into a set of SWE coefficients that was then used in the P O analysis of the 34-m BWG antenna at S-band Figure 8 shows the input and output of the magnifying ellipse, M_5, along with the output of the BWG system The 19-dB pattern of

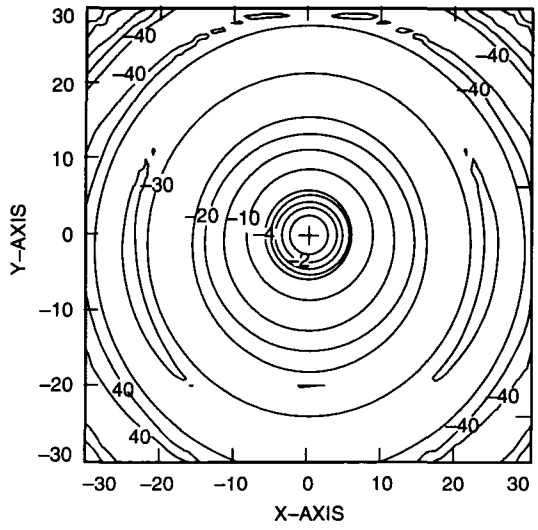

Fig 6 Contour plot of currents induced on plane located at f_3 using the focal-plane method

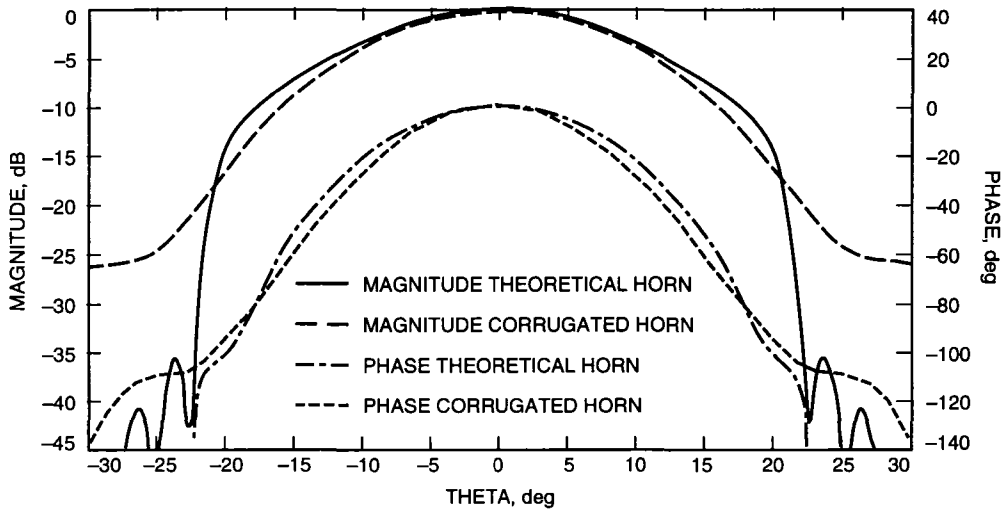

Fig 7 E-plane near-field (R = 4 2 m, referenced to f_3) patterns

the corrugated horn is magnified into a 28 7-dB pattern by the ellipse, the BWG mirrors add an extra 1 1 dB, so that at the output of the system, the gain of the pattern is 29 8 dB, the gain from which the dual-shaped system was synthesized

Basically, the focal-plane method provided an unexpected solution to the defocusing problem of the 34-m BWG antenna at S-band the use of a lower-gain horn Previous work done on the antenna at X-band and Ka-band had shown that its G/T would improve if corrugated horns with higher gains than the original-design 22 dB were used For instance, an X-/Ka-band feed system uses corrugated horns with gains of 25 0 and 26 dB, respectively [9] Thus, when the task of implementing an S-band feed system in the antenna was initiated, a solution that required a higher-gain horn was expected

Part of the skepticism was in the area of noise temperature It was well known that a lower-gain horn would contribute more spillover, which would increase the noise temperature of the system What was

not understood at the time was that the 19-dBi corrugated horn would only have a higher spillover loss at the first reflector, M_5, and that its performance through the remainder of the BWG system would be better than for the standard 22-dBi corrugated horn Table 1, which lists P O and Jacobi–Bessel analysis results of the antenna at S-band, corroborates this observation In this table, the spillover of the antenna mirrors, the antenna efficiency, and system noise temperature are listed for the 19-dBi corrugated horn and the theoretical horn pattern predicted by the focal-plane method Also, for comparison purposes, the calculated performance of a 22-dBi corrugated horn is presented from [10]

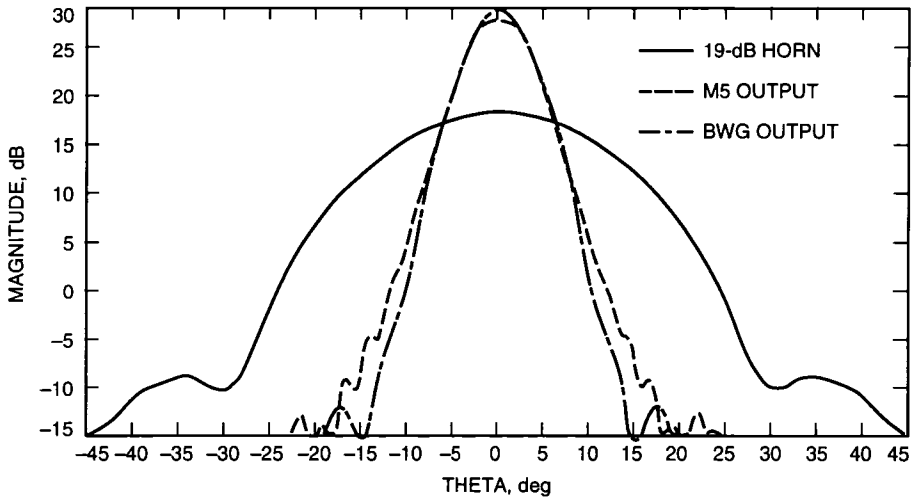

Fig 8 Beam-waveguide input and output radiation patterns at S-band

Table 1 S-band P O and Jacobi–Bessel calculations

Parameter	22-dBi corrugated horn [10]	19-dBi corrugated horn	Theoretical horn
Spillover, percent			
M_6	—	0 41	—
M_5	2 05	2 46	0 24
M_4	1 57	0 70	1 19
M_3	5 91	0 73	0 86
M_2	5 55	0 96	1 29
M_1	1 36	0 26	0 46
Subreflector	—	1 14	1 94
Main reflector	—	0 94	3 61
Efficiency			
Total efficiency	0 48415	0 6827	0 69502
Total efficiency, dB	55 102	56 594	56 672
Noise temperature			
Total noise, K	73 574	37 10	35 314
Total noise, dB	18 67	15 69	15 48
G/T, dB	36 43	40 90	41 19

V. BWG S-/X-Band Feed System

The S-band feed is part of a simultaneous S-/X-band receive system implemented on the new BWG antenna The general configuration of the feed system, the detail design, and measured performance are described in this section

A. Theory of Operation

Figure 9 shows the main components of the S-/X-band feed system the X-band feed, the S-band feed, the S-/X-band dichroic reflector, and the X-band flat reflector The S-band receive frequency band is 2200 to 2300 MHz, and the X-band receive frequency band is 8200 to 8600 MHz

The S-band signal received from deep space is collected by the main/subreflector and is focused at f_1 Reflectors M_1 through M_4 guide the signal to the rotating ellipsoid focus f_2 The signal is then scattered off the ellipsoid mirror, reflected by the dichroic reflector, and focused at the other focal point of the elliptical mirror This signal is received by the S-band feedhorn in the S-band feed package

The X-band signal is guided by the beam waveguide to the basement in the same manner as the S-band signal However, after scattering off the ellipsoid, it passes through the dichroic mirror with very little loss, reflected by the X-band flat reflector, and is focused at the other focal point of the ellipsoid This signal is received by the X-band feedhorn in the X-band package

B. Detail Design

A block diagram of the S-/X-band feed packages is provided in Fig 10 The low-noise amplifier (LNA) is a dual-frequency LNA, i e , it contains both an X-band LNA and an S-band LNA in one cryogenic package The S- and X-band feeds are packaged separately, however, they are physically connected since they share the same LNA package The feedhorns are corrugated with the same corrugations and flare angle as the standard JPL feedhorns [11] The gain of the feedhorns is 19 1 dB for S-band and 25 0 dB for X-band As discussed in the previous section, a 25-dB horn was used at X-band instead of the originally designed system (using the 22-dB horn) since it was discovered that a 25-dB horn would reduce the noise temperature Although the 25-dB horn reduced the efficiency somewhat, the gain in noise temperature more than offset the loss in efficiency, and the 25-dB-gain horn maximized the G/T of the system Right-hand circular polarization (RCP) or left-hand circular polarization (LCP) polarizers provide the capability to select the reception In the S-band package, the position of the polarizer can be changed easily because of the use of the rotary joints, but in the X-band package, the position of the polarizer is fixed To change polarization on the X-band, the polarizer has to be unscrewed and then rotated The couplers are used for injection of noise to check the linearity of the LNAs The waveguide switches are used to connect the LNAs to the feedhorns or to the ambient loads for noise temperature and linearity measurements

The S-/X-band dichroic reflector is a frequency selective surface that passes the X-band signal but reflects the S-band signal The S-/X-band dichroic plate used at DSS 13 is a 198 1-cm × 141 5-cm × 3 576-cm rectangular aluminum plate with an elliptical perforated area (see Fig 11) The holes in the perforated area are based on an old dichroic plate design [12] This design employs the Pyleguide holes originally used by Pyle [13] However, to reduce the fabrication cost, the corner radius of the holes was increased from 0 013 to 0 318 cm, as shown in Fig 11 An analysis of the propagation constant of the fields in the Pyleguide holes shows that the change in the propagation constant due to this modification is far less than the change due to the tolerances of the other critical dimensions of the holes [1] This minor change reduced the fabrication cost of the S-/X dichroic reflector by more than 60 percent

[1] J C Chen and P H Stanton, "Effect of Corner Radius on the Performance of an S-/X-Band Dichroic Plate With Pyleguide Aperture," JPL Interoffice Memorandum 3327-92-078 (internal document), Jet Propulsion Laboratory, Pasadena, California, November 24, 1992

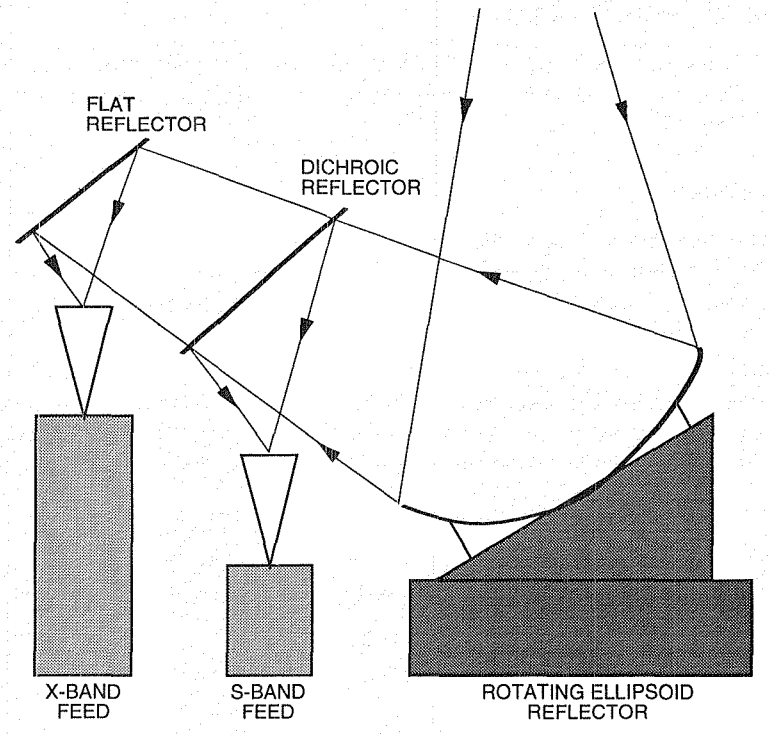

Fig. 9. DSS-13 S-/X-band feed system.

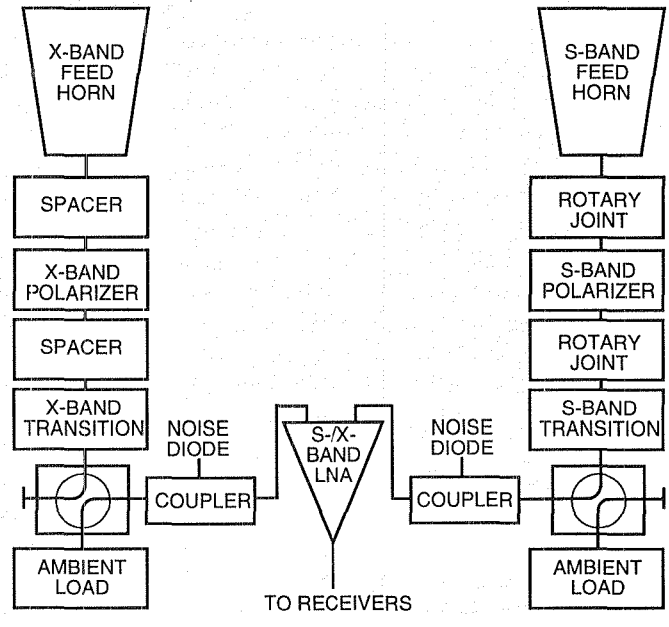

Fig. 10. DSS-13 S-/X-band feed block diagram.

The frames for the S- and X-band packages were fabricated using Bosch extruded aluminum struts. These struts are prefabricated, strong, lightweight, and flexible. Their anodized aluminum surface finish is scratch and corrosion resistant. Since all the elements of the frames are bolted together, it is very easy to modify these frames as needed in the future. The use of these materials resulted in a cost savings of more than 50 percent compared to conventional welded steel framing.

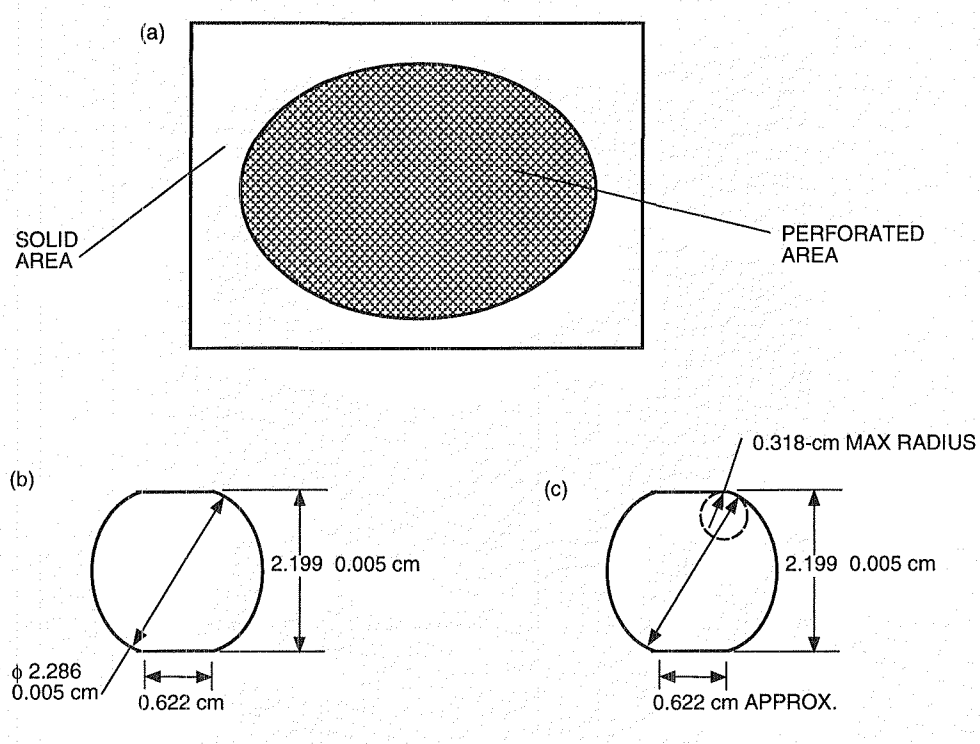

Fig. 11. DSS-13 S-/X-band dichroic reflector: (a) layout, (b) original Pyleguide design, and (c) modified Pyleguide design.

Figure 12 shows a picture of the S- and X-band microwave feed assembly installed in the DSS-13 BWG antenna.

C. Feed System Performance

The predicted and measured noise temperatures of the S-/X-band LNAs, microwave feeds, and the overall DSS-13 BWG antenna are shown in Table 2. The higher-than-standard DSN noise temperature measured for the X-band LNA is due to the age of the package, which was acceptable for its intended use. The predicts are calculated from the theoretical or measured loss of the individual component of each system. The measurements for the feeds were made at Goldstone before installation in the antenna pedestal room. The measurements for the overall antenna were made after the feed packages were installed and aligned in the pedestal room.

The predicted S-band efficiency from Table 1 was 68 percent, and the measured efficiency was 67.5 percent, demonstrating the successful design and implementation. For comparison, the predicted X-band efficiency (at the rigging angle of 45 deg) was 72.7 percent, and the measured efficiency, including the dichroic plate, was 70.1 percent.

There are two interesting observations on the variation of efficiency with azimuth and elevation. The main reflector surface shape changes slightly with elevation due to backup structure distortion caused by uneven gravitation loading as a function of elevation angle. This is only a problem at the higher frequencies of X- and Ka-band. The surface is optimized for 45-deg elevation and falls off more or less symmetrically at the zenith and horizon. This is illustrated in Fig. 13, which shows the variation of X-band efficiency with elevation. For X- and Ka-band, there is almost no variation of efficiency with azimuth. However, for S-band (which has virtually no variation with elevation), there is both a calculated

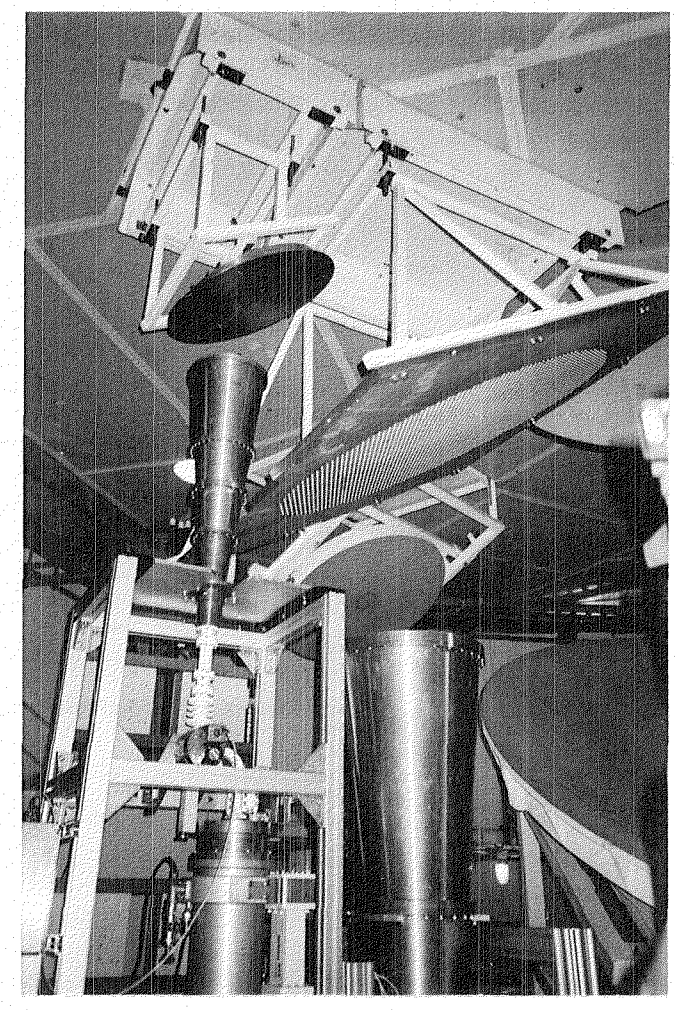

Fig. 12. Feed system installed in BWG antenna.

Table 2. Noise temperature predicts and measurements, K.

System	S-band predict	S-band measurement	X-band predict	X-band measurement
LNA	8.3	8.72	12.0	14.09
Feed system (including LNA)	17.69	17.5	23.07	24.0
Antenna (total)	37.26	38.0	32.9	33.0

and a measured variation with azimuth, as shown in Fig. 14.[2] This is due to the rotation of the ellipse with respect to the upper BWG mirrors. At S-band, there is more asymmetry at the ellipse output than at X- or Ka-band, probably attributable to more of the ellipse being illuminated due to the lower-gain horn.

[2] The measured data are courtesy of Michael Klein, Jet Propulsion Laboratory, Pasadena, California, May 1995.

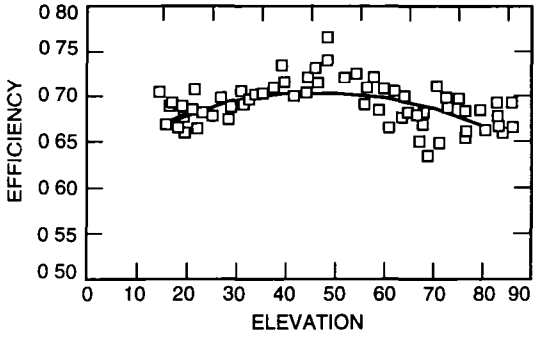

Fig 13 Measured X-band efficiency variation with elevation

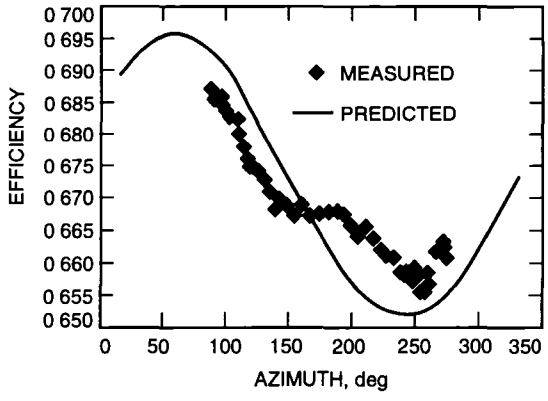

Fig 14 S-band efficiency variation with azimuth

VI. Conclusions

A novel solution to the S-band design problems in a geometrically designed BWG system has been demonstrated The proposed design was implemented as part of an S-/X-band feed system in the DSS-13 antenna located at Goldstone, California The measured and predicted performances of the feed systems and the overall antenna agree very closely

Acknowledgments

This task owes its successful completion to the teamwork and dedication of the people who were involved Many people from different organizations have made valuable contributions by offering their expertise and hard work In particular, the authors would like to acknowledge J Chen and P Stanton for dichroic plate analysis, T Otoshi, M Franco, and S Stewart for feed and antenna measurements, J Fernandez and J Loreman for repair and testing of the S-/X-band LNA, D Ball, R Bryant, and D Ohashi for mechanical design, and M Gatti for funding support

References

[1] M Mizusawa and T Kitsuregawa, "A Beam-Waveguide Feed Having a Symmetric Beam for Cassegrain Antennas," *IEEE Trans Antennas Propagat*, vol AP-21, pp 844–846, November 1973

[2] T Veruttipong, J R Withington, V Galindo-Israel, W A Imbriale, and D Bathker, "Design Considerations for Beam-Waveguide in the NASA Deep Space Network," *IEEE Trans Antennas Propagat*, vol AP-36, pp 1779–1787, December 1988

[3] T Veruttipong, W Imbriale, and D Bathker, "Design and Performance Analysis of the New NASA Beam-Waveguide Antenna," *National Radio Science Meeting*, Boulder, Colorado, p 59, January 1990

[4] T Veruttipong, W Imbriale, and D Bathker, "Design and Performance Analysis of the DSS-13 Beam-Waveguide Antenna," *The Telecommunications and Data Acquisition Progress Report 42-101, January–March 1990*, Jet Propulsion Laboratory, Pasadena, California, pp 99–113, May 15, 1990

[5] S Rengaragan, V Galindo-Israel, and W Imbriale, "A Study of Amplitude and Phase Shaping Effects in Beam Waveguides," *IEEE AP-S International Symposium*, Dallas, Texas, pp 1502–1505, May 1990

[6] W A Imbriale and R E Hodges, "The Linear-Phase Triangular Facet Approximation in Physical Optics Analysis of Reflector Antennas," *Applied Computational Electromagnetic Society*, vol 6, no 2, pp 74–85, Winter 1991

[7] Y Rahmat-Samii and V Galindo-Israel, "Shaped Reflector Antenna Analysis Using the Jacobi–Bessel Series," *IEEE Trans Antennas Propagat*, vol AP-28, no 4, pp 425–435, July 1980

[8] A C Ludwig, "Near-Field Far-Field Transformations Using Spherical-Wave Expansions," *IEEE Trans Antennas Propagat*, vol AP-19, no 2, pp 214–220, March 1971

[9] D A Bathker, W Veruttipong, T Y Otoshi, and P W Cramer, Jr, "Beam-Waveguide Antenna Performance Predictions With Comparisons to Experimental Results," *IEEE Transactions on Microwave Theory and Techniques*, vol 40, no 6, pp 1274–1285, June 1992

[10] T Cwik and J C Chen, "DSS-13 Phase II Pedestal Room Microwave Layout," *The Telecommunications and Data Acquisition Progress Report 42-106, April–June 1991*, Jet Propulsion Laboratory, Pasadena, California, pp 298–306, August 15, 1991

[11] S A Brunstein, "A New Wideband Feedhorn With Equal E- and H-Plane Beamwidths and Suppressed Sidelobes," *Deep Space Network, Space Programs Summary 37-58*, vol II, Jet Propulsion Laboratory, Pasadena, California, pp 61–64, July 1969

[12] P D Potter, *Improved Dichroic Reflector Design for the 64-Meter Antenna S- and X-Band Feed Systems*, JPL Technical Report 32-1526, vol XIX, Jet Propulsion Laboratory, Pasadena, California, pp 55–62, February 15, 1974

[13] J R Pyle, "Cutoff Wavelength of Waveguides With Unusual Cross Sections," *IEEE Transactions on Microwave*, Correspondence, vol MTT-12, no 5, pp 556–557, September 1964

Analysis of Tipping-Curve Measurements Performed at the DSS-13 Beam-Waveguide Antenna at 32.0 and 8.45 Gigahertz

D D Morabito
Communications Systems and Research Section

L Skjerve
Tracking Systems and Applications Section

This article reports on the analysis of the Ka-band Antenna Performance Experiment tipping-curve data acquired at the DSS-13 research and development beam-waveguide (BWG) antenna. By measuring the operating system temperatures as the antenna is moved from zenith to low-elevation angles and fitting a model to the data, one can obtain information on how well the overall temperature model behaves at zenith and approximate the contribution due to the atmosphere. The atmospheric contribution estimated from the data can be expressed in the form of (1) atmospheric noise temperatures that can provide weather statistic information and be compared against those estimated from other methods and (2) the atmospheric loss factor used to refer efficiency measurements to zero atmosphere. This article reports on an analysis performed on a set of 68 8.4-GHz and 67 32-GHz tipping-curve data sets acquired between December 1993 and May 1995 and compares the results with those inferred from a surface model using input meteorological data and from water vapor radiometer (WVR) data. The general results are that, for a selected subset of tip curves, (1) the BWG tipping-curve atmospheric temperatures are in good agreement with those determined from WVR data (the average difference is 0.06 ± 0.64 K at 32 GHz) and (2) the surface model average values are biased 3.6 K below those of the BWG and WVR at 32 GHz.

I. Introduction

Several studies in DSN telecommunications have shown that by utilizing 32-GHz frequencies (31.8–32.3 GHz, Ka-band) over 8.4 GHz (8.4–8.45 GHz, X-band) on a spacecraft-to-ground communications link, an advantage of 6 to 8 dB can be realized for a given spacecraft telecommunications system [1,2]. The advantage comes from increased antenna gain at the smaller wavelengths, but it is also reduced by higher atmospheric noise, antenna performance deficiencies, and weather susceptibility at 32 GHz.

The concept of conducting a 32-GHz link experiment to verify these studies and to discover any impediments that could deter this gain from being realized was proposed by Riley et al. [3]. The first

experiment planned was for Mars Observer to carry a small Ka-band transmitter on board, this became reality with the first Ka-band Link Experiment (KaBLE) experiments [4] KaBLE ended with the loss of Mars Observer in August 1993

The Ka-band Antenna Performance Experiment (KaAP) was initiated to observe natural radio sources at both Ka-band and 8 4 GHz in order to characterize this link advantage at DSS 13 and to characterize the gain or efficiency of the antenna at both bands as improvements and configuration changes are implemented The KaAP experiment consists of observing natural calibrator radio sources over the sky, usually one to two tracks per month, with each track typically being 8 to 16 hours in duration Each track consists of performing a series of boresight observations over different radio sources at 32 and 8 4 GHz Each individual observation consists of stepping the antenna beam over the radio source in two orthogonal directions The radio source temperature is measured by fitting linearized Gaussians over the boresight data [5] The source temperatures are converted to efficiencies by using an equation that includes (1) the source's known flux strength, (2) a factor to correct for the source's angular extent over the antenna beam, (3) the atmospheric loss factor, and(4) a correction for any system nonlinearity In addition to the boresight observations, system calibrations are routinely conducted to calibrate out gain changes as the experiment progresses and to allow the system nonlinearity (usually very small) to be determined A detailed discussion of the system calibration methodology is provided in [6]

In addition to the boresight observations and system gain/linearity calibrations, a sequence of observations, known as tip curves, that characterizes the effect of the atmosphere during the data-acquisition period is performed These tip curves provide a measure of the atmospheric noise temperatures (used in statistical characterizations) and atmospheric loss factors (used in the efficiency determination) The atmospheric noise-temperature measurements and their statistics can also be compared with those determined from a surface model using input meteorological data and from water vapor radiometer (WVR) data

This article focuses on the data analysis of the tip-curve measurements performed during the KaAP experiments and describes the DSS-13 antenna and system used to acquire the measurements, the data-acquisition technique and model used to fit the data, the results obtained from the tip-curve data, including comparisons with surface-model and WVR data, and suggested recommendations for future studies

II. Ground Station and Equipment

The research and development (R&D) 34-m beam-waveguide (BWG) antenna at DSS 13 in Goldstone, California, is shown in Fig 1 The locations of focal points and mirror configurations are presented in Fig 2 This antenna was developed in two phases In phase I, the antenna was designed, constructed, and tested for performance at 8 4 GHz and Ka-band In phase II, the antenna was transformed into a functioning tracking station for KaBLE under a set of requirements given in [4] The station was required to simultaneously track the dual X-/Ka-band signals from Mars Observer, demodulate and decode the telemetry, and store the relevant tracking statistics for future analysis

A block diagram of the configuration for the KaAP system as it is currently realized for natural radio source observations is shown in Fig 3 The ground station system can be described in terms of several subsystems antenna microwave, receiver, data acquisition, monitor and control, and frequency and timing Each subsystem will be described briefly below

A. Antenna Subsystem

The pointing subsystem at the 32-GHz band requires more accurate pointing when tracking objects than it does at 8 4 GHz Whereas an accuracy of 8 mdeg for 8 4 GHz is sufficient, for KaAP an accuracy of 2 mdeg is required to limit pointing loss to less than 0 5 dB [4] Pointing calibrations had been shown

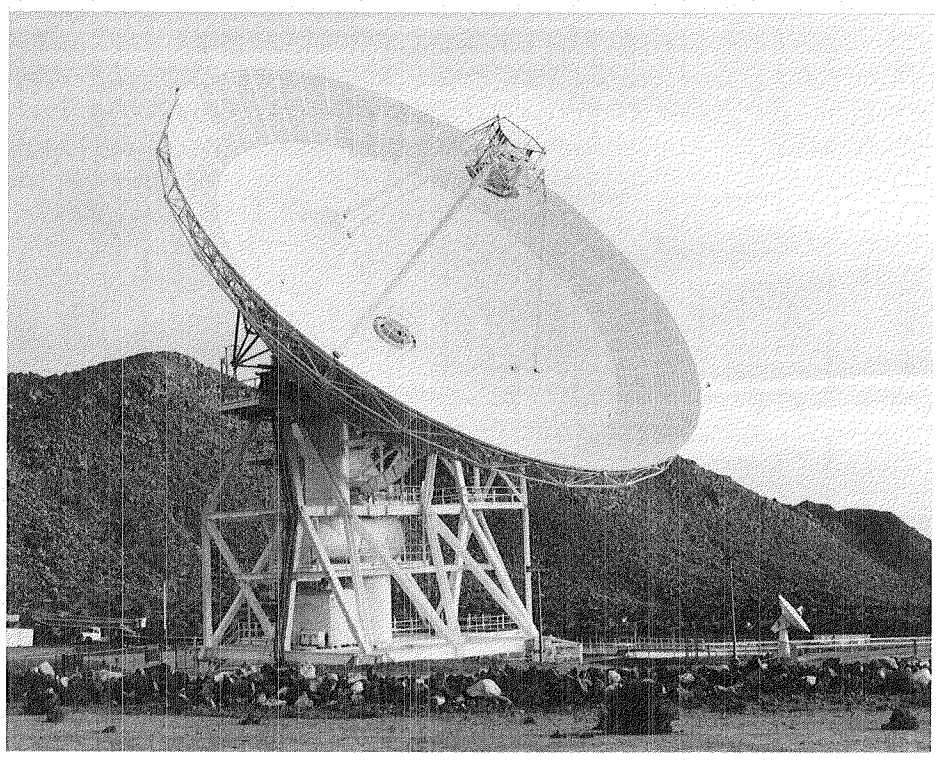

Fig. 1. DSS-13 34-m beam-waveguide antenna.

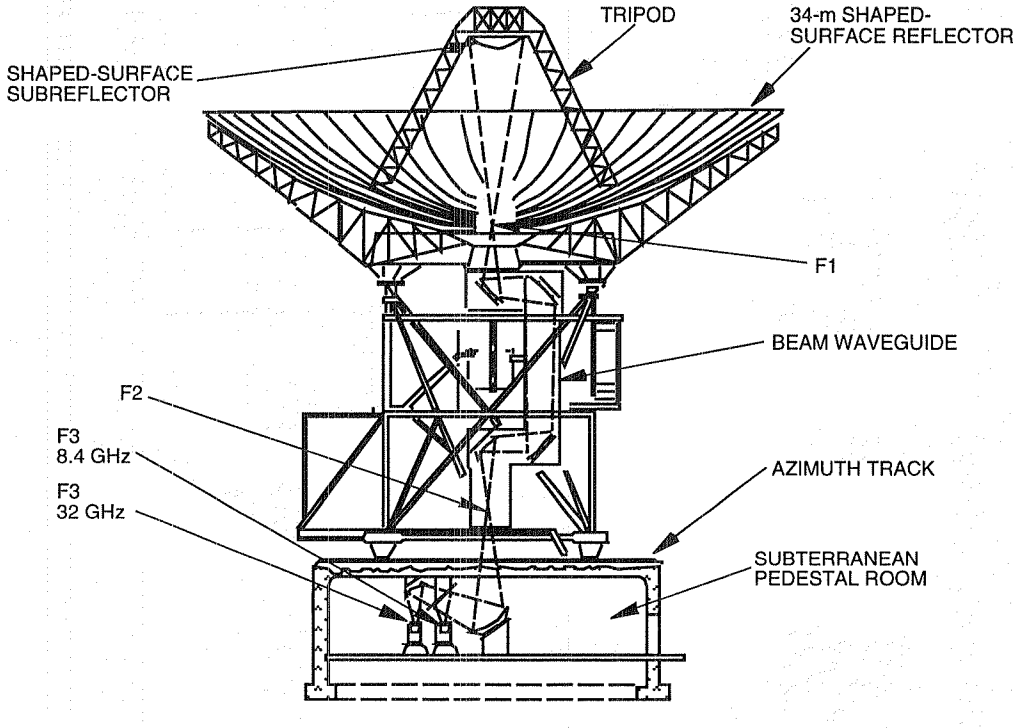

Fig. 2. Geometric configuration of reflectors and mirrors of DSS-13 BWG antenna along with positions of focal points.

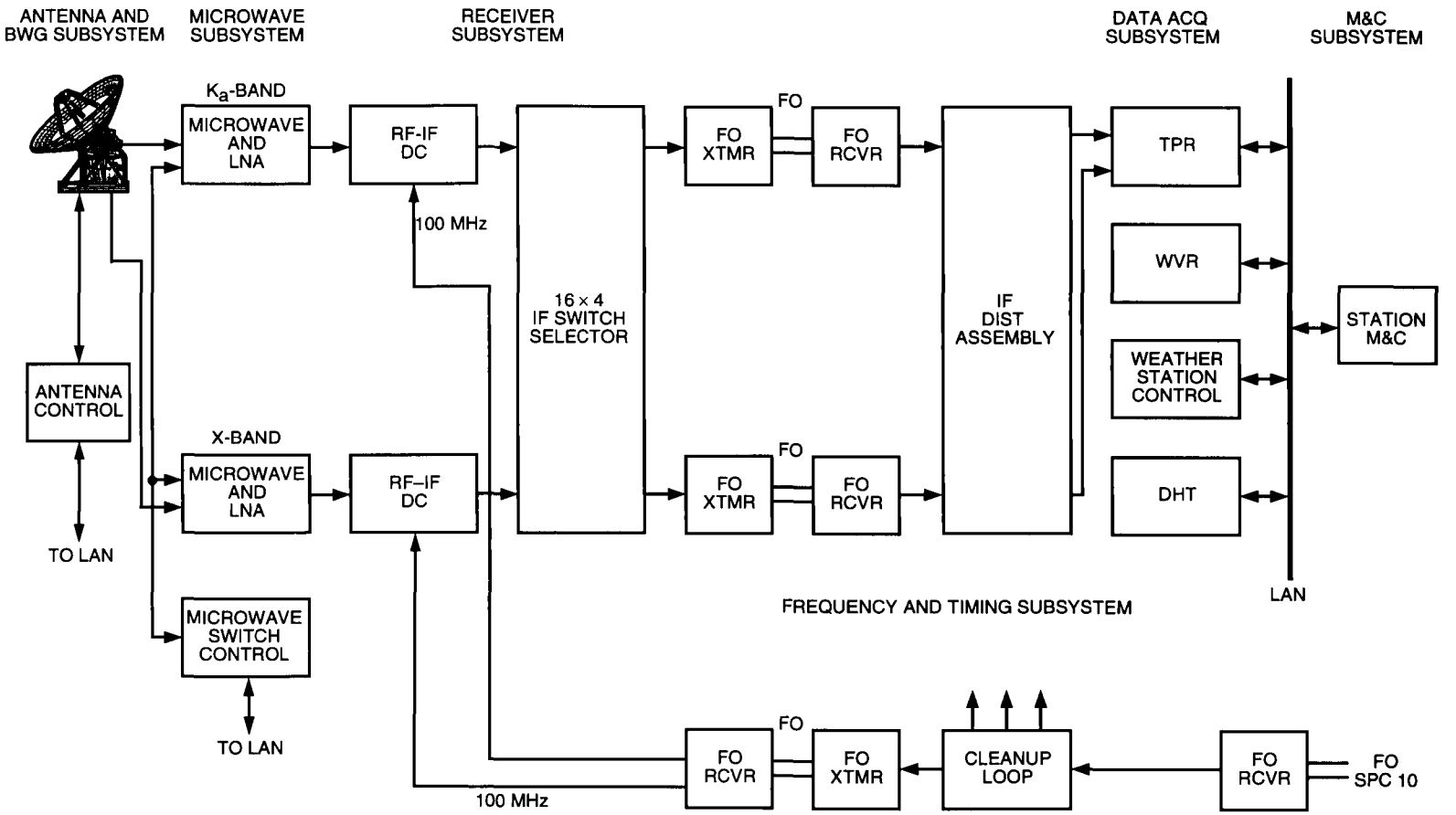

Fig 3 The KaAP X-/Ka-band system at DSS-13

to correct errors to about 5-mdeg rms in a blind or open-loop mode Pointing errors were reduced by utilizing an improved automatic boresight technique, which corrects pointing errors in real time [5] Since the tip-curve data involve cold sky observations, the pointing accuracy is not as critical as it is for the boresight observations used to estimate efficiency

B. Microwave Subsystem

The microwave subsystem takes advantage of the pedestal room layout to allow switching between different feed packages arranged in a ring around a rotating ellipsoid reflector The feed package used for KaAP consists of an X-/Ka-band dichroic plate, a 25-dBi horn for 8 4 GHz, a 26-dBi horn for 32 GHz, and high-electron mobility transistor (HEMT) low-noise amplifiers (LNAs) for both bands The X-/Ka-band dichroic plate is essentially transparent at 32 GHz and reflective at 8 4 GHz It was designed to study performance at the DSN-allocated 32 0-GHz frequency (to receive) and 34-GHz frequency (to transmit) However, because Mars Observer used a simple $\times 4$ to multiply its 8 4-GHz frequency up to 33 7 GHz, the downlink KaBLE 33 7-GHz frequency occurs at a nonoptimal location between two well-matched bands Thus, the first data acquired for KaAP (December 93 to September 94) were at the 33 7-GHz frequency With the installation of the new equipment designed to operate at the intended DSN-allocated 32 0-GHz frequency, the Ka-band data acquired since (October 94 to the present) have been at 32 0 GHz The dichroic plate along with the added temperature of the HEMT contributes approximately 11 K of additional noise temperature at 33 7 GHz above that at 32 GHz A description of the dichroic plate is found in [7]

For the LNA packages, HEMT devices were used at 8 4 and 32 GHz The noise temperature contributions of 16 6 K (0 24 dB) by the 8 4-GHz feed in the low-noise path and 12 K by the 8 4-GHz LNA HEMT result in a contribution of 28 6 K for the full package [1] This estimated value agrees well with a measured value of 28 4 K [2] Temperature contributions of the follow-on equipment (downconverters, fiber-optic link) ranged from about 0 3 to 1 4 K

The 32-GHz KaAP feed system includes a 26-dBi horn that is an extension to a 22-dBi corrugated horn, followed by a waveguide window at room temperature An ellipsoidal reflector is located above the 32-GHz feed The cool components include a round-to-square transition copper thermal isolator followed by a copper polarizer a cross-guide coupler, a copper isolator, and a WR-28 copper waveguide going into the LNA The KaAP 32-GHz LNA utilizes four stages of General Electric (GE) and Fujitsu transistors of basic National Radio Astronomy Observatory (NRAO) design, resulting in a total noise temperature of about 28 K The cryogenic loss factor of the waveguide/feed package is estimated to be about 0 325 dB at both 32 and 33 7 GHz [3] After adding room temperature contributions due to the window (0 02 dB) and the horn (0 04 dB), this results in an overall horn/waveguide/feed package loss of about 0 4 dB for a noise temperature contribution of about 5 K The resulting estimated temperature of the total package (32 K) is somewhat lower but in reasonable agreement with 34- to 36-K values measured at the station in March 1994 [4]

For 32 GHz, an ambient load is swung over the horn for noise calibrations For the 8 4-GHz system, a waveguide switch located in front of the LNA is used Both ambient loads have embedded temperature sensors used in the calibration algorithms Compressed helium gas is used to cool the LNA/waveguide feed package in closed-vessel systems For the 32-GHz refrigerator system, there are four temperature sensors For the 8 4-GHz system, there are two sensors

---

[1] S Stewart, personal communication, Jet Propulsion Laboratory, Pasadena, California, October 6, 1994

[2] G Bury, personal communication, Jet Propulsion Laboratory, Pasadena, California, October 4, 1994

[3] J Bowen, unpublished report (internal document), Jet Propulsion Laboratory, Pasadena, California, February 7, 1995

[4] G Bury and J Garnica, personal communication, Jet Propulsion Laboratory, Pasadena, California, March–April 1994

C Receiver Subsystem

The receiver subsystem, used for both frequency bands, consists of RF-to-IF downconverters, a 16 × 4 IF switch selector, fiber-optic links from the pedestal room to the control room, and an IF distribution assembly in the control room The 8 4-GHz downconversion is performed using a 8 1-GHz first local oscillator (LO) For the Ka-band path, two configurations have been used During the 33 7-GHz data acquisition period (from December 1993 to October 1994), the incoming 33 7-GHz signal was mixed with a 25 2-GHz first LO followed by a 8 2-GHz second LO The bandwidth of the second IF filter was 100 MHz All LOs are coherent with the station frequency and timing subsystem (FTS) For the 32 0-GHz data acquisition, the incoming 32 0-GHz signal was mixed with a 23 6-GHz first LO followed by a 8 1-GHz second LO The bandwidth of the second IF filter was 500 MHz The downconverter outputs are amplified by IF amplifiers and fed into a 16 × 4 (16 input ports/4 output ports) switch selector, where two output signals, the 8 4-GHz and Ka-band IFs, are sent over fiber-optic links to the control room The IFs are then input to an IF distribution assembly (amplifiers and power dividers) and ported to various subsystems in the control room

D Data Acquisition Subsystem

The instruments included in this subsystem include the total power radiometer (TPR) for measuring system noise temperature, the WVR for measuring the quantity of water in the atmosphere, the weather station, and the data handling terminal (DHT) for displaying data from other instruments and recording KaAP-specific data to disk

The TPR operates together with the microwave switch controller (USC) to perform calibrated operating temperature, T_{op}, measurements during the track The two IF channels are further filtered (usually 20 MHz for 8 4 GHz and 30 MHz for 32 GHz) to limit the noise coming in, such that radio frequency interference (RFI) can be minimized The bandwidth of these filters together with the radiometer integration time and system gain stability define the contribution of the noise fluctuations of the temperature measurements These filters together with a 5-s radiometer integration time constrain the random fluctuation contribution to below 0 01 K Variable step attenuators are used to set the power levels to a 0 8- to 0 9-μW level when the antenna is on ambient load with the noise diode on Measurements of the total IF noise power are made with two Hewlett Packard (HP)8481 power sensors followed by HP437 power meters—one each for 8 4 GHz and Ka-band The power sensors operate from 10 MHz to 18 GHz and output 100-pW to 10-μW dc power levels A local terminal reads these measurements and converts them to temperatures at a rate of 1 per second, based on a transfer function derived from a previous calibration

Calibrations are performed alternately throughout the track with the boresight observations During each calibration, the TPR measures the total IF noise power while the USC switches the HEMT input from (1) sky, to (2) sky plus noise diode, to (3) ambient load, and to (4) ambient load plus noise diode The measurements are converted into a transfer function (T_{op} versus total noise power) and also allow for the estimation of system linearity

The R6 WVR is a small stand-alone package positioned near the antenna that determines the presence of water in the atmosphere in vapor and droplet form (hydrometeors) along the antenna beams by measuring noise levels at 20 7 and 31 4 GHz over effective bandwidths of 320 MHz It consists of a platform with a small feedhorn and mirror assembly that can observe any point in the sky with a beamwidth of 7 deg It is located 300 m from the BWG antenna on the roof of the control building A description of the R6 WVR is found in [8]

The WVR performs periodic tipping curves from zenith to 30-deg elevation and, when provided with pointing predicts, can track along the line of sight of the 34-m BWG antenna The measured brightness temperatures have accuracies of about 0 5 K and precisions of about 0 1 K, based on intercomparisons with other WVRs [5] During the KaAP data-acquisition period, the radiometer operates in a continuous

[5] S Keihm, personal communication, Jet Propulsion Laboratory, Pasadena, California, May 5, 1995

tip-curve mode, obtaining both gain calibration and zenith brightness temperature data with a 4 25-min sampling rate at both channels

Data collected by the WVR are periodically delivered for correlation with the KaAP tipping-curve measurements Both magnitudes and deviations of atmospheric temperatures between the two systems can be cross-compared One expects better agreement between the BWG and WVR data on dry, clear days when the water vapor content is minimal During inclement or cloudy conditions, the agreement is not expected to be as good The results of the cross-comparison will be discussed in Section IV A 2

The weather system samples and records a range of meteorological parameters, including atmospheric pressure, air temperature, relative humidity, wind speed, and wind direction The data are stored locally and routed through the station's monitor and control computer to a central storage device, the data handling terminal (DHT) The surface data can be input to a surface model, and the resulting atmospheric noise temperature at zenith can be cross-compared against those from the BWG tip curves and the WVR

The DHT is routinely monitored for insight into the state of the data Such data types are the operating temperature, elevation angle, and wind speed, which can be displayed simultaneously versus time on a single monitor Most data arrive in the DHT through the station data recorder (SDR), a gateway terminal that serves to back up data archiving and relieve some of the real-time load from the DHT

E. Monitor and Control Subsystem

Tying all of the systems together into an operational system with a high degree of flexibility is the monitor and control (M&C) subsystem The main strength of the M&C is its user-friendly window-driven display system As a step toward the goal of developing semiautomated monitor and control of operational procedures in the DSN, an operational prototype known as Link Monitor Control Operator Assist (LMCOA) was implemented at DSS 13 The LMCOA automation software was developed in a SUN/UNIX environment in C and RTworks Originally targeted for automating KaBLE experiments, LMCOA was implemented for KaAP and has been used successfully for running KaAP experiments, including the tipping-curve data acquisition sequences Several of the early data sets were acquired using an M&C system that ran on a 486 platform and one that ran on a SUN workstation (DEXTERITY), which is the current backup to LMCOA Interfacing to the other subsystems is provided by the local area network (LAN) Each subsystem host computer taps into the LAN through a special board plugged into its chassis A driver for handling real-time commands is loaded into the host computer's random-access memory (RAM) at power-up

F. Frequency and Timing Subsystem

Fiber-optic technology is employed to provide all of the sensitive reference frequency distributions, including (1) the distribution of the reference first LO to the downconverters in the pedestal room and (2) the transmission of the broadband IF signals from the pedestal room to the control room Optical fiber provides better stability than coaxial cable

III. Model and Fit Scenario

KaAP data acquisition began in December 1993 The observation strategy and the model used to fit the tipping-curve data will be described in this section

A. Description of Measurement Sequence

Tipping curves are performed at the start and/or end of a KaAP pass The tipping-curve data-acquisition strategy involves taking a set of operating-temperature measurements at a series of different elevation angles (T_{op} versus θ), where θ goes from horizon to zenith or vice versa Each elevation angle

corresponds to a specific number of air masses along the path The operating temperature as a function of air mass typically has a signature as shown in Fig 4 for the case of 32 GHz Zenith system temperatures typically run at about 40 K at 8 4 GHz, 68 K at 33 7 GHz, and 57 K at 32 0 GHz A tipping-curve sequence typically takes about 1/2 to 1 hour to perform Normally, the atmosphere is sampled from 1 air mass (zenith) to about 4 air masses (14 5-deg elevation)

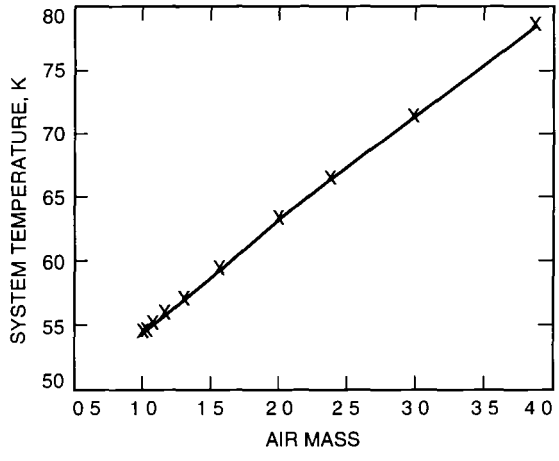

Fig 4 Example of temperature versus air mass for a 32-GHz tip curve performed on 95-051

From December 1993 to January 1994, the first series of KaAP experiments was performed The tipping-curve data for this set of experiments utilized direct measurements from the TPR However, these measurements were subject to uncalibrated gain changes during the tipping-curve measurement period Beginning in February 1994, a new tipping-curve algorithm was employed at the DSS-13 BWG station that involved performing mimicals in place of the regular radiometer temperature measurements A mimical employs an alternating sequence of the following temperature measurements output device terminated (T_1), antenna on cold sky (T_2), antenna on cold sky plus noise diode (T_3), ambient load (T_4), and ambient load plus noise diode (T_5) The use of mimicals calibrates gain variations as the tipping-curve data are acquired and allows for the determination of any small nonlinearity that may be in the system The cold sky temperatures with the noise diode off (T_2) extracted from the mimical output files are the observable data for the periods that these tipping curves were performed

B Description of Operating Temperature Model

The measured system operating noise temperature, T_{op}, is referenced at the input plane of the horn for 32 GHz, where an aperture load is swung above the horn during ambient temperature measurements, and at the input plane of the HEMT for 8 4 GHz, where a waveguide switch connects an ambient load during the measurements T_{op} is expressed in terms of several contribution and loss factors that closely follow the formulation in [9], as given below

$$T_{op} = \frac{(T^*_{cb}/L_{atm}) + T_{atm}}{L_{F1}L_{F3}L_{wg}} + \frac{T_{ant,F1}}{L_{F3}L_{wg}} + \frac{T_{ant,F3}}{L_{wg}} + T_{wg} + T_{lna} + T_f \tag{1}$$

where

T^*_{cb} = effective cosmic background temperature, K

T_{atm} = atmospheric noise temperature, K

L_{atm} = atmospheric loss factor

L_{F1} = Cassegrain reflector dissipative loss factor

L_{F3} = mirrors and dichroic plate dissipative loss factor

L_{wg} = loss factor due to components between feed horn and input flange of HEMT

$T_{ant,F1}$ = noise temperature due to spillover, leakage, and scattering of main reflector and subreflector, K

$T_{ant,F3}$ = noise temperature due to spillover, leakage, and scattering between F1 and F3, K

T_{wg} = noise temperature between the feed horn and input flange of HEMT, K

T_{lna} = temperature of the LNA, K

T_f = temperature contribution of follow-on electronics, K

Table 1 lists the current best-known values of several of these factors

Table 1 Values of parameters used in Eq (1)

Parameter	8 4 GHz	32 0 GHz	33 7 GHz
L_{F1}	1 011[a]	1 02[a]	1 02[a]
L_{F3}	1 0043[a]	1 01[a]	1 03[a]
L_{wg} (ambient)	1 057[b]	1 01742[c]	1 01742[c]
L_{wg} (cooled)	1 0[d]	1 078[e]	1 078[e]
T_{lna}	12 0[f]	28 0[f]	28 0[f]
T_f	0 3–0 9[g]	0 3–1 4[g]	0 3–1 4[g]

[a] Current best-known values
[b] S Stewart, op cit
[c] R Clauss, personal communication, Jet Propulsion Laboratory, Pasadena, California, February 22, 1995
[d] Negligible cryogenic loss, assumed close to unity
[e] J Bowen, op cit
[f] Baseline values inferred from lab measurements
[g] Typical values routinely measured during prepass period

The model typically used for the atmospheric noise temperature, T_{atm}, in the tipping-curve analysis assumes a stratified atmosphere that makes use of the equation of radiative transfer [10], which can be shown to reduce to a simplified exponential form For the purpose of this analysis, we make use of a two-layer model of Kutner [11] in which the oxygen and water contributions to the opacity are treated separately The atmospheric noise temperature, T_{atm}, and atmospheric loss factor, L_{atm}, thus assume elevation (air mass) dependent forms given by

$$T_{atm}(\theta) = T_{O_2}\left[1 - e^{-[\tau_{O_2}+\tau_{H_2O}]A(\theta)}\right] + [T_{H_2O} - T_{O_2}]\left[1 - e^{-\tau_{H_2O}A(\theta)}\right] \tag{2}$$

$$L_{atm}(\theta) = e^{(\tau_{O_2}+\tau_{H_2O})A(\theta)} \tag{3}$$

where

$A(\theta)$ = air mass number at elevation $\theta, \sim \sin^{-1}(\theta)$

T_{O_2} = radiating temperature of oxygen, K

T_{H_2O} = radiating temperature of water vapor and hydrometeors, K

τ_{O_2} = opacity of oxygen contribution

τ_{H_2O} = opacity of water contribution

Prior to performing a fit, all known contributions due to equipment (HEMT and follow-on), waveguide, and antenna losses (spillover, scatter, and leakage) are removed from T_{op} in Eq (1) as follows

$$\Delta T^*_{op} = T_{op} - \frac{T_{ant}(\theta)}{L_{F3}L_{wg}} - T_{wg} - T_{lna} - T_f \tag{4}$$

The contributions remaining in the residual temperature of Eq (4) include the cosmic and atmospheric noise temperature contributions Since the cosmic term includes a dependence on the atmospheric loss factor, it is retained in the residual data prior to the fit Each contributing quantity removed prior to fitting a model is discussed below

1 Antenna Temperature Contribution In order to simplify the analysis, we consider that most of the elevation-dependent signature in the antenna temperature is due to the tripod scatter and main reflector dissipative losses in the $T_{ant,F1}$ term We assume that the elevation-dependent signature in the mirrors, $T_{ant,F3}$ in Eq (1), is small and, thus, effectively a constant and, therefore, lumped with $T_{ant,F1}$ in the T_{ant} term in Eq (4) The antenna noise temperature, T_{ant}, is removed from the data as shown in Eq (4) for 8 4 and 32 0 GHz prior to performing the fit It is the sum of contributions due to spillover, mirror/gap losses, and tripod scatter, and is a known function of elevation angle Veruttipong provides values of the antenna noise temperature, $T_{ant}(\theta)$, at three elevation angles, 10, 30, and 90 deg, for both 8 4 and 32 GHz [6] A quadratic form for $T_{ant}(\theta)$ was used and coefficients derived from the "predicted" values of Veruttipong at the three elevation angles as defined by

$$T_{ant}(\theta) = C_1 + C_2(90 - \theta) + C_3(90 - \theta)^2 \tag{5}$$

where θ is the elevation angle in deg

For 32 GHz, the coefficients inferred from Eq (5) using Veruttipong's data are $C_1 = 9\ 25$ K, $C_2 = 0\ 00020835$ K/deg, and $C_3 = 0\ 0002278$ K/deg^2 At 33 7 GHz, a constant 11 K is added to the bias term (C_1) to account for additional loss contributions (e g , dichroic) at this frequency

While the Veruttipong results imply that the antenna noise temperature dependence with elevation angle, $T_{ant}(\theta)$, is essentially the same for both 8 4 GHz and Ka bands, attempts to use the three (similarly derived) coefficients at 8 4 GHz resulted in unreasonable estimates The predicted values may have been derived under assumptions that do not apply for DSS 13's tripod structure and forward and rear spillover differences between 8 4- and 32-GHz frequencies

The coefficients for 8 4 GHz were derived by first assuming a constant term (C_1) and setting the other terms to zero ($C_2 = C_3 = 0$) For this analysis, the elevation-dependent signature of the atmosphere

[6] W Veruttipong, "Detailed Gain/Noise Budgets at X- and Ka-Bands for KABLE Experiment," JPL Interoffice Memorandum 3328-92-0190 (internal document), Jet Propulsion Laboratory, Pasadena, California, December 29, 1992

is assumed to be uncoupled to that of the antenna The data were processed for a select subset of dry weather passes The resulting postfit residuals had repeated signatures with a significant 0 2-K change over elevation angle, consistent with the quoted 0 2-K uncertainty of earlier work at 8 4 GHz [12], where an elevation-dependent antenna temperature model was also not employed The authors of [12] attributed the 0 2-K level of agreement to the low amount of scattering due to the slim tripod legs of the BWG antenna The signature of the postfit residuals appeared remarkably repeatable between data sets The second-degree polynomial model [Eq (5)] was then fit to these postfit signatures The average values of C_1, C_2, and C_3 derived from the dry weather subset of tip curves were used for the antenna temperature model of Eq (5) at 8 4 GHz This model was fed back in Eq (4), resulting in lower rms scatters in the postfit residuals and negligible remaining systematic signatures The derived 8 4-GHz coefficients used for T_{ant} in Eq (5) were $C_1 = 7\ 0$ K, $C_2 = -0\ 0087$ K/deg, and $C_3 = 0\ 000110$ K/deg^2 Figure 5 displays the 8 4- and 32 0-GHz antenna temperature versus elevation angle models [Eq (5)] that were removed from the data [Eq (4)] prior to performing the fit

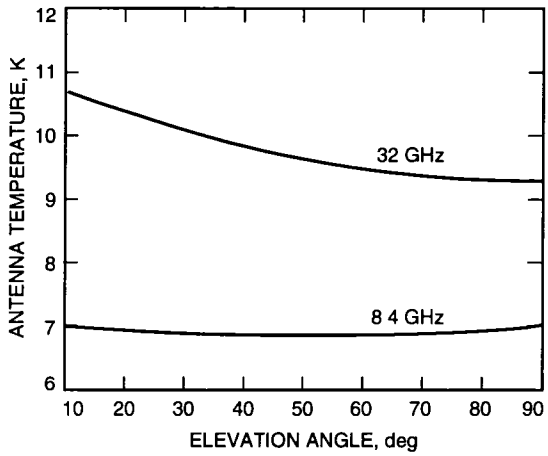

Fig 5 The 8 4- and 32-GHz antenna temperature model versus elevation angle

2 Ambient Feed Component Contributions. The waveguide noise temperature contribution, T_{wg}, of the horn, window, and other components at ambient is computed from the loss factor, L_{wg}, and physical temperature, T_p, as follows

$$T_{wg} = \left[1 - \frac{1}{L_{wg}}\right] T_p$$

In practice, T_{wg} cannot be measured unless the waveguide/feed package is physically removed from the LNA The combined waveguide/LNA temperature can be measured during cold load/warm load measurements performed during maintenance periods and compared against preinstallation measurements (or predictions) of the LNA and waveguide/feed package temperatures The current best-known values of the ambient waveguide package loss factors are $L_{wg}(X) = 1\ 057$ (0 24 dB),[7] and $L_{wg}(K_a) = 1\ 01742$ (0 075 dB) [8]

3 Cryogenically Cooled Component Contributions. The noise temperature contributions of cryogenically cooled components in front of the LNA are assumed embedded in the T_{lna} baseline values Baseline values of the temperatures of the cooled components, T_{lna} (LNA and waveguide), are removed from the measurements (12 K for 8 4 GHz and 28 K for Ka-band) If all other contributors have been

[7] S Stewart, op cit

[8] R Clauss, personal communication, Jet Propulsion Laboratory, Pasadena, California, February 22, 1995

accurately removed, then we expect the variation of any bias terms fit from the data will reflect the variation of the temperature of these components The results will be discussed in a later section

4 Follow-On Equipment Contribution The follow-on equipment (T_f) noise temperature contributions are routinely measured prior to each pass and are removed from the observed temperatures as given in Eq (4) Typical values of T_f range from about 0 3 to 1 4 K and depend upon the state and configuration of the equipment for a particular pass For a few of the earlier passes, a significant 1 4-K follow-on measurement at 32 GHz was attributed to faulty equipment

C Description of Fitting Algorithm

1 Nominal Two-Parameter Fits After removing all known contributions from the data with the model in Eq (4), the residual data are fit to provide the unmodeled bias and the cosmic and atmospheric contributions The bias or constant term should indicate how well the model agrees with the measurements at zenith and how it varies from tip curve to tip curve or pass to pass The elevation-dependent signature of the remaining contributions allows the atmospheric noise temperature contribution at zenith to be determined By rearranging and combining terms in Eq (4) using Eqs (1) through (3), the model used to fit the data ΔT^*_{op} versus θ is given by

$$\Delta T^*_{op}(\theta) = T_{off} + \frac{(T^*_{cb}/[L_{atm}(\theta)]) + T_{atm}(\theta)}{L_{ant}} \tag{6}$$

where

$$L_{ant} = L_{F1} L_{F3} L_{wg}$$

From the residual temperatures in Eq (6) for each tip-curve data set, a two-parameter model fit is performed, yielding the bias, T_{off}, and the opacity of water, τ_{H_2O}, which appears in Eq (6) in the term T_{atm}, as shown in Eq (2) Constant values are used for all other terms The opacity of atmospheric oxygen (τ_{O_2}) used in Eq (2) is estimated from the surface data using the SDSATM4S program [9] The radiating temperature of water, T_{H_2O}, is computed from the surface temperature, T_0, as $T_{H_2O} = T_0 - 10$ K The radiating temperature of oxygen, T_{O_2}, is taken to be 265 K The effective cosmic background temperature (T^*_{cb}) assumed for 8 4 GHz is 2 5 K, and for 32 GHz it is 2 0 K

2 Special Case Three-Parameter Fits Significantly higher than usual postfit rms scatters for some of the earlier data sets conducted between 93-336 (December 2, 1993) and 94-024 (January 24, 1994) were attributed to linear drifts in temperature over the tip-curve measurement period These passes did not employ mimicals (which calibrate gain variations) during the tip-curve measurement sequences During this period, the few cases of observed high-temperature gradients significantly skewed the fit results A three-parameter model was employed to process these data sets This model included the solve-for terms T_{off} and τ_{H_2O} as before in Eq (6) and an additional term, $R(t - t_0)$, where R, the linear drift rate in K/h, is the additional solve-for parameter, t is the time tag of the data point, and t_0 is the reference time tag For all passes conducted since 94-053 (February 22, 1994), mimicals were performed for the tipping curves in place of the regular radiometer measurements, and these were processed as described in Section III C 1 above

IV. Results

A Model Fit Results

A total of 67 Ka-band (33 7- and 32 0-GHz) and 68 X-band (8 425-GHz) tipping-curve data sets from the KaAP experiments conducted between 93-336 (December 2, 1993) and 95-137 (May 17, 1995) were

[9] Courtesy of S Slobin, Jet Propulsion Laboratory, Pasadena, California, program version dated February 8, 1993

processed with the KaAP tipping-curve analysis software The Ka-band data acquired prior to and up to 94-270 were at 33 7 GHz, and data acquired since were at 32 0 GHz

Two-parameter or three-parameter fits of each tip-curve data set using Eq (6) were performed solving for the offset temperature, T_{off} (which is a measure of any remaining bias not accounted for in the model), and the opacity of water, τ_{H_2O} (which provides information on the atmosphere) The atmospheric temperature at zenith, T_{atm} (90 deg), is computed from τ_{H_2O} and other terms using

$$T_{atm}(90 \text{ deg}) = T_{O_2}\left[1 - e^{-(\tau_{H_2O}+\tau_{O_2})}\right] + [T_{H_2O} - T_{O_2}]\left[1 - e^{-\tau_{H_2O}}\right] \quad (7)$$

After fitting and removing the fitted model from the data, the postfit residuals can be inspected against time and air mass The resulting residuals have time-dependent signatures, as shown in Fig 6 for the 32-GHz data of Fig 4

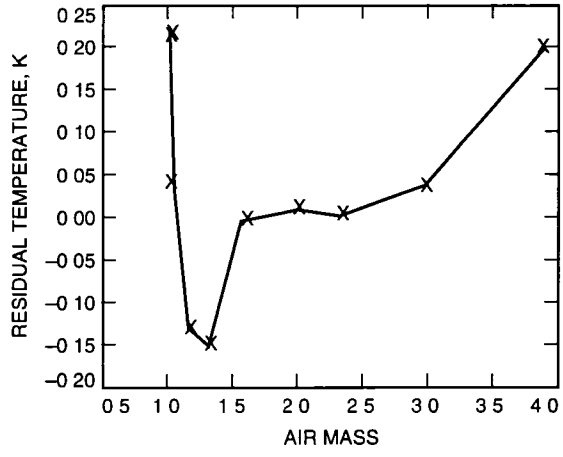

Fig 6 Temperature residuals of tip-curve data of Fig 4 after removing the fit model Data from one to three air masses were fit

Although data were routinely acquired from one air mass (zenith) to four air masses (14 5 deg), only the data from zenith to three air masses (19 5 deg) were fit in order to reduce the effect of unmodeled ground pickup and scatter at the lower elevations Tables 2 and 3 display the results of the fit from the data sets for Ka-band and 8 4 GHz, respectively

1 **Bias Term of Solution.** Figures 7 and 8 display the bias temperatures at zenith resulting from the fits of all of the tipping-curve data sets listed in Table 2 (32 GHz) and Table 3 (8 4 GHz), respectively The few-K agreement with the baseline zenith model (zero) is reasonable given that they are correlated with known logged temperatures of the HEMT refrigeration units Higher than usual temperature variations appear to be correlated with the state of the refrigeration units as they degrade over time prior to servicing, and the lower values are correlated with periods right after the units have been serviced For instance, drops in observed bias temperatures, such as the 2 4-K drop on day 482 (94-117) for the 32-GHz case (Fig 7), agree with drops of the refrigerator temperatures observed from the refrigeration servicing logs Other differences of the bias term from the baseline may be attributed to uncertainties in the antenna-elevation model terms at zenith, such as the dissipative temperatures being different before and after periods of mirror or subreflector alignments or fluctuations of the atmosphere during the tipping-curve data acquisition period manifesting themselves into the bias term

Table 2 The 32-GHz tipping-curve fit results

Year	DOY	UTC Time		Zenith bias temperature, K	Atmosphere temperature, K	RMS, K	Notes
		Start	End				
93	336	15 52	15 59	5 84 ± 0 08	10 940 ± 0 064	0 133	
93	354	16 01	16 45	6 12 ± 0 06	9 689 ± 0 040	0 243	
93	354	22 37	22 55	5 81 ± 0 04	8 924 ± 0 027	0 104	
93	361	16 42	17 02	4 83 ± 0 18	12 791 ± 0 132	0 611	
93	361	22 13	22 33	5 42 ± 0 06	11 971 ± 0 049	0 209	
94	10	16 02	16 41	4 74 ± 0 04	9 700 ± 0 030	0 190	
94	17	15 57	16 25	5 65 ± 0 05	10 504 ± 0 040	0 227	
94	17	22 30	22 47	5 62 ± 0 03	11 025 ± 0 022	0 085	
94	24	16 16	16 45	7 58 ± 0 37	9 687 ± 0 282	1 199	
94	53	00 11	00 38	6 07 ± 0 17	9 760 ± 0 138	0 112	
94	59	15 42	17 00	6 50 ± 0 13	10 927 ± 0 101	0 100	
94	67	09 21	10 06	6 25 ± 0 16	11 050 ± 0 130	0 099	
94	73	13 46	14 37	9 81 ± 0 22	9 811 ± 0 181	0 141	
94	73	23 02	23 45	6 51 ± 0 15	10 322 ± 0 142	0 103	
94	80	22 38	23 01	2 35 ± 0 76	11 831 ± 0 624	0 185	
94	115	15 27	16 04	9 26 ± 0 32	10 280 ± 0 258	0 209	
94	122	15 05	16 02	2 94 ± 0 07	12 342 ± 0 055	0 033	
94	122	21 44	22 42	2 49 ± 0 28	12 846 ± 0 265	0 195	
94	123	22 55	23 44	3 37 ± 0 23	13 154 ± 0 213	0 145	
94	124	05 11	06 01	3 46 ± 0 07	13 573 ± 0 057	0 033	
94	129	08 31	08 58	3 17 ± 0 26	13 685 ± 0 201	0 061	
94	136	14 44	15 26	3 31 ± 0 39	10 718 ± 0 324	0 147	
94	137	22 44	23 10	3 18 ± 0 57	11 305 ± 0 489	0 212	
94	143	15 07	15 53	3 55 ± 0 25	9 972 ± 0 232	0 114	
94	158	15 10	16 08	3 44 ± 0 17	10 420 ± 0 134	0 082	
94	158	21 29	22 03	3 38 ± 0 27	11 179 ± 0 251	0 100	
94	160	23 14	23 42	3 00 ± 0 06	10 001 ± 0 057	0 016	
94	166	18 52	19 19	2 90 ± 0 45	10 539 ± 0 386	0 111	
94	172	22 38	23 07	3 13 ± 0 64	13 729 ± 0 642	0 237	
94	178	22 49	23 12	2 68 ± 0 68	16 667 ± 0 668	0 161	Cloudy
94	192	14 58	15 23	4 49 ± 0 34	8 854 ± 0 314	0 129	
94	199	15 20	15 38	2 37 ± 1 62	20 161 ± 1 606	0 574	Cloudy
94	206	15 41	16 05	2 91 ± 0 05	11 839 ± 0 036	0 025	
94	220	15 01	15 25	3 79 ± 0 27	17 373 ± 0 264	0 098	
94	229	23 19	23 39	4 05 ± 0 38	22 111 ± 0 316	0 233	Cloudy
94	255	22 44	23 07	2 97 ± 0 51	10 646 ± 0 364	0 335	
94	265	22 46	23 16	3 74 ± 0 15	14 304 ± 0 117	0 096	
94	269	15 25	15 51	3 10 ± 0 20	14 433 ± 0 158	0 142	Cloudy
94	270	05 23	05 48	4 19 ± 0 15	12 419 ± 0 110	0 097	Cloudy
94	283	14 57	15 20	1 30 ± 0 20	10 292 ± 0 140	0 132	
94	284	05 31	05 53	1 79 ± 0 16	10 918 ± 0 116	0 107	
94	286	14 52	15 13	1 32 ± 0 16	10 583 ± 0 102	0 103	

Table 2 The 32-GHz tipping-curve fit results (continued).

Year	DOY	UTC Time		Zenith bias temperature, K	Atmosphere temperature, K	RMS, K	Notes
		Start	End				
94	286	18 47	19 08	1 48 ± 0 17	11 009 ± 0 113	0 108	
94	297	16 02	16 25	2 09 ± 0 25	14 149 ± 0 177	0 160	
94	298	05 53	06 15	1 58 ± 0 14	13 942 ± 0 098	0 089	
94	306	16 01	16 23	−0 73 ± 0 82	16 310 ± 0 706	0 298	Windy
94	311	18 25	18 48	1 72 ± 0 41	9 258 ± 0 271	0 271	
94	325	18 52	19 15	1 50 ± 0 20	8 721 ± 0 125	0 130	
94	340	07 15	07 40	7 71 ± 2 07	9 449 ± 1 318	1 367	
95	3	07 08	07 31	9 43 ± 0 81	11 462 ± 0 511	0 531	Rainy
95	6	16 35	16 59	3 93 ± 1 07	16 517 ± 0 706	0 676	Rainy
95	9	23 13	23 33	2 65 ± 0 36	13 074 ± 0 242	0 232	Rainy
95	23	16 53	17 12	8 18 ± 1 27	21 557 ± 0 861	0 794	Rainy
95	23	17 34	18 11	24 83 ± 4 45	12 448 ± 3 060	3 938	Rainy
95	37	19 22	19 46	1 90 ± 0 15	8 641 ± 0 106	0 103	
95	38	04 53	05 43	1 82 ± 0 13	10 258 ± 0 085	0 132	
95	51	02 32	03 12	1 66 ± 0 13	9 524 ± 0 088	0 108	
95	51	20 05	20 46	1 76 ± 0 11	9 752 ± 0 084	0 106	
95	66	15 13	15 36	1 77 ± 0 16	8 129 ± 0 102	0 107	
95	81	14 40	15 28	2 76 ± 0 10	8 565 ± 0 061	0 110	
95	95	00 23	01 56	2 80 ± 0 18	8 946 ± 0 132	0 122	
95	109	13 16	14 04	3 85 ± 0 17	10 470 ± 0 103	0 178	
95	117	19 28	14 08	3 29 ± 0 33	12 299 ± 0 253	0 820	
95	122	11 36	11 55	3 68 ± 0 15	11 184 ± 0 110	0 101	
95	125	22 02	22 19	3 00 ± 0 24	10 493 ± 0 161	0 158	
95	128	15 28	15 45	3 91 ± 0 21	12 129 ± 0 140	0 137	
95	137	17 46	19 47	4 77 ± 0 17	12 047 ± 0 113	0 083	
Averages				4 18 ± 3 33	11 845 ± 2 898	0 277	

Figures 9 and 10 display the zenith temperatures for each tip-curve data set at 32 and 8 4 GHz, respectively The large drop of about 11 K around day 650 on the 32-GHz plot (Fig 9) occurs after the system was modified from 33 7 to 32 0 GHz

During passes when the weather was rainy, the model breaks down, as seen for tip curves conducted in January 1995 During these tip-curve periods, the large variability in the atmospheric noise temperature introduces signatures that couple into the bias term This effect is significant at 32 GHz (see passes 95-003 through 95-023 in Table 2 and days 733 through 753 in Fig 9)

2. Atmospheric Noise Temperature Term of Solution. Figures 11 and 12 display the T_{atm} estimated from the fits for each tipping-curve data set listed in Tables 2 (32 GHz) and 3 (8 4 GHz), respectively The 32-GHz values range from 8 1 to 22 K with typical rms scatters of about 0 1 K The excessively large rms scatter of 4 K for pass 95-023 is illustrative of the case of very stormy weather conditions, discussed previously in Section IV A 1 The 8 4-GHz atmosphere temperatures range from 2 0 to 3 9 K with typical rms scatters of about 0 03 K with values as high as 0 7 K Atmospheric fluctuations

Table 3 The 8 4-GHz tipping-curve fit results

Year	DOY	UTC Time		Zenith bias temperature, K	Atmosphere temperature, K	RMS, K	Notes
		Start	End				
93	336	15 52	15 59	0 84 ± 0 02	2 263 ± 0 018	0 042	
93	354	16 01	16 45	1 19 ± 0 03	2 186 ± 0 018	0 125	
93	354	22 37	22 55	1 34 ± 0 01	2 289 ± 0 009	0 040	
93	361	16 42	17 02	1 02 ± 0 04	2 389 ± 0 024	0 130	
93	361	22 13	22 33	1 72 ± 0 02	2 330 ± 0 013	0 066	
94	10	16 02	16 41	0 71 ± 0 02	2 216 ± 0 011	0 080	
94	17	15 57	16 25	1 19 ± 0 02	2 239 ± 0 012	0 080	
94	17	22 30	22 47	1 12 ± 0 02	2 239 ± 0 013	0 059	
94	24	16 16	16 45	1 32 ± 0 02	2 249 ± 0 017	0 078	
94	67	09 20	10 05	0 33 ± 0 04	2 296 ± 0 037	0 029	
94	73	13 45	14 36	−0 02 ± 0 04	2 264 ± 0 034	0 027	
94	73	22 59	23 40	0 32 ± 0 14	1 985 ± 0 127	0 087	
94	80	22 33	23 00	−0 22 ± 0 01	2 326 ± 0 010	0 003	
94	87	16 00	16 25	0 18 ± 0 08	2 294 ± 0 069	0 054	
94	87	22 07	22 35	0 07 ± 0 02	2 280 ± 0 018	0 014	
94	94	14 49	21 54	1 18 ± 0 06	2 279 ± 0 049	0 052	
94	101	15 07	15 32	1 44 ± 0 20	2 904 ± 0 145	0 244	
94	122	15 03	16 01	1 49 ± 0 05	2 431 ± 0 042	0 026	
94	122	21 42	22 41	1 46 ± 0 06	2 338 ± 0 061	0 047	
94	123	22 53	23 43	1 14 ± 0 05	2 469 ± 0 049	0 035	
94	124	05 09	06 00	1 91 ± 0 03	2 467 ± 0 026	0 016	
94	129	08 29	08 56	1 68 ± 0 04	2 473 ± 0 033	0 011	
94	136	14 58	15 25	1 23 ± 0 11	2 565 ± 0 093	0 038	
94	137	22 42	23 08	1 35 ± 0 14	2 316 ± 0 119	0 053	
94	143	15 05	15 51	0 92 ± 0 02	2 284 ± 0 022	0 011	
94	158	15 08	16 07	1 10 ± 0 03	2 242 ± 0 026	0 017	
94	158	21 27	22 03	0 67 ± 0 04	2 340 ± 0 033	0 014	
94	160	23 12	23 40	0 47 ± 0 01	2 164 ± 0 013	0 006	
94	166	18 51	19 18	0 86 ± 0 13	2 109 ± 0 115	0 034	
94	172	22 37	23 06	0 35 ± 0 07	2 448 ± 0 072	0 029	
94	178	22 43	23 11	0 30 ± 0 06	2 700 ± 0 058	0 016	Cloudy
94	192	14 56	15 22	0 66 ± 0 05	2 172 ± 0 050	0 021	
94	199	15 18	15 33	0 63 ± 0 16	2 905 ± 0 159	0 065	Cloudy
94	206	15 39	16 04	−0 41 ± 0 11	2 356 ± 0 075	0 057	
94	220	14 59	15 24	−0 59 ± 0 01	2 796 ± 0 011	0 012	
94	229	23 18	23 37	−1 08 ± 0 14	3 154 ± 0 105	0 096	Cloudy
94	255	22 42	23 05	−0 90 ± 0 08	2 354± 0 059	0 057	
94	265	22 44	23 14	−0 96 ± 0 06	2 683 ± 0 043	0 040	
94	269	15 23	15 49	−0 80 ± 0 07	2 674 ± 0 054	0 054	Cloudy
94	270	05 26	05 47	−0 79 ± 0 12	2 528 ± 0 086	0 082	Cloudy
94	283	14 55	15 18	0 00 ± 1 45	3 903 ± 1 198	0 717	
94	284	05 29	05 52	1 26 ± 0 05	2 620 ± 0 035	0 034	

Table 3 The 8 4-GHz tipping-curve fit results (continued)

Year	DOY	UTC Time		Zenith bias temperature, K	Atmosphere temperature, K	RMS, K	Notes
		Start	End				
94	286	14 50	15 11	1 78 ± 0 08	2 571 ± 0 054	0 059	
94	286	18 45	19 06	1 39 ± 0 73	2 587 ± 0 472	0 466	
94	297	16 00	16 23	−0 57 ± 0 06	2 679 ± 0 041	0 041	
94	298	05 51	06 13	−0 81 ± 0 07	2 699 ± 0 052	0 052	
94	306	15 59	16 21	−0 44 ± 0 17	2 887 ± 0 113	0 119	Windy
94	311	18 24	18 46	0 04 ± 0 04	2 358 ± 0 023	0 024	
94	325	18 50	19 14	0 40 ± 0 04	2 386± 0 029	0 031	
94	340	07 14	07 38	0 74 ± 0 10	2 406 ± 0 067	0 071	
95	3	07 06	07 29	0 62 ± 0 13	2 571 ± 0 084	0 093	Rainy
95	6	16 34	16 58	0 68 ± 0 41	3 046 ± 0 255	0 281	Rainy
95	9	23 12	23 32	0 44 ± 0 17	2 580 ± 0 113	0 119	Rainy
95	23	16 51	17 14	0 29 ± 0 25	3 724 ± 0 154	0 178	Rainy
95	23	17 32	18 10	0 76 ± 0 74	3 596 ± 0 509	0 701	Rainy
95	37	19 20	19 44	−0 12 ± 0 10	2 353 ± 0 072	0 072	
95	38	04 51	05 41	0 12 ± 0 04	2 468 ± 0 029	0 047	
95	51	02 31	03 10	0 14 ± 0 07	2 335 ± 0 046	0 058	
95	51	20 04	20 45	0 07 ± 0 07	2 331 ± 0 056	0 074	
95	66	15 11	15 34	0 46 ± 0 08	2 254 ± 0 052	0 055	
95	81	14 38	15 27	0 59 ± 0 07	2 278 ± 0 040	0 074	
95	95	01 31	01 50	0 00 ± 0 09	2 289 ± 0 065	0 063	
95	109	13 14	14 02	0 82 ± 0 06	2 368 ± 0 035	0 063	
95	117	13 46	14 07	0 93 ± 0 09	2 357 ± 0 054	0 060	
95	122	11 34	11 53	0 10 ± 0 06	2 376 ± 0 045	0 044	
95	125	22 01	22 15	0 51 ± 0 13	2 443 ± 0 081	0 068	
95	128	15 26	15 43	0 70 ± 0 06	2 490 ± 0 040	0 043	
95	137	17 46	19 46	0 59 ± 0 22	2 379 ± 0 142	0 114	
Averages				0 53 ± 0 73	2 490 ± 0 350	0 086	

over the time scale of the tip-curve period are assumed to be the dominating contributor to the rms scatters for most of the data sets, where the rms scatter exceeds the expected 0 04-K gain fluctuations

Tables 4 and 5 display the BWG, WVR, and surface model (SURF)-derived atmospheric noise temperatures at zenith for 32- and 8 4-GHz, respectively, for a select subset of data sets Also provided are the difference temperatures BWG–WVR and BWG–SURF The differences of the tip-curve values with those derived from the WVR data for this select subset are displayed in Figs 13 and 14 for 32 and 8 4 GHz, respectively

The 32- or 33 7-GHz WVR-derived values were computed by (1) fitting a straight line over the 31 4-GHz zenith WVR data across the BWG tip-curve interval, (2) taking the linear fit value at the midpoint of the interval, (3) removing the effective cosmic contribution for 32 GHz, and (4) then correcting the WVR value to the frequency of the tip-curve data by adding 0 2 K to refer to 32 GHz and 0 95 K for 33 7 GHz The 8 4-GHz WVR-derived values were computed from the 31 4-GHz zenith WVR data as

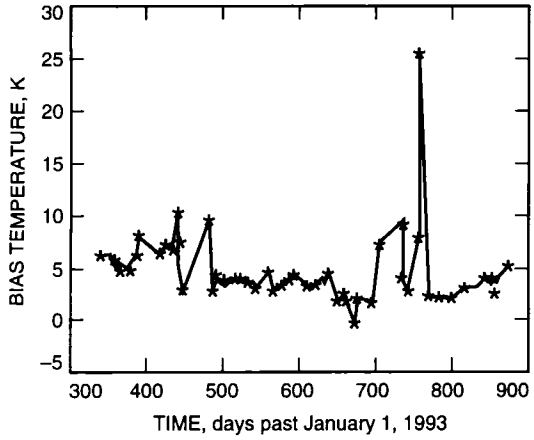

Fig 7 Bias temperatures at 32 GHz

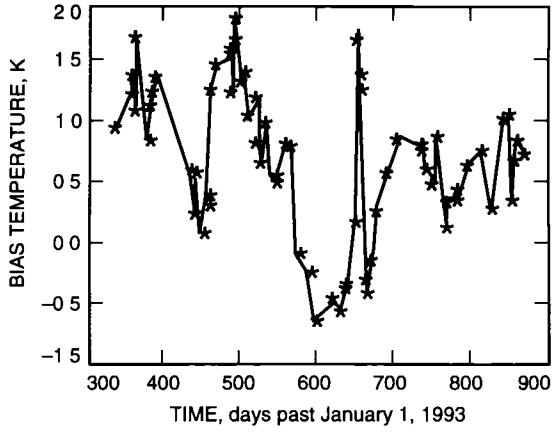

Fig 8 Bias temperatures at 8 4 GHz

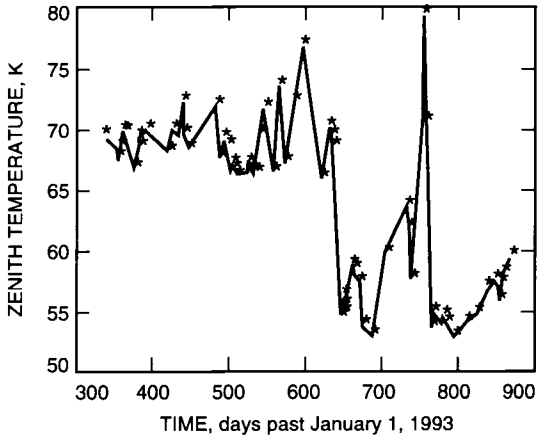

Fig 9 Zenith temperatures at 32 GHz over the tip-curve period

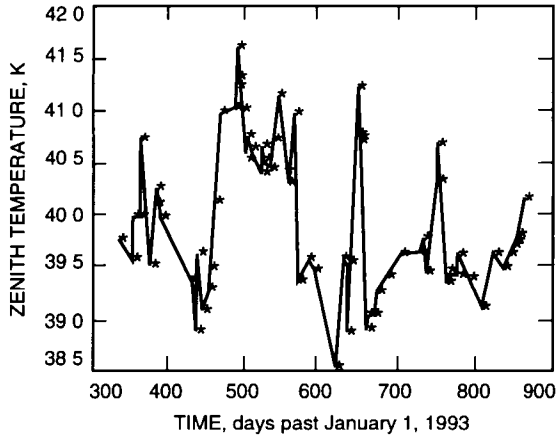

Fig 10 Zenith temperatures at 8 4 GHz over the tip-curve period

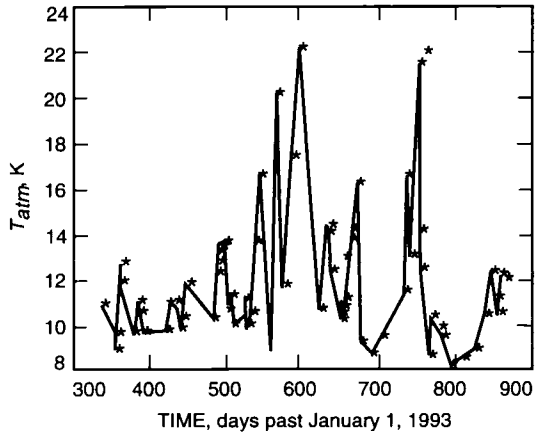

Fig 11 Atmospheric noise temperatures at zenith for 32 GHz from fit of tip-curve data

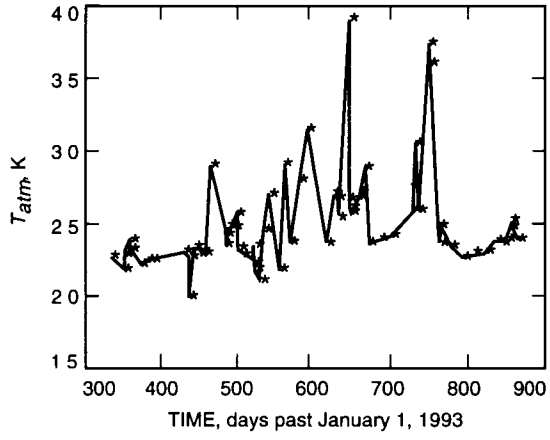

Fig 12 Atmospheric noise temperatures at zenith for 8 4 GHz from fit of tip-curve data

Table 4 The 32-GHz BWG, WVR, and surface model (SURF)-derived zenith atmospheric noise temperatures and scatters

Year	DOY	UTC Time		T_{BWG}, K	RMS	T_{WVR}, K	RMS	T_{SURF}, K	$T_{BWG} - T_{WVR}$, K	$T_{BWG} - T_{SURF}$, K
		Start	End							
94	17	15 57	16 25	10 504	0 227	10 420	0 159	6 994	0 084	3 510
94	17	22 30	22 47	11 025	0 085	10 745	0 131	7 154	0 280	3 871
94	24	16 16	16 45	9 687	1 199	9 911	0 130	11 285	−0 224	−1 598
94	115	15 27	16 04	10 280	0 209	11 208	0 117	9 168	−0 928	1 112
94	122	15 05	16 02	12 342	0 033	12 511	0 114	10 779	−0 169	1 563
94	122	21 44	22 42	12 846	0 195	12 326	0 413	8 483	0 520	4 363
94	123	22 55	23 44	13 154	0 145	13 633	0 158	8 731	−0 479	4 423
94	124	05 11	06 01	13 573	0 033	13 951	0 137	11 051	−0 378	2 522
94	158	15 10	16 08	10 420	0 082	10 554	0 170	9 715	−0 134	0 705
94	158	21 29	22 03	11 179	0 100	11 895	0 100	8 493	−0 716	2 686
94	178	22 49	23 12	16 667	0 161	16 142	0 297	10 384	0 525	6 283
94	199	15 20	15 38	20 161	0 574	18 341	0 130	11 259	1 820	8 902
94	220	15 01	15 25	17 373	0 098	17 282	0 093	10 010	0 091	7 363
94	229	23 19	23 39	22 111	0 233	22 293	0 200	16 984	−0 182	5 127
94	255	22 44	23 07	10 646	0 335	10 617	0 376	9 329	0 029	1 317
94	297	16 02	16 25	14 149	0 160	14 287	0 194	8 141	−0 138	6 008
94	298	05 53	06 15	13 942	0 089	13 214	0 262	10 848	0 728	3 094
94	306	16 01	16 23	16 310	0 298	15 142	0 647	11 137	1 168	5 173
94	311	18 25	18 48	9 258	0 271	9 463	0 202	6 646	−0 205	2 612
94	325	18 52	19 15	8 721	0 130	9 122	0 062	5 980	−0 401	2 741

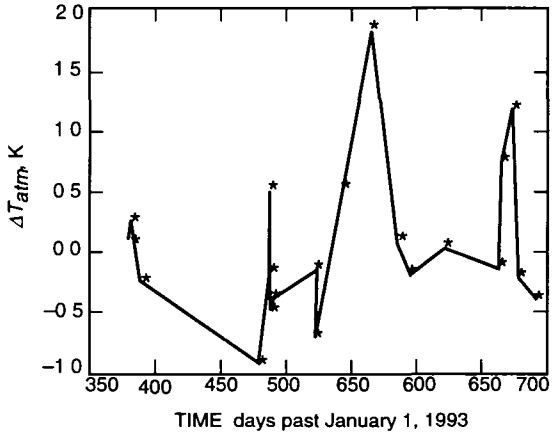

Fig 13 Differences of 32-GHz tip curve T_{atm} from those estimated from 31 4-GHz WVR zenith data

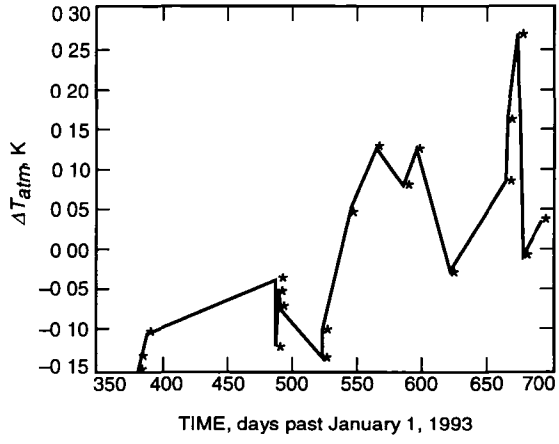

Fig 14 Differences of 8 4-GHz tip curve T_{atm} from those estimated from 31 4-GHz WVR zenith data

Table 5 The 8 4-GHz BWG, WVR, and surface model (SURF)-derived zenith atmospheric noise temperatures and scatters

Year	DOY	UTC Time		T_{BWG}, K	RMS	T_{WVR}, K	RMS	T_{SURF}, K	$T_{BWG} - T_{WVR}$, K	$T_{BWG} - T_{SURF}$, K
		Start	End							
94	17	15 57	16 25	2 239	0 080	2 374	0 040	2 139	−0 135	0 100
94	17	22 30	22 47	2 239	0 059	2 388	0 032	2 138	−0 149	0 101
94	24	16 16	16 45	2 249	0 078	2 353	0 034	2 460	−0 104	−0 211
94	122	15 03	16 01	2 431	0 026	2 468	0 021	2 399	−0 037	0 032
94	122	21 42	22 41	2 338	0 047	2 461	0 089	2 196	−0 123	0 142
94	123	22 53	23 43	2 469	0 035	2 523	0 031	2 207	−0 054	0 262
94	124	05 09	06 00	2 467	0 016	2 540	0 026	2 400	−0 073	0 067
94	158	15 08	16 07	2 242	0 017	2 379	0 042	2 338	−0 137	−0 096
94	158	21 27	22 03	2 340	0 014	2 440	0 022	2 189	−0 100	0 151
94	178	22 43	23 11	2 700	0 016	2 654	0 048	2 322	0 046	0 378
94	199	15 18	15 33	2 905	0 065	2 779	0 025	2 411	0 126	0 494
94	220	14 59	15 24	2 796	0 012	2 718	0 016	2 283	0 078	0 513
94	229	23 18	23 37	3 154	0 096	3 030	0 028	2 869	0 124	0 285
94	255	22 42	23 05	2 354	0 057	2 383	0 083	2 259	−0 029	0 095
94	297	16 00	16 23	2 679	0 041	2 594	0 024	2 260	0 085	0 419
94	298	05 51	06 13	2 699	0 052	2 539	0 046	2 473	0 160	0 226
94	306	15 59	16 21	2 887	0 119	2 620	0 095	2 488	0 267	0 399
94	311	18 24	18 46	2 358	0 024	2 366	0 052	2 132	−0 008	0 226
94	325	18 50	19 14	2 386	0 031	2 351	0 016	2 105	0 035	0 281

in (1) and (2) above, then a conversion to reference to 8 4 GHz was applied,[10] and then the effective 8 4-GHz cosmic contribution was removed

Based on an examination of the WVR scatters about the tip-curve intervals, the scatters at 32 GHz (see Table 4) for typical "dry" days range from 0 06 to 0 6 K and are in reasonable agreement with the BWG tip-curve postfit rms scatters At 32 GHz, the few cases of significantly different scatters of the WVR data relative to the BWG data may be attributed to (1) the effects of averaging time and algorithm of the WVR, (2) cases of higher than usual gain instability for the BWG system, or (3) the difference in atmospheric noise between the regions of the sky observed with the BWG and WVR

The average 13 2 K of T_{atm} at zenith for 32 GHz is in agreement with the 13 2 K of the WVR for this subset The average of the difference temperatures between the BWG tip curve and the WVR is 0 06 $\pm$ 0 64 K, which is consistent with the 0 5-K absolute accuracy of the WVR [11] As the WVR and BWG data were acquired in different parts of the sky, this agreement is indicative of the good weather conditions under which most of the KaAP experiments have been conducted The average difference of the BWG atmospheric temperatures minus those of the surface model is 3 6 $\pm$ 2 5 K If the BWG and WVR data are indicative of the true statistical weather conditions at Goldstone, then the surface model for Goldstone will require refinement The 2 5-K average value of the BWG T_{atm} at zenith for 8 4 GHz over this subset is in agreement with the 2 5-K average value derived from the WVR data The 8 4-GHz scatters about the fit of the BWG tip-curve data and the scatter of the WVR data over the tip-curve measurement

[10] S Keihm, "Conversion of WVR 31 4 GHz Zenith TB Measurements to X-band," JPL Interoffice Memorandum 3833-94-440/SJK (internal document), Jet Propulsion Laboratory, Pasadena, California, December 15, 1994

[11] S Keihm, personal communication, Jet Propulsion Laboratory, Pasadena, California, May 1995

period are usually in reasonable agreement (typically 0 03 K) The average of the temperature differences between BWG and WVR values for 8 4 GHz is $-0\ 001 \pm 0\ 12$ K, while the corresponding average for the BWG relative to the surface model is $0\ 2 \pm 0\ 2$ K

Previous work at 32 GHz by Otoshi et al [9] at DSS 13 also found that their 32-GHz measurements significantly disagreed with values derived from the surface model This was explained as being due to either (1) the theoretical weather model not being as good at 32 GHz as it was at 8 4 GHz or (2) the elevation-dependent noise contributions of the antenna being corrupted more from tripod leg scatter, spillover, and panel leakage Based on these studies ([9] and this article), it appears that the surface weather model at 32 GHz for Goldstone requires refinement

3. RMS Scatter About Fitted Model The contributions to the rms noise in the BWG tip-curve post-fit residual temperatures are (1) thermal noise, (2) uncalibrated gain changes, (3) atmospheric noise, and (4) systematic mismodeling,

$$\sigma_T = T_{op}\sqrt{\frac{1}{B\tau} + \left(\frac{\Delta G}{G}\right)^2 + \frac{\sigma_{atm}^2}{T_{op}^2} + \frac{\sigma_{mod}^2}{T_{op}^2}}$$

where T_{op} is the operating temperature measurement (K), B is the radiometer bandwidth (Hz), τ is the radiometer integration time (s), $\Delta G/G$ is the normalized uncalibrated gain variation between minicals, σ_{atm} is the atmospheric fluctuation (K), and σ_{mod} is mismodeling noise (K)

Random fluctuations are expected to lie below 0 01 K given the noise bandwidths and integration time of the TPR Uncalibrated gain fluctuations for most passes are expected to be on the order of 0 1 percent of the operating noise temperatures (0 04 K at 8 4 GHz and 0 07 K at 32 GHz) based on the gain changes observed between minicals These levels appear to be consistent with many of the lower-value rms scatters in Tables 2 and 3 Higher values of rms scatters in Tables 2 and 3 are usually attributed to atmospheric fluctuations over the tip-curve interval, especially those observed during known turbulent weather conditions

The major contribution to the rms noise at 32 GHz for the majority of the data sets is expected to be due to a small amount of systematic mismodeling of the temperature model The quadratic model used for antenna temperature at 32 GHz, which is removed from the data [Eq (5)], varies about 1 5 K from 10 deg to zenith (see Fig 5), most of which is attributed to tripod scatter The remaining ± 0 2-K signature seen in the postfit residuals (see Fig 6) is more complex The variation as the antenna moves off zenith is the unmodeled effect of the side lobes sweeping against the ground The typical rms scatter of this effect over the typical tip-curve sequence is about 0 1 K at 32-GHz

The elevation-dependent antenna temperature model used in this study at 32 GHz appears to be consistent within 0 5 K (the quoted accuracy of the WVR data used in the intercomparison with the tip-curve data) The good agreement of the BWG tip-curve data with the WVR data supports this The smaller remaining signature of order 0 2 K visible in the postfit residuals at 32 GHz (see Fig 6) was not considered significant to remove for the purpose of this first study From the postfit residual plots of Fig 6 and other tip-curve data sets, this systematic signature appears repeatable and can, therefore, be extracted from the data by using an appropriate model As more data sets conducted in good weather are acquired, such a refinement in the model may be a possible output product of the data

4. Cumulative Distributions of Atmospheric Noise Temperatures. Figure 15 is a plot of the cumulative distribution of the 32-GHz zenith atmospheric noise temperatures determined from the tip-curve data, and Fig 16 is the corresponding plot for the 8 4-GHz values Included on the plots are

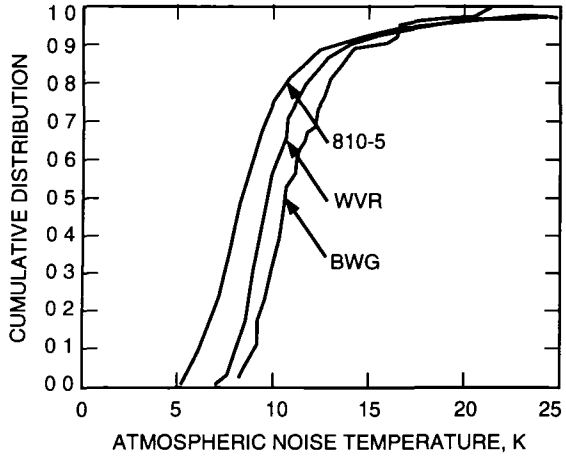

Fig 15 Cumulative distribution of 32-GHz BWG tip-curve zenith atmospheric noise temperatures, WVR data, and 810-5 model

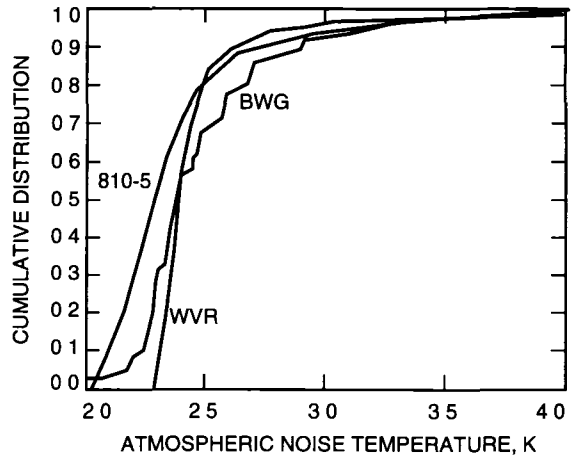

Fig 16 Cumulative distribution of 8 4-GHz BWG tip-curve zenith atmospheric noise temperatures, WVR data, and 810-5 model

the corresponding statistics derived from 31 4-GHz WVR data[12] (after removing the cosmic contribution and applying the necessary corrections to the appropriate frequency) and the cumulative statistics for Goldstone from a DSN design document referred to as 810-5 [13]

A few important points should be considered when interpreting these curves First, all of the KaAP data points were acquired over a limited set of weather conditions that were mostly daytime observations conducted during prime shifts The tip-curve and supporting surface meteorological data were indicative of observing conditions not spanning the full gamut of possible very dry or very wet conditions The WVR statistics were determined from a virtually continuous set of R6 WVR data that covered a 10-month interval from October 6, 1993, to July 31, 1994 (not to be confused with the small subset of WVR data used in the previously discussed intercomparison) The 810-5 model was originally derived from data acquired at the overseas sites and then translated to reflect Goldstone conditions [14] The surface model used in the intercomparison has statistics similar to the 810-5 model at 32 GHz Figure 15 shows the 810-5 model's temperature for a given cumulative distribution (0 8 and under) significantly below those of the WVR and tip-curve-derived values at 32 GHz The apparent biased 1-K lower value of the WVR over the BWG tip-curve values may reflect the fact that the WVR continuous data set was sampled over a greater number of drier periods than the fewer BWG tip curves, which were conducted primarily during daytime, when more water vapor may be present Another possibility may be a bias error of order 1 K in one or both of the data acquisition systems and algorithms As more DSS-13 BWG tipping-curve data sets are acquired over a longer time interval and over a wider range of weather conditions, a more meaningful characterization of the cumulative statistics can be realized

V. Future Work

Efforts to further correlate the tipping-curve statistics with those of the WVR data should be performed as more BWG tipping-curve data are acquired This will allow the availability of a large database of weather statistics derived from diverse equipment and data reduction methods Such statistics will be useful to derive link strategies at 32 GHz for Goldstone

[12] S Keihm, "Goldstone 31 4 GHz WVR Statistics, October 93–July 94," JPL Interoffice Memorandum 3833-94-410/SJK (internal document), Jet Propulsion Laboratory, Pasadena, California, August 26, 1994

[13] *Deep Space Network/Flight Project Interface Design Handbook, Volume I Existing Capabilities*, 810-5, Rev D (internal document), Module TCI-40, Jet Propulsion Laboratory, Pasadena, California, pp 5–6, May 1, 1992

[14] Ibid

An improved elevation angle–dependent model for the antenna noise temperature at both 32 and 8 4 GHz should be estimated using the appropriate methodology and assumptions and then checked against the model derived from the data in this study The estimate should characterize or set limits on the contribution of the tripod scatter The tip-curve data (along with supporting WVR data) could be used to refine the antenna temperature versus elevation model at 32 GHz

An updated, intensive, and careful analysis to estimate the loss factors of the antenna reflectors, mirrors, and tripod structures should be performed The loss factors can change due to the amount of reflector or mirror misalignment present Given that the original noise accounting budget was performed several years ago, a reassessment of these factors is in order

Losses due to mismatch have not been considered in the analysis presented in this article Future work should consider the effect of these losses in the temperature model and make use of any new values that become available from theoretical studies

Acknowledgments

We thank R Clauss, C Stelzried, S Stewart, L Teitelbaum, P Richter, S Slobin, and G Resch for several informative discussions and comments, the DSS-13 station personnel for acquiring data and promptly addressing data acquisition issues as they came up (L Tanida, G Bury, C Goodson, R Reese, J Garnica, R Littlefair, J Crook, and C Mitchell), C Smyth and L Lee for providing LMCOA capability, E Paulsen, J Bowen, S Stewart, L Alvarez, W Veruttipong, and A Bernardo for providing information on equipment and station specifications, S Keihm for providing and interpreting the WVR data, and T Rebold for assistance in software development

References

[1] J G Smith, "Ka-Band (32-GHz) Downlink Capability for Deep Space Communications," *The Telecommunications and Data Acquisition Progress Report 42-88, October–December 1986*, Jet Propulsion Laboratory, Pasadena, California, pp 96–103, February 15, 1987

[2] J W Layland and J G Smith, "A Growth Path for Deep Space Communications," *The Telecommunications and Data Acquisition Progress Report 42-88, October–December 1986*, Jet Propulsion Laboratory, Pasadena, California, pp 120–125, February 15, 1987

[3] A L Riley, D M Hanson, A Mileant, and R W Hartop, "A Ka-Band Beacon Link Experiment (KABLE) With Mars Observer," *The Telecommunications and Data Acquisition Progress Report 42-88, October–December 1986*, Jet Propulsion Laboratory, Pasadena, California, pp 141–147, February 15, 1987

[4] T A Rebold, A Kwok, G E Wood, and S Butman, "The Mars Observer Ka-Band Link Experiment," *The Telecommunications and Data Acquisition Progress Report 42-117, January–March 1994*, Jet Propulsion Laboratory, Pasadena, California, pp 250–282, May 15, 1994

[5] L S Alvarez, "Analysis and Applications of a General Boresight Algorithm for the DSS-13 Beam Waveguide Antenna," *The Telecommunications and Data Acquisition Progress Report 42-111, July–September 1992*, Jet Propulsion Laboratory, Pasadena, California, pp 48-61, November 15, 1992

[6] C T Stelzried and M J Klein, "Precision DSN Radiometer Systems Impact on Microwave Calibrations," *Proc of the IEEE*, vol 82, pp 776–787, May 1994

[7] J C Chen, P H Stanton, and H F Reilly, "Performance of the X-/Ka-/KABLE-Band Dichroic Plate in the DSS-13 Beam Waveguide Antenna," *The Telecommunications and Data Acquisition Progress Report 42-115, July–September 1993*, Jet Propulsion Laboratory, Pasadena, California, pp 54–64, November 15, 1993

[8] S J Keihm, "Water Vapor Radiometer Measurements of the Tropospheric Delay Fluctuations at Goldstone Over a Full Year," *The Telecommunications and Data Acquisition Progress Report 42-122, April–June 1995*, Jet Propulsion Laboratory, Pasadena, California, pp 1–11, August 15, 1995

[9] T Y Otoshi, S R Stewart, and M M Franco, "A Portable Ka-band Front-End Test Package for BWG Antenna Performance Evaluation, Part II Tests on the Antenna," *The Telecommunications and Data Acquisition Progress Report 42-106, April–June 1991*, Jet Propulsion Laboratory, Pasadena, California, pp 266–282, August 15, 1991

[10] S D Slobin, "Microwave Noise Temperature and Attenuation of Clouds Statistics of these Effects at Various Sites in the United States, Alaska, and Hawaii," *Radio Science*, vol 17, pp 1443–1454, November–December 1982

[11] M L Kutner, "Application of a Two-Layer Atmospheric Model to the Calibration of Millimeter Observations," *Astrophysical Letters*, vol 19, pp 81–87, 1978

[12] T Y Otoshi, S R Stewart, and M M Franco, "A Portable X-band Front-End Test Package for BWG Antenna Performance Evaluation Part II Tests on the Antenna," *The Telecommunications and Data Acquisition Progress Report 42-105, January–March 1991*, Jet Propulsion Laboratory, Pasadena, California, pp 54–68, May 15, 1991

Performance of a Ka-Band Transponder Breadboard for Deep-Space Applications

N R Mysoor, J P Lane, S Kayalar, and A W Kermode
Spacecraft Telecommunications Equipment Section

This article summarizes the design concepts applied in the development of an advanced Ka-band (34 4 GHz/32 GHz) transponder breadboard for the next generation of space communications systems applications The selected architecture upgrades the X-band (7 2 GHz/8 4 GHz) deep-space transponder (DST) to provide Ka-band up/Ka- and X-band down capability In addition, it can also be configured to provide X-band up/Ka- and X-band down capability The Ka-band transponder breadboard incorporates several state-of-the-art components, including sampling mixers, a Ka-band dielectric resonator oscillator, and microwave monolithic integrated circuits (MMICs) The MMICs that were tested in the breadboard include upconverters, downconverters, automatic gain control circuits, mixers, phase modulators, and amplifiers The measured receiver dynamic range, tracking range, acquisition rate, static phase error, and phase jitter characteristics of the Ka-band breadboard interfaced to the advanced engineering model X-band DST are in good agreement with the expected performance The results show a receiver tracking threshold of −149 dBm with a dynamic range of 80 dB and a downlink phase jitter of 7-deg rms The analytical results of phase noise and Allan standard deviation are in good agreement with the experimental results

I. Introduction

Telecommunications transponders for deep-space spacecraft applications [1,2] provide uplink command, turnaround ranging, differential one-way ranging (DOR), downlink telemetry, and radiometric capabilities The Ka-band transponder breadboard provides these capabilities at a Ka-band uplink [3] frequency of 34 415 GHz and a downlink frequency of 31 977 GHz Operation at Ka-band allows the use of smaller antennas, it provides both a higher transmission bandwidth to allow a 4- to 6-dB improvement over X-band on downlink data rate capability and increased accuracy in DOR applications Furthermore, Ka-band has a unique advantage for missions such as Solar Probe, Mercury, and Venus missions as it suffers negligible signal-to-noise degradation due to signal scintillation in the solar plasma The signal-to-noise degradation at X-band is estimated to be about 5 to 10 dB in solar flux environment To enable flexibility in spacecraft design and modularity in spacecraft hardware, the design was chosen to provide the Ka-band functionality by adding conversion circuitry to the existing X-band (7 2-GHz/8 4-GHz) deep-space transponder (DST) design [2], as shown in Fig 1 This modularity allows either X- or Ka-band uplink and X- and/or Ka-band downlink operation This article describes the Ka-band transponder design, analysis, and breadboard performance results The Ka-band transponder block diagram, functional requirements,

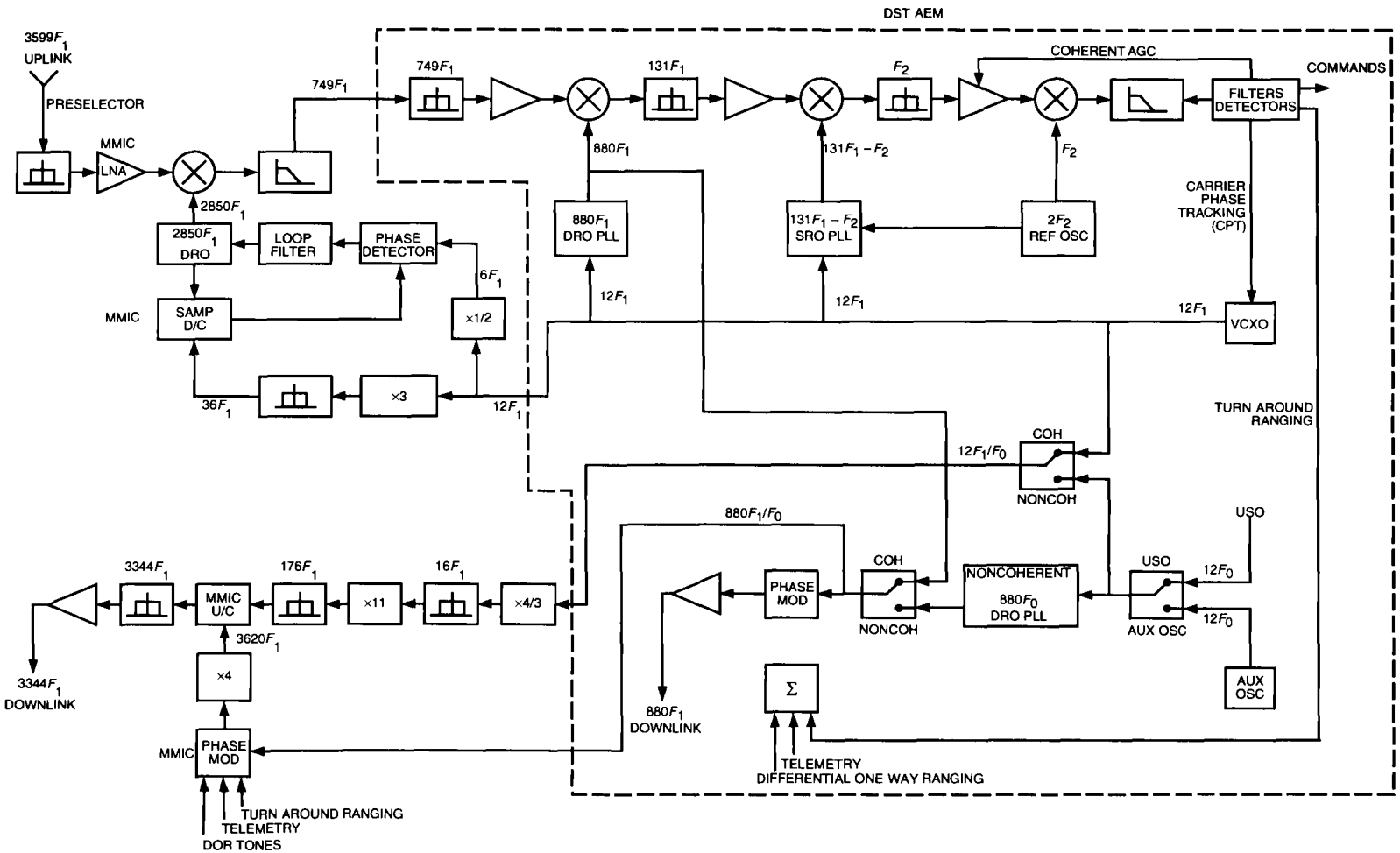

Fig 1 Ka-band transponder functional block diagram

and design specifications are summarized in Section II The transponder phase noise analysis is described in Section III The breadboard performance results and conclusions are presented in Sections IV and V, respectively

II. Ka-Band Transponder Block Diagram and Functional Requirements

A. Block Diagram and Frequency Scheme

The Ka-band transponder functional block diagram and frequency generation scheme are shown in Fig 1 The Ka-band transponder design uses the X-band DST and Ka-band receiver and exciter circuitry to implement the transponder functions at Ka-band uplink and downlink frequencies [2,3] The Ka-band receiver and exciter circuits are designed to interface directly with either the X-band DST breadboard or the X-band DST advanced engineering model (DST-AEM) developed by Motorola for JPL The Ka-band receiver circuitry performs preselection and low-noise amplification at Ka-band and downconversion to the X-band DST uplink frequency The Ka-band exciter circuitry performs telemetry, ranging, and DOR phase modulation on the X-band DST downlink reference and frequency multiplication and conversion to the Ka-band downlink frequency

The design requirements for the Ka-band transponder and frequency translation ratios are listed in Table 1 The uplink and downlink frequencies are expressed in terms of the reference frequency, F_1 The exact F_1 frequency is determined by the Deep Space Network (DSN) channel in operation The DSN channel frequencies [2,3] selected for this implementation correspond to channel number 14 at $2F_1$ with F_1 equal to 9 5625 MHz for coherent mode, and channel number 16 at $2F_0$ with F_0 equal to 9 565586 MHz for noncoherent mode The turnaround ratio of the uplink-to-downlink frequency is equal to 3599/3344 (34 4 GHz/32 GHz) The criteria [3] used in the selection of the turnaround ratio include the maximum possible number of DSN channels for simultaneous X- and Ka-band operation, transmit/receive channel separation for diplexer implementation, central Ka-band allocation considerations, transponder implementation complexity, and uplink/downlink interference considerations

1. X-Band Deep-Space Transponder Advanced Engineering Model Frequency Plan. The functional block diagram for the X-band deep-space transponder advanced engineering model is shown in Fig 1 The X-band receiver [2] is implemented as a double-conversion superheterodyne phase-lock carrier-tracking receiver with a fixed second intermediate frequency (IF) The first and second intermediate frequencies are at $131F_1$ (1252 7 MHz) and F_2 (12 25 MHz), respectively Coherent carrier automatic gain control (AGC) is employed in both of the IF sections to provide a constant signal plus noise at the carrier loop phase detector The first local oscillator (LO) signal at $880F_1$ (8415 MHz) and the second LO signal at $131F_1 - F_2$ are generated by a dielectric resonator oscillator (DRO) [4] and a surface acoustic wave resonator oscillator (SRO), respectively Both of these oscillators are phase locked to the $12F_1$ (114 75 MHz) voltage controlled oscillator (VCO) The $12F_1$ VCO is in turn phase locked to the uplink carrier The SRO phase-locked loop (PLL) consists of an SRO, a $\times 11$ multiplier, a -6 divider, two mixers, a -2 divider, and a phase detector The $\times 11$ multiplier and -6 divider are used in the SRO PLL to generate the frequencies $132F_1$ and $2F_1$ from 12_1 The $2F_1$ and the reference oscillator output at $2F_2$ are applied to a mixer followed by a -2 divider to obtain a reference signal at $F_1 + F_2$ to the SRO PLL phase detector The SRO output at $131F_1 - F_2$ and the $132F_1$ signals are applied to a mixer to obtain the second input signal at $F_1 + F_2$ to the SRO PLL phase detector A $\times 73$ multiplier and a -3 divider are used in the DRO PLL to generate reference signals at $836F_1$ and $4F_1$, respectively

The coherent downlink carrier at $880F_1$ is provided by the LO DRO when the DST is operating in the coherent mode from the VCO In the noncoherent mode, an $880F_0$ frequency is generated by the exciter DRO phase locked to the DST $12F_0$ auxiliary oscillator (AUX OSC) or the external ultra-stable oscillator (USO) The noncoherent downlink signal is automatically selected by the receiver AGC function upon the absence of an uplink signal An X-band phase modulator is used to phase modulate the downlink signal with telemetry signals, turnaround ranging, or DOR tones

Table 1 Ka-band transponder design requirements

Parameter	Design requirement
Uplink frequency allocations	
Ka-band uplink	34,200–34,700 MHz, deep space
X-band uplink	7145–7190 MHz, deep space
Downlink frequency allocations	
Ka-band downlink	31,800–32,300 MHz, deep space
X-band downlink	8400–8450 MHz, deep space
Frequency translation ratios	
Channel 14 Ka-band uplink frequency	34,415 4375 MHz ($3599F_1$)
Channel 14 X-band uplink frequency	7162 3125 MHz ($749F_1$)
X-band downlink	880/3599 (8415 MHz)
Ka-band downlink	3344/3599 (31,977 MHz)
Ka-band receiver parameters	
Carrier threshold	≤ -149 dBm, unmodulated carrier
Dynamic range	$\geq$79 dB (carrier threshold to -70 dBm)
Noise figure at Ka-band receiver input	$\leq$6 dB
Acquisition and tracking rate	$\geq$550 Hz/s at carrier level > -110 dBm
Tracking range	$\geq \pm 100$ kHz minimum
Tracking error	$\leq$1 deg/40 kHz at carrier level > -110 dBm
Capture range	$\geq \pm 1$ 3 kHz at carrier level > -110 dBm
Ka-band exciter parameters	
Frequency, coherent operation	3344/3599 × uplink frequency
Frequency, noncoherent operation	31,987 320988 MHz ($3344F_0$)| channel 16
RF output power level	$\geq$+3 dBm
Output voltage standing wave ratio	$\leq$1 5 1, 50 ± 5 ohms
Spurious signals	$\geq$60 dBc below the carrier
Modulation bandwidth	$\geq$50 MHz at ±0 5 dB
Peak phase modulation index	±2 5 rad at ±8% linearity
Modulation sensitivity	2 rad peak/volt peak
Modulation index stability	±10% over −20 deg C to +75 deg C
Modulation index	
Turnaround ranging	3–9 dB carrier suppression
Telemetry	0–15 dB carrier suppression
DOR	0–1 1 dB carrier suppression
Residual phase noise	$\leq$8 deg rms, coherent mode
	$\leq$8 deg rms, noncoherent mode
Carrier phase delay variation	$\leq$12 ns over −20 deg C to +75 deg C
Differential phase delay variation	$\leq$2 ns Ka-/X-band over −20 deg C to +75 deg C
Ranging phase delay variation	$\leq$30 ns over −20 deg C to +75 deg C

2. Ka-Band-to-X-Band Downconverter. The Ka-band receiver circuitry performs preselection and low-noise amplification at $3599F_1$ (34 415 GHz) and downconversion to the $749F_1$ (7 16 GHz) X-band DST uplink frequency A five-pole Chebychev waveguide iris preselector filter is used to filter the receiver Ka-band uplink frequency at 34 415 GHz, reject the Ka-band downlink frequency at $3344F_1$ (31 977 GHz), and attenuate the receiver LO leakage After a waveguide-to-coax transition, a microwave

monolithic integrated circuit (MMIC) low-noise amplifier (LNA) sets the noise figure of the receiver A triple balanced hybrid mixer is used for downconversion to X-band

A phase-locked Ka-band DRO generates the LO signal at $2850F_1$ (27 253 GHz) needed for the $3599F_1$-to-$749F_1$ downconversion The phase-locked DRO yields lower spurious output and phase noise than could be achieved with a direct multiplication implementation A hybrid MMIC sampling downconverter is used to sample the Ka-band LO output with a $36F_1$ reference and downconvert it to $6F_1$ for phase detection with a digital phase/frequency detector The $6F_1$ and $36F_1$ loop references are derived from the $12F_1$ reference with a divide-by-two analog Miller divider and a bipolar junction transistor (BJT) multiplier, respectively

3. Ka-Band Exciter. The Ka-band exciter circuitry performs phase modulation on the $880F_1$ (8 415 GHz) X-band DST downlink reference and frequency multiplication and conversion to the $3344F_1$ (31 977 GHz) Ka-band downlink frequency An X-band MMIC phase modulator [5] modulates the telemetry, ranging, and DOR signal on the X-Band DST downlink reference The modulated X-band signal is multiplied to $3520F_1$ (33 66 GHz) with a hybrid $\times 4$ varactor multiplier The harmonics are filtered to reduce in-band spurious signals on the downlink The $3520F_1$ modulated signal is converted to the $3344F_1$ downlink frequency by mixing it with a $176F_1$ (1683 MHz) signal using a MMIC upconverter The conversion spurious signals are filtered out The $176F_1$ reference for the conversion is generated from the $12F_1$ reference signal from the DST with a Miller divider and step-recovery diode multiplier The Miller divider multiplies the $12F_1$ reference by 4/3 to give $16F_1$ The signal is multiplied with a $\times 11$ step-recovery diode circuit and filtered to produce the $176F_1$ reference

B. Key Design Requirements

The key design requirements for the Ka-band transponder are summarized in Table 1 These requirements apply to Ka-band receiver and exciter breadboards operating with the X-band DST-AEM These requirements can be satisfied with no modifications to the X-band DST-AEM The Ka-band receiver performance includes a noise figure of 5 4 dB, an unmodulated carrier-tracking threshold of -149 dBm, and a tracking range of ± 100 kHz at the assigned channel frequency The acquisition and tracking rate is specified to be at least 550 Hz/s The specified nominal output power of the Ka-band exciter is +3 dBm The exciter output is phase modulated to a maximum phase deviation of ± 2 5 rad with a radio frequency ± 0 5-dB modulation bandwidth of 50 MHz The phase noise measured from 5 Hz to 25 MHz is required to be less than 8-deg root mean square (rms) in both the coherent and the noncoherent modes

III. Ka-Band Transponder Phase Noise Analysis and Results

The downlink phase-noise power spectral density of the Ka-band transponder is predicted using noise models [6–11] for various devices and the loop transfer functions in a custom JPL software package A complete description of the phase noise model is given in Appendix A, and carrier threshold calculations are given in Appendix B The phase noise models for the Ka-band receiver and exciter are shown in Fig A-1 The phase noise outputs of the local oscillator loops are used in the receiver loop and the exciter to determine the resultant downlink phase noise The loop transfer functions modify the noise spectral density of the individual contributors when referenced to the loop output The models for phase noise contributors common to all loops are developed first These contributors include oscillators, varactors, phase detectors, buffer amplifiers, multipliers, dividers, operational amplifiers, power converter circuits, regulators, and phase modulators These devices are modeled with the appropriate white phase, flicker phase, white frequency, and flicker frequency noise characteristics Each contributor is shown in the receiver and exciter block diagram (Fig A-1) as an ideal component plus an additive block that represents the phase-noise power spectral density of the component As shown in the block diagram, the phase noise density of each contributor is modified by the transfer function from the contributor to the output For example, the noise at the phase detector input will be modified by the receiver loop transfer function, which is a low-pass response, whereas the noise at the $12F_1$ VCO output will be modified by the loop error

transfer function, which is a high-pass response The receiver phase noise at the phase-locked VCO output is predicted by first calculating the contributions from the Ka-band, X-band, and L-band (1240 44 MHz) local oscillator circuits and using these phase noise density functions in the receiver loop The receiver VCO output phase noise density thus obtained is used in the exciter to predict the coherent downlink phase noise density at Ka-band The Ka-band downlink phase noise densities for the noncoherent AUX OSC mode are obtained by replacing the receiver VCO phase noise density by the AUX OSC oscillator phase noise density The predicted theoretical phase noise results are compared to the measured results in the following section

IV. Experimental Results

The Ka-band transponder breadboard (Fig 1), consisting of the Ka-band-to-X-band downconverter, Ka-band exciter, and DST-AEM, was implemented, and performance characterization was accomplished The evaluation measurements include receiver tracking-threshold sensitivity, static phase errors for Ka-band uplink frequency offset, swept acquisition characteristics, and AGC versus uplink signal level All measurements were made at a room temperature of 25 deg C The measured tracking-threshold sensitivity at the receiver best-lock frequency, approximately at channel center, is -149 dBm The measured receiver threshold characteristics show good correlation with expected performance (Appendix B) over the tracking range, as shown in Fig 2 The receiver acquisition characteristics were measured at an input signal level of -110 dBm The measured values for tracking range and tracking rate are ± 1 2 MHz at design center frequency and 800 Hz/s, respectively, and they meet the specified requirements (Table 1) Figure 3 shows a linear relationship for the static phase error voltage versus uplink frequency offset over the receiver tracking range The AGC loop-filter amplifier output voltage controls the gain in the first and second IF amplifiers The AGC voltage versus uplink signal level at the best-lock frequency and at frequency offsets of ± 1 2 MHz from best-lock frequency are shown in Fig 4 As the receiver input signal varies from a strong signal level (-70 dBm) to the threshold level, the AGC control voltage varies approximately linearly with better than 5 percent linearity No receiver false lock or self-lock resulted during the test phase

In the coherent carrier mode, residual phase noise is defined for a noise-free received-signal case The phase noise on the downlink carrier signal consists primarily of contributions from the four phase-locked oscillators, $12F_1$ VCO, SRO, X-band DRO, and Ka-band DRO, used in the Ka-band transponder implementation Individual phase-noise power spectral-density functions for these contributors are used in a comprehensive computer program (Appendix A) to predict the phase noise of the closed-loop receiver Total residual phase noise in the output is the mean square sum of all noise sources The predicted phase noise for the Ka-band transponder in the coherent mode is compared to the measured results in Fig 5

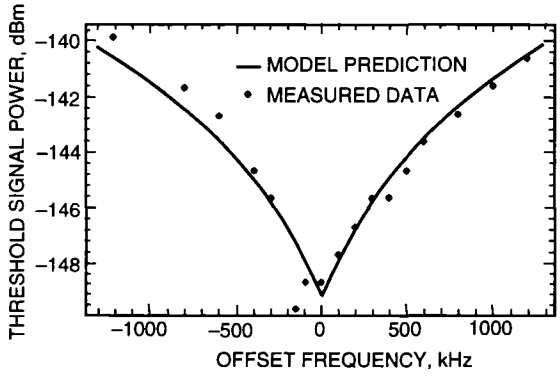

Fig 2 Ka-band transponder carrier tracking threshold versus offset frequency

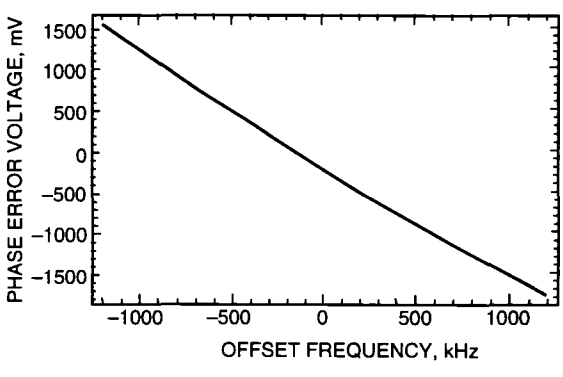

Fig 3 Ka-band static phase error voltage versus offset frequency

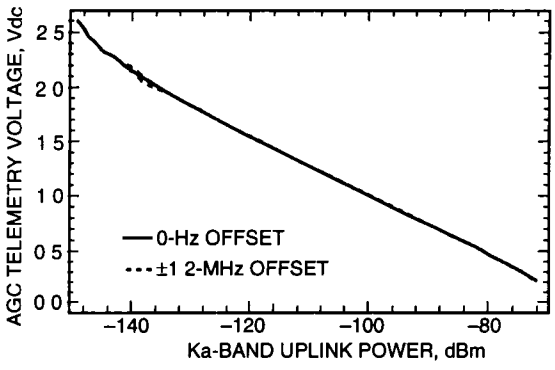

Fig 4 Ka-band transponder AGC voltage versus uplink signal level

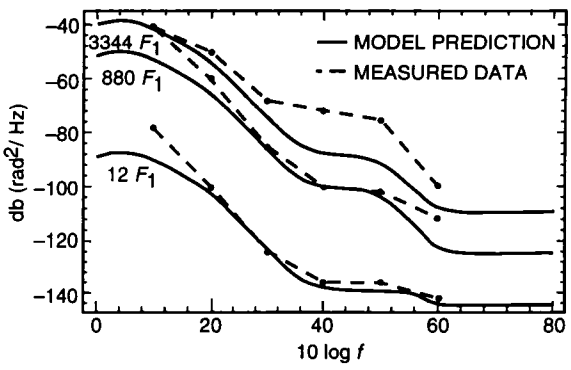

Fig 5 Comparison of theoretical and measured coherent-mode phase noise densities (uplink = −100 dBm)

Table 2 Predicted phase jitter and Allan deviation for coherent and noncoherent modes

Mode	Frequency	Phase jitter (5 Hz–25 MHz), deg rms	Allan deviation		
			$T = 0.01$ s	$T = 1$ s	$T = 1000$ s
Coherent	$12F_1$	0.02	1.5×10^{-10}	1.3×10^{-12}	9.3×10^{-16}
($P = -100$ dBm)	$880F_1$	0.80	3.6×10^{-11}	4.6×10^{-13}	4.5×10^{-16}
	$3344F_1$	3.10	4.6×10^{-11}	5.3×10^{-13}	4.9×10^{-16}
Noncoherent	$12F_1$	0.08	6.1×10^{-10}	3.2×10^{-11}	3.2×10^{-11}
(AUX OSC)	$880F_1$	1.98	4.8×10^{-11}	3.2×10^{-11}	3.2×10^{-11}
	$3344F_1$	7.60	5.8×10^{-11}	3.2×10^{-11}	3.2×10^{-11}

In the intervals between 5 Hz and 25 MHz on each side of the carrier, the rms phase noise is 7 deg, which is below the maximum allowable 8-deg rms for coherent downlink The dominant contributor to this rms phase noise is the $12F_1$ VCO and the ×4 multiplication process from X-band to Ka-band, the remaining contributions are less than 10 percent of the VCO contribution Predicted rms phase noise and Allan deviation are presented in Table 2 The results of the analysis indicate that the coherent mode specifications will be met for both the rms phase noise and Allan deviation The receiver PLL band limits the VCO spectrum, thus providing the superior performance in the coherent mode

A comparison of measured-to-calculated Allan standard deviation characteristics as a function of integration time is shown in Fig 6 The measured Allan standard-deviation values for the Ka-band transponder breadboard are in good agreement with the predicted values Figure 7 shows good agreement between the theoretical and measured phase-noise density curves for the noncoherent AUX OSC mode operation

A GaAs MMIC phase modulator developed under a Small Business Innovative Research Program contract at Pacific Monolithics, Inc , was used to modulate the X-band reference signal and upconvert (×4 multiplication) it to a Ka-band downlink signal, as shown in Fig 1 The modulator MMIC chip incorporates a single-stage input buffer amplifier and a three-stage lumped-element hybrid-coupled reflection phase shifter with metal-gate Schottky field-effect transistor (MESFET) varactors to provide a phase deviation of ±2 5 rad with better than 3-percent linearity The chip size is 2 49 × 0 91 mm Sinusoidal and square modulating waveforms were applied to the phase modulator, and their resulting spectra [12,13] were monitored on a calibrated spectrum analyzer All measurements were performed at 25 deg C

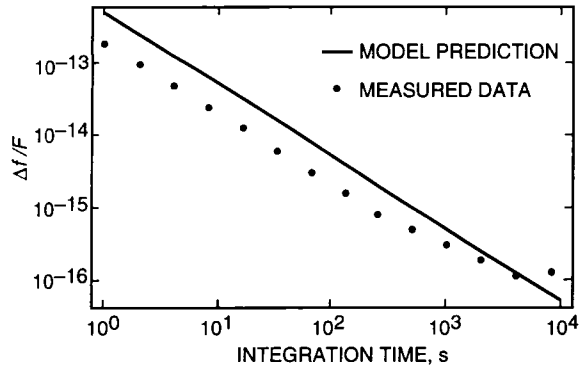

Fig 6 Ka-band transponder Allan deviation versus integration time

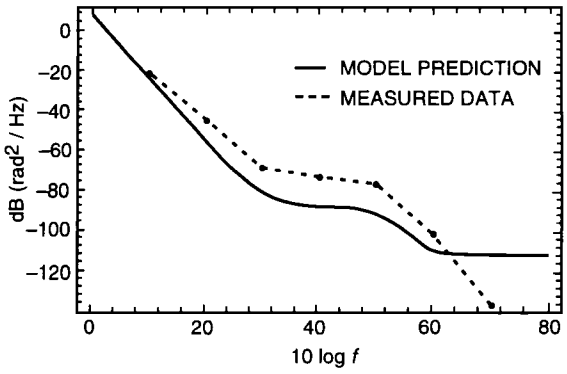

Fig 7 Comparison of theoretical and measured noncoherent-mode phase noise densities

and with a carrier frequency of 31,977 MHz A comparison of measured and predicted carrier, first, second, third, and fourth side-band levels for the case of sinusoidal modulation is shown in Fig 8 A modulation frequency of 100 kHz was used in the measurements The peak phase modulation index, β, ranges from 0 2 to 2 4 rad The predicted relative carrier and side-band levels were computed [12,14] by evaluating the appropriate Bessel functions of the first kind of order $n, J_n(\beta)$ The subscript n is an integer It represents the carrier for $n = 0$ and the side bands for $n \neq 0$ The relative carrier level for a given modulation index is determined by evaluating $20 \log |J_0(\beta)|$ Similarly, the relative side-band levels are determined by evaluating $20 \log |J_n(\beta)|$ for $|n| > 0$ Figure 8 shows excellent agreement between theory and measurement for sinusoidal phase modulating waves Negligible amplitude modulation distortion was observed in this case

A comparison of measured and predicted carrier, first, third, and fifth side-band levels for the case of square-wave modulation is shown in Fig 9 A modulation frequency of 100 kHz was used in the measurements The relative carrier level in decibels is determined by evaluating $20 \log |\cos(\beta)|$, where β is the peak modulation index The relative side-band levels is determined by evaluating $20 \log |2 \sin(\beta)/(n\pi)|$, where $n = 1, 3, 5,$, is the number of the side band Good agreement between predicted and measured square-wave modulation results is shown in Fig 9

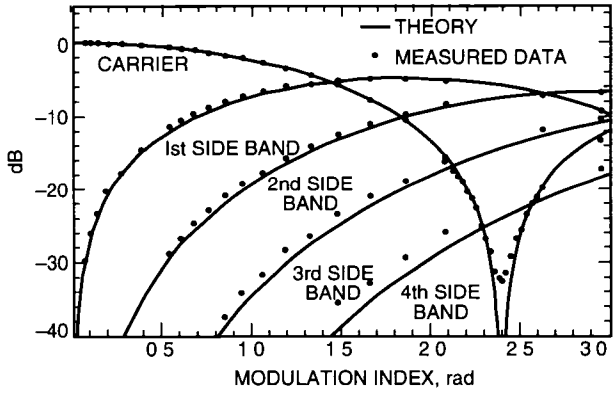

Fig 8 Measured and predicted Ka-band carrier, first, second, third, and fourth side band levels versus phase modulation index for the case of a sinusoidal modulating wave of 100-kHz frequency

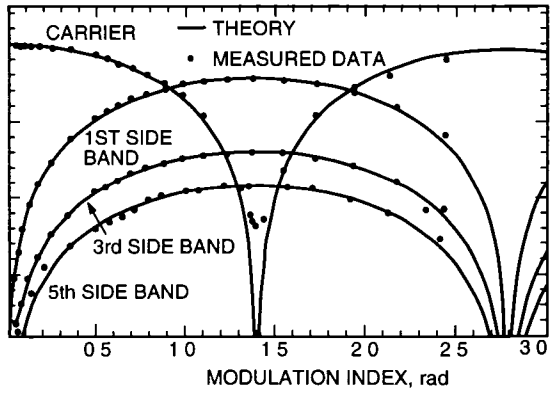

Fig 9 Measured and predicted Ka-band carrier, first, third, and fifth side band levels versus peak phase modulation index for the case of a square modulating wave of 100-kHz frequency

V. Conclusions

Design concepts and system architecture for a high-performance Ka-band transponder for deep-space spacecraft applications have been presented The Ka-band transponder has been successfully breadboarded and evaluated New technologies, such as a Ka-band DRO, X-band MMIC phase modulator, MMIC amplifiers, MMIC upconverter, and sampling mixers, have been integrated into the design The Telecommunication Development Laboratory measurements on the breadboard transponder achieved a threshold level of −149 dBm with a dynamic range of 80 dB and excellent acquisition and tracking characteristics The measured phase noise, Allan standard deviation, and phase jitter data are in good agreement with the predicted characteristics Measured carrier and relative side-band amplitudes resulting from phase modulation of the Ka-band downlink signal by sinusoidal and square-wave modulating functions agree well with the predicted results with negligible amplitude modulation distortion

References

[1] J H Yuen, *Deep Space Telecommunications Systems Engineering*, New York Plenum Press, 1983

[2] N R Mysoor, J D Perret, and A W Kermode, "Design Concepts and Performance of NASA X-Band (7162 MHz/8415 MHz) Transponder for Deep-Space Spacecraft Applications," *The Telecommunications and Data Acquisition Progress Report 42-104, October–December 1990*, Jet Propulsion Laboratory, Pasadena, California, pp 247–256, February 15, 1991

[3] J A Koukos, "Selection of Ka-Band Transponder Turnaround Frequency Ratios," *Report of the Proceedings of RF and Modulation Subpanel 1E Meeting at the German Space Operations Center, September 20-24, 1993*, CCSDS B20 0-Y-1, Consultative Committee for Space Data Systems, Oberpfaffenhofen, Germany, February 1994

[4] N R Mysoor, "An Electronically Tuned, Stable 8415 MHz Dielectric Resonator FET Oscillator for Space Applications," *Proc IEEE 1990 Aerospace Applications Conference*, Vail, Colorado, February 5–9, 1990

[5] N R Mysoor and F Ali, "Miniature X-Band GaAs MMIC Analog and Digital Modulators for Spaceborne Communications Applications," *Technology 2001 Conference Proceedings*, NASA Conference Publication 3136, vol 1, San Jose, California, pp 82–88, December 3–5, 1991

[6] F M Gardner, *Phaselock Techniques*, New York John Wiley, 1979

[7] A Blanchard, *Phase-Locked-Loops Applications to Coherent Receiver Design*, New York John Wiley and Sons, 1976

[8] J P Frazier and J Page, "Phase-Lock Loop Frequency Acquisition Study," *IRE Trans* , vol 8, pp 210–227, September 1962

[9] D B Leeson, "A Simple Model of Feedback Oscillator Noise Spectrum," *Proc IEEE*, vol 54, pp 329–330, February 1966

[10] J A Barnes, A R Chi, and L S Cutler, *Characterization of Frequency Stability*, National Bureau of Standards Technical Note 394, Washington, DC National Bureau of Standards, October 1970

[11] D W Allan, "Time and Frequency (Time-Domain) Characterization, Estimation, and Prediction of Precision Clocks and Oscillators," *IEEE Transactions on Ultrasonics, Ferroelectronics, and Frequency Control*, vol UFFC-34, no 6, pp 647–654, November 1987

[12] N R Mysoor and R O Mueller, "Performance of a 300-Degree Linear Analog Phase Modulator for Communications Applications," *Proc of IEEE 1993 Aerospace Applications Conference*, Steamboat Springs, Colorado, pp 43–52, February 1–5, 1993

[13] E A Whitman, "Phase Modulation Measurement Techniques for Improved Accuracy," *Microwave Journal*, vol 6, pp 113–116, June 1978

[14] F Stocklin, *Relative Side-Band Amplitudes vs Modulation Index for Common Functions Using Frequency and Phase Modulation*, Goddard Space Flight Center, distributed by National Technical Information Service, U S Department of Commerce, Springfield, Virginia, November 1973

Appendix A
Phase Noise Models

The phase noise models [6–11] and the equations used to calculate the downlink residual phase noise of the Ka-band transponder in the coherent and noncoherent modes are presented in this appendix

A block diagram of the Ka-band receiver and exciter phase noise models along with the major phase noise contributors are shown in Fig A-1 Each contributor is shown in the block diagram as an ideal component plus an additive block that represents the phase-noise power spectral density of the component

I. Phase Noise Models of Individual Contributors

A brief description of the phase noise models for the contributing circuits to all common loops is given below

(1) Buffer Amplifiers/Multipliers/Dividers/Phase Detector The buffer amplifiers are modeled to have a $1/f$ Halford noise plus a thermal noise floor The thermal noise floor is set by the input power level and the noise figure of the amplifier The phase noise density of operational amplifiers used in the loop filters is modeled similarly Also, phase noise contributions of multipliers, dividers, and phase detectors are obtained from a similar model

(2) Oscillators The oscillator phase noise density is based on Leeson's model [9] The phase noise model has a $1/f^3$ slope from a 1-Hz offset from the oscillator center frequency, followed by a $1/f$ slope and a thermal noise floor The model uses the flicker $1/f$ noise corner frequency of the FET, the noise figure of the FET, the bandwidth of the oscillator, and the varactor noise

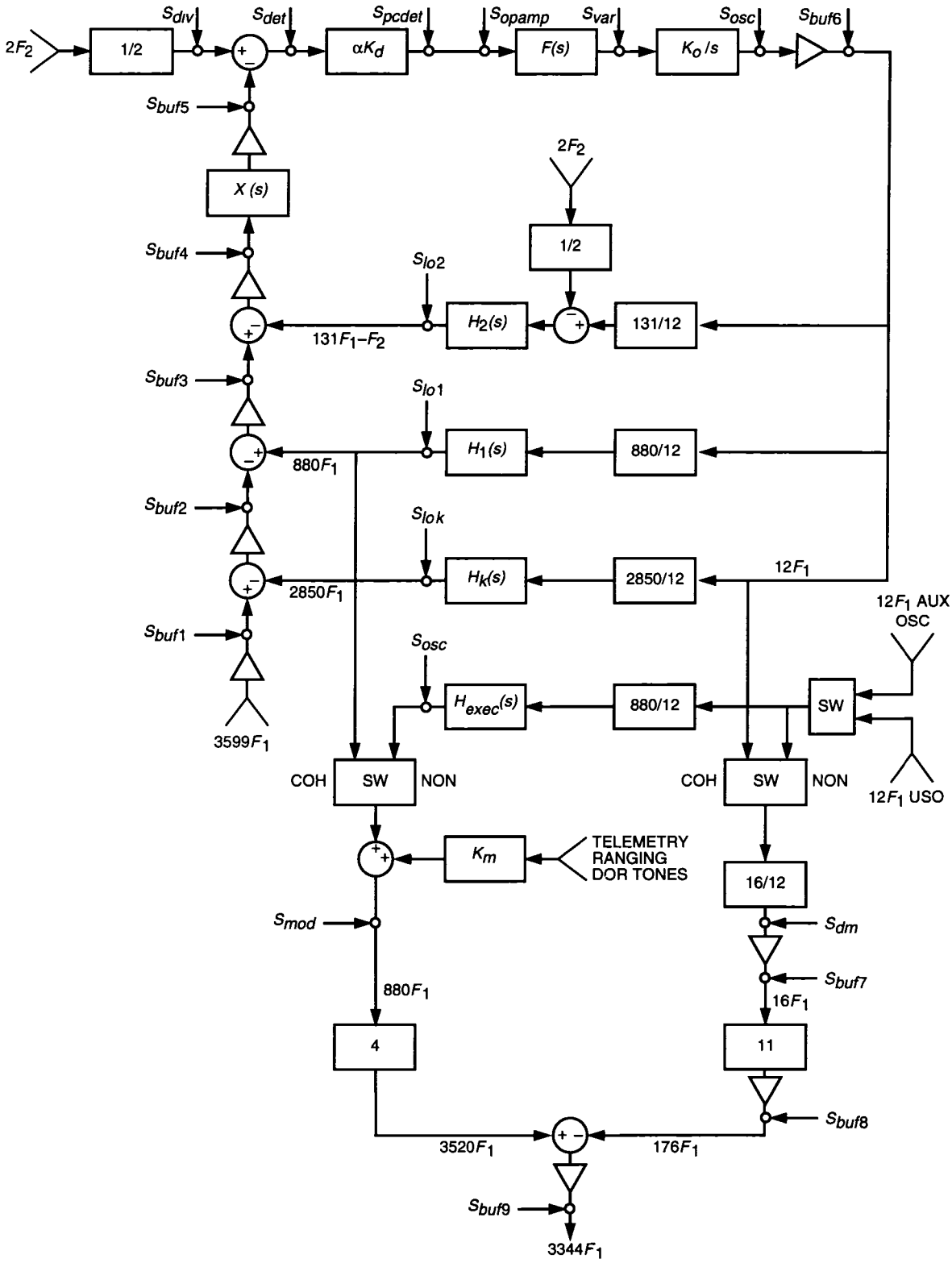

Fig A-1 Phase noise model for the Ka-band receiver and exciter circuit.

(3) Power Converter The phase noise model for the power converter is obtained from empirical data measured on the Tracking Data Relay Satellite Systems (TDRSS) second-generation user transponder

(4) Regulator The regulator is modeled as a high-pass filter response and a thermal noise floor The high-pass filter response of the regulator reduces the power converter noise at low frequencies to that of the reference zener diode

(5) Varactors The phase noise of varactors is modeled as the regulator output noise plus a thermal noise floor

(6) Phase Modulator The phase noise density of the phase modulator is caused by the power converter noise directly modulating the downlink and by the regulator noise driving the varactors

II. Downlink Noise Density at Ka-Band

The downlink phase noise density is shaped by the closed-loop transfer function of the receiver (H_c), the error transfer function of the receiver (H_e), and the transfer function from the input of the crystal filter to the output of the receiver (H_x) These transfer functions are given by

$$\left.\begin{aligned} H_c &= \frac{H_o}{1 + H_o H_{xtal} H_r} \\ H_e &= \frac{1}{1 + H_o H_{xtal} H_r} \\ H_x &= \frac{H_o H_{xtal}}{1 + H_o H_{xtal} H_r} \end{aligned}\right\} \tag{A-1}$$

where

$$\left.\begin{aligned} H_o &= \frac{\alpha K_d K_o H_{flt}}{s} \\ H_r &= \frac{880}{12} H_{lo1} - \frac{131}{12} H_{lo2} + \frac{2850}{12} H_{lok} \end{aligned}\right\} \tag{A-2}$$

In these equations, α is the signal suppression factor due to the limiter [1,5,6], H_{flt} is the receiver-loop filter transfer function, H_{lo1} is the DST-AEM receiver X-band DRO-loop transfer function, H_{lo2} is the DST-AEM receiver S-band SRO-loop transfer function, H_{lok} is the Ka-band DRO-loop transfer function, and H_{xtal} is the crystal filter transfer function The phase-noise power spectral density at the output of the $12F_1$ phase-locked VCO is given by

$$S_{12f} = S_1|H_c|^2 + S_2|H_e|^2 + S_3|H_x|^2 \tag{A-3}$$

where

$$\left.\begin{aligned} S_1 &= S_{buf5} + S_{det} + S_{div} + \frac{S_{pcdet} + S_{opamp}}{\alpha K_d^2} \\ S_2 &= S_{osc} + S_{buf6} + S_{var}\left(\frac{K_o}{f}\right)^2 \\ S_3 &= S_{buf1} + S_{buf2} + S_{buf3} + S_{buf4} + S_{lo1} + S_{lo2} + S_{lok} \end{aligned}\right\} \quad \text{(A-4)}$$

In these equations, $S_{buf_i}, S_{det}, S_{pcdet}, S_{opamp}, S_{div}, S_{var}, S_{lo1}, S_{lo2}, S_{lok}$, and S_{osc} denote the phase noise contributions of the ith buffer amplifier, the phase detector, the power converter at the phase detector, the operational amplifier, the divide-by-two divider, the varactor diode, the DST-AEM receiver X-band DRO loop, the DST-AEM receiver S-band SRO loop, the Ka-band DRO loop, and the DST-AEM receiver $12F_1$ VCO, respectively The remaining symbols, K_d, K_o, and f, denote the phase detector sensitivity in V/rad, the $12F_1$ VCO sensitivity in Hz/V, and the frequency in Hz, respectively

The phase noise density at the receiver PLL VCO output is used in the exciter to estimate the coherent Ka-band downlink phase noise density For noncoherent mode, the downlink phase noise density is obtained by replacing the PLL VCO phase noise density (S_{12f}) by the AUX OSC or USO phase noise density Thus, the Ka-band downlink phase noise density at $3344F_1$ is given by

$$S_{3344f} = 4^2 S_{12f}\left|\frac{220}{3}H_{880f} - \frac{11}{3}\right|^2 + 4^2\left(S_{880f} + S_{mod}\right) + 11^2\left(S_{buf7} + S_{dm}\right) + S_{buf8} + S_{buf9} \quad \text{(A-5)}$$

where H_{880f} and S_{880f} are, respectively, the transfer function and the phase noise density of the DST-AEM exciter X-band DRO loop for noncoherent operation or the receiver X-band DRO loop for coherent operation, S_{mod} is the phase noise contribution of the X-band phase modulator, and S_{dm} is the phase noise contribution of the 16/12 divider–multiplier circuit

Appendix B
Carrier-Tracking Threshold Calculations

The equations used to calculate carrier-tracking threshold data are presented in this appendix The carrier-tracking threshold of a PLL receiver [1,6,7] is defined as the minimum uplink signal required to maintain lock at any given offset from best-lock frequency It is a measure of an important limitation on spacecraft receiver performance At the best-lock frequency, the carrier-tracking threshold signal level is determined from the following equation

$$\frac{SL}{kTF\left(2B_{LO}\right)} = 1 \quad \text{(B-1)}$$

where S is the receiver input-signal power level, k is Boltzmann's constant, T is the reference system temperature, F is the receiver noise figure at the transponder input, B_{L0} is the one-sided noise-equivalent receiver carrier-tracking loop bandwidth at threshold, and L is the receiver carrier channel loss The

calculated value of the worst-case receiver carrier-tracking threshold is equal to −149 dBm for a $2B_{LO}$ of 72 Hz, channel loss of 1 dB, and a noise figure of 5 4 dB (including isolator, filter, LNA, and connectors) at 290 K

Note that the carrier-tracking threshold signal level can also be expressed in terms of the variance of the phase error due to additive channel noise by

$$\sigma_\theta^2 = \frac{kTFB_{LO}}{SL} = \frac{1}{2} \tag{B-2}$$

Therefore, at threshold, the standard deviation of the phase error is $\sigma_\theta = 0\ 707$ If the uplink signal frequency is offset from the best-lock frequency by Δf Hz, the phase detector is required to operate with a static phase error of Θ_e rad, given as

$$\Theta_e = \sin^{-1}\left(\frac{2\pi\Delta f}{\alpha K_v}\right) \tag{B-3}$$

where K_v is the dc gain of the PLL and α is the receiver limiter suppression factor, given by

$$\alpha = \frac{1}{\sqrt{1 + \frac{4}{\pi}\frac{kTFB_{if}}{SL}}} \tag{B-4}$$

Here B_{if} is the noise-equivalent predetection bandwidth This static phase error reduces the threshold phase-error standard deviation to $\sigma_\theta = 0\ 707 - \Theta_e$, such that the carrier-tracking threshold corresponding to the frequency offset of Δf Hz needs to satisfy

$$\sigma_\theta^2 = \frac{kTFB_{LO}}{SL} = \left(\frac{1}{\sqrt{2}} - \Theta_e\right)^2 \tag{B-5}$$

The one-sided noise-equivalent carrier-tracking loop bandwidth at threshold, B_{LO}, is given by

$$B_{LO} = \frac{1 + \frac{K\tau_2^2}{\tau_1}}{4\tau_2\frac{1+1}{K\tau_2}} \tag{B-6}$$

where τ_1 and τ_2 are the loop filter time constants and K is the open loop gain of the PLL, given by

$$K = \alpha K_v \cos(\Theta_e) e^{-0\ 5(0\ 707 - \Theta_e)^2} \tag{B-7}$$

Note that the open loop gain of the PLL includes factors for the reduction of the phase detector sensitivity due to the static phase error and the additive channel noise

Referees

The following people have refereed articles for *The Telecommunications and Data Acquisition Progress Report* By attesting to the technical and archival value of the articles, they have helped to maintain the excellence of this publication during the past year

D A Bathker	M L Belongie	J C Breidenthal	M J Britcliffe
M Calhoun	C C Chen	U Cheng	K -M Cheung
J J Cucchissi	T Cwik	D Divsalar	S Dolinar
L Ekroot	J Ellis	M S Esquivel	M Gatti
J Gevargiz	R S Gross	G Hajj	M Herman
R L Horttor	W A Imbriale	A Kiely	C L Lawson
K M Liewer	R P Linfield	L Maleki	F McLaughlin
T T Pham	F Pollara	P Priest	D L Rascoe
D Rogstad	R Sadr	E M Standish	P Stanton
S Stewart	L Swanson	M Thorburn	S W Thurman
S A Townes	S Tyler	V A Vilnrotter	J Yu

End of Document